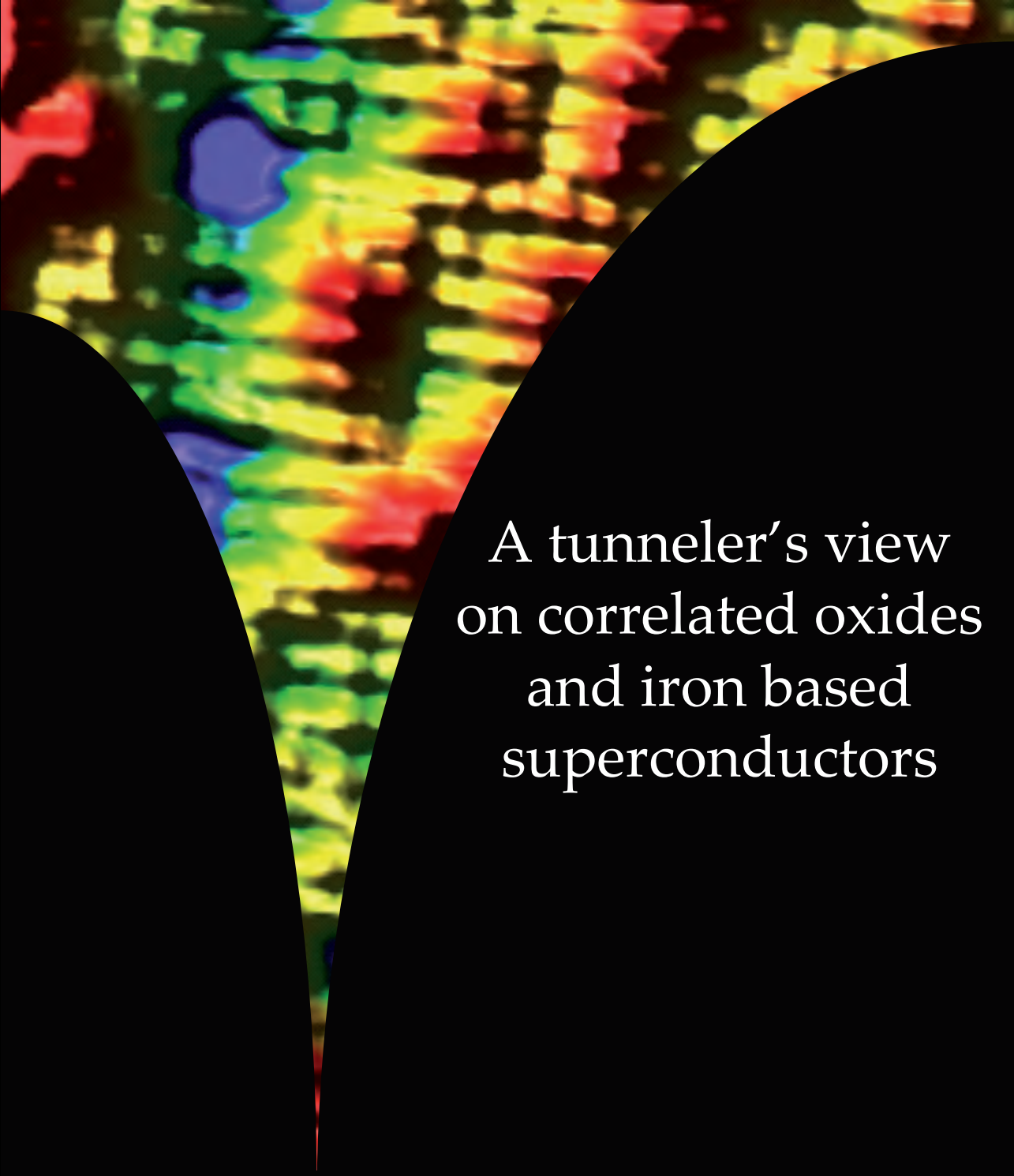

A tunneler's view on correlated oxides and iron based superconductors

Freek Massee

Stellingen behorende bij het proefschrift

'A tunneler's view on correlated oxides and iron based superconductors'

door Freek Massee

1. Het oppervlak van de Ba122 pnictide supergeleiders bestaat uit een halve bariumlaag die zich in verschillende patronen kan ordenen of wanordelijk is. *Hoofdstuk 4 van dit proefschrift*

2. De pseudogaptoestand is geen vereiste voor onconventionele supergeleiding. *Hoofdstuk 6 van dit proefschrift*

3. Stapelfouten in $La_{2-2x}Sr_{1+2x}Mn_2O_7$ zijn de natuurlijke verklaring voor lokaal afwijkend elektronisch gedrag in een groot deel van het 'metallische' gebied van het fasediagram. *Hoofdstuk 9 van dit proefschrift*

4. Het 'minder is meer' principe is uitermate van toepassing op vacuümsystemen.

5. Een STM kan een bijzonder dure oplossing zijn om de werktijden van bouwvakkers te registreren. *Appendix D van dit proefschrift*

6. De vraag wat eerder kwam, de kip of het ei, is in het licht van de evolutietheorie niet goed gedefinieerd.

7. Voor een fysiek verantwoorde ontspanning kan men beter met de Wii console zelf overgooien.

8. Aan dit proefschrift liggen een aantal goede tips ten grondslag die helaas inmiddels onbruikbaar zijn voor volgend werk.

9. Het begrip 'welvaart' lijkt vreemd genoeg omgekeerd evenredig te zijn met de daadwerkelijke fysieke en geestelijke toestand van de bewoners van een maatschappij.

10. Beperkte financiële middelen en/of een gebrek aan binding met de medewerkers zijn de enige geldige redenen voor de invoering van kantoortuinen (o.a. binnen de academische wereld).

Propositions belonging to the dissertation entitled

'A tunneler's view on correlated oxides and iron based superconductors'

by Freek Massee

1. The surface of the Ba122 pnictide superconductors consists of half a barium layer which can order in various patterns or disorder. *Chapter 4 of this dissertation*

2. The pseudogap state is not a requirement for unconventional superconductivity. *Chapter 6 of this dissertation*

3. Stacking faults in $La_{2-2x}Sr_{1+2x}Mn_2O_7$ are the natural explanation of locally deviating electronic behaviour over a large part of the 'metallic' region of the phase diagramme. *Chapter 9 of this dissertation.*

4. The 'less is more' principle is particularly appropriate when dealing with vacuum systems.

5. A STM can be a rather expensive solution to monitor the hours of construction workers. *Appendix D of this dissertation*

6. The question what came First, the chicken or the egg, is in light of the theory of evolution not well defined.

7. For a physically sensible exercise one should rather play catch with the Wii console itself.

8. At the basis of this thesis are several good tips, of which unfortunately none is still useful for future work.

9. The term 'prosperity' seems oddly enough inversely proportional to the actual physical and mental state of the inhabitants of a society.

10. Limited financial resources and/or a lack of bonding with the employees are the only valid reasons for installing office gardens.

A tunneler's view on correlated oxides and iron based superconductors

Academisch Proefschrift

ter verkrijging van de graad van doctor
aan de Universiteit van Amsterdam,
op gezag van de Rector Magnificus prof. dr. D.C. van den Boom,
ten overstaan van een door het college voor promoties ingestelde
commissie, in het openbaar te verdedigen in de Agnietenkapel
op dinsdag 12 april 2011, om 14.00 uur

door

FREEK MASSEE

geboren te Hoorn

Promotiecommissie:

Promotor:	Prof. dr. M. S. Golden
Copromotor:	Dr. J. B. Goedkoop
Overige leden:	Prof. dr. M. Bonn
	Prof. dr. J. C. Davis
	Dr. A. A. Golubov
	Prof. dr. D. M. de Leeuw
	Prof. dr. Ch. Renner
	Prof. dr. J. T. M. Walraven

Faculteit der Natuurwetenschappen, Wiskunde en Informatica

ISBN: 978-94-91211-09-6

Cover: impression of a tip used for the tunneling experiments constructed from an image of bilayered LSMO with atomic resolution.

Printed by Ipskamp Drukkers, typeset with LaTeX.

The work described in this thesis was performed at the Van der Waals - Zeeman Institute of the University of Amsterdam, The Netherlands, and is part of the research programme of the Foundation for Fundamental Research on Matter (FOM), which is part of the Netherlands Organisation for Scientific Research (NWO). A digital version of this thesis can be obtained from `http://dare.uva.nl/` or `http://www.science.uva.nl/research/cmp/`.

Contents

Symbols and Abbreviations

Symbols

Δ_{pp}	peak-to-peak energy gap
E_F	Fermi energy
k_B	Boltzmann constant
$g(r, E)$	local density of states
Φ	work function
σ	spread in the superconducting gap
T_c	superconducting transition temperature
T_C	Curie temperature

Abbreviations

AFM	anti-ferromagnetic metallic
ARPES	angle resolved photoemission spectroscopy
BCFA	$BaCo_xFe_{2-x}As_2$
BCS	Bardeen-Cooper-Schrieffer
BFPA	$BaFe_2P_xAs_{2-x}$
Bi2212	$Bi_2Sr_2CaCu_2O_{8+\delta}$
BRFA	$BaRu_xFe_{2-x}As_2$
CMR	colossal magneto resistant/resistance
CO/OO	charge order/orbital order
FFT	fast Fourier transform
FOV	field of view
LEED	low energy electron diffraction
LDA	local density approximation
LDOS	local density of states
LSMO	$La_{2-2x}Sr_{1+2x}Mn_2O_7$
*M*122	$MFe_{2-x}As_2$
(Pb,Bi)2212	$Pb_xBi_{2-x}Sr_2CaCu_2O_{8+\delta}$
SDW	spin density wave
STM	scanning tunneling microscope/microscopy
STS	scanning tunneling spectroscopy
UHV	ultra high vacuum
ZBC	zero bias conductance

CHAPTER

1 Introduction

Within the field of condensed matter physics many materials can be found that have complex, often exotic and usually not well understood properties. Aside from the drive to understand what brings about these properties, the prospect of putting such materials to use for applications is one of the main motivations to study them. The work described in this thesis is concentrated on two different families of such complex materials, namely the superconducting iron based pnictides and the colossal magnetoresistant manganites. Although the properties of these two families are rather different, comparisons can still be drawn between them. For instance, in both systems magnetism plays a crucial role and the interplay between the lattice and the electronic structure, although different in detail, is important in both cases. Unlike their famous cuprate cousins, an important part of the complexity both these quantum matter systems lies in their orbital degrees of freedom, whereby the frontier electronic states have two or more different 3d orbitals to choose from. The explicit role of - for example - orbital ordering has been clear in the manganites from the outset, while this realisation is currently growing in the iron pnictides. Interestingly, the crystal structure of the manganites is nearly identical to that of the cuprates, whereas many properties of these cuprates are, in turn, seen back in the pnictides. Therefore, even though this thesis is split into two seemingly independent parts, the underlying physics describing both emergent types of complex matter systems might in fact be very similar.

1.1 Iron based high temperature superconductivity

While trying to find a transparent oxide semi-conductor, H. Hosono and co-workers stumbled upon an iron based material with an unusually large superconducting transition temperature of 26 K [1]. Within a short period of time several different families of iron based materials were found with superconducting transition temper-

atures reaching as high as 55 K [2], well in excess of the originally predicted limit of ~ 40 K for conventional superconductors [3] [1]. These discoveries resulted in a world wide drive to study the origin of superconductivity in these iron based materials, partly in the hope it could add to the ongoing debate on the physics driving superconductivity in the well established family of high-T_c superconductors, the cuprates, but also from an applications point of view. For instance, although these newly discovered materials are, like the cuprates, layered, their anisotropy is generally much smaller, and the parent compounds are metallic. Moreover, as the pairing symmetry is now believed to be of s-wave character, grain boundaries will pose less of a problem than they are for instance for d-wave cuprate superconducting wires. Lastly, the mechanical properties are considerably advantageous over those of the cuprates as wires are for instance more easily drawn.

At the time of the discovery of the iron based superconductors, the main focus of the Ph.D. work presented here was the investigation of the colossal magnetoresistant manganites. However, when synthesis of the '122' family of pnictides was achieved in our research group by Y. K. Huang, it was decided to also investigate the pnictides. At that time, only two preprints reporting scanning tunneling microscopy and spectroscopy (STM/S) measurements on pnictides existed, and the field was fresh and wide open: basically everything was uncharted territory. Having got up to speed with the STM/S system on the bilayered manganites - and after getting the machine up and running on typical calibration samples such as graphite, writing analysis programs and modifying the setup to increase its capabilities and effectiveness - the pnictides formed a welcome change of subject displaying a zoo of surface topographies and strongly varying superconducting gaps, all of which are discussed in the first four experimental chapters.

1.2 Colossal magnetoresistant manganites

Next to the high temperature superconductors, the colossal magnetoresistant manganites are one of the main thrusts of both theoretical and experimental investigations in complex hard condensed matter physics. Despite years of research, the physics underlying the colossal change in resistivity upon application of a magnetic field is not fully understood and remains a hot topic. For application purposes, this knowledge is essential for the tuning of the transition temperature and of the magnitude of the change in resistivity. The existence of coherent quasi-particle weight at the Fermi level seen with angle resolved photoemission (ARPES) on the bilayered material $La_{2-2x}Sr_{1+2x}Mn_2O_7$, despite evidence from bulk probes that this material is a poor metal at most, i.e. one with a relatively high resistivity, has started a lively discussion as to the origin of these truly metallic spectra, all the more since ongoing research within our research group found that only a very small portion of the sample surface displays such peaked spectra [6].

[1] although Refs. [4, 5] have shown that this limit is actually not a limit at all, it is still commonly seen as a special temperature for a T_c to exceed

In an effort to elucidate the origin of these quasi-particle peaked regions and to find an explanation for the colossal magnetoresistant effect that is particularly strong in these bilayered manganites, the focus of this part of the Ph.D. research was to try and find such regions and determine their properties on the atomic scale using the newly installed scanning tunneling microscope. The first year and a half of the research presented in this thesis were therefore devoted to scanning surfaces of bilayered manganites with various doping concentrations. Combined with the ARPES investigations, a compelling explanation of the quasi-particle peaked areas and the 'metallic' bilayered manganites as a whole was found, which is presented in chapter 9.

1.3 Outline of this thesis

The first 'real' chapter of this thesis, chapter 2, introduces the technique of scanning tunneling microscopy and spectroscopy (STM/S), both from a theoretical and experimental point of view, and gives an introduction to low energy electron diffraction (LEED). To improve the readability of the chapter, details on the art of making tips, tip characterisation and a number of calibration measurements are given in the various appendices.

Having introduced the experimental setup, the main body of the thesis is divided into two parts. Part I describes the research done on the iron based superconductors, and Part II that on the bilayered manganite $La_{2-2x}Sr_{1+2x}Mn_2O_7$.

The first chapter of part I, chapter 3 introduces superconductivity in general and the iron based pnictides in particular by giving a short overview of the existing literature on the subject. Chapter 4 then tackles an important part of any surface sensitive study: the cleavage surface of the '122' pnictide family of materials. Before being able to make any statement about a material from its investigation with a surface sensitive technique such as STM/S or angle resolved photoemission (ARPES), one should know what the properties of the surface layer are and whether or not the presence of a surface affects the results obtained by the study. In this chapter a combination of temperature dependent STM, STS and LEED investigations on various '122' pnictide systems demonstrate that cleavage of these systems occurs within the Ba layer, leaving half a Ba layer on each side of the cleave. This Ba layer is shown to be disordered or to be ordered into ($\sqrt{2} \times \sqrt{2}$) and (2×1) structures, all of which can cross over into one another. A considerable, non-reversible temperature dependence of the structures is furthermore observed. At the end of the chapter a simple model explaining the various surface appearances is presented.

Having thoroughly investigated the properties of the cleavage surface, chapter 5 describes the investigation of the electronic states of the optimally doped Ba122 compound, focusing in particular on the superconducting energy gap. In the first place, it is found that the electronic states as seen with STM are little affected by the details of the surface topology. Secondly, a large variation in the peak-to-peak separation, which is interpreted as the superconducting gap size, is found as a func-

tion of real space position. A correlation between the peak height, gap size and zero bias conductance is found in the system, similar to what is seen in the cuprates. As measurements on non-doped Ba122 show relatively small variation in zero bias conductance, the variation seen in the electronic properties of the superconductor are shown to be connected to the superconducting state and not the material in general. The size of the normalised gap is shown to be well beyond the BCS s- and d- wave values, suggesting an unconventional mechanism of superconductivity. By examining the autocorrelation traces of gap maps, the length scales of the variation in gap magnitude are seen to be on the order of the Co-Co separation, hinting at a connection between these two.

The observation of a large spatial variation in peak-to-peak separation in the tunneling spectra discussed in chapter 5 are very reminiscent of the cuprate systems, where similar variations have been observed, which turned out to be related to a pseudogap rather than the superconducting gap. In order to see whether in the pnictides this variation is also related to a pseudogap that does not close at T_c, temperature dependent measurements of the superconducting gap have been performed for various doping concentrations. It is shown that the observed gaps all close at T_c, ruling out a pseudogap and assigning the peak-to-peak separation to the superconducting gap.

In chapter 7, the origin of the large variation in superconducting gap size is further investigated by a detailed doping dependent study and measurements on differently doped Ba122 materials.

Part II of this thesis describes the STM/S investigations performed on the bilayered colossal magnetoresistant manganite $La_{2-2x}Sr_{1+2x}Mn_2O_7$, which was the original subject of this Ph.D. research. Various doping concentrations of this manganite material were investigated using STM/S, at the same time as detailed ARPES investigations were performed on identical crystals during numerous visits to large scale light source facilities in Berlin and Villigen (CH). After introducing the manganite family of materials and in particular the bilayered manganite $La_{2-2x}Sr_{1+2x}Mn_2O_7$ in chapter 8, the last chapter will discuss these STM/S investigations, which taken together with ARPES form the basis of a compelling description of the manganites and their colossal magnetoresistant effect in terms of polaronic conduction close to a metallic breakdown, contrary to the commonly adopted picture of a double exchange driven metal to insulator transition.

This thesis describes the first Ph.D. research at the van der Waals Zeeman Institute performed with a Createc ultra high vacuum, low temperature scanning tunneling microscope. To benchmark the system, measurements on
$Bi_2Sr_2CaCu_2O_{8+\delta}$ and $Pb_xBi_{2-x}Sr_2CaCu_2O_{8+\delta}$ which have been intensively studied in the literature, have been performed, which are discussed in appendix A. It will be shown that with the commercially available setup used it is possible to obtain not only high resolution topographic images, but also spatial maps of the energy gap over large fields of view as well as maps of the local density of states at energies that show quasi-particle interference scattering patterns. Following the literature on

these two systems closely, all these different types of measurement and their analysis will be presented.

As considerable time in this research has been devoted to the art of making one of the crucial elements in tunneling microscopy, the tip, appendix B reviews various methods used to produce both tungsten and platinum-iridium tips and the characterisation thereof on a Au(788) sample. Adaptations to the setup to incorporate *in situ* oxide removal of tips and to have a higher measurement efficiency will also be discussed.

Appendix C will discuss the calibration of the temperature of the STM, using a thermometer in the place of a sample holder in the STM and by temperature dependent measurements on the BCS superconductor Nb. Experimental and thermal broadening of the spectra will be discussed in detail, which are relevant in the discussion of the temperature dependence of the pnictide superconductor data presented in chapter 6.

The resolution of any STM is mainly limited by noise, both electromagnetic and vibrational. Appendix D will therefore discuss the detection and reduction of noise in the setup and will give an overview of the noise present in the system used and its effect on the resolution.

In the last appendix (E), the software written throughout this research will be briefly discussed, focusing on the routines used to load data saved by the Createc measurement software into the analysis program Igor. It should be noted that this appendix is rather specific and therefore less of general interest, most probably being of more use to following generations of STM practitioners in Amsterdam than to for instance members of the Ph.D. committee. It is (like the other appendices) not required for a full understanding of the work described in this thesis. The algorithm used to construct gap maps will be described and the appendix will close with a section on various parameters used throughout this work on different systems (setup currents, modulation frequencies, approach settings, etc.).

CHAPTER

2 Experimental background and technique

In this chapter the experimental background and setup will be described in some detail. A theoretical and experimental description of the STM system used will be given. One system was used for all STM/S measurements described in this thesis. The system is the commercially available LT-STM from *SPS-CreaTec GmbH* [7] which has been adapted during the course of the research described in this thesis, so as to better match the demands of the experiments undertaken. The basic workings of the machine and essential changes will be described. At the end of the chapter, a short introduction to LEED and the corresponding setup used will be given. This technique will be used in the next chapter in the discussion of the cleavage surface of the '122' pnictides.

2.1 Scanning Tunneling Microscopy / Spectroscopy

'When two metals are separated by a thin insulating film, electrons can flow between the two conductors due to the quantum mechanical tunnel effect.'[1] The first observation of tunneling through an insulating barrier was reported in 1960 by I. Giaever [8], who measured current-voltage characteristics of superconducting metals such as Al and Pb separated by an oxide layer of 15-20 Å. These experiments formed the basis of the development of the scanning tunneling microscope two decades later by G. Binnig and H. Rohrer at IBM Zürich [9]. A detailed account of events leading up to the formation of the first STM are addressed in the lecture given by both discoverers at the presentation of their 1986 Nobel Prize in Physics [10]. Within a year, mono-atomic steps were observed [11] and even atomic resolution was obtained [12]. Within a few years, other groups were convinced of the power of this new technique, which can non-destructively probe the electronic structure with an unprecedented spatial resolution and high energy resolution. In the context of this thesis, it is noteworthy that the first observation of spatial variations, on the order of 13 nm, of a superconducting gap magnitude were reported in 1985 on Nb_3Sn, only a few years after the first STM was build [13].

Despite many improvements in the detailed design of STMs over the years, in order to increase the sensitivity and reduce the noise, the key ingredient is still one or multiple piezoelectric crystals [2] which drive a metallic tip to the surface under investigation and enable picometer resolution spatial control. At the time of writing, a typical STM setup can keep a tip on the same atomic position up to a few days at low temperature (i.e. a few Kelvin). The limiting factor is actually the temperature, as the setup needs to be refilled with liquid helium and nitrogen every few days which cannot be performed while measuring.

2.1.1 Tunneling theory

The wavelike nature of electrons allows for tunneling from one conductor to another through a classical barrier such as vacuum. Considering the simplest tunneling configuration, where two conductors are separated by a two-dimensional uniform barrier, the tunneling current is found by solving the one dimensional Schrödinger equation (see for instance Ref. [14], pages 328-330, for the full derivation):

$$I \propto \exp[-\sqrt{\frac{8m_e\Phi}{\hbar^2}}d], \tag{2.1}$$

where m_e is the electron mass, d is the width of the barrier and Φ is the barrier height, or work function. In practice, the relation for one dimensional tunneling is a good approximation to the height dependence of the tunneling current in an actual STM experiment, although for a more exact description refinements should

[1] first sentence of I. Giaever, Phys. Rev. Lett. **5**, 464 (1960)

[2] piezoelectric crystals deform upon application of a voltage across the crystal, typically a few to a few tens of ångstroms per Volt

be made to take into account for instance a difference in the work function of the sample and the tip. The (sub-) picometer height sensitivity of the STM stems from the exponential dependence of the tunneling current on the barrier width.

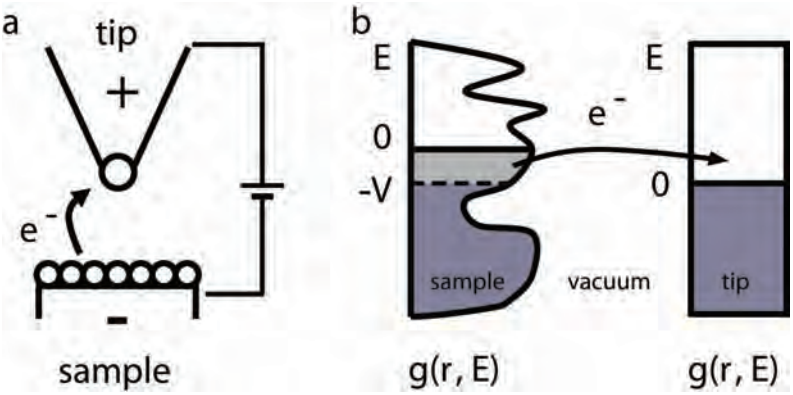

Figure 2.1: (a) Schematic of an atomically sharp metallic tip in proximity of a surface. (b) Cartoon of the density of the states of the sample (left) and tip (right), where the occupied DOS is shaded. A negative bias voltage, V, is applied to the sample, shifting the Fermi level of the sample with an amount V with respect to the Fermi level of the tip. Electrons will tunnel from the region of the sample DOS shaded in light grey to the tip through the vacuum leading to a current.

In order to arrive at an expression for the bias voltage dependence of the tunneling current, in addition to the barrier height dependence described by Equation (2.1), Fermi's golden rule is commonly used to describe electron transitions within perturbation theory. Consider the situation sketched in Fig 2.1a. The current that will flow between the tip and the sample is described by [15]:

$$I = \frac{4\pi e}{\hbar}\int_{-\infty}^{\infty} |M|^2 g_t(r,E) g_s(r,E+eV_{bias}) \times\{f(E)[1-f(E+eV_{bias})] - f(E+eV_{bias})[1-f(E)]\}dE, \quad (2.2)$$

where f(E) is the Fermi function, V_{bias} the applied bias voltage and M the matrix element for tunneling between the tip and the sample, which have a local density of states $g_t(\vec{r},E)$ and $g_s(\vec{r},E-eV_{bias})$, respectively. Incorporated in Equation (2.2) are both tunneling from the sample to the tip and vice versa. However, if for instance $V_{bias} < 0$, tunneling from the sample to the tip will dominate and the reverse contribution can be neglected. In the limit where the temperature goes to zero, and assuming a constant tip density of states, i.e. $g_t(\vec{r},E) = g_t(\vec{r},0)$, Equation (2.2) reduces to:

$$I = \frac{4\pi e}{\hbar} g_t(r,0)\int_{-eV}^{0} |M|^2 g_s(r,E+eV_{bias})dE, \quad (2.3)$$

where the integral now runs over the energy range of interest only, namely from -eV to 0 (or from 0 to eV for a positive bias voltage), where 0 is the Fermi energy of the tip. The details of the tunneling process are hidden in the tunneling matrix element M. Shortly after the first tunneling experiments by Giaever [8] and Nicol, Shapiro and Smith [16], Bardeen showed that 'it is plausible to treat M as a constant in the interpretation of the experiments' [17]. If one assumes a uniform 2D barrier and a tip to sample distance large enough that the wavefunctions of the tip and the sample do not hybridise, $|M|^2$ reduces to the exponential in Equation (2.1).

In a real life STM experiment, the barrier is not uniform, and the shape and orbital character of the tip have to be taken into account to be able to describe the current in detail. Tersoff and Hamann [18, 19] were the first to simulate STM measurements and already found excellent agreement with experimental results using a simple model where the tip was assumed to be of s-wave character with a spherical apex. Since then, refinements of this model have lead to even more striking agreement with experiment, enabling one to explain the fine details of images with atomic resolution, see for instance Ref. [20, 21] for an overview of the developments in this field. The dependence of the tunneling current on the details of the tip is nicely illustrated by measurements on a metallic material such as gold (see Ref. [22] for an overview of STM measurements on various Au(111) vicinal surfaces). As the electrons in single crystalline gold are highly delocalised, the observation of atoms on the surface [23] has been shown to require either a special tip orbital to pick up the atomic corrugation [24] or a deformation of the tip and/or surface due to tip-sample interactions [25].

By taking the matrix tunneling element, M, out of the integral in Equation (2.3), the current can thus to a good approximation be described by a prefactor times the integral from 0 to the bias voltage over the sample density of states. In case there is no spatial variation in the local density of states of the sample, scanning the surface, while adjusting the tip-sample distance to keep the current constant, will give the height profile of the surface. Such a measurement will be referred to as a constant current image or topograph. However, if the local density of states, g(r,E) or LDOS, is spatially inhomogeneous, a convolution of the height and LDOS is captured and care should be taken in the interpretation of the constant current images. A good example of the influence of the LDOS on topographs is graphite, where only half of the surface atoms are imaged due to an inequivalence in the LDOS of the atomic sites of the top layer [26].

The full power of the STM lies in the combination of its ability to image the surface profile on an atomic scale and probe the LDOS *simultaneously*. Using a straightforward lock-in technique, the derivative of the current with respect to the energy (= voltage) is obtained, which, as can be seen from Equation (2.3), is directly proportional to the local density of states of the sample, g(r,E). If such a differential conductance, or dI/dV, measurement is performed on a spatial grid of pixels, a 3D block of data is obtained: a conduction- or LDOS map. A slice through a conduction map, where for a certain energy the spatial distribution of the LDOS is imaged, is

called an LDOS or g(r,E) image.

2.1.2 Barrier height or work function, Φ

Before moving on to the design of the STM used in this work, the apparent barrier height briefly mentioned in the previous section will be discussed in more detail. The barrier height, or work function Φ, appearing in Equation (2.1) is the energy an electron requires to escape from a material to the vacuum and is typically on the order of a few eV. However, in tunneling experiments, electrons do not escape into vacuum, but tunnel from one material to another with a vacuum in between. The apparent barrier height will then be equal to the average of the work functions of the two materials, i.e. $\Phi = \frac{1}{2}(\Phi_{\text{tip}} + \Phi_{\text{sample}})$ [27,28].

The work function extracted from tunneling experiments has been shown to be independent of the tip-to-sample separation as long as this separation is not in the point contact regime [29]. Since the barrier height is a material dependent property, the STM is in principle capable of determining what element(s) reside(s) at the surface of a material. As most materials have a similar work function, and different tips can have different work functions, this is unfortunately rather intricate in practice. However, the average barrier height from measurements on several samples with several tips can give a good indication of the surface atomic character. Moreover, from the comparison of work functions of different surface structures on the same material measured with the same tip, one can decide if the different surface structures are due to a different surface atom. This will be used in chapter 4 in the discussion of the cleavage surface layer of the pnictide '122' high-T_c superconductors.

2.1.3 STM design

Since STM/S is only sensitive to the surface layer of a material, measurements have to be performed under extremely clean conditions to prevent the surface from contaminating. All measurements presented in this thesis were therefore performed in ultra high vacuum (UHV), i.e. at pressures $<1.5\text{x}10^{-10}$ mbar. Figure 2.2 shows an image of the system, highlighting its main parts. The vacuum chamber consists of three separate compartments, the STM chamber, the preparation chamber and the load lock, each of which have their own specific functions. The load lock is used to insert and extract tips and samples in and out of the vacuum, and contains a home build stage to treat tungsten tips (see section B.1.2). In the preparation chamber, up to four samples and six tips can be stored, samples can be cooled, heated and cleaved, LEED can be done on cleaved samples and samples can be sputtered with Ne (see Fig. 2.2c). The STM head is located in the STM chamber and is optically accessible via a small viewport (see Fig. 2.2d).

Each compartment has its own pumping power to sustain ultra high vacuum conditions. The load lock is pumped by a *Pfeiffer Vacuum* turbo pump coupled to

an *Edwards Vacuum XDS* scroll pump. However, both of these pumps have rotating parts and must therefore be switched off during STM/S measurements to avoid noise. Both the preparation chamber and the STM chamber are pumped by a *Leybold Heraeus* ion pump and titanium sublimation pump. Since these types of pump have no mechanically vibrating parts, they do not have to be turned off during a measurement, ensuring proper vacuum conditions throughout the measurement period. The entire vacuum chamber is furthermore placed on four *Newport* laminar flow isolators to reduce mainly translational vibrations.

In order to measure at temperatures down to 4.2 K (and lower), the STM head is suspended with springs from a cryostat which can be filled with liquid helium. A shield fixed to the He cryostat thermally encloses the STM head to thermally isolate it from the rest of the system. The helium bath is in turn shielded by an outer cryostat filled with liquid nitrogen. The inner cryostat can be pumped to a few tens of millibars to reduce the temperature of the STM head even further down to ~2.4 K. At the time of writing, the stand time of the system at 4.2 K is approximately 72 hours and is limited by the lifetime of both the liquid nitrogen and liquid helium in the outer cryostat. A Zener diode that enables controlled heating in the range of 2.5 K - 350 K is mounted on the base of the STM head. It should be noted that the best results, i.e. those with the least amount of noise, are currently obtained between 2.5 K and 30 K. A silicon diode serving as temperature sensor of the STM is placed on the STM head as far away from the Zener diode as possible in order to have an accurate readout. Calibration of this temperature sensor with respect to the actual temperature of the sample is described in more detail in appendix C. A *Neocera LTC-21* temperature controller unit was used to control the temperature of the STM to within an accuracy of a few milli-Kelvin.

The electronics and software used to control the STM setup were supplied by *SPS-CreaTec GmbH* and were upgraded during this thesis. The electronics contain several 32-bit **D**igital to **A**nalog **C**onverters (DACs) to send signals from a computer to the STM and 32-bit **A**nalog to **D**igital **C**onverters (ADCs) to read out the tunneling current and differential conductance. The tunneling current is amplified by nine orders of magnitude by a *Femto DLPCA-200* variable gain low noise current amplifier. Differential conductance spectra were taken using a *Stanford Research System SR830 DSP* lock-in amplifier. A Createc high voltage supply amplifies the $\pm$10V signal from the computer to a $\pm$200V signal to control the piezos. LEED is performed using a *VG Microtech LEG110S/8011*, see section 2.2 for more details.

Besocke Beetle

The STM head is of a Besocke Beetle type [30, 31], which basically consists of three outer piezos that support a ramp onto which the main piezo is mounted. In this case, the main piezo is pointing downwards and the sample is inserted into the STM pointing upwards. The tip is attached to the main piezo by means of a magnet (see section 2.1.3 for details on the magnetic field of the z-piezo). Figure 2.3 shows a

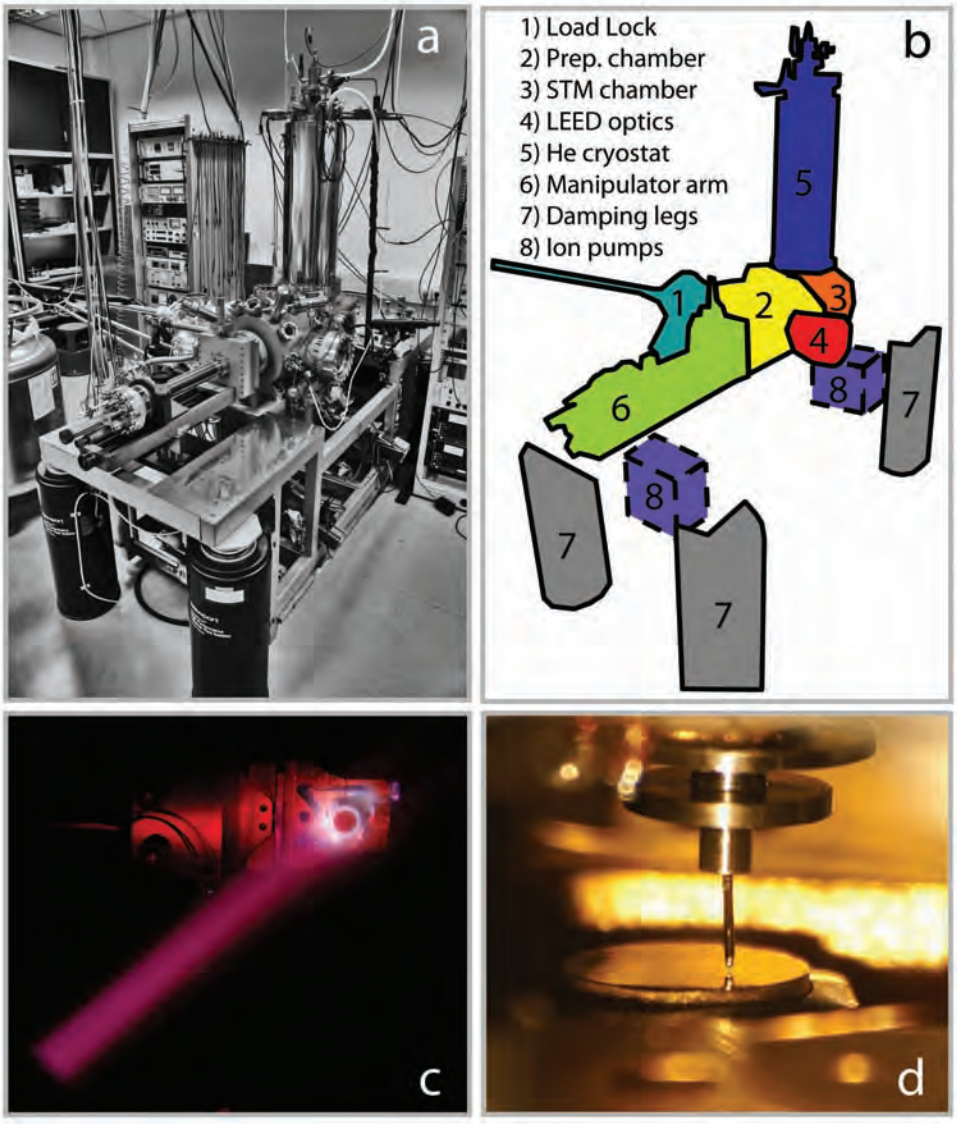

Figure 2.2: (a) The STM vacuum system and (b) corresponding schematic with the various parts indicated. The images underneath highlight a particular function of the three vacuum compartments: (c) sputtering of the Au(788) sample, the beam of Ne ions comes from left below and (d) a Pt/Ir tip and its reflection in the Au(788) sample.

schematic drawing of the Beetle design and an image of the STM head used in this work. All four piezos have electrodes on the $\pm$x and $\pm$y directions to be able to bend them in all in-plane directions. The main piezo also has an electrode connected to the heart of the piezo in order to extend and retract it.

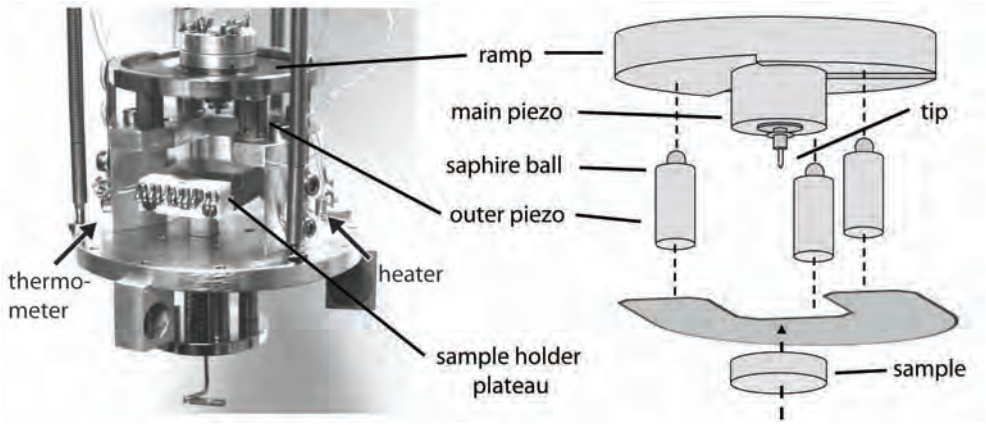

Figure 2.3: Left: image of the STM head. A sample holder can be placed onto the sample holder plateau which can be raised to bring the sample into range of the tip. Right: schematic drawing of the Beetle design STM with the different components indicated.

To transfer samples in and out of the STM head, the sample holder plateau can be lowered by means of a push-pull mechanism. This mechanism has three positions: fully retracted, halfway up, and fully extended. In the fully retracted position, the STM head is pulled onto the cryo-shield that is mounted underneath the He cryostat. This way, the STM head is cooled quickly and samples can be transferred in and out of the STM head. Once a sample is placed into the STM head, it can be positioned in the position halfway up. The STM head is then still in contact with the cryoshield, but now the sample holder is in direct contact with the STM head, so the sample is cooled. Once the sample is cooled, the push-pull mechanism can be released into the fully extended position. The STM head is then disconnected from the He cryostat and is floating freely from the springs, ensuring both electrical and mechanical isolation from the vacuum chamber. Eddy current dampening at the bottom of the STM head further reduces noise.

Once the STM head is floating freely, the tip can be brought closer to the sample or further from it by rotating the ramp plate. The ramp plate is divided into three sections with an identical height gradient. Each of the three outer piezos touches one of these sections. By a combined stick-slip motion of the outer piezos, the ramp plate is rotated into a different position and thus height. Using stick-slip motion of the outer piezos, the x and y orientation of the tip with respect to the sample can also be altered. Combining both rotation and translation of the ramp plate, the tip can be brought in close proximity to the sample anywhere in the xy-plane. The full reach of the ramp is approximately 0.5 mm in height. Therefore, in order to avoid tip crashes or not being able to reach a sample, care should be taken when making tips and mounting samples on the sample holders. Once the tip is optically near the sample, the last few micrometer can be bridged by invoking the computer to

start the approach sequence. During the approach, the outer piezos rotate the ramp step by step, checking in between steps if there is a tunneling current established by fully extending the main piezo. If no tunneling contact between the sample and the tip is made, the main piezo is fully retracted and the ramp is rotated another step. If a tunneling current is detected, the approach is stopped and a measurement can commence.

There are two types of measurement: topography and spectroscopy. During topography, the xy-movement is controlled by a combined tilting of the three outer piezos. For a given tunneling voltage between the tip and the sample, the main piezo will adjust its length to keep the tunneling current constant, while scanning the surface. For such an adjustment of the main piezo, a feedback loop has to be turned on which monitors the tunneling current as a function of the change of the main piezo length. Aside from the voltage and set current, the frequency with which this monitoring takes place is therefore an important parameter in topography mode. In spectroscopy mode, the feedback loop is turned off so the main piezo is not adjusted anymore. Subsequently, the voltage can be swept while measuring the tunneling current. To obtain useful results, the tip-sample distance should be constant during a voltage sweep. Since piezos are especially sensitive to temperature gradients, the temperature should be stable to within a few milli-Kelvin to be able to take thousands of spectra (required to for instance construct a gap map) without either the main or the outer piezos drifting from their initial position. In principle, the xy movement and z movement can be regulated by any combination of the main and outer piezos, but the above (z = main, xy = outer) has been used to decouple xy from z movement and to avoid having to use stick slip motion while measuring.

Main piezo magnetic field calculations

As mentioned in the previous section, the tip is attached to the main piezo by means of a small magnet at the end of the main piezo. Initially this was a single magnet with its magnetisation axis along the length of the main piezo. This configuration, however, also produces a nonzero magnetic field at the surface of the sample. Since this could in principle interfere with the measurements, especially those on superconductors, a calculation was performed to estimate the magnetic field at the sample surface [3].

In this calculation, the magnet, the attached tip holder and the surrounding vacuum are reconstructed using a finite number of elements. All of these elements are given their own magnetic moment depending on the material the element consists of. For the tip holder non-magnetic stainless steel has been used in the calculation. The size and strength of the magnet have been measured. The magnetic field at a distance of ~3 mm from the tip holder, i.e. at the sample surface, has subsequently been calculated using several models of which the details go beyond the scope of this thesis. In the calculation, both the situation with a tip holder and without a

[3] calculations were performed by E. Hennes, Technology department FNWI, UvA

holder have been simulated, giving nearly identical results. The axial component of the magnetic field, B_z, is approximately 45 ± 5 Gauss without tip holder, and 55 ± 5 Gauss with tip holder.

As this field is rather large, a different magnetic configuration was considered, namely one where instead of one magnet, two anti-parallel aligned magnets are used to keep the tip holder into position. This configuration has been modeled using the same method as has been used for the single magnet configuration and resulted in a field of 4 ± 0.5 Gauss without tip holder and < 1 Gauss with tip holder. Therefore, during the coarse of this Ph.D. research, the z-piezo has been switched to one with a double anti-parallel aligned magnet configuration.

2.2 Low energy electron diffraction

In order to determine the crystallographic orientation of each individual sample that is measured in the STM, *in situ* low energy electron diffraction (LEED) has been performed. As depicted in Fig. 2.4, the LEED optics basically consist of a gun which emits a beam of monochromatic electrons onto the sample surface, and a phosphorus screen which is illuminated by the backscattered electrons after they are diffracted at the surface. Grids are placed in front of the screen in order to provide a high pass filter ensuring that only elastically scattered electrons reach the screen, whereas secondary, inelastically scattered electrons will be removed.

Considering a one dimensional chain of atoms with a periodicity a that is illuminated at right angles by a plane electron wave, there will be intensity of scattered electrons only if the Bragg criterium is met:

$$d = a \sin\theta = n\lambda, \tag{2.4}$$

where d is the difference in path length between two beams scattered from adjacent scattering centers (i.e. the atoms), a is the distance between two scattering centers, θ is the angle between the incident and scattered beam and λ is the wavelength of the incident beam. From this it follows that increasing the energy of the beam, i.e. decreasing λ since $E = \frac{h\nu}{\lambda}$, will bring diffraction spots on the phosphorus screen closer together. Secondly, a smaller lattice constant, i.e. smaller a, will increase the distance between diffraction spots.

The advantage of using LEED over other diffraction probes such as for instance Laue is that the electron beam which typically has an energy in the range 50-500 eV has a penetration depth of typically 5-10 ångstrom. Therefore, like STM, LEED is a very surface sensitive probe. To describe a real LEED measurement, the three dimensional equivalent of Equation (2.4) should be used. However, due to the small penetration depth, the coherence of the electron beam in the c direction is smeared out, leading to diffraction 'rods' instead of spheres. Upon changing the energy of the incident beam, one is effectively scanning through these rods of intensity. By tracking the intensity of a particular diffraction spot as a function of energy, a LEED I(V) curve can be constructed. Since the specific details of the near-surface structure

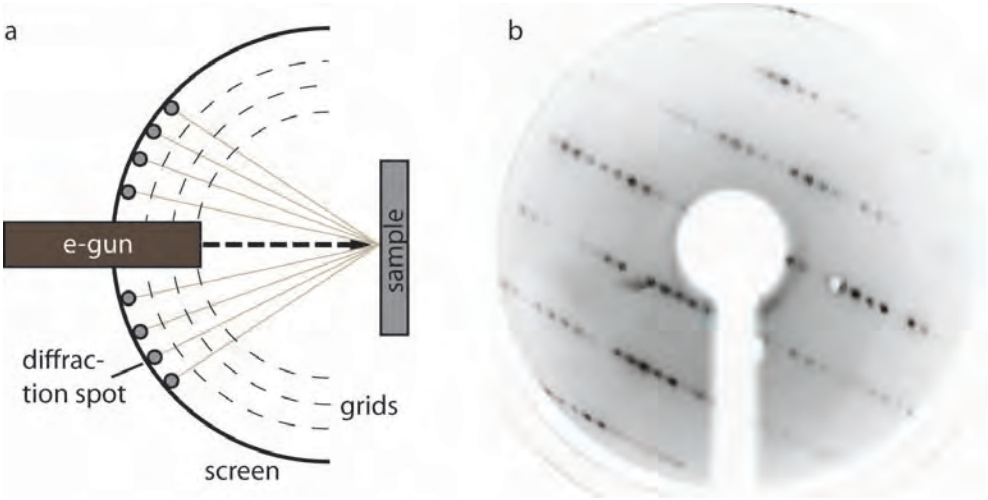

Figure 2.4: (a) Schematic drawing of a LEED setup, the main parts are indicated in the figure. (b) Optical negative of an actual LEED image, in this instance of $Bi_2Sr_2CaCu_2O_{8+\delta}$, taken at 94 eV. The ~5b supermodulation is clearly reflected by the rows of spots in one direction only.

are encoded in such a LEED I(V) curve, the details of the surface structure can be uncovered to a high precision by comparison with calculations, a technique which will be used in chapter 4 in the investigation of the '122' pnictide cleavage surface. In this work, a *VG Microtech LEG110S/8011* LEED optics were used to characterise the samples *in situ* after each STM investigation. LEED I(V) curves were obtained on identical samples on a separate setup using a *Specs ErLEED 100/150*.

2.3 Single crystal growth and characterisation

Unless stated otherwise, the samples were grown in Amsterdam by Y. K. Huang. $La_{2-2x}Sr_{1+2x}Mn_2O_7$, $Bi_2Sr_2CaCu_2O_{8+\delta}$ and $Pb_xBi_{2-x}Sr_2CaCu_2O_{8+\delta}$ samples were grown with the traveling solvent floating zone method using a mirror furnace. Pnictide samples were grown using the Bridgeman method in an Al_2O_3 crucible using self flux (i.e. FeAs-flux). All compositions given throughout this thesis were those obtained using electron probe micro analysis after growth, performed by Y. K. Huang and T. Gortenmulder. Magnetisation measurements and/or resistivity measurements were subsequently used to further characterise the samples. These measurements were performed by R. Huisman, H. Luigjes, S. de Jong, Y. K. Huang and the author. Further relevant details on the samples will be given in the various chapters themselves. For more details on sample growth and characterisation methods other than those given in the chapters the reader is referred to Ref. [6] and/or [32].

Part I

Iron based superconductors

CHAPTER

3 Introduction to the superconducting pnictides

In this chapter a brief introduction will be given to superconductivity in general and to the recently discovered pnictides superconductors in specific. First, a short summary is given of the discovery and the subsequent theoretical understanding of superconductivity. After reviewing the most important results from the benchmark theory of superconductivity, BCS theory, the most studied family of high temperature, unconventional superconductors, the cuprates, is briefly discussed. After having touched on the various anomalies observed in the cuprates and having sketched the current status of understanding of this family of superconductors, the most recent family of high temperature superconductors, the iron-pnictides, will be discussed, including the crystals structure, band structure and pairing symmetry.

3.1 Superconductivity

One of the most fascinating phenomena in (condensed matter) physics is superconductivity, which is the ability of a material to lose its electrical resistivity completely below a certain temperature, and expel any external magnetic field. To illustrate how remarkable the effect is, Heike Kamerlingh Onnes initially believed there was something wrong with his equipment when he discovered superconductivity in 1911, almost to date 100 years ago [33]. However, the contacts to his mercury sample were fine and later experiments indeed showed that there is no detectable drop in the current through a superconducting ring over the course of several years. Effectively, the lifetime of the superconducting current can be considered infinite. Zero resistivity alone does not make a material a superconductor. The formation of ring currents on the surface of a superconductor enables it to counter external magnetic fields perfectly, resulting in zero net magnetic field inside the superconductor [34]. This so called Meissner effect, which was discovered by Meissner's student Ochsenfeld, leads (in type II superconductors) to levitation of a superconductor above a magnet [1].

3.2 A brief introduction to BCS theory

After the initial reluctance to believe that superconductivity was a real phenomenon, more and more materials were found to display the effect with increasing superconducting transition temperatures (T_c). A theoretical understanding of the effect was emerging in the 50's and eventually led in 1957 to the publication by J. Bardeen, L. N. Cooper and J. R. Schrieffer of their 'Microscopic theory of superconductivity', which was later dubbed BCS theory after their initials [35, 36]. The theory is mainly based on earlier work by L. N. Cooper, who showed that any attractive interaction between electrons in a free electron gas, regardless how small, enables electrons to form pairs [37]. In a spin-singlet superconductor, the two electrons that form a pair must have opposite spin and momentum. The Fermi sea of electrons is unstable against formation of these so called Cooper pairs and will condense into a ground state where all electrons are paired: the BCS ground state. Without going in the details of the theory, the most important predictions will be discussed below. For a detailed history of the events leading to the postulation of the BCS theory, and a derivation thereof, see for instance Ref. [38].

Two electrons that form a Cooper pair will lose energy in doing so. Therefore, in order to extract an electron from the BCS condensate, for instance in a tunneling experiment, a Cooper pair has to be broken, which costs the pairing energy, 2Δ (each electron gains an energy Δ). This means that there is a finite energy range which is insufficient to break a Cooper pair: the superconducting gap. For a BCS super-

[1] in type II superconductors immobile flux lines can penetrate the superconductor which keep the superconductor in place above the magnet; a type I superconductor, which does not allow for flux lines to penetrate, would simply slide off

conductor, this energy gap at T = 0 K (i.e. $\Delta(0)$) is related to the superconducting transition temperature by:

$$2\Delta(0) = 3.52 k_B T_c, \tag{3.1}$$

where k_B is the Boltzmann constant. Since the gap is temperature dependent, a more general relation, which is valid for all temperatures T is given by the following expression [39,40]:

$$2\Delta(T) = 2\Delta(0) tanh(\frac{\pi}{2}\sqrt{T_c/T - 1}). \tag{3.2}$$

The superconducting density of states (N_s) in terms of the normal state density of states (N_n) is furthermore given by:

$$N_s = \begin{cases} 0 & (E < \Delta), \\ N_n \frac{E}{\sqrt{E^2-\Delta^2}} & (E > \Delta). \end{cases} \tag{3.3}$$

The density of single particle states in the superconducting state at T = 0 is thus zero at energies less than the Cooper pairing energy and diverges at the gap energy. If temperature is taken into account, the equation becomes an integral over the zero temperature density of states convolved with the derivative of the Fermi function. In order to compare theory to a real tunneling experiment, R. C. Dynes and coworkers showed [41] that broadening due to a finite life-time of the quasi-particles and broadening due to limited experimental resolution can effectively be captured by introducing a broadening factor, Γ:

$$\frac{dI}{dV} \propto \int_{-\infty}^{\infty} Re[\frac{|E - i\Gamma|}{\sqrt{(E - i\Gamma)^2 - \Delta^2}}] \times (\frac{exp[(E + eV)/k_B T]}{k_B T(1 + exp[(E + eV)/k_B T])^2}) dE, \tag{3.4}$$

where $\frac{dI}{dV}$ is the derivative of the tunneling current, which can be directly related to the density of states, see section 2.1.1. This relation will be used in appendix C to fit tunneling spectra taken on the BCS superconductor niobium.

BCS theory furthermore predicts that the transition temperature is related to the Debye cut-off energy, E_D, the density of states at the Fermi level, N(0), and the pairing potential, V, in the following manner:

$$k_B T_c = 1.14 E_D e^{-1/N(0)V}, \tag{3.5}$$

where $N(0)V = \lambda$ is the coupling parameter which expresses the material dependent strength of the coupling of the electrons to the bosonic mode that leads to Cooper pair formation. The regime where this parameter is small, $\lambda << 1$, is called the weak coupling limit, which is the limit where BCS theory is valid. Although extensions of BCS theory have been made to the strong coupling regime, i.e. where $\lambda << 1$ is no longer valid, a more general description of electron-boson coupling in superconductors of arbitrary strength was developed by Éliashberg in 1960 [42], see also Ref. [43].

As the Debye cut-off energy for different isotopes of the same element should be proportional to $M^{-\alpha}$, where $\alpha = 0.5$, Equation (3.5) correctly reproduces the isotope effect, which was first observed by E. Maxwell in 1950 in mercury [44].

Before moving on to discuss the successes of BCS theory and its limitations, two important parameters need to be introduced. The first one is the coherence length, ξ_{coh} which is a measure of the spatial extent of the Cooper pair wave function. Applying the uncertainty principle to the gap energy, 2Δ, the coherence length can be shown to be [14]:

$$\xi_{coh} \sim \frac{E_F}{k_F \Delta}. \tag{3.6}$$

For typical low temperature superconductors such as mercury and aluminium, the coherence length is on the order of 10^3 to 10^4 Å.

The second parameter is the electron mean free path, ℓ. For a perfect, infinite material, the mean free path would be infinite, but due to impurities, defects and a finite temperature, there will be a finite distance over which an electron can travel without being scattered (see section 3.7). The mean free path is given by $\ell = \tau v_F$, where v_F is the Fermi velocity and τ is the time interval between collisions of conduction electrons with impurities in the sample.

An important measure of the purity of a superconductor is the ratio of these two length scales, ℓ/ξ_{coh}. If $\ell/\xi_{coh} >> 1$, electrons can move around over distances much larger than the size of the Cooper pair wave function without being scattered, in which case the superconductor is said to be in the clean limit. On the other hand, in very impure materials the mean free path can become much smaller than the coherence length, $\ell/\xi_{coh} << 1$, and the superconductor is in the dirty limit.

3.3 Beyond BCS - from cuprates to pnictides

BCS theory correctly explained all superconductors known at the time of its postulation and many more that were discovered since, and has revolutionised the understanding of superconductivity. However, even though for many known superconducting materials the isotope effect has been observed, all with the isotope coefficient α equal to 0.5, over the course of a century many conventional superconducting materials have been found with $\alpha \neq 0.5$. Similarly, the relation between the gap magnitude and the transition temperature predicted by BCS theory is not 3.52 for all materials: for instance in pure Pb it is as high as 4.2 [8]. Extensions to the basic theory have been developed to account for these discrepancies, for example for systems such as Pb, where the weak limit approach is not valid and a strong coupling approach has to be adopted.

The discovery of the cuprate family of superconductors by J. G. Bednorz and K. A. Müller in 1987 changed this picture [45]. The copper oxide perovskite superconductor $Ba_xLa_{5-x}Cu_5O_{5(3-y)}$ they created, had a transition temperature above 30 K, well in excess of any previously discovered superconductor. Within two years,

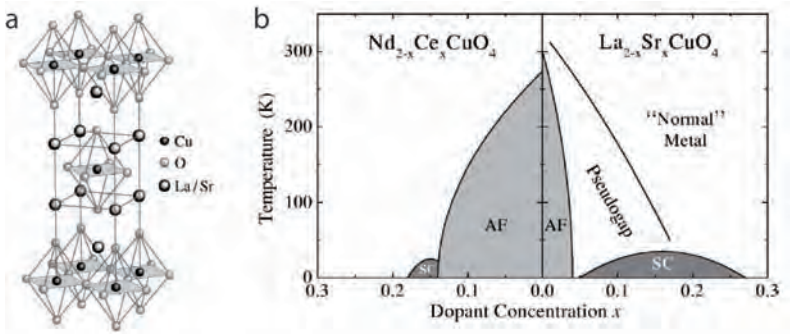

Figure 3.1: Cuprate structure and phase diagram, taken from [50]: (a) Cuprate crystal structure (shown here for $La_{2-x}Sr_2CuO_4$), where Cu-O planes are sandwiched between layers of a different character. (b) Generic phase diagram of electron- (left) and hole doped (right) cuprates. The precise of the behaviour of the pseudogap region as a function of doping is still under debate and could be sample dependent, hence it is only indicated schematically.

cuprates were found with T_c's of up to 127 K, of which the most widely studied are $Y_2Ba_2Cu_3O_7$ (T_c = 93 K) [46] and $Bi_2Sr_2CaCu_2O_{8+\delta}$ (T_c = 95 K) [47]. The current record holder at ambient pressure is $HgBa_2Ca_2Cu_3O_x$ with T_c = 135 K [48]. Not only are the transition temperatures of these materials far beyond what is deemed possible within the BCS framework, they also support anomalous isotope effects and have reduced gaps, $2\Delta/k_BT_c$, up to 5 [49]. Clearly, these materials seem beyond a 'simple' adaptation of BCS theory.

Central to all cuprate superconductors is a Cu-O plane that is sandwiched between a number of interstitial layers, see Fig. 3.1a. The stoichiometric material has a half-filled 3d shell, leading to a Hubbard splitting of the main band into an upper and lower Hubbard band, turning the material into an anti-ferromagnetic Mott insulator. Upon adding or removing charges by changing the oxygen content, the anti-ferromagnetism is suppressed and eventually superconductivity emerges in the form of a superconducting dome. A schematic phase diagram is shown in Fig. 3.1b.

The original BCS theory considered only an s-wave symmetry of the superconducting gap, meaning that the gap magnitude is isotropic as a function of momentum. In the cuprates, however, the gap symmetry has been the subject of discussion for quite some time, but has been shown to be one with a d-wave character [2]. This means that there are nodes at certain momenta where the gap vanishes even down to the lowest temperatures, and that the sign of the order parameter changes as a function of momentum. Extending BCS theory to a d-wave gap symmetry, $2\Delta/k_BT_c$ becomes 4.3 [53], which is considerably closer than the s-wave BCS value to the values obtained from experiments. However, such an extension alone is insufficient to explain the wealth of properties observed in the cuprates, for which reason the

[2] at least for the hole-doped cuprates, it is still unclear for electron-doped systems, see for instance Refs. [51,52])

cuprates are commonly termed unconventional, or high T_c superconductors.

The anomalous isotope effect for instance has been the focus of intense research and heated debate (see for an example of the latter the abstracts of [54–56]). Though not essential for BCS theory itself, the 'glue' that binds the electrons into Cooper pairs comes for conventional superconductors from a coupling of the electrons to the lattice, i.e. electron-phonon coupling. Initially, either no or very small isotope effects were observed in the cuprates, which seemed to indicate that electron-phonon coupling plays a minor role in the cuprate superconductors, and a different pairing mechanism must be the driving force of superconductivity. Later though, isotope effects were found to change as a function of doping concentration, x, increasing to values even larger than BCS theory for strongly underdoped systems, leading to a plethora of theories to explain the origin of the pairing mechanism. See for instance Refs. [57,58] and references therein for a recent overview of the experimental reports on the isotope effect in cuprates and references in Ref. [59] for an overview of several theoretical models proposed.

Closely connected to the ongoing debate on the pairing mechanism in the cuprates is the appearance of a region in the phase diagram of all cuprates where there is a depletion of spectral weight at the Fermi level at a temperature T^*, far in excess of the superconducting transition temperature. This region, which strongly resembles in many aspects the superconducting state without actually being superconducting, is commonly called the pseudogap region, and is wedged in between the antiferromagnetic insulating regime and the superconducting dome, see Fig. 3.1b. The main question that has kept the community busy over the past decades is whether the pseudogap is a precursor to superconductivity or is competing with superconductivity, and what its importance is for high temperature superconductivity in general.

In light of the impasse in the cuprate superconductors sketched above, a completely new family of high temperature superconductors was discovered in February of 2008 [1]. Within a short period of time a maximum transition temperature of 55 K was found [2], not as high as in the cuprates, but well in excess of the BCS maximum T_c. Perhaps even more surprisingly, this new superconductor contains iron, a magnetic metal which is usually thought of as the worst starting point for a superconductor.

3.4 Pnictide crystal structure

Like the cuprate superconductors, the pnictides [3] have a layered structure, where for these systems an Fe-As layer is the central building block, see Fig. 3.2a. Importantly, this Fe-As layer is three dimensional, with the As atoms sticking out above and below the plane of Fe atoms as shown in Fig. 3.2b, setting it apart from the two dimensional Cu-O plane in the cuprates. To date, five different groups within the

[3] any binary compound of a pnictogen (i.e. an element from the nitrogen group) is called a pnictide

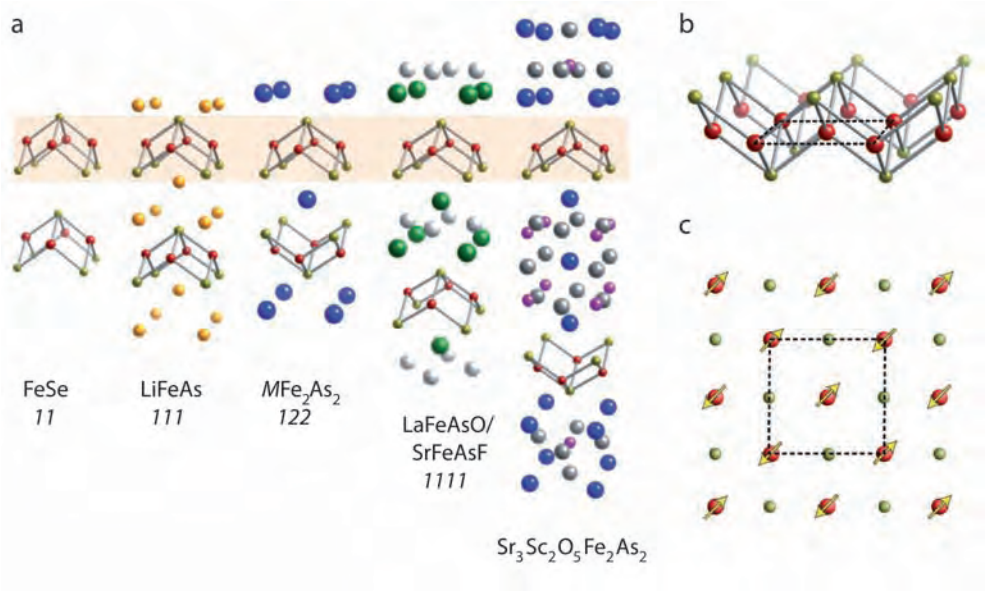

Figure 3.2: Pnictide structure, adapted from [61]: (a) The five known different structural groups within the pnictide family of superconductors. The shaded region indicates the Fe-As/Se layer common to all groups. Below each structure a prominent composition within the group is given and the generic name for each group. (b) Fe - As block where the 2D nature of the layer can clearly be seen. The dotted square indicates the tetragonal unit cell (in the magnetic phase the structure is actually orthorhombic, giving a unit cell rotated by 45 degrees and $\sqrt{2}$ times larger on each side). (c) The same Fe-As block as is shown in (b) but seen from above. The spins are located on the Fe atoms and form an anti-ferromagnetic structure in the out-of-plane direction.

family of pnictides have been found, of which the simplest one, the FeSe or 11 system (which is actually a chalcogenide [4]) has no interstitial layers and the other four groups have one or more interstitial layers between the Fe-As building blocks. Since large, millimeter sized single crystals of the $M\mathrm{Fe_2As_2}$ or 122 system, where M is an alkaline- or rare earth element, are relatively easy to grow and have transition temperatures of up to 38 K [60], these materials are the most studied within the group of pnictide superconductors. The main part of the iron-pnictide part of this thesis will focus on these 122 crystals, although the 11 system has also been investigated for a short period of time.

3.5 Phase diagram, magnetism and band structure

Most of the pnictide parent compounds (i.e. the structures shown in Fig. 3.2a) are not superconducting, but require doping of some sort to enter the superconducting

[4] the pnictogen, As, is replaced in these systems by the chalcogen Se or Te.

phase. An important difference with the cuprate parent compounds, which are anti-ferromagnetic Mott insulators at T = 0 K, is that the pnictide parent compounds are metallic at low temperature. Like the cuprates, they undergo a magnetic transition at finite temperature, which in the pnictides is accompanied by a structural transition from a tetragonal to an orthorhombic crystal symmetry. The spin structure of the iron lattice is shown in Fig. 3.2c and is anti-ferromagnetic in the out-of-plane direction. Though the origin of the magnetic order is still a hotly debated topic, (π,π) nesting of electron- and hole-like Fermi surface pockets (see below) is commonly thought to be (at least partly) the driving force of the magnetic order, see for instance Refs. [62, 63].

Focusing on the 122 system, there are plenty of routes to get the system in the superconducting phase. All of the three basic constituents of the material (*M*, Fe and As) can be partially replaced by other atoms to achieve superconductivity. The highest T_c of 38 K is reached by changing *M* for K [60, 64–66] and is effectively hole doping the system. Changing Co or Ni for Fe, which can be seen as electron doping, leads to a maximum T_c of 22 K [67–71]. Isovalent substitution of for instance As by P [72–74], or Fe by Ru [75–77], also brings about superconductivity with maximum transition temperatures of 30 K and 20 K, respectively. Figure 3.3a-d displays the phase diagrams of examples of these hole-, electron-, and isovalently doped 122 systems. The fact that relatively large amounts of dopants can be introduced even within the superconducting Fe layer is rather puzzling, and in stark contrast to the extreme sensitivity of for instance the cuprates to dopants within the superconducting layers [78, 79].

With such a wealth of options to reach superconductivity, the question immediately arises what drives the material to become superconducting. The striking resemblance of the pnictide phase diagrams to the phase diagrams of several other classes of unconventional, non-phonon mediated superconductors, including the cuprates, organic- and heavy fermion superconductors, suggests that the pairing mechanism in the pnictide superconductors is also of unconventional nature. Although no official identification of the pairing mechanism has been proven, the general consensus seems to be that magnetic spin fluctuations are the pairing 'glue' that binds the electrons [81, 82].

In order to get a handle on the physics underlying the superconductivity in these materials, it is imperative to calculate and experimentally determine their band structure. The electronic states at the Fermi level, E_F, are almost exclusively Fe 3d states with little hybridisation with As 4p states, as determined from hard x-ray photoemission experiments [83]. From simple crystal field considerations these Fe states have a d^6 configuration and should give rise to at least four hole bands at E_F. Local density approximation (LDA) calculations indeed predict a band structure with four or five bands crossing the Fermi level, see for instance Ref. [84] for an overview of LDA calculations to date.

Although these calculations are not perfect, for instance the magnetic moment of the Fe atoms is systematically overestimated, the calculations match rather well with experiment. Fig 3.4a shows a schematic view of the Fermi surface of the pnictides,

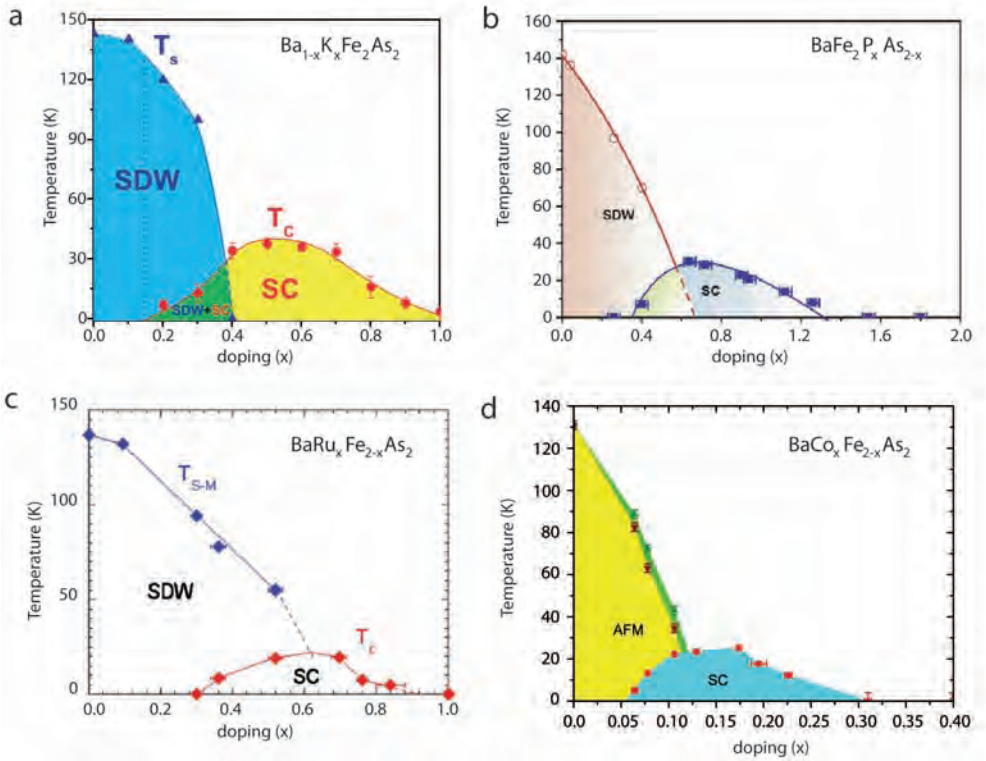

Figure 3.3: 122 pnictide phase diagrams: (a) 'Hole doped' $Ba_{1-x}K_xFe_2As_2$, which has a maximum T_c of 38 K for x ~ 0.5, adapted from [80]. (b) Isovalently doped $BaFe_2P_xAs_{2-x}$, T_c^{max} = 30 K (x ~ 0.6), adapted from [73]. (c) Isovalantly doped $BaRu_xFe_{2-x}As_2$, T_c^{max} = 20 K (x ~ 0.6), adapted from [77]. (d) 'Electron doped' $BaCo_xFe_{2-x}As_2$, T_c^{max} = 25 K (x ~ 0.15), courtesy of R. Huisman.

with two or three hole-like pockets around the Γ-point, i.e. **k**=(0,0), and two electron like Fermi surface sheets around the M-point, **k**=(π,π)[5]. Due to the three dimensional structure of the Fe-As block, the Fermi surface is not as two dimensional as is the case in the cuprates, but has a warping in the z-direction. The (π,π) nesting scattering vector, believed to be the origin of the magnetic order, is indicated with an arrow.

3.6 Pairing symmetry of the order parameter

As already mentioned, conventional BCS theory assumes an s-wave symmetry of the superconducting gap function, $\Delta(k)=\Delta_0$. The cuprate superconductors on the other hand possess a d-wave gap function, leading to nodes and sign changes in the order parameter as a function of momentum, $\Delta(k)=\Delta_0 \cos(2\Phi)$, where Φ is the

[5]Throughout this thesis a simple tetragonal Brillouin zone is used, i.e. one with two iron sites per unit cell

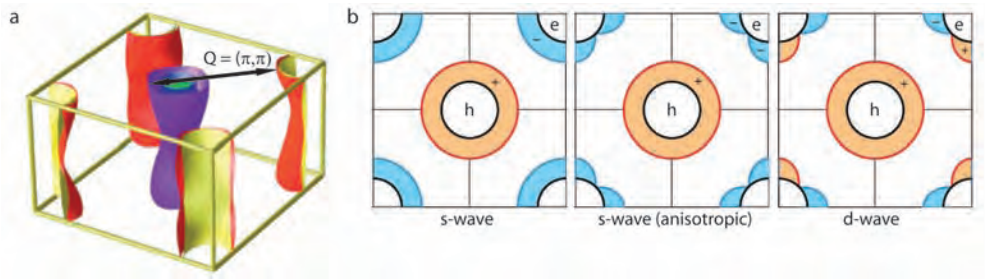

Figure 3.4: Pnictide band structure, from [61]: (a) DFT calculation of $BaCo_{0.1}Fe_{1.9}As_2$ showing two hole-like pockets (purple and blue) around the Γ-point and two electron-like Fermi surfaces around the (π, π)-point, from [82]. (b) k-dependence of the sc gaps on the hole and electron Fermi surfaces for three different for three different pairing scenarios. For simplicity multiple electron or hole bands have been reduced to a single band, the corners of the schematic are (±π, ±π). (Left) $s_\pm$ symmetry with isotropic gaps on the Fermi surface sheets. (Center) anisotropic $s_\pm$ symmetry, where aside from the opposing sign of the gap between the electron and hole bands the gap on the electron pocket has accidental nodes. (Left) Going one step further from the anisotropic $s_\pm$ symmetry, by allowing the sign of the gap on the electron pocket to change at the nodes, gives a d-wave symmetry.

angle of the k-vector with respect to (0,0)-(0,π). One of the big questions that still needs an answer is what the pairing symmetry in the pnictides is, as knowledge of the pairing symmetry is an important ingredient for unraveling the mechanism of superconductivity in these systems.

Unlike the cuprates, where only one band crosses the Fermi level, the pnictides have at least four bands at E_F, opening up the possibility of multiband superconductivity. A beautiful example of the theoretical and experimental implications of multiband superconductivity is MgB_2. While the material has been known for decades [85], its unusual superconducting properties were only discovered in 2001 [86]. With a transition temperature of 39 K, well in excess of the BCS limit of ~30 K, it was initially believed to be an unconventional superconductor. However, MgB_2 is now commonly accepted to be an electron-phonon mediated, two band, conventional BCS superconductor [87], with two s-wave gaps that both close at T_c and have a value of $2\Delta/k_BT_c$ of 4.18 and 0.60-1.65, respectively.

With not two, but four (or five) bands at E_F in the pnictides, ample scenarios are possible, including ones with ungapped Fermi surface sheets, sheets with or without nodes and sheets with opposite sign to one another. The most likely of these options are depicted in Fig. 3.4b. All three of these options have a sign change between the electron and hole bands of the order parameter, which is unavoidable in a spin-fluctuation induced interaction [82]. Early angle resolved photoemission (ARPES) studies have reported different gap sizes for the various bands. Other experimental techniques similarly report either one or two gaps (depending on the technique), which support values of $2\Delta/k_BT_c$ of approximately 3 and 7 (see Ref. [40] and refer-

ences therein for an overview of the gaps reported in literature). This reduced gap value gives an indication whether the pnictide superconductors can be explained within conventional BCS theory or not, and seems to be rather large for the big gap. More details on reduced gaps, specifically as seen in STM/S experiments, will be discussed in chapters 5 and 7.

3.7 Impurity scattering

One important aspect in superconductivity, especially in the context of STM/S, is impurity scattering. If an impurity is added to an otherwise pure system, it will act as a scattering center for the electrons. The strength of the scattering is usually divided into two limits, the weak scattering limit, known as the Born limit, and the strong scattering limit, known as the unitary limit. In the Born approximation the average over all scattering events, results in a spatially uniform superconducting state (usually with a T_c reduced compared to that of the pure system). In the unitary limit, scattering from a single impurity is so strong that in-gap bound states appears rather than uniformly suppressing superconductivity. Depending on the type of scattering, different models have to be used and different results will be obtained.

Early on, it was established experimentally that non-magnetic impurities added to a pure s-wave superconductor initially effect a sharp drop in the transition temperature and energy gap, but that this drop rapidly levels off for higher impurity concentrations [88]. Adding magnetic impurities on the other hand will have the same initial drop in T_c, which will continue up to higher impurity concentrations, rapidly destroying superconductivity [89].

Anderson [90, 91] and Abrikosov/Gor'kov [92] subsequently showed that this can be understood from symmetry arguments, a notion that was later refined by many others [93–95]. Assuming purely elastic scattering, a scattering event that preserves the time-reversal invariance of the BCS s-wave ground state, such as scattering off a non-magnetic impurity potential, will barely affect the gap energy and T_c. After an initial drop due to the reduction of the mean free path length, these parameters remain more or less constant.

A magnetic impurity on the other hand breaks time-reversal symmetry, so scattering from such a center will break the time-reversal invariance of the Cooper pair, and therefore acts as a pair breaker. Unlike for non-magnetic impurities, small amounts of magnetic impurities are already sufficient to destroy the superconducting state. A material with such pair-breaking scattering centers will support quasi-particle excitations within the superconducting gap, as was demonstrated on microscopic scale using scanning tunneling microscopy [96].

With the arrival of the cuprates, impurity scattering in superconductors gained renewed interest. Magnetic impurities will be a strong pair-breaker for all spin-singlet superconductors, so not only for s-wave, but also for d-wave superconductors. Moreover, in a d-wave superconductor, the order parameter changes sign as a function of momentum, with nodes at the points where the sign changes. Therefore,

also non-magnetic impurities will act as pair-breakers as they violate Anderson's theorem that time-reversal should be a symmetry of the system. Differently put, in d-wave superconductors, potential scattering centers can induce scattering between k-locations with a different sign of the order parameter while not affecting the spin of the electron, leading to a breaking of time-reversal symmetry of the system. In the same situation, a magnetic impurity will also flip the sign of the electron spin, and time-reversal symmetry is preserved. In general, a scattering path for which magnetic scattering is pair-breaking (i.e. when there is no change of sign of the order parameter), non-magnetic scattering will not be pairbreaking, and vice versa [82]. Indeed, it has been experimentally established that non-magnetic impurities such as Zn in cuprate superconductors are strongly pair-breaking [78, 79]. Atomically resolved tunneling measurements beautifully showed the difference between these two types of scatterers, magnetic Ni and non-magnetic Zn, and thereby once more confirmed the d-wave symmetry of the cuprates [97–99], see also appendix A.

So far, only scattering in single band superconductors has been considered. However, in the pnictides it is clear that at least four bands are present at the Fermi level. Therefore not only intraband scattering, i.e. scattering within a single band, has to be taken into account, but also interband scattering, i.e. scattering between two bands. Although generalisations of the BCS equations to multiband systems were already put forward in the late 50's [100], the discovery of multiband superconductivity in MgB_2 reactivated the field. MgB_2 can be described as a superconductor with two Fermi surface sheets, a σ and π band, that have different orbital character and are characterised by strong and weak intraband electron-phonon coupling interaction, respectively. Due to the different orbital character, and for other reasons (see for instance Ref. [101]), interband pairing interactions are small, as is interband scattering. Without going into the details of the theory, in this multiband superconductor non-magnetic impurities appear to suppress superconductivity as magnetic ones do in a single band superconductor and only the interband scattering acts as pair-breaking.

In the pnictides, the bands at the Fermi level all have d-orbital character (see Ref. [102]) and it is believed that the pairing interaction is predominantly interband, while intraband pairing is weak, see Ref. [82] and references therein. Furthermore, the most likely pairing symmetry is believed to be one with a sign change of the order parameter between the bands, but not within the bands, the so called $s_\pm$ state (see Fig. 3.4b left). The effect of impurities, both magnetic and non-magnetic, on the transition temperature in this situation is strongly dependent on the strength of the impurity potential, i.e. whether the Born approximation is valid or if unitary scattering has to be considered. Within the Born limit, nonmagnetic impurities can lead to pair breaking only via interband scattering, as interband scattering does not violate Anderson's theorem. In this case high impurity concentrations will drastically reduce T_c. In the unitary limit, however, it has been argued that large concentrations of non-magnetic impurities will *not* affect T_c as Anderson's theorem is restored [103, 104]. Only when the intraband and interband scattering potentials are equal, T_c is strongly suppressed, as the interband pair-breaking effect is strongly amplified by the intra-

band one. On the other hand, magnetic impurities in the Born limit have been found to be pair-breaking for intraband scattering, but pair-preserving for interband scattering, completely opposite to the non-magnetic impurities [105].

From the above it is clear that impurity scattering effects in multiband, sign reversing superconductors is not a straightforward matter. Furthermore, the local effect of impurities in the superconducting pnictides, as seen with STM/S, is not a priori clear. This in contrast to impurity scattering effects in single band (or merely bilayer split) d-wave superconductors, such as the cuprate $Bi_2Sr_2CaCu_2O_{8+\delta}$. In fact, STM/S investigations on this cuprate system - where impurities were added on purpose - formed one of the compelling pieces of evidence for the d-wave pairing symmetry of the material, see also appendix A. The fact that in for instance the '122' pnictides superconductivity survives, and even emerges, upon replacing relatively large amounts of Fe atoms by Co, Ni or Ru indicates that impurity scattering effects could in fact be a key factor in the mechanism of superconductivity of these systems. The influence of impurity scattering effects on the tunneling signal in STM/S investigations on various pnictide systems will be further discussed in chapter 7.

CHAPTER

4 The cleavage surface of '122' pnictide superconductors

The termination surface of single crystals of the $BaCo_xFe_{2-x}As_2$ and $Fe_{1+y}Se_xTe_{1-x}$ families of the high temperature iron based superconductors is elucidated. By combining scanning tunneling microscopic data with low energy electron diffraction we prove that the termination layer of the $BaCo_xFe_{2-x}As_2$, or Ba122, systems is a remnant of the Ba layer, which exhibits a complex diversity of ordered and disordered structures. The observed surface topographies and their accompanying superstructure reflections in electron diffraction depend on the cleavage temperature. In stark contrast, $Fe_{1+y}Se_xTe_{1-x}$ possesses only a single termination structure - that of the tetragonally ordered (Se,Te) layer. Measurements on a differently doped system, $BaFe_2P_xAs_{2-x}$, where a third of the As atoms is replaced by P atoms strongly support our findings. First principles calculations of the surface structure energies and STM measurements on a related compound, $CaCo_xFe_{2-x}As_2$, suggest that our findings hold in general for all members of the *M*122 family, where *M* = Ba, Ca, Sr or Eu.

Parts of this chapter have been published as F. Massee et al., Phys. Rev. B ***80****, 140507(R) (2009) and E. van Heumen et al., Phys. Rev. Lett.* ***106****, 027002 (2011)*

4.1 Introduction

Scanning tunneling microscopy and spectroscopy (STM/S) and angle resolved photoemission (ARPES) are powerful and direct probes of the electronic states of solids and are making important contributions to our understanding of the new iron pnictide superconductors [1, 106, 107]. Determination of the termination surface of the cleaved single crystals is a pre-requisite for meaningful application of STM/S and ARPES, as is clarification whether possible departures from the bulk structure and co-ordination at the surface have a significant effect on the near-surface electronic states. A recent hard x-ray photoemission study [83] of room temperature cleaved $BaFe_2As_2$ (or Ba122) showed that the surface supports electronic states similar to those in the bulk, underpinning the relevance and reliability of surface sensitive techniques in the investigation of the pnictide superconductors. As will be shown in the next chapter, low temperature STS of room temperature cleaved $BaCo_xFe_{2-x}As_2$ also showed no correlation between the spatial superconducting gap variation and the surface topography [108]. However, studies on low temperature (<80K) cleaved samples report a correlation between features in the electronic spectra and the structure of the termination of the crystal, [109, 110] highlighting the role of the cleavage temperature. In the cuprate superconductors, it is known that macroscopic departures from the simple lattice structure such as the incommensurate modulation in $Bi_2Sr_2CaCu_2O_{8+\delta}$, can have a pronounced effect on the spectroscopic data, leading to diffraction replicas in ARPES which can complicate matters considerably [111]. In the pnictide superconductors, the existence of diffraction replicas in ARPES data has already been pointed out [110].

The first STM/S studies of cleaved single crystals of the 122-based family of superconductors [108–110, 112] either suggested or assumed that on average half of the alkaline earth ions (depending on the system involved) remain on each side of the cleave (see Fig. 3.2a for a figure of the crystal structure). Recent STM and low energy electron diffraction (LEED) studies, however, have concluded that the atomic contrast seen in STM of both Ba122 and Sr122 is from inequivalent As sites due to the spin density wave in the underlying Fe plane and that there is no cleavage temperature dependence [113, 114]. Obviously, the fundamental importance of the surface termination question and the contrasting reports make it imperative to resolve these issues. In this chapter, temperature dependent LEED analyses of cleaved $BaCo_xFe_{2-x}As_2$ (x=0.08, 0.14 and 0.21) single crystals is presented, together with an extensive STM topographic database on this system obtained from cleavage both at low and high temperature. Comparison to the $Fe_{1+y}Se_xTe_{1-x}$ system which has the same Fe*Pn* building block (where *Pn* = As, Se or Te) as Ba122 but lacks the interstitial Ba layer, consequently enables us to isolate the Ba contribution to the cleavage surface in the 122 systems.

This picture, published in Ref. [115], was later confirmed by additional measurements on two closely related systems, namely $CaCo_xFe_{2-x}As_2$ and $BaFe_2P_xAs_{2-x}$. In $CaCo_xFe_{2-x}As_2$, the Ba cation layer is replaced by a Ca layer, while the structure is

otherwise unchanged. In line with first principles calculations, which predict a difference in the energetics of certain structures for different alkaline earth layers, the modal surface appearance on this compound is different from that of Ba122. The latter compound, $BaFe_2P_xAs_{2-x}$ is a system where a considerable amount of As atoms is replaced by P atoms. If the As layer would be imaged instead of the Ba layer as is proposed here, replacement of As atoms should be reflected in the constant current images, which is not the case. Lastly, the apparent barrier height, or local work function, on various systems and on the variety of apparent surface topographies for measurements on the same system is investigated. This analysis further supports our findings and strongly suggests that the various surface structures seen on 122 pnictides are of identical origin.

4.2 Cleavage temperature dependence of $BaCo_xFe_{2-x}As_2$ and $Fe_{1+y}Se_xTe_{1-x}$

Single crystals of $BaCo_xFe_{2-x}As_2$ (x=0.08, 0.14 and 0.21), $Fe_{1+y}Se_xTe_{1-x}$(x=0.45, y=0.07), $CaCo_xFe_{2-x}As_2$ (x=0.14) and $BaFe_2P_xAs_{2-x}$ (x=0.64) were grown in self flux. All samples were characterised prior to the STM and LEED measurements by resistivity and AC susceptibility. Cleavage took place both at low (<80K) and room temperature at a pressure better than 5×10^{-10} mbar directly before insertion into the STM head, where the samples were cooled to 4.2 K. LEED was performed *in situ* after each STM survey to obtain the azimuthal orientation of the crystal. The temperature dependent LEED experiments took place in a different vacuum system at a pressure of 7×10^{-11} mbar using identical crystals as those studied using STM, but cleaved at < 25 K.

Figure 4.1 shows typical STM topographs obtained for low temperature cleaves of $BaFe_{1.86}Co_{0.14}As_2$. In Fig. 4.1a the topography combines regions with very little contrast with stripe-like structures, the latter being very clear in Fig. 4.1b. This type of (2×1) or stripe feature has been observed previously both in the superconducting and parent 122 compound [109,112,114]. Furthermore, the data clearly show that the stripes possess phase shifts of half a unit (perpendicular to the stripes), which results in a ribcage-like topography, in which the phase shift lines correspond to the backbone (marked with an arrow in Fig. 4.1b). The inset shows a Fourier transform of the topographic image exhibiting dominant spots corresponding to the stripe/ribcage structures with a period of 8 Å (arrow) as well as weaker tetragonal unit cell spots (marked by circles). We note that the predominant stripe orientation is perfectly along the lattice and roughly perpendicular to the direction in which cleavage was performed. A third type of topographic situation is that shown in Fig. 4.1c: with larger (~20 Å wide), one dimensional rod-like features displaying a relatively large corrugation of approximately 1.5 Å. Completing our topographic survey of low-T cleaved crystals, Fig. 4.1d shows a large field of view in which two previously mentioned structures (seen in Fig. 4.1a and b) can be seen to smoothly cross over. Interestingly, Fig. 4.1a and d show that the backbone-features often terminate on pinning

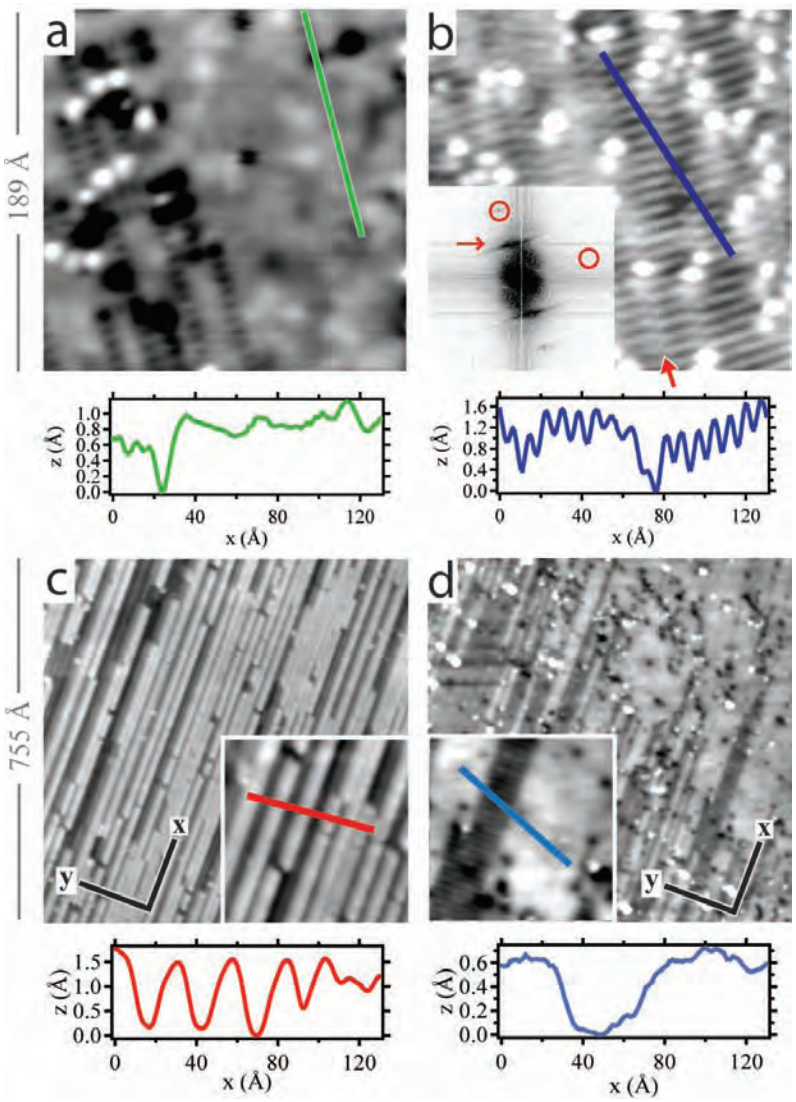

Figure 4.1: Constant current images for cleavage of Ba122 (x=0.14) at low temperature (<80K). (a) and (b) are taken on the same cleave using a junction resistance R_J=2.4 GΩ, (c) and (d) on a different cleave (R_J=0.65 GΩ). Inset of (b): FFT of (b) highlighting the unit cell spots (circles) and (2×1) reconstruction spot (arrow). All topographic types shown have been observed on numerous cleaves. Line scans along the paths indicated are shown below each panel. The insets of (c) and (d) show enlargements of size 189 Å. Axes indicate the crystallographic orientation as determined from LEED.

centers taking the form of a very bright or dark spot. Finally, we note that the line-scan shown in Fig. 4.1d lacks steps corresponding to inter-plane distances (i.e. of

order 1.4 Å and larger), thus indicating that the majority of the observed structures form part of the same crystallographic plane.

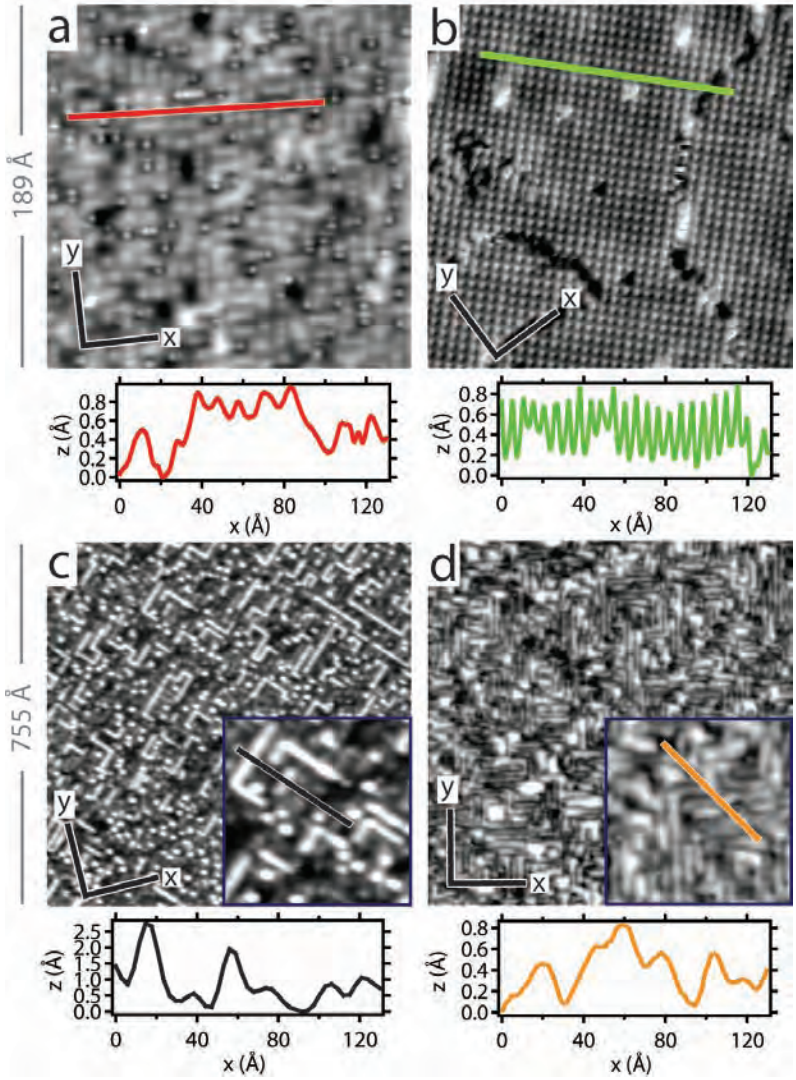

Figure 4.2: Constant current images for various cleaves of $BaFe_{1.86}Co_{0.14}As_2$ at room temperature (R_J ~0.75 GΩ). Line scans along the paths indicated are shown below each panel. The insets to (c) and (d) show enlargements of size 189 Å. Axes indicate the crystallographic orientation as determined from LEED.

We now go on to show that room temperature cleavage results in quite a different set of constant current images of which four frequently occurring types are shown in Fig. 4.2. The top left panel shows a highly disordered cleavage surface layer, [108] whereby the most frequent separation is ~8 Å. Fig. 4.2b shows a very clear ($\sqrt{2} \times$

$\sqrt{2}$) topography with a period of 5.5 Å, cut by meandering anti-phase domain walls ('black rivers' in the topograph). Figure 4.2c displays one of the more exotic cleavage surface structures encountered: a two dimensional network of stripes and dots, with a relatively large corrugation. Lastly, a diffuse maze-like landscape without atomic resolution, seen both on superconducting Ba122 and the parent compound, [108] is shown in Fig. 4.2d and has also been reported in other studies [110].

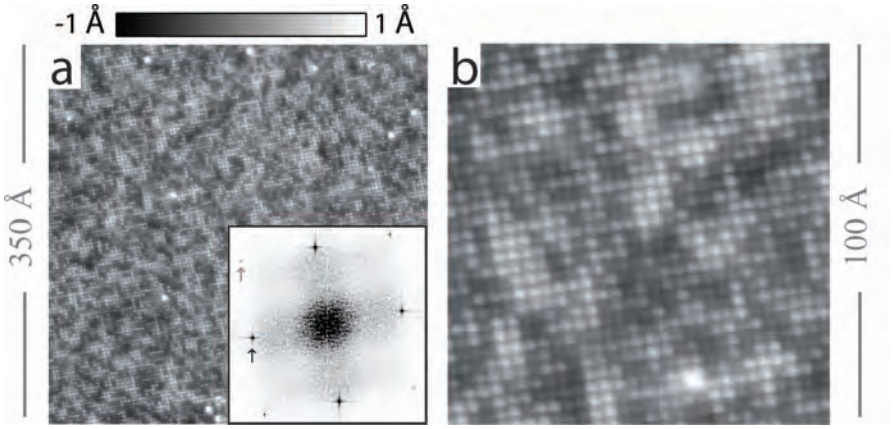

Figure 4.3: Constant current images of $Fe_{1.07}Se_{0.45}Te_{0.55}$, V_{sample} = -20 mV, I_{set} = 40 pA. (a) Large field of view with the inset showing the Fourier transform with spots corresponding to the atomic lattice vector (black arrow) and higher order spots (grey arrow). (b) Zoom of panel (a) showing clear atomic resolution. As the atoms are still visible in the occasional bright blob, which can be shown to be located at the center of four surface atoms, these are attributed to sub-surface excess iron in the lattice.

We now turn our attention to $Fe_{1+y}Se_xTe_{1-x}$. For this system, both low and high temperature cleavage yield - without exception - identical results, in sharp contrast with the great variety of topographies observed in the Ba122 case. Fig. 4.3 shows a typical constant current image, in this case for a room temperature cleave. Very clear atomic resolution is obtained over the entire field of view, with a total corrugation of less than 2 Å and a periodicity of 3.9 Å corresponding to the (Se,Te)-(Se,Te) distance. Clearly, no reconstruction is present on these surfaces, the simple tetragonal lattice being the only coherent structural pattern. The Fourier transform in the inset of Fig. 4.3a emphasises this: only tetragonal spots, also as higher harmonics, are observed. An interesting feature of the $Fe_{1+y}Se_xTe_{1-x}$ topographs is the occurrence of bright blobs on the field of view on top of which the atomic lattice is imaged. Their spatial abundance matches perfectly the excess Fe content (7%) in the crystals, which seems a highly plausible explanation for these features.

To summarise the STM results so far, a large variety of cleavage surface termination structures is observed in the $BaFe_{1.86}Co_{0.14}As_2$ compound, which possess a strong cleavage temperature dependence. In contrast, the $Fe_{1+y}Se_xTe_{1-x}$ system,

which lacks the interstitial Ba layer, has only a single type of topography, independent of cleavage temperature.

4.3 The surfaces of $CaCo_xFe_{2-x}As_2$, $BaFe_2P_xAs_{2-x}$ - STM and first principles calculations

First principles calculations to determine the most energetically favourable surface structure of the *M*122 system have been reported in literature [116]. The strong bonds between the Fe and As atoms makes cleavage between these two layers highly unlikely, leaving two options: (i) cleavage between the Ba and As layer or (ii) cleavage within the Ba layer. The energy of the two ordered structures possible with half a Ba layer: ($\sqrt{2} \times \sqrt{2}$) and (2×1), has been compared to the energy of an unreconstructed (1×1) As plus (1×1) *M* surface layer where *M* is Ba or Ca.

MFe_2As_2	$2\times(\sqrt{2} \times \sqrt{2})$	$2\times(2 \times 1)$
$BaFe_2As_2$	-411.6	-217.8
$CaFe_2As_2$	-34.0	-97.0

Table 4.1: First principle calculations of the relative energies of two ($\sqrt{2} \times \sqrt{2}$) and two (2×1) reconstructed *M* surfaces with respect to an unreconstructed (1×1) As plus (1×1) *M* surface for two *M*122 materials. Surface energies are given in meV/(1×1 cell) and have been calculated for the tetragonal phase with the atoms in the bulk positions. Table adapted from [116].

As can be seen from Table 4.1, all relative energies are negative, meaning that it is energetically favourable to have a reconstructed Ba layer on either side of the cleave, as opposed to an unreconstructed full As and full Ba layer. From the energetics of the reconstructions of the two *M* atoms, it can be expected that the ($\sqrt{2} \times \sqrt{2}$) structure is more dominant in the Ba system than in the Ca system. From our extensive STM investigation described above on dozens of Ba122 samples, where on each sample multiple locations have been probed across the entire mm-sized surface, we conclude that the modal surface is ($\sqrt{2} \times \sqrt{2}$) reconstructed in this material, with the (2×1) reconstruction and disordered structures present in lesser amounts.

Although less extensively than the Ba122 system, we also investigated the Ca122 system using STM. Having scanned ~0.5×0.5 μm on locations all over a 1x1 mm sample, only a tiny region of no more than 25×25nm^2 was found to have a ($\sqrt{2} \times \sqrt{2}$) reconstruction, see Fig. 4.4a. Everywhere else, (2×1) surface structures were encountered of which an example is shown in Fig. 4.4b, perfectly in line with the first principles calculations.

As a further test to see if an As terminated layer could be the surface layer, despite an overwhelming body of evidence pointing towards a Ba reconstructed surface, $BaFe_2P_xAs_{2-x}$ samples were measured. With a doping concentration of x=0.64, a total of 32% of all As atoms are replaced by P atoms. Resistivity measurements on these samples showed sharp transitions into the superconducting state, $T_c = 31 \pm 1$ K, in-

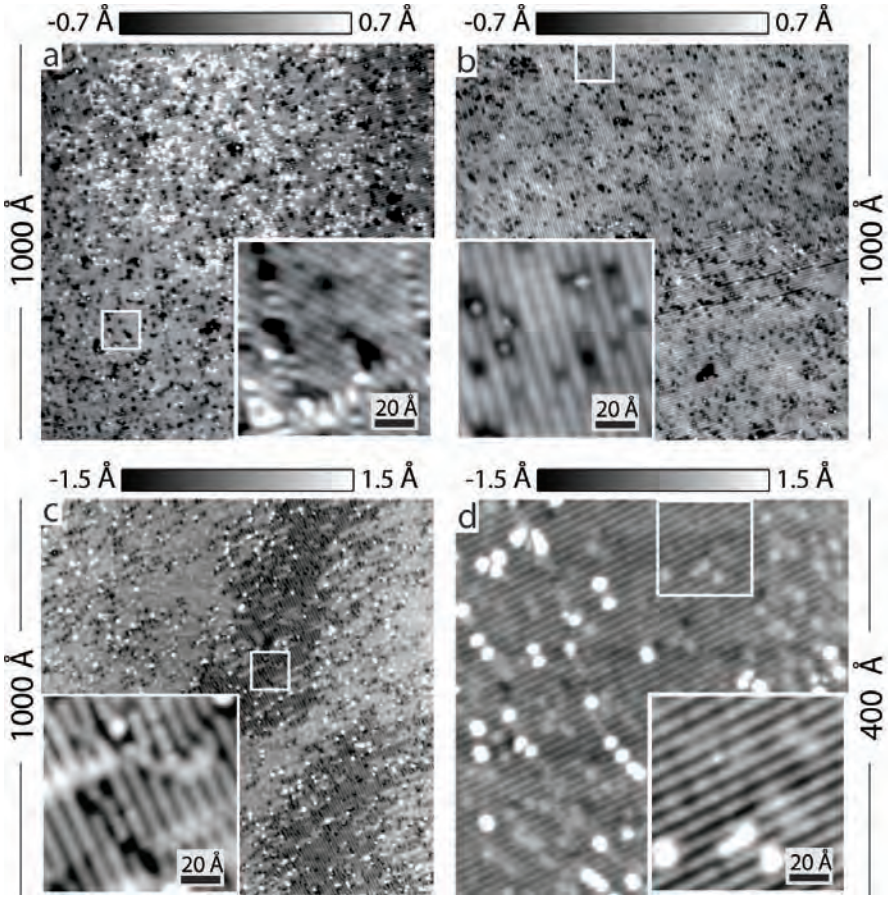

Figure 4.4: Constant current images on Ca122 and P doped Ba122, V_{sample}=50 mV, I_{set}=40 pA. (a) The only instance on $CaCo_xFe_{2-x}As_2$ a ($\sqrt{2} \times \sqrt{2}$) reconstructed surface was encountered on an otherwise completely (2×1) reconstructed surface of which an example is shown in (b). (c)-(d) (2×1) surface structures on $BaFe_2P_xAs_{2-x}$, which are identical in appearance to the (2×1) structures seen on compounds without substitution of the As atoms. All insets are 100×100Å^2 enlargements of the areas indicated with boxes.

dicating that the samples are homogeneous, high quality crystals. With such a large fraction of As atoms replaced by the much smaller, but isovalent P atoms, one would expect to see a change in the constant current images if indeed the As surface would be imaged, similar to for instance N doping of As sites in GaAs [117]. However, as can be seen from Figs. 4.4c-d, the topographs obtained on $BaFe_2P_xAs_{2-x}$ are indistinguishable from those obtained on for instance $BaCo_xFe_{2-x}As_2$ or $CaCo_xFe_{2-x}As_2$.

4.4 Apparent barrier height on pnictides

An intriguing property of the 122 pnictides is the difficulty with which atomic resolution is obtained, for instance the individual atoms on the (2×1) reconstruction are only seen for rather high currents (i.e. small tip-to-sample distances). In case of the pnictides, this is a direct consequence of the unusual small value of the apparent barrier height, Φ. From Equation (2.1) it follows that the work function can be extracted by measuring the tunneling current as a function of tip-to-sample distance, a so called I(z) measurement. As the barrier height is a measure of the steepness of the exponential drop in the current for increasing distance, the higher this value, the higher the z-resolution. This is the reason that one of the selection criteria for a good tunneling tip is a high work function when characterising the tip on Au(788). As mentioned in chapter 2, the barrier height or work function is a material dependent property and is usually a few eV. Several elemental work functions relevant in the context of the pnictides are listed in Table 4.2. For elemental Au, the work function is 5.1-5.47 eV, similar to the work functions of Pt and Ir (the tip material mainly used in the investigation of the 122 pnictides), values which are typically found for good tips on the Au(788) crystal.

Element	Φ (eV)	Element	Φ (eV)	Element	Φ (eV)
Se	5.9	Te	4.95	As	3.75
Pt	5.12-5.93	Fe	4.67-4.81	Ca	2.87
Au	5.1-5.47	Bi	4.34	Ba	2.52-2.7
Ir	5.00-5.67	Pb	4.25	K	2.29

Table 4.2: List of work functions of several elemental materials, taken from Ref. [118]. For single crystalline materials different orientations can have a slightly different work function, indicated by the spread in the work function.

The work function on the Ba122 pnictides, however, for the dozens of samples measured throughout this research is never seen to be higher than 1.8 eV, and is usually around 1.5 eV, see Fig. 4.5a for a typical example. Even though the work function is a property of the whole material, it will be most strongly affected by the surface layer. A monolayer of Ba on W(001) has for instance been reported to lower the work function with ~ 2 eV, to approximately the bulk Ba work function [119]. Looking at Table 4.2, the lowest work function of the pure elements of which Ba122 consists is that of Ba, followed by As and Fe, in steps of nearly 1 eV. This alone is already an indication that the surface layer is half a Ba layer, but is in itself inconclusive. Interesting to note at this point is that the work function is not seen to change as a function of surface topography on the 122 pnictides, i.e. the $(\sqrt{2} \times \sqrt{2})$ and (2×1) reconstructions have very similar work functions, suggesting that the two surface structures are both reconstructed Ba terminations.

From Table 4.2 it can be seen that elemental Ca has a slightly higher work function than Ba. As nothing is changed other than replacing the Ba layer for a Ca layer, it is

not an unreasonable assumption that the work function will track the difference in work function between Ba en Ca, but only if the Ba and Ca layers are at the cleavage surface. Indeed, the work function on (2×1) structures encountered on Ca122 is at 1.9 eV slightly higher (Fig. 4.5b). If As (or Fe) would be the surface layer, one would not have expected the work function to be influenced this much as the cation layer in that case would be buried deep underneath the top few layers. Although not a direct proof, this observation once again adds to the notion that indeed the *M*-layer is the topmost layer in the *M*122 pnictides.

$Fe_{1+y}Se_xTe_{1-x}$on the other hand, where clear atomic contrast is readily obtained, and where the surface layer consists of Se (Φ = 5.9 eV) and Te (Φ = 4.95 eV) atoms, has a work function that is considerably higher than that seen on the *M*122 systems, see Fig. 4.5c. As a comparison to these iron based superconductors, three other materials are shown in Fig. 4.5d-f with a relatively large work functions where atoms are clearly resolved. As these materials are imaged using identical tips in the same setup as the pnictides were investigated in, the low work function seen in the pnictides is clearly shown to be a property of the material, that can only be explained by having a Ba (or equivalent) terminated surface layer.

One could still speculate that the work function seen with STM does not reflect the properties of the surface, but of the tip. Accidentally picking up a Ba atom during approach would change the work function of the tip and thereby the average work function of the sample and the tip that is actually measured. Since a large number of samples has been measured, most of which gave (2×1) or ($\sqrt{2} \times \sqrt{2}$) structures over a large field of view upon the first touchdown directly after characterisation on the Au(788) crystal, this scenario is highly unlikely. Moreover, many tips were confirmed to be unaltered after measuring a 122 pnictide by characterisation on the same Au(788) crystal afterwards.

4.5 Low energy electron diffraction on $BaFe_{1.86}Co_{0.14}As_2$ and $Fe_{1.07}Se_{0.45}Te_{0.55}$

Figure 4.6 shows LEED data with E_0=110 eV. In Fig. 4.6a, the low temperature cleavage surface (17 K) of the Ba122 superconductor gives rise to spots very clearly at positions other than those originating from the tetragonal unit cell of either Ba or As. Spots corresponding to both ($\sqrt{2} \times \sqrt{2}$) and (2×1) reconstructions in both a and b directions of the crystal are present. In the STM topographs of Fig. 1, we clearly image the (2×1) structures as the basic unit forming the ribcages. However, under our imaging conditions, the ($\sqrt{2} \times \sqrt{2}$) structures seen clearly in the high-T cleave do not generate sufficient contrast in the low-T cleaved data of Fig. 4.1a and b. For very low junction resistances, the ($\sqrt{2} \times \sqrt{2}$) topography has been imaged directly in the STM of low-T cleaved crystals of the parent compound Ba122 in Ref. [113].

Returning to the LEED data, upon increasing the temperature, all non-tetragonal LEED spots start to lose intensity above 100K, and by reaching 200K, only the tetragonal reflections remain (Fig. 4.6b). More importantly, on re-cooling the sample back

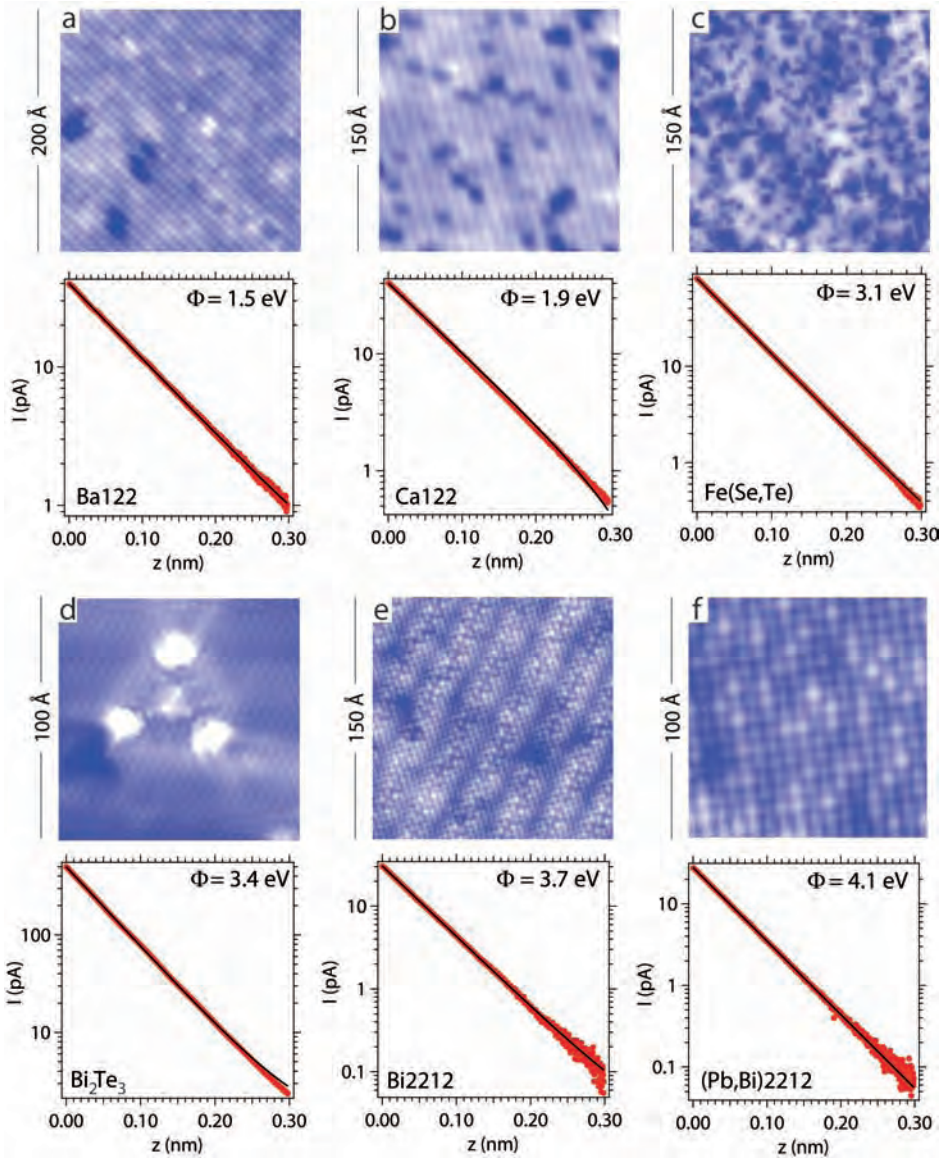

Figure 4.5: Typical constant current images (top) on various materials imaged on the same system using identical tips together with I(z) curves (bottom) taken on each surface. From the I(z) curves, the average work function of the sample and the tip, Φ, is extracted using Equation (2.1). The values for the work function are indicated in the I(z) curves, as well as the material in question. The unusually low work function seen on the *M*122 systems is a strong indication of a Ba as opposed to As terminated surface (panel (d) courtesy of J. Kaas).

to 17K, *none* of the non-tetragonal spots reappear. The main spots, however, be-

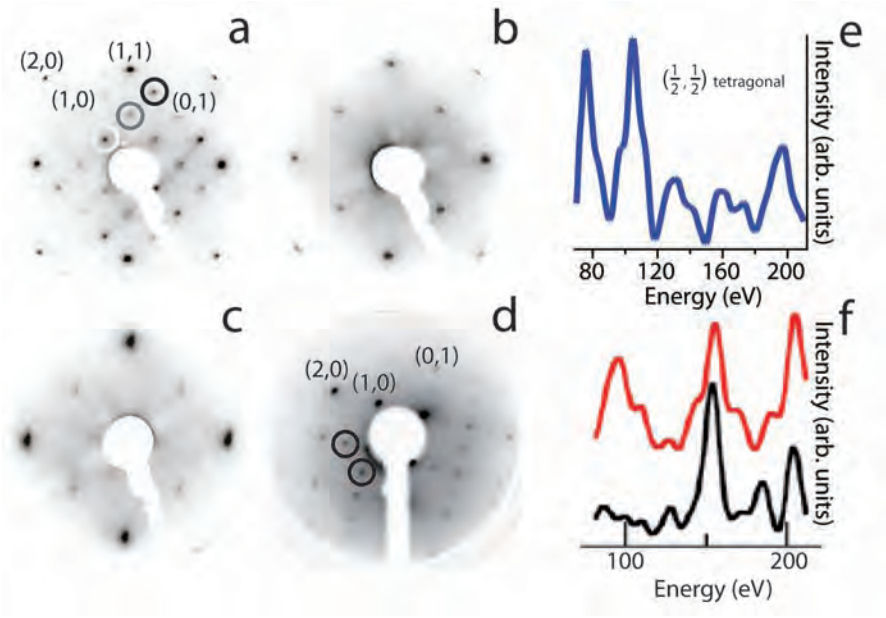

Figure 4.6: Low energy electron diffraction, taken at 110eV, unless stated otherwise. (a) $BaFe_{1.86}Co_{0.14}As_2$ cleaved and measured at 17K. The spots marked with a circle are the tetragonal ($\frac{1}{2}$,0) (white), ($\frac{1}{2}$,$\frac{1}{2}$) (grey) and ($\frac{1}{2}$,1) (black) reflections. (b) Same surface, but warmed up and measured at 200K. (c) $Fe_{1+y}Se_xTe_{1-x}$ cleaved and measured at 17K. (d) Low temperature cleaved $CaCo_xFe_{2-x}As_2$, taken at 141 eV. The relative abundance of (2×1) and (1×2) structures with respect to the ($\sqrt{2} \times \sqrt{2}$) structure is reflected in the LEED pattern which only supports spots corresponding to striped reconstructions (marked by the black circles). (e) I(V) trace of the ($\frac{1}{2}$,$\frac{1}{2}$) spot of Ba122. (f) LEED I(V) trace (top, red) and theoretical calculation (bottom) corresponding to the same spot as shown in (e) adapted from [113]. The mismatch rules out the As layer as the origin of the extra diffraction spots.

come more diffuse once the cleave is or has been at higher temperature, signalling increased surface disorder or the presence of structurally incoherent reconstructions. Having presented the LEED data for $BaFe_{1.86}Co_{0.14}As_2$, we now show in Fig. 4.6c a typical LEED pattern from the $Fe_{1+y}Se_xTe_{1-x}$compound cleaved and measured at low temperature. Not surprisingly, since the STM images only show the tetragonal atomic lattice, none of the extra LEED spots appearing in the Ba122 case are present in the $Fe_{1+y}Se_xTe_{1-x}$ data. Similarly, the LEED data taken on the $CaCo_xFe_{2-x}As_2$ system (see Fig. 4.6d), in which the surface structure seen with STM is dominated by (2×1) and (1×2) reconstructions, only supports spots corresponding to these two orientations of the striped structure, in line with the calculations.

Returning to the LEED data from the Ba122 system, tracking the intensity of the main (tetragonal) spots seen in Fig. 4.6a and b results in I(V) curves which follow the theoretical curves for diffraction from the As layer reported in Fig. 4a of Ref. [113].

This agreement between our data with LEED theory would appear to confirm that the outermost *complete* layer after cleavage consists of As atoms [113]. However, and importantly, the LEED data from the low temperature cleaves of $BaFe_{1.86}Co_{0.14}As_2$ and the parent compound $BaFe_2As_2$ (data not shown) clearly show $(\frac{1}{2},\frac{1}{2})_{\text{tetragonal}}$ spots, in contrast to the data of Ref. [113]. The I(V) trace of our $(\frac{1}{2},\frac{1}{2})_{\text{tetragonal}}$ spots (see Fig. 4.6e) is very different to both the experimental and theoretical I(V) curves in Ref. [113], possessing peaks and minima at totally different energy values, see Fig. 4.6f. The mismatch between our experiment and the theory in Ref. [113] rules out the As layer as the origin of our extra LEED spots, leaving the partially ordered Ba atom overlayer as the obvious candidate to explain the $(\frac{1}{2},\frac{1}{2})_{\text{tetragonal}}$ spots in LEED and the topographic features seen in STM with periods greater than the tetragonal repeat unit of 3.9 Å. A surprising observation in the STM topograph of Fig. 4.2b is the clear $(\sqrt{2}\times\sqrt{2})$ lattice on the surface of a high temperature cleaved sample, whereas the corresponding $(\frac{1}{2},\frac{1}{2})_{\text{tetragonal}}$ spots in LEED have ceased to be observable above the background upon warming up the sample. At this point, we mention that theoretical calculations predict that the $(\sqrt{2}\times\sqrt{2})$ (or checkerboard) reconstructed surface is the most energetically favourable ordered distribution of the remaining half of the Ba atoms on either side of the cleave [116]. One approach to understand why the $(\sqrt{2}\times\sqrt{2})$ LEED spots disappear at higher temperature is offered by consideration of the dislocation networks seen in the STM topographic data in the high temperature cleaved surfaces (the 'black rivers' seen in Fig. 4.2b), which are absent in the low-T cleave topographs. Upon warm cleavage or increase of the sample temperature above ca. 200K, it is conceivable that fragmentation of the checkerboard order into nanoscopic domains causes the coherence length of the reconstruction to drop sufficiently such that the $(\sqrt{2}\times\sqrt{2})$ spots fade into the background of the LEED pattern, which itself is the result of a measurement which spatially integrates on a mm length-scale.

The measurements presented above formed the basis of a more detailed LEED investigation, where in collaboration with M. Lindroos and co-workers the LEED I(V) data were fitted to calculations as was done in Ref. [113]. As the number of fitting parameters is rather large, for a reliable result it is imperative to have as many diffraction spots as possible tracked over an as large as possible energy range. To this end, more datasets were taken which were subsequently fitted to calculations of both an As terminated surface and a Ba terminated surface. In the fit, the positions of the surface atoms were not fixed, but free to reorganise, mimicking a surface reconstruction, to give the best result. I(V) curves for a number of spots are shown in Fig. 4.7 along with the fits to the experimental data.

To quantify the level of agreement of the experimental data and the simulations, so called Pendry R factors (R_p) were used [120]. These factors are calculated using the position and width in energy of diffraction spots, but are little affected by the intensity of the spots as this is a function of various factors that are not well understood. The lower the Pendry R factor, the higher the agreement between simulation and data, where a satisfactory fit generally has $R_p < 0.3$. Using only the half integer

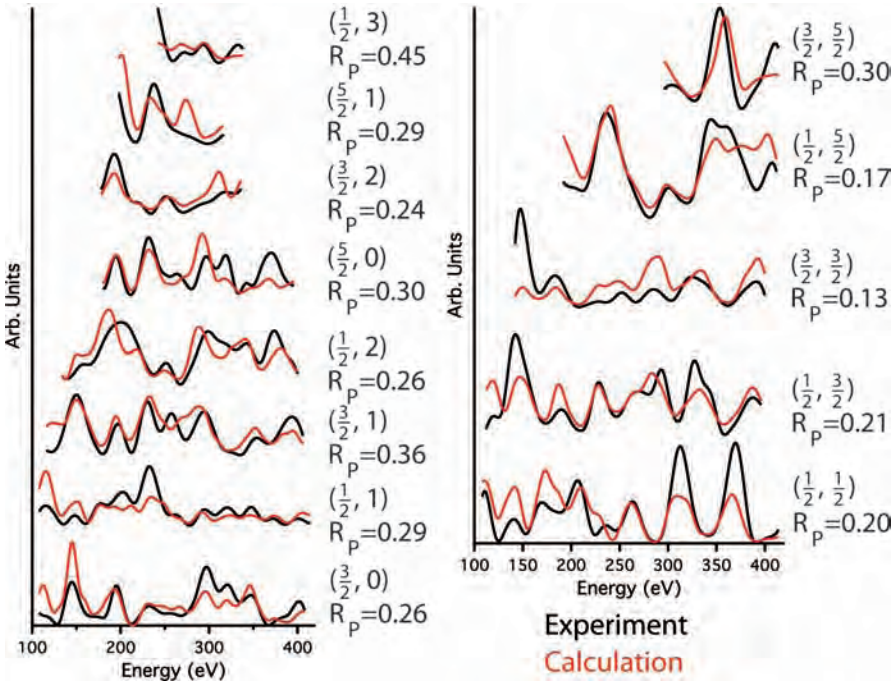

Figure 4.7: LEED I(V) curves for various half-integer spots. The left and right parts correspond to spots originating from the (2×1) and ($\sqrt{2}\times\sqrt{2}$) reconstruction respectively. Pendry R factors are indicated for each fit to a Ba terminated simulation, showing the excellent agreement. Courtesy of E. van Heumen.

spots, which are resulting from a surface reconstruction and cannot be a higher order diffraction of the bulk lattice, the experimental data was fitted with either a Ba or a As terminated simulation for both the ($\sqrt{2} \times \sqrt{2}$) and (2×1) reconstructions. As expected from the initial measurements shown in Fig. 4.6e, the As surface termination gives unacceptably high Pendry factors of 0.42 and 0.48 for the two reconstructions respectively. A Ba terminated surface on the other hand gives remarkably low factors of R_p =0.19 and 0.29 respectively, indicating the excellent agreement between experiment and simulation, and unambiguously showing that the cleavage surface is a reconstructed Ba layer. It should be noted that a Ba terminated surface alone is not sufficient to get this agreement, but a structural distortion of the first unit cell is required as well. As this distortion is seen to have a considerable impact on the surface density of states [121], its effect on the tunneling signal picked up in STM/S experiments should not be overlooked.

4.6 Surface model for the '122' systems

By now it is clear that the topographical diversity of the cleavage surface of the alkaline earth-122 material family is due to the partial alkaline earth atom overlayer that remains after cleavage. In fact, we can reconcile all our experimental STM data from the 122 systems within a very simple structural model, based only on differences in the distribution of the Ba atoms within the overlayer that remains on the surface after cleavage. A sketch of the model is shown in Fig. 4.8. When a sample is cleaved at low temperature, the Ba surface atoms are not mobile enough to re-arrange themselves into the energetically most favourable structure, with metastable situations such as the (2×1), or rib-cage reconstruction as the result. Increasing temperature enables the overlayer atoms to re-arrange, thus patches of checkerboard reconstruction are formed separated by domain walls ('black rivers'). Alternatively, more disordered configurations such as those seen in Fig. 4.2a are also possible, depending on the local concentration of Ba atoms.

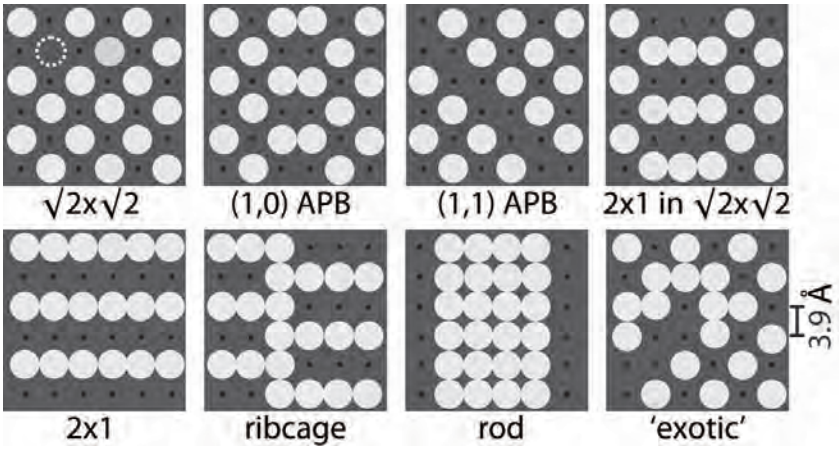

Figure 4.8: Sketch of various possible Ba surface overlayer configurations. Large (small) circles indicate the presence (absence) of a Ba atom. The dotted atom (left top) indicates a missing atom resulting in a black spot in topography. Extra atoms can similarly lead to bright spots. Anti-phase boundaries (APB) are shown running along two observed directions. Broader 'backbones' in the ribcage structure are created by adding atoms at the phase-shift boundary.

Ordering of the Ba surface atoms in locally densely packed structures surrounded by a relatively Ba-free region could lead to an increased corrugation in STM, matching the rods seen in Fig. 4.1 and the bright regions in Fig. 4.2c. However, these kind of structures are still within the same Ba layer as the locally less densely packed ordered ($\sqrt{2} \times \sqrt{2}$) and (2×1) regions, and thus these different topographies can cross over into one another as indeed has been observed. Evidently, more random distribution of the Ba atoms in the overlayer could lead to topographs as in Fig. 4.2a and d.

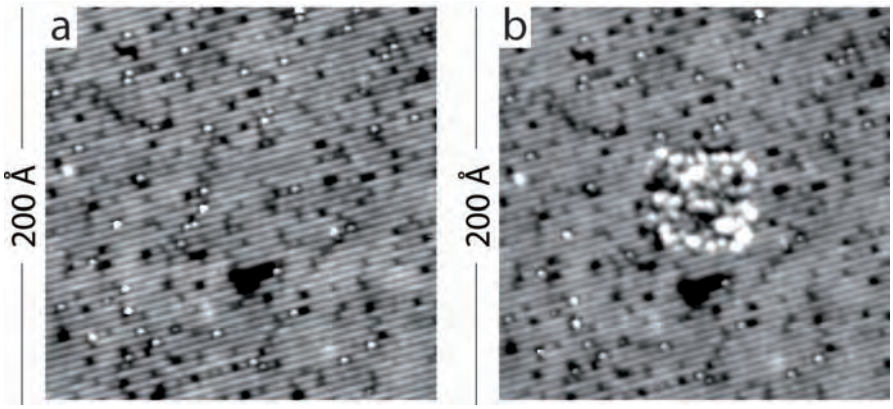

Figure 4.9: (a) Regular (2×1) surface reconstruction imaged on a Ca122 sample (V_{sample} = 50 mV, I_{set} = 40 pA). After scanning the central part of the surface using a rather violent combination of bias voltage and setup current (a few mV and a tens of nA), this area is completely disordered as shown in (b), whereas the part of the surface where no such treatment has been performed remains identical.

A nice illustration of the ease with which the surface atoms are rearranged is shown in Fig. 4.9. In this example, initially a regular (2×1) surface structure on Ca122 is imaged (Fig. 4.9a). Subsequently, the tip is scanned over the central 10×10 nm^2 area using a rather violent combination of bias voltage and tunneling partial current, resulting in the tip stirring the surface[1]. After a few minutes of playing with the surface atoms in this way, the original 40 nm square field of view is imaged again. The result shown in Fig. 4.9b shows an otherwise unaffected (2×1) structure, where the central 10 nm part is completely randomised, but where the average height is still identical to the rest of the image. No atoms have therefore been picked up or deposited on the surface, the surface atoms have only been rearranged. Once again, this could only be possible for loosely bound Ca surface atoms, and is unlikely in case strongly bound As atoms are the surface atoms being imaged in the STM measurements.

4.7 Summary

In summary, the Ba122 cleavage surface exhibits a large variety of topographies and has pronounced cleavage temperature dependence. In LEED, spots corresponding to large scale coherent structures of dimensions larger than the 3.9 Å tetragonal unit cell, i.e. (2×1) and ($\sqrt{2} \times \sqrt{2}$), appear for low temperature cleaved samples. These spots vanish upon warming the sample to 200 K and do not reappear after cooling back to 17 K. Since superconducting $BaFe_{1.86}Co_{0.14}As_2$ possesses no spin density

[1] similar to the rummaging around in a bowl of balls by contestants of the Dutch television show 'Lingo' after guessing a word right

wave at 4.5 K [122], the (2×1) and ($\sqrt{2} \times \sqrt{2}$) topographies in STM cannot be explained by a SDW-driven creation of two distinct As sites, but only by the ordering of the Ba atoms remaining on the surface after cleavage. It is proposed that the disappearance of the extra spots seen in LEED at higher temperatures is a signal of fragmentation of these structures due to a re-distribution of the Ba atoms at the surface into energetically more favourable configurations on a small length scale. These still appear as ordered patterns in STM, yet possess insufficient long range order to support LEED spots. The longer range order does not re-establish itself upon re-cooling, thus the non-tetragonal spots do not reappear and the tetragonal LEED spots themselves become more diffuse. The argument that the non-tetragonal LEED spots originate from the Ba termination layer is underpinned by the fact that our experimental LEED I(V) profiles of various fractional spots have an unusually high degree of resemblance to simulations using a Ba terminated surface, in contrast to calculations using As terminated surfaces. Furthermore, the observation of practically identical surface structures on both Ca122 and P doped Ba122 offer additional evidence that the observed surface topographies are dominated by the half-*M* layer on the cleavage surface of the crystal. These additional data also indicate that a generalisation to all *M*122 systems, where *M*=(Ba, Eu, Sr...) may be valid. Comparison of work functions on various pnictide superconductor cleavage surfaces all fall within the picture of a Ba terminated surface. Moreover, since the work function on various surface structures, i.e. (2×1), ($\sqrt{2} \times \sqrt{2}$), etc., on the same 122 sample with the same tip are identical, these different structures are all believed to reconstructed Ba terminations. In stark contrast to the richness and complexity of the surface topography of the 122 family of compounds, $Fe_{1+y}Se_xTe_{1-x}$ displays only one type of cleavage surface and LEED pattern without any sign of reconstructions, independent of the cleavage temperature, explained by the undisputed cleavage between adjacent SeTe layers.

CHAPTER

5 Nanoscale superconducting gap variations and lack of phase separation in $BaCo_xFe_{2-x}As_2$

Having determined the cleavage surface of the '122' pnictides in the previous chapter, tunneling data from superconducting $BaFe_{1.86}Co_{0.14}As_2$ and its parent compound, $BaFe_2As_2$ will be presented, and the influence of the surface on the electronic states will be discussed. In the superconductor, clear coherence-like peaks are seen in STS across the whole field of view, and their analysis reveals nanoscale variations in the peak-to-peak separation, Δ_{pp}. The average peak-to-peak separation gives a 2Δ of $\sim$7.4 k_BT_c, which exceeds the BCS weak coupling value for either s- or d-wave superconductivity. The characteristic length scales of the deviations from the average gap value, and of anti-correlations observed between the gap magnitude and both the zero bias conductance and coherence peak strength, match well with the average separation between the Co dopant ions in the superconducting FeAs planes.

This chapter is published as F. Massee et al., Phys. Rev. B ***79****, 220517(R) (2009)*

5.1 Introduction

The pnictide high T_c superconductors [1] with maximal T_c's currently exceeding 55 K [2], are the subject of global scrutiny at a level on a par with that seen for the cuprates. One of the most debated issues are their similarities and differences with respect to the cuprates [123]. The pnictides display many features we recognise from the cuprate repertoire, yet there are arguments that they are essentially different [124]. In the last few years, scanning tunneling microscopy and spectroscopy (STM/S) have played a major role in investigating the electronic structure of the cuprates on length scales down to those of the atom [98, 125–128]. This effort has brought the role of intrinsic disorder introduced by dopant atoms into sharp focus. Consequently, $BaCo_xFe_{2-x}As_2$ is of great interest, not only as an electron-doped pnictide, but also because the electronically active dopants in this system are situated in the superconducting layers themselves.

5.2 Experimental

Single crystals of superconducting $BaFe_{1.86}Co_{0.14}As_2$ and the non-superconducting parent compound $BaFe_2As_2$ (Ba122) were grown using a self flux method. Typical crystal sizes are $1\times1\times0.1mm^3$ (see Fig. 5.1b). The high quality of our crystals is illustrated in Fig. 5.1a, with the parent compound displaying the well-known resistivity kink at 130 K which has been associated with the magnetic transition to an anti-ferromagnetically ordered state and the associated transition from tetragonal to orthorhombic crystal symmetry [129–132]. Co doping erases any sign of these transitions in the resistivity, but brings with it a very sharp transition into the superconducting state, which takes place at 22 K $\pm$ 0.25 K in this case.

For the STM investigation, crystals were cleaved at a pressure of $< 5x10^{-10}$ mbar at room temperature in a preparation chamber and immediately transferred into the STM chamber (base pressure $< 1.5x10^{-11}$ mbar), where they were cooled to 4.2 K. The experiments were carried out using electrochemically etched W and cut Pt/Ir tips, which were conditioned before each measurement on a Au(778) single crystal and yielded identical results. In all cases, the spectral shapes obtained were independent of the tip to sample distance [133].

Low energy electron diffraction (LEED) was performed *in situ*, directly after the STM/S measurements. For all measured samples cleaved at room temperature, only the tetragonal unit cell spots were seen in LEED (see Fig. 5.2a), with no sign of extra spots (or extinctions). In the previous chapter this has been interpreted as a breaking up of ordered structures into patches smaller than the LEED coherence length at high temperatures.

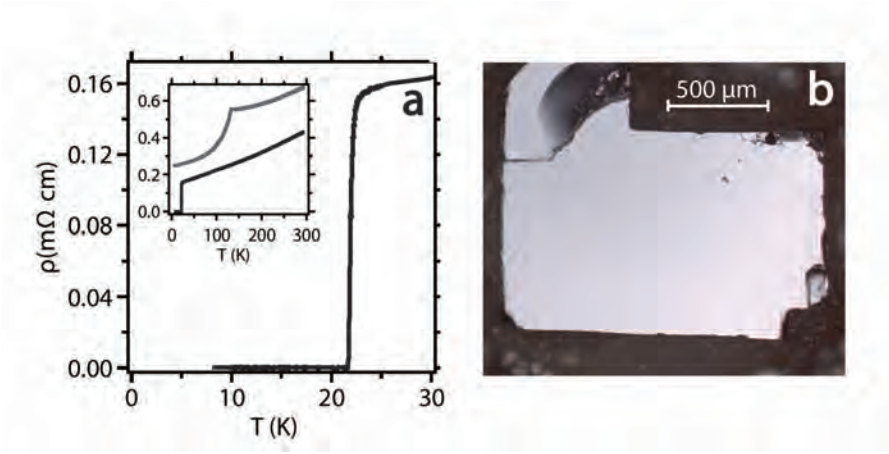

Figure 5.1: (a) Co-doped Ba122 shows a sharp superconducting transition (ΔT_c ~0.5 K) at 22 K (red curves). The inset displays the full temperature range, with data from the parent compound (blue trace). (b) Optical micrograph of the very flat cleavage surface typically obtained.

5.3 Surface topography

To begin, the Co-doped crystals will be discussed. A constant current image with atomic resolution is shown in Fig. 5.2a. In general, over areas of up to 150x150 nm^2, no sign of steps on the surface was seen, with the maximal apparent corrugation being less than 1.5 Å on all the data shown here.

From the zooms shown in Figs. 5.2b and 5.2c, one can immediately see that the surface atoms lie arranged along the direction of the clear (1×1) tetragonal unit cell measured using LEED, but that the inter-atomic spacing is quite irregular. The most frequent separation seen is ~8 Å: twice the tetragonal unit cell. Occasionally a row of atoms with a separation of 3.9 Å occurs, as seen in panel (c), and sometimes, the (bright) atoms sit on a black background. The irregularity in inter-atomic distances is reflected in the Fourier transform shown in Fig. 5.2d, in which smeared out features predominate, corresponding to a real space separation of ~8 Å (marked with an 'X' on the FFT). The tetragonal lattice is barely visible in the form of weak spots, highlighted in Fig. 5.2d with a yellow arrow.

As has been shown in chapter 4, the cleavage surface of Ba122 consists of half a Ba layer, which has ordered or disordered structures that are cleavage temperature dependent. For a room temperature cleave, the Ba ions may re-order to minimise their mutual Coulomb repulsion, resulting in inter-atomic distances larger that the in-plane tetragonal lattice constant, as seen in Fig. 5.2. We note that since there are structures observed with a lower symmetry, and thus higher energy, other factors than pure Coulomb repulsion - e.g. possibly the orthorhombicity of the Fe/As layer and strain or defects - are also playing a role. A commonly encountered variation

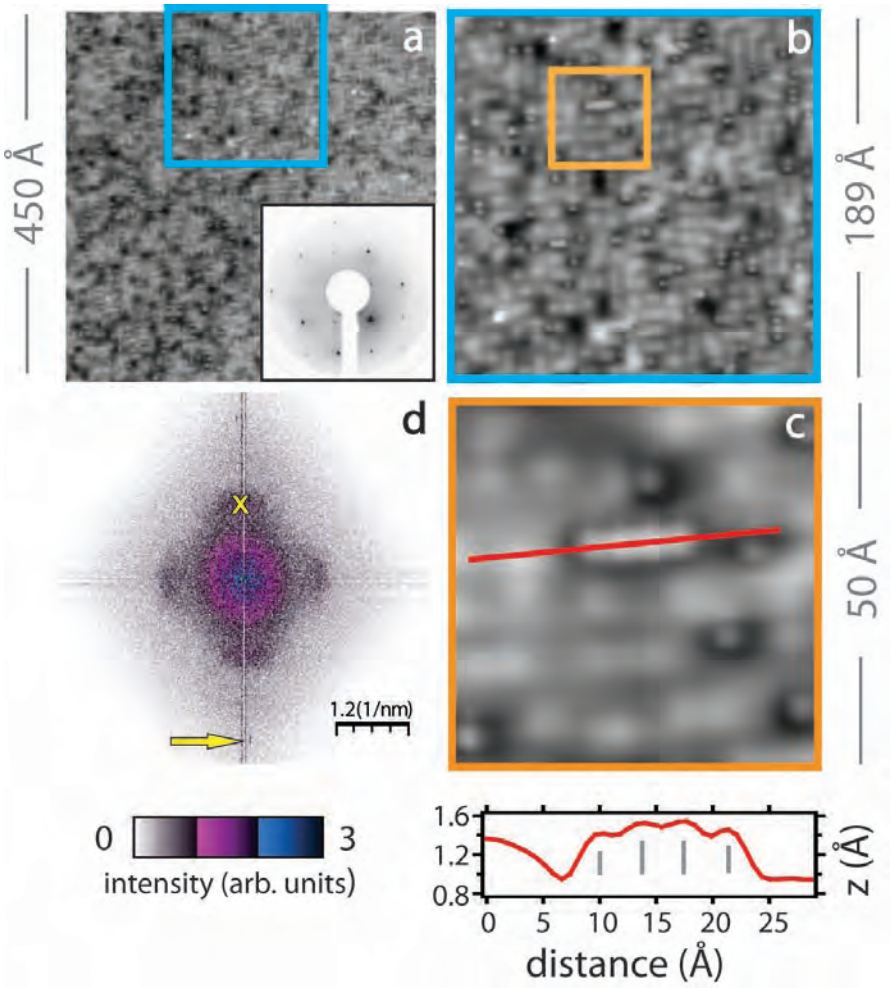

Figure 5.2: (a) Constant current image (V_{sample} = -35 mV, I_{setup} = 40 pA) of Co-doped Ba122. The inset shows LEED from the same surface with E_0=114eV. (b) Zoom of panel (a): the surface atoms can be seen as bright dots. (c) Further zoom of (b), showing a row of four surface atoms separated by the tetragonal cell dimension of 3.9 Å. (d) Fourier transform of panel (a), whereby the yellow X and arrow indicate real-space distances of 8 and 3.9 Å, respectively. All data (with exception of the LEED) were recorded at 4.2 K.

is shown in Fig. 5.3a from a different crystal of the same doping level, in which the atomic contrast is absent, and a 2D, maze-like network is seen, oriented along the tetragonal axes with typical a period of ~12 Å. This image resembles previously reported one-dimensional stripe-like structures, [109,112] whereby the 'stripes' shown here appear cut into shorter and more disordered segments, probably as a result of the higher cleavage temperature. This is in keeping with a recent report of the temperature dependence of the surface topology in a related system [110]. In Fig.

5.3b, an image from pristine Ba122 is shown, which displays a very similar surface topology as in panel (a), as can also be seen from the line scans through both images shown in panel (c).

5.4 Tunneling spectroscopy on $BaCo_xFe_{2-x}As_2$ and $BaFe_2As_2$

Differential conductance spectra (dI/dV) of both the Co-doped and pristine Ba122 systems were recorded on a square 64x64 pixel grid at 4.2 K using a modulation amplitude of 2 mV at a lock-in frequency of 427.3 Hz. The spectra for the Co-doped system vary significantly between different locations within a single field of view (FOV).

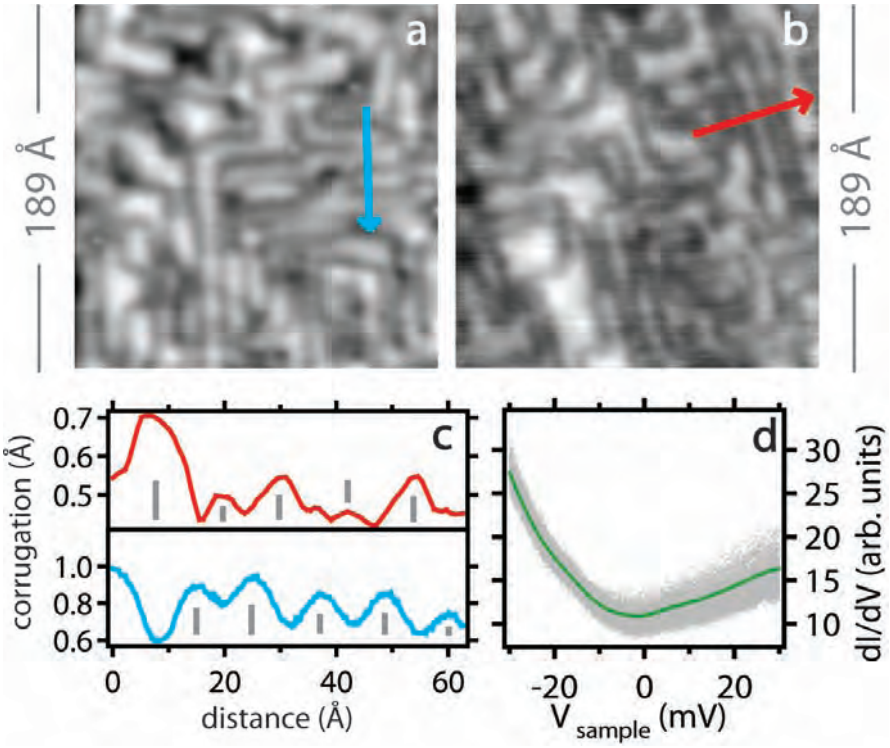

Figure 5.3: (a) Constant current image from a $BaFe_{1.86}Co_{0.14}As_2$ sample (V_{sample} = -88 mV, I_{setup} = 40 pA). (b) Analogous topography from $BaFe_2As_2$ (V_{sample} = -100 mV, I_{setup} = 33 pA). (c) Line scans from the superconducting (top) and parent (bottom) compounds taken along the arrows. Typical distances between the bright rows in the images is 12 Å indicated by grey ticks in the line scans. (d) Overlay of 400 dI\dV conductance spectra from pristine Ba122, together with their average (bold line). All data recorded at 4.2 K.

In Fig. 5.4a representative STS spectra for differing gap values (each spectrum is an average of four adjacent pixels) are plotted. The spectra show not only a clear

variation in peak-to-peak separation, hereafter taken as a measure of the superconducting gap ($2\Delta_{pp}$), but also in the value of the conductance at zero bias (ZBC) and in the strength of the coherence peaks. The spectra also vary in their asymmetry, and in the form of their higher energy structures. While the variation in the high energy tunneling signatures are more pronounced than those reported in Ref. [112], they are less dramatic than what has been observed in a study of the related $Sr_{1-x}K_xFe_2As_2$ compound [109]. Naturally, one is interested in the real-space $2\Delta_{pp}$ distribution, and thus the peak-to-peak separation from all 4096 spectra is plotted as a gap map in Fig. 5.4b. The map indicates that the major part of the FOV supports a gap, Δ_{pp}, of 7 meV (green areas), with smaller patches of dimension between 5 and 10 Å possessing significantly smaller (red/yellow) and larger (blue) gaps. From this FOV, only a handful of spectra did not exhibit coherence-like peaks, and thus if these peaked structures give the superconducting gap, phase separation between superconducting and non-superconducting (magnetic) regions can be excluded from these data.

From Figs. 5.4a & b it is clear that $BaFe_{1.86}Co_{0.14}As_2$ supports $2\Delta/k_BT_c$ values between 5.3 for the smaller gaps, through 7.4 for the modal gap value (7 meV) to 10.6 for the largest gaps. The modal gap is close to that seen recently in ARPES from optimally Co-doped Ba122 for the outermost Γ centered (Γ_2 or β) Fermi surface [62], and is in keeping with data from another STS experiment on Co-doped Ba122 [112]. The observation that STS measurements mainly seem to pick up the Γ centered Fermi surface is in line with the notion that the tunneling rate along the out-of-plane direction is strongly suppressed for increasing in-plane momentum, $|k_{||}|$ [18,19]. Note that the normalised gap values found here are in line with ARPES data from the outer hole pocket Fermi surface in the hole-doped (Ba,K)-122 system [134]. As the small and big gap Fermi surfaces are swapped in (Ba,K)-122 with respect to (Ba,Co)-122, tunneling experiments on the former system are expected to show a small gap instead of the big gap seen on (Ba,Co)-122. In any case, all of the normalised gap values we observe on (Ba,Co)-122 are greater than those expected for a weakly coupled BCS s- or d-wave superconductor.

5.5 $2\Delta_{pp} \leftrightarrow$ zero bias conduction relation

Closer inspection of Fig. 5.4a reveals a relation between the ZBC, $2\Delta_{pp}$, and the coherence peak strength: when $2\Delta_{pp}$ is small (large), the ZBC is large (small) and the coherence peaks are strong (weak). To see whether these relations hold for the whole data set, three qualitative tests are conducted. First, in Fig. 5.4c the results of binning all the STS spectra into five groups, depending on their peak-to-peak separation is plotted[1]. Secondly, in Fig. 5.4d a map of the ZBC value is shown, with an inverted colour scale to ease comparison with panel (a). Thirdly, the spatial distribution of the coherence peak strength for this sample (Fig. 5.4f) is mapped, which gives a nearly identical image to the ZBC map in panel (d). The fact that the inverse relation

[1] Δ_{pp} values have been binned as follows: 0-5.5 meV, 5.5-6.5 meV, 6.5-7.5 meV, 7.5-8.5 meV, 8.5-$\Delta_{pp,\,max}$ meV.

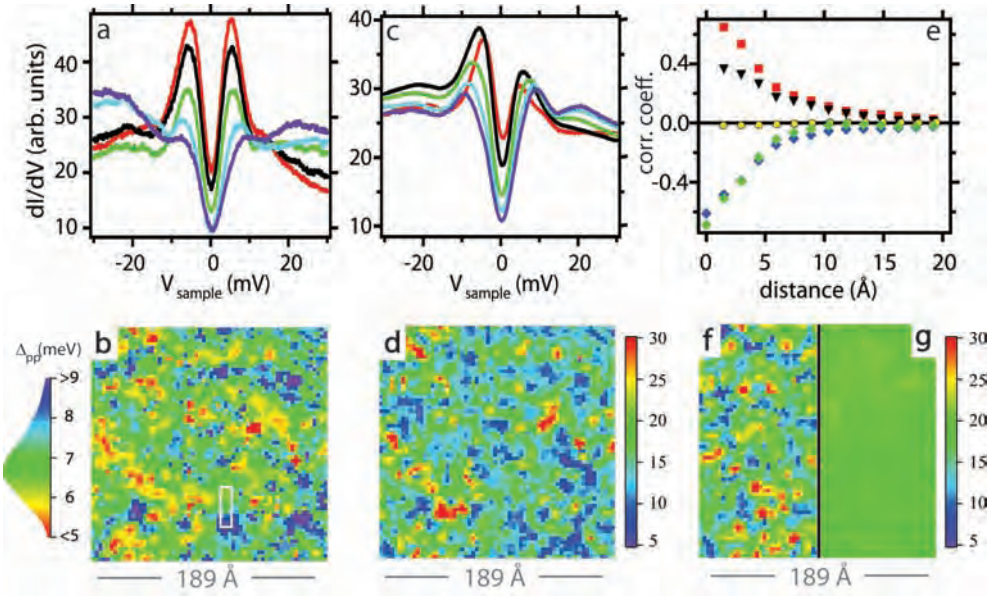

Figure 5.4: (a) STS spectra from $BaFe_{1.86}Co_{0.14}As_2$ (averages of four adjacent pixels) displaying different values of Δ_{pp}, taken from the region marked in panel (b). (b) Gap map with identical FOV as Fig. 5.2b, taken with the same setup conditions. (c) Binned spectra for five ranges of Δ_{pp} [1], plotted in colours matching those in the gap map, whereby black has been swapped for yellow, for clarity. (d) Map of the zero bias conductance on an inverted colour scale from the same data set as panel (b). (e) Correlation functions. From top to bottom: autocorrelation of the gap map shown in panel (b) (red squares) and of an analogous dataset recorded from the FOV shown in Fig. 5.3a (black triangles). Yellow dots: cross correlation of the gap map of panel (b) with the corresponding topograph (Fig. 5.2b). Blue (green) diamonds: cross correlations between the gap and ZBC (peak-strength) maps. (f) Map of the coherence peak strength (for half of the FOV of panels (b) and (d), and on an inverted colour scale), extracted from a comparison of the coherence peak weight to the high energy background. (g) ZBC map of pristine Ba122 recorded from half the FOV shown in Fig. 5.3b. The conductance scale (shown on the right) is the same as that used in panel (d).

between $2\Delta_{pp}$ and ZBC (and between $2\Delta_{pp}$ and the coherence peak strength) is also clearly visible in the binned (i.e. highly averaged) STS spectra and the fact that the gap, ZBC and peak strength maps resemble each other closely (providing the colour scale in the latter two maps is inverted) indeed indicates that the relation between $2\Delta_{pp}$, ZBC and peak strength holds for the data set as a whole, and not just for the STS spectra shown in Fig. 5.4a.

In a next step, the relations between the $2\Delta_{pp} \Leftrightarrow$ ZBC and peak-strength maps is formalised by comparing their azimuthal-integrated cross correlation traces. Fig. 5.4e shows the results, indicating a clear anti-correlation which dies off over 8-10 Å. The question arises as to the origin of the observed spatial disorder in the $2\Delta_{pp}$ values. As a first suspect, the non-trivial surface topography illustrated in Figs. 5.2 and

5.3 is considered. Here, pristine Ba122 offers the best test of this point, as it possesses the same complex Ba termination topography, and yet is void of substitutional disorder within the FeAs structural unit. Fig. 5.3d shows a compilation of one tenth of a complete STS data set (400 of 4096 STS spectra) - and their average - taken from pristine Ba122 across the same FOV as the topograph shown in Fig. 5.3b. The near-E_F electronic states in the parent compound are fairly spatially homogeneous in terms of both the shape of the spectra and the absolute dI/dV value.

5.6 Superconducting gap disorder due to Co dopants

To compare the variation in absolute conductance with that seen in the superconductor, a ZBC map from pristine Ba122 is shown in Fig. 5.4g, using the same color scale as Fig. 5.4d, after correction for the difference in junction resistance. Although the two ZBC maps are from different cleaves of differing materials, it is still obvious that the pristine material has much less variation and does not possess structure on the length scales of the superconductor. Thus, the gap disorder seen in Fig. 5.4 is a property of the superconducting system, and the finger is quickly pointed in the direction of the Co dopants as the culprit. For the used doping level, 1 in 14 Fe atoms is replaced by a Co dopant, and at a zeroth level this gives a Co - Co separation of a little over 10 Å. The first length scale over which Co disorder would be visible is therefore 10 Å, as observed here. In Fig. 5.4e autocorrelation traces are shown for the gap map in Fig. 5.4b and the analogous trace for a gap map recorded from an identical FOV as Fig. 5.3a, i.e. a superconductor cleave with a clearly different topography yet similar STS spectra. Both these (positive) correlation traces show that 8 Å is the characteristic length scale of the significant gap variations, which is very close to the Co - Co length scale. The fact that the atomically-resolved cleaves (Fig. 5.2a) and those with the 2D maze-like structure (Fig. 5.3a) both give the same length scales for the deviations from $\overline{2\Delta_{pp}}$ is a further indication that in these cases the topographic details - which most likely track the particulars of the surface Ba (dis)order - do not have much direct effect on the superconducting system. We note that - albeit on a somewhat coarser energy scale, similar conclusions have been drawn from a recent photoemission study of the Ba122 system [83]. Finally, we remark that the cross correlation traces between the gap map and the topography are zero for both types of topography (see Fig. 5.4e).

How do the spatial gap variations found here in an electron doped pnictide compare with those from STS studies of the cuprate high T_c's at analogous doping levels? Optimally doped Bi2212 yields a similar total spread of a factor two in normalised gap values, but upshifted with respect to those here to lie between 6 and 13 $k_B T_c$ [126], see also appendix A. Recently, the emphasis has come to lie on the role played by the pseudogap in the observed large apparent superconducting gap disorder seen in the cuprates [135]. In the pnictide STS data presented here, it would be natural to take the modal gap value as that representing areas with Co doping occurring in the FeAs plane at the nominal level. Consequently, the small gaps could

either be under- or overdoped regions formed due to clustering of Co since both would - in principle - lead to a lower T_c (and presumably Δ_{pp}). This would leave only the larger peak-to-peak separations unaccounted for. To decide whether, as in the cuprates, these large-gap regions are related to the presence of a pseudogap or not will require detailed temperature dependent measurements, which will be the topic of the next chapter.

5.7 Summary

In summary, detailed STM and STS investigations of pristine Ba122 and samples of the electron doped superconductor $BaFe_{1.86}Co_{0.14}As_2$ are presented. In the first part of the chapter the complex topography of the surfaces of these single crystals is revisited, and shown to be a result of partial lift-off of the Ba ions upon cleavage. It is subsequently demonstrated that the termination-plane topographic disorder encountered here has little effect on the low lying electronic states of these systems.

The STS data from the superconducting samples display clear coherence-peak-like features defining an energy gap of on average 7.4 k_BT_c. There exist, however, significant spatial deviations from this modal gap value, with the gap distribution ranging from 5-10 k_BT_c. If these gaps are indeed superconducting gaps, we can clearly rule out nanoscopic phase separation in these samples. There is a robust anti-correlation between the peak-to-peak separation and the zero bias conductance, and coherence peak strength, operating over length scales of ~8 Å. The spatial correlation of the low and high gap deviations from the modal gap value also displays the same length scale, one which is very close to the average separation of the Co atoms in the FeAs superconducting blocks, highlighting their importance as local dopants.

CHAPTER

6 Pseudogap-less high T_c superconductivity in $BaCo_xFe_{2-x}As_2$

The pseudogap state, already alluded to in chapter 2 (see also appendix A), is one of the peculiarities of the cuprate high temperature superconductors. Having seen features in the tunneling data presented in the previous chapter hinting at a possible pseudogap (i.e. the large spread in peak-to-peak separation) its presence in $BaCo_xFe_{2-x}As_2$ will be investigated in this chapter with temperature dependent scanning tunneling spectroscopy. It is observed that for under, optimally and overdoped systems the gap in the tunneling spectra always closes at the bulk T_c, ruling out the presence of a pseudogap state.

Most material in this chapter is published as F. Massee et al., EPL ***92****, 57012 (2010)*

6.1 Introduction

At first glance, the phase diagrams of the cuprates and the pnictides are strikingly similar. In both systems, electron or hole doping suppresses the magnetic ground state of the parent compound and produces a superconducting dome, see also chapter 2. However, whereas the cuprates are Mott insulators at low dopings and upon doping first completely lose their long range magnetic order before superconductivity emerges, the pnictides have a metallic ground state and upon doping directly cross from a magnetic to a superconducting phase. The nature of this transition is still under debate, as some studies find that the two regions can coexist [136–138] while others indicate a phase separation scenario [139, 140].

At low doping concentrations, the cuprates furthermore display a second energy scale, characterised by a depression of spectral weight at the Fermi level, which is observed both in the superconducting and normal state, the so called pseudogap [141, 142]. Since the role of the pseudogap phase in the cuprates is still under heavy debate, the establishment of the presence or absence of such a phase in the iron pnictides is of particular importance. There are several indications that at least some of the pnictides have a pseudogapped region at the underdoped side of the phase diagram. For instance, anomalous resistivity characteristics in $LaFeAsO_{1-x}F_x$ and $SmFeAsO_{1-x}F_x$ have been interpreted in a pseudogap-like scenario [143]. Nuclear magnetic resonance (NMR) investigations [144, 145] and angle resolved photoemission (ARPES) measurements [146] have found signs of a pseudogap in the former system as well. It should be noted, however, that Andreev spectroscopy measurements argue against a pseudogap in the latter system [147]. In $Ba_{1-x}K_xFe_2As_2$ ARPES [148], optical conductivity [149] and pump-probe spectroscopy [150] measurements showed pseudogap-like behaviour, and claims of possible pseudogap behaviour have been made in the $FeSe_{1-x}Te_x$ system [151]. In the case of $BaCo_xFe_{2-x}As_2$, ARPES measurements have reported a slight depression above the superconducting transition temperature [62], possibly caused by a weak pseudogap.

Another observation that could be linked to a pseudogap phase is the large spread in the separation between the quasi-particle peaks ($2\Delta_{pp}$), observed in tunneling spectra of the pnictides as is shown in the previous chapter and reported by [108, 112], which is difficult to reconcile with the sharpness of the superconducting transition. In underdoped cuprates, these spectra are dominated by the pseudogap features, and the true superconducting quasi-particle spectrum has been resolved only very recently [135]. The question is therefore whether also in the pnictides tunneling spectra show a mix of pseudogap and superconducting gap features.

In this chapter, temperature and doping dependent scanning tunneling spectro scopy measurements on under-, optimally and overdoped $BaCo_xFe_{2-x}As_2$ crystals (x=0.08, 0.14 and 0.21) will be reported to determine whether tunneling experiments indeed observe the superconducting gap, which closes at T_c, or a pseudogap, which does not.

It has been shown in chapter 4 that the 122 pnictides cleave through the Ba layer,

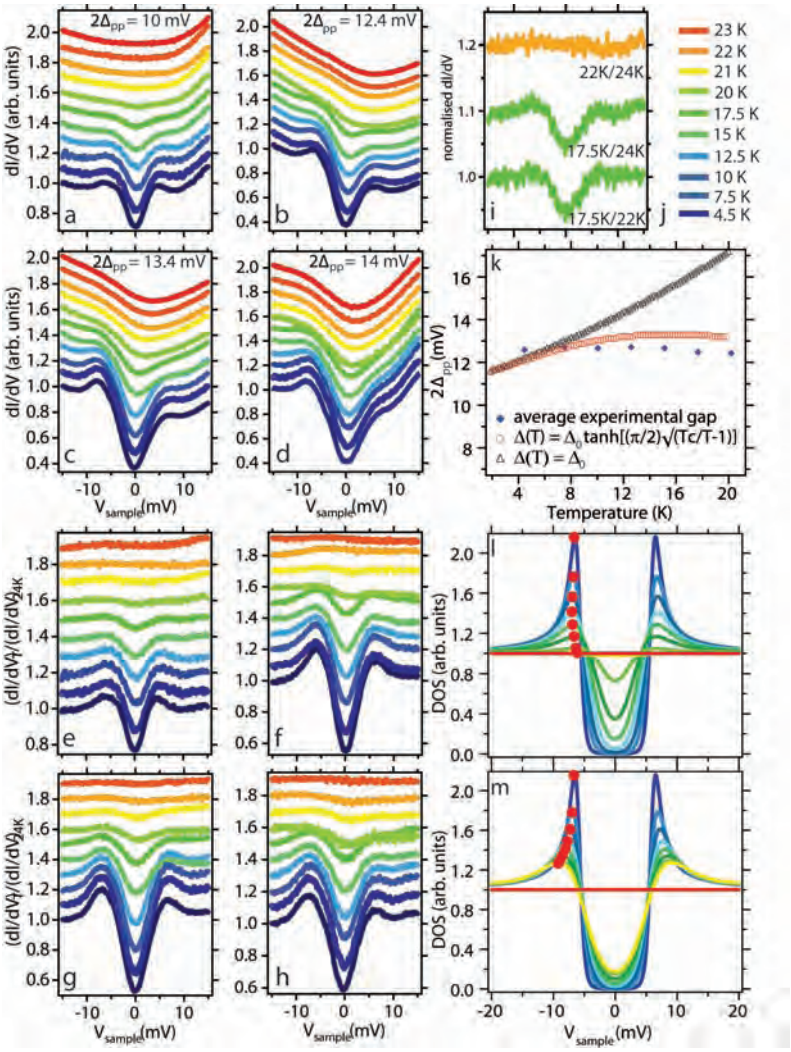

Figure 6.1: Optimally doped $BaCo_xFe_{2-x}As_2$ (x=0.14, T_c = 22 $\pm$ 0.5 K): (a-d) Differential conductance spectra for four different superconducting gap sizes as a function of temperature. The spectra are offset in discrete steps with respect to each other for clarity, V = 45 mV, I = 40 pA. (e-h) The same spectra as shown in (a-d), but normalised to the spectrum for each location taken at 24 K. (i) Comparison between different normalisation temperatures, excluding an influence of the normalisation on the results. (j) Color legend. (k) Δ_{pp} as a function of temperature (solid symbols). As a comparison, Δ_{pp} of a temperature broadened T-independent gap and T-dependent BCS-like gap (Eqn. (3.2)) with Δ_0 = 6 mV and T_c = 21 K are plotted (open symbols). The corresponding curves are shown in panel (l) and (m), respectively, where the peak maxima at negative bias are indicated by red dots.

exposing half a Ba layer on either side of the cleave. Although a comparison of regular and hard x-ray photoemission data suggests that the cleavage surface does not have a strong influence on the global near-surface electronic environment [83], LDA calculations report electronic properties differing from the bulk on $(\sqrt{2} \times \sqrt{2})$ reconstructed Ba surfaces [152]. However, as identical superconducting gaps are observed throughout this Ph.D. research on both $(\sqrt{2} \times \sqrt{2})$ as well as (2×1) or other surface terminations, data will be presented from spectroscopic surveys recorded on the modal termination topography. It should be noted that areas with a relatively large z-corrugation (>2 Å) show anomalous spectroscopic signatures, likely caused by a local Ba surplus or deficiency, which were therefore not used for spectroscopic surveys.

6.2 Optimally doped $BaCo_xFe_{2-x}As_2$

First, the optimally doped $BaCo_xFe_{2-x}As_2$ (x = 0.14) samples were studied ($T_c = 22 \pm 0.5$ K). Figure 6.1a-d shows the evolution of the gap for four different locations on the surface for temperature ranging from 4.5 K to 24 K. As can be seen in the figure, the clear coherence peaks at 4.5 K are smoothly depressed and are completely gone at temperatures above T_c. Due to the U-shaped background, it is difficult to follow the temperature dependence in great detail. To overcome this problem, an often used procedure is to divide the differential conductance at a temperature, T, by that taken in the normal state, i.e. $(dI/dV)_T/(dI/dV)_{T_{normal}}$. The result of this analysis is plotted in Fig. 6.1e-h. Here, unlike in the cuprates, $2\Delta_{pp}$ extracted from the normalised spectra are identical to those extracted from the raw data for all four shown sizes of superconducting gap.

To ensure that the normalisation temperature used in the procedure described above does not influence the normalised spectra, normalisation of a spectrum taken at 17.5 K both to the spectra taken at 22 K, i.e. very close to T_c, and that taken at 24 K are compared in Fig. 6.1j. Both normalised spectra are clearly very similar, whereas the spectrum taken at 22 K normalised to the one taken at 24K is basically a straight line. From this we can conclude that spectra taken above T_c do not show an observable variation and the choice of normalisation temperature is not critical, as long as it is $> T_c$. It is thus safe to say that the gaps observed are indeed the superconducting gaps.

The exact temperature at which the gap closes or fills is difficult to estimate, but for all gap sizes it is within 1 K of the bulk T_c. The fact that the peak-to-peak separation is seemingly temperature independent (see Fig. 6.1k) can be well understood by taking into account temperature broadening effects. Fig. 6.1k illustrates this by plotting the peak-to-peak separation of a temperature broadened BCS gap, i.e. a gap described by Eqn. (3.2), and a temperature broadened fixed gap, i.e. $\Delta(T) = \Delta_0$ ($T<T_c$) and $\Delta(T) = 0$ ($T>T_c$). The curves from which these simulated peak-to-peak separations are extracted are plotted in Figs. 6.1l and m respectively, where the peak maxima at negative bias are indicated by a dot. As is clear form Fig. 6.1k, the curve

for the temperature broadened BCS gap predicts the data quite well, while for the fixed gap an effective increase of Δ_{pp} is obtained.

6.3 Underdoped $BaCo_xFe_{2-x}As_2$

We now turn our attention to lower doping concentrations, where, in analogy with the cuprates, one is more likely to expect a pseudogap behaviour and where magnetic correlations that could produce a gap are stronger. Figure 6.2a shows the average of ~4000 spectra taken both at 5 K and 20 K on the same 100x100 Å^2 field of view on a $BaCo_xFe_{2-x}As_2$ sample with x=0.08 (T_c = 14 $\pm$ 1 K, T_{SDW} = 70 $\pm$ 3 K). The low temperature average, normalised to the high temperature spectrum is shown in Fig. 6.2b.

One peculiarity valid for all measurements performed on underdoped samples is

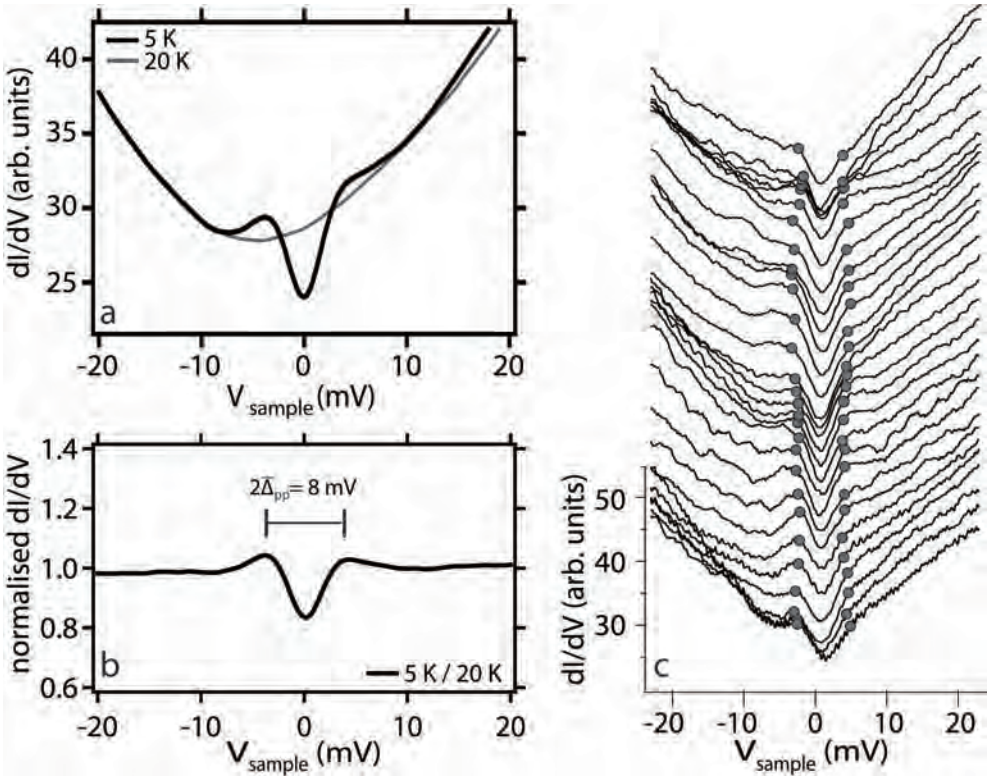

Figure 6.2: Underdoped $BaCo_xFe_{2-x}As_2$ (x=0.08, T_c = 14 $\pm$ 1 K): (a) Average of ~4000 spectra taken both at 5 K and 20 K on a square grid on the same 100x100 Å^2 field of view. (b) Spectrum obtained by normalising the 5 K spectrum shown in (a) to the 20 K spectrum. (c) Several single pixel spectra taken along a random line from the conduction map of which the average is shown in (a) illustrating the variation in the spectra, the gap edges are indicated by circles.

that the superconducting gap signatures are less pronounced than in the optimally doped materials. At this point we note that temperature broadening at 5 K of a pure single band BCS spectrum will already effectively fill the flat bottomed gap [153]. Furthermore, as other experiments have already alluded to, it might very well be possible that there is a nonzero density of states at the Fermi level in the superconducting states due to non gapped bands [62, 154]. Nevertheless, the single pixel spectra, of which several are shown in Fig. 6.2c, clearly show there are gaps all over the field of view, after normalisation have the same peak-to-peak separation as is apparent in the raw data and all close at T_c. These observations strongly suggest that the gaps observed at low temperature are indeed the superconducting gaps and not pseudogaps.

Since at 20 K the system is still well within the orthorhombic, magnetically ordered state, one might expect gap-like features in the spectra due to a depression of spectral weight as a result of gapping of parts of the Fermi surface [155–157]. Assuming a mean field gap, such features would be typically at ~10 mV. However, since these are not observed, they either occur at higher energies, are not picked up due to tunneling matrix element effects, or are simply not present due to phase separation between magnetic and superconducting regions. Additional measurements, for instance to higher energies, should be performed to address this point. The presence of superconducting gaps over the entire field of view sets a lower limit length scale of tens of nanometers to a possible phase separation between superconducting and non-superconducting magnetically ordered regions.

6.4 Overdoped $BaCo_xFe_{2-x}As_2$

To complete the survey of the phase diagram of $BaCo_xFe_{2-x}As_2$, attention is turned to the overdoped compound (x=0.21, $T_c = 13 \pm 1$ K). Fig. 6.3a-c show the detailed temperature dependence of four locations with a different $2\Delta_{pp}$. Analogous to the analysis used for the optimally doped sample, Fig. 6.3d-f show the spectra normalised to the spectrum taken at the exact same location for $T > T_c$. As was the case for the under- and optimally doped samples, the gaps seen at low temperature in the normalised spectra are identical in magnitude as the raw data gaps and all vanish above T_c.

6.5 Summary

To summarise, for underdoped, optimally doped, and overdoped $BaCo_xFe_{2-x}As_2$ (x=0.08, 0.14 and 0.21), $2\Delta_{pp}$ observed in tunneling spectroscopy measurements has been tracked as a function of temperature. The gaps for all doping concentrations studied and all gap sizes are observed to vanish at the bulk T_c, excluding a pseudogap scenario in these pnictide superconductors. Since gaps have been seen across the entire field of view of hundreds of square ångstrom, nanoscale phase separation of magnetic and superconducting patches is unlikely, also in the underdoped

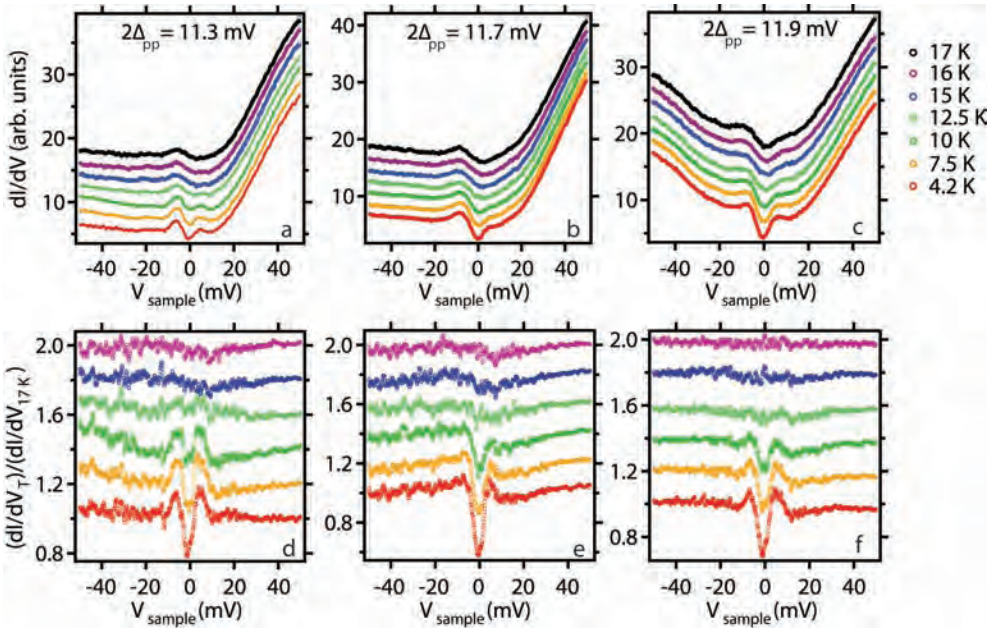

Figure 6.3: Overdoped $BaCo_xFe_{2-x}As_2$ (x=0.21, T_c = 13 $\pm$ 1 K): (a-c) STS spectra taken at four different positions. All spectra taken above T_c fall perfectly on top of each other, contrary to those taken below T_c. (d-f) The spectra shown in (a-c) normalised to the respective spectra taken at 17 K, i.e. $> T_c$.

material. The indications of the presence of a pseudogap in several compounds closely related to the one studied here makes the family of pnictide superconductors a theoretical challenge to understand, as the action of specific dopant atoms can lead to completely differing behaviour. An interesting observation is the possible relation between the dopant atom carrier type and the presence or absence of a pseudogap. Signatures of a pseudogap in the electron doped cuprates have been reported (see [158] and references therein), but these are far less pronounced than in the hole doped cuprates, where it dominates a large portion of the phase diagram. Similarly, whereas we show here that there is no pseudogap in the electron doped pnictide $BaCo_xFe_{2-x}As_2$, there are indications of a pseudogap in hole doped $Ba_{1-x}K_xFe_2As_2$ [148–150]. Mapping out the presence or absence of a pseudogap in more related compounds, both electron and hole doped, will determine if this is a generic behaviour and should give a better understanding of the role of the pseudogap for high temperature superconductivity.

CHAPTER

7 Inhomogeneity induced gap disorder in $BaCo_xFe_{2-x}As_2$ and $BaFe_2P_xAs_{2-x}$

An anomalous behaviour of the reduced gap, $2\overline{\Delta}_{pp}/k_BT_c$, as a function of doping in the pnictide high temperature superconductor $BaCo_xFe_{2-x}As_2$ is presented. The reduced gap, as well as the variation in gap size normalised to the average gap, $\sigma/\overline{\Delta}_{pp}$, is seen to increase as a function of doping. From this trend, combined with the observation that both parameters are relatively small for optimally doped $BaFe_2P_xAs_{2-x}$, Co scattering effects are suggested to play an important role in these materials, which in turn puts constraints on the interpretation of reduced gap values.

7.1 Introduction

From the previous chapter it is clear that the strong spatial variation in peak-to-peak separation can be attributed to the superconducting gap, and not to a pseudogap as has been seen in the cuprates. One now may wonder how such a large variation in gap size on length scales similar to the coherence length is possible. Secondly, since the gap varies as a function of position while the superconducting transition temperature is the same for every gap size, the reduced gap, $2\Delta/k_BT_c$, is also spatially varying. As this value is commonly used to determine whether a material is a conventional phonon mediated or an unconventional superconductor (see Chapter 3), the question arises what a spatial variation of this reduced gap means.

In the cuprates the reduced gap is seen to be constant as a function of doping, i.e. 2Δ tracks T_c [49, 159]. To investigate the doping dependence of the superconducting gap in the pnictide superconductors, doping dependent STM/S measurements on $BaCo_xFe_{2-x}As_2$ (BCFA) samples (x=0.08, x=0.14 and x=0.21), and on optimally doped $BaFe_2P_xAs_{2-x}$ (BFPA) single crystals (x=0.64) and slightly overdoped $BaRu_xFe_{2-x}As_2$ (BRFA) samples (x=0.7) as control experiments have been performed. One of the striking characteristics of the MFe_2As_2, or 122, pnictides is the fact that superconductivity can be reached by doping with a large variety of dopants, both charged and isovalent, and in all three layers of the material. As in the cuprates [160] there seems to be a trend in that the further the dopant atom is situated from the superconducting Fe plane, the higher T_c. Since the systems studied here introduce Co dopants in the superconducting Fe layer, scattering effects could start to play an important role. Scattering effects in the two-band superconductor MgB_2 have been seen to bring the system in the dirty limit, where the two distinct gaps merge into a single gap, and T_c is reduced [161]. At the same time, impurity scattering will increase the number of in-gap states and push out the coherence peak by smearing of the BCS singularity, which can effectively be seen as an increase in the lifetime-broadening parameter, Γ, in the Dynes function [41].

In this chapter the doping and spatial dependence of the superconducting gap will be discussed, indicating that impurity scattering effects in the Co-doped systems studied play an important role. These results put a constraint on the applicability of the reduced gap as an independent measure of the pairing strength in these systems.

As mentioned in the previous chapters, the particulars of the surface which have been shown to be due to the partial lift-off of the topmost Ba layer, do not seem to affect the superconducting gap spectra. Therefore, data will be presented from spectroscopic surveys recorded on the modal termination topography. It should be noted though that areas with a large corrugation (>2 Å) show anomalous spectroscopic signatures which might be caused by impurities on the surface or by a significant deviation from the average surface cationic population. Such regions were not used for spectroscopic surveys. Spatial correlations between topographical information and variation in $2\Delta_{pp}$ were checked to be absent for each measurement.

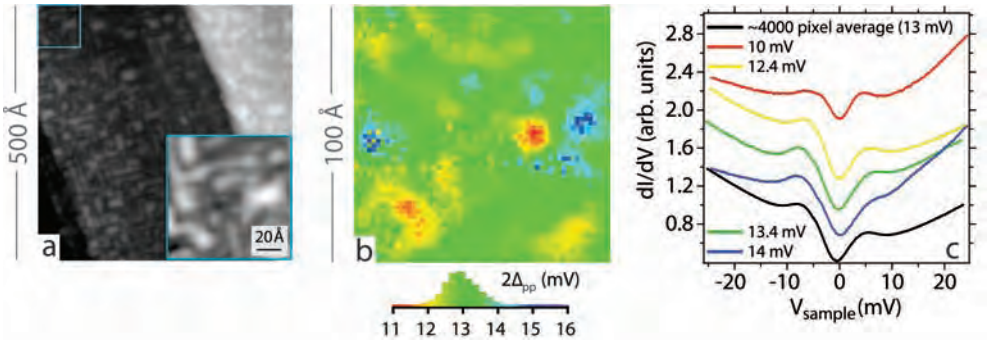

Figure 7.1: Constant current image taken on near-optimally doped $BaCo_xFe_{2-x}As_2$ (x=0.14, T_c = 22 ± 0.5 K) at 4.2 K, V = 50 mV, I = 40 pA (these settings were used throughout this study unless stated otherwise). The inset is a zoom of the region of the image which is marked by a box. (b) Gap map corresponding to the field of view shown in the inset of (a). (c) Averaged spectrum of the conduction map taken on the inset of (a), together with four representative single pixels spectra which illustrate the variation in $2\Delta_{pp}$.

7.2 Doping dependence of under-, optimally and overdoped $BaCo_xFe_{2-x}As_2$

First, near-optimally doped BCFA samples (x=0.14, T_c = 22 ± 0.5 K) were studied. Figure 7.1a shows a constant current image representative for a large portion of a particular cleavage surface, in which atomic contrast is absent, and a 2D, maze-like network is seen with typical periods of ~12 Å, oriented along the tetragonal axes, as determined by *in situ* low energy electron diffraction (LEED). Figure 7.1b shows the gap map taken on the inset of Fig. 7.1a, which is in accordance with previously reported results from Ref. [112] and those shown in chapter 5, although the variation in gap magnitude is slightly reduced and has a slightly longer characteristic length scale, which might reflect the improvement in sample quality, or a locally more homogeneous area on the sample. To show the variation in the tunneling spectra, four single pixel spectra are shown in Fig. 7.1c, which range in gap from 10 to 14 mV corresponding to a value of $2\Delta/k_BT_c$ of 5.3 to 7.4, together with the average of the ~4000 spectra of which the map consists. The temperature dependence of these four spectra has already been shown in the previous Chapter in Fig. 6.1.

Next, lower doping concentrations are considered, where conduction maps were recorded in a similar fashion to those obtained on the optimally doped sample. From the average of such a map on a BCFA sample with x=0.08 (T_c = 14 ± 1 K) the average magnitude of the superconducting gap ($2\overline{\Delta}_{pp}$) is determined to be 8 mV ± 1 mV, corresponding to a value of $2\overline{\Delta}_{pp}/k_BT_c$ of 6.5 ± 0.5. One peculiarity valid for all STS measurements performed throughout this work on underdoped samples is that the superconducting gap signatures are less pronounced than in the optimally doped materials. As the gap in these samples is smaller in magnitude as well, a reliable gap

map could not be obtained. However, the single pixel spectra, of which several are shown in the previous chapter in Fig. 6.2c, clearly show there are gaps all over the field of view.

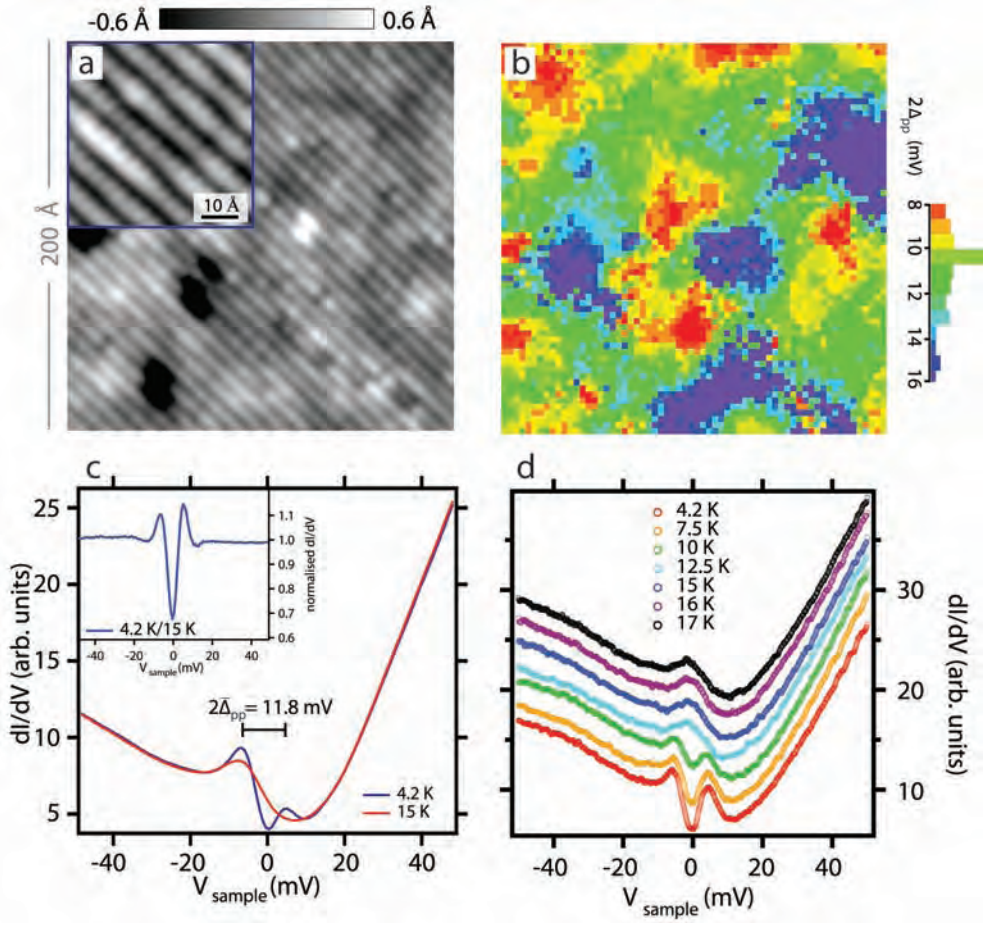

Figure 7.2: Overdoped $BaCo_xFe_{2-x}As_2$ (x=0.21, $T_c = 13 \pm 1$ K): (a) 200x200 Å^2 topograph displaying a (2×1) structure on which conduction maps are taken at 4.2 K and 17 K. The inset shows the individual atoms on the (2×1) structure (V = 5 mV, I = 5 nA). (b) Gap map constructed after division of the low temperature by the high temperature conductance map, the histogram indicates the variation in gap size. The average spectrum of both maps are shown in (c). The inset in (c) shows the division of the average spectrum below T_c by that above T_c. (d) Detailed temperature dependence of a spectrum with $2\Delta_{pp}$ = 11.3 mV. All spectra taken above T_c fall perfectly on top of each other, contrary to those taken below T_c.

To complete the survey of the phase diagram of BCFA, an overdoped compound (x=0.21, $T_c = 13 \pm 1$ K) is investigated. Fig. 7.2a shows a typical (2×1) surface structure on which a conduction map has been taken. The gap map extracted from this conduction map is shown in Fig. 7.2b. Interestingly, the gap magnitude ($2\bar{\Delta}_{pp}$ =

11.8 meV) is comparable to the gap seen at optimal doping, meaning that since T_c is smaller, the reduced gap is considerably larger, i.e. $2\overline{\Delta}_{pp}/k_BT_c = 10.5 \pm 3$. To ensure that this relatively large gap is really the apparent superconducting gap, the average spectrum of a conduction map taken above T_c is plotted on top of the average spectrum on the same area at 4.2 K, see Fig. 7.2c. This comparison, and the more detailed temperature dependence of a representative single pixel spectrum shown in Fig. 7.2d confirm that the gaps are indeed gone above T_c. More details on the temperature dependence of the tunneling spectra, also of compounds with a different doping concentration, are given in the previous chapter.

7.3 Control experiments

7.3.1 $BaFe_2P_xAs_{2-x}$

As a control experiment, measurements are performed on optimally doped $BaFe_2P_xAs_{2-x}$ (BFPA) (x = 0.64, $T_c = 31 \pm 1$ K). A typical (2×1) topography is shown in Fig. 7.3a. Fig. 7.3b shows the average spectrum of ~4000 spectra taken on the inset of Fig. 7.3a, with every 100th spectrum plotted on top of the average. The figure clearly shows the homogeneity of the spectra and of the gap magnitude, $2\overline{\Delta}_{pp}$ = 12 mV, on this material, in stark contrast to what is seen on the Co doped materials. It should be noted that analogous to BCFA samples, a large variety of cleavage surfaces was observed on BFPA. The gaps from different topographies are equally homogeneous as the one shown here. To illustrate the homogeneity of the superconducting gap size, Fig. 7.3c shows a gap map using the same energy range as the gap map plotted in Fig. 7.2b. Despite having similar average gap values, the BFPA map clearly lacks the variation observed on the BCFA samples. This observation strongly suggests that

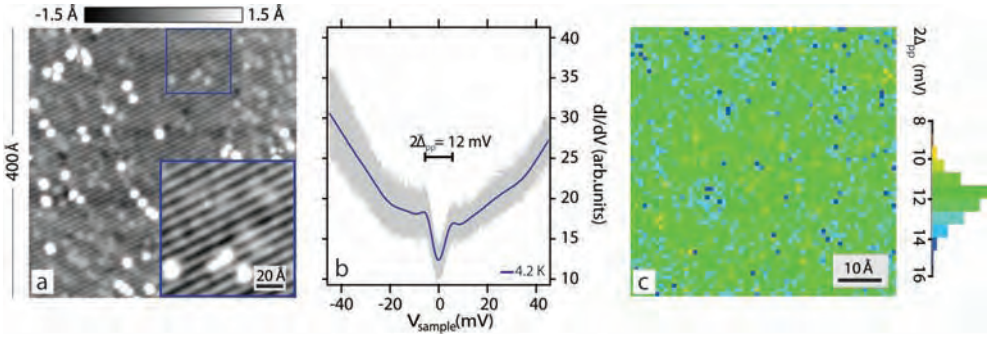

Figure 7.3: (a) Typical (2×1) surface structure on optimally doped $BaFe_2P_xAs_{2-x}$ (x=0.64, T_c = 31 ± 1 K). (b) Average tunneling spectrum (blue) of ~4000 spectra taken on the 100×100 Å^2 inset in (a) with every 100th spectrum (grey) plotted on top of the average. (c) Gap map corresponding to the spectra shown using the same color scale as Fig. 7.2b, illustrating the homogeneity of the BFPA spectra with respect to the BCFA spectra.

indeed the Co dopants are responsible for the observed variation in gap size in the Co doped materials. Furthermore, the gap of the P-doped material itself is comparable in size to that of the overdoped BCFA samples, but since T_c is significantly higher the reduced gap is relatively small, $2\overline{\Delta}_{pp}/k_BT_c = 4.6 \pm 0.3$.

7.3.2 $BaRu_xFe_{2-x}As_2$

Interestingly, Ba122 can also become superconducting when some of the Fe atoms are replaced by Ru instead of Co. As Ru has the same valency as Fe, the effect of the extra electron in case of Co doping can be appreciated. Unfortunately Ru doped samples are rather difficult to grow and are, if possible, even smaller than the P doped Ba122 samples (see Fig. S1c for an image of three typical samples and their sizes). Moreover, the transition width of the $Ru_xFe_{2-x}As_2$ samples (x = 0.7, T_c = 17 $\pm$ 3 K) that were kindly provided by V. Brouet et al. [77, 162] proved to be rather broad (see Fig. 7.4a). Therefore, only preliminary results will be presented here. However, in the near future samples with a sharper transition will be available for further studies.

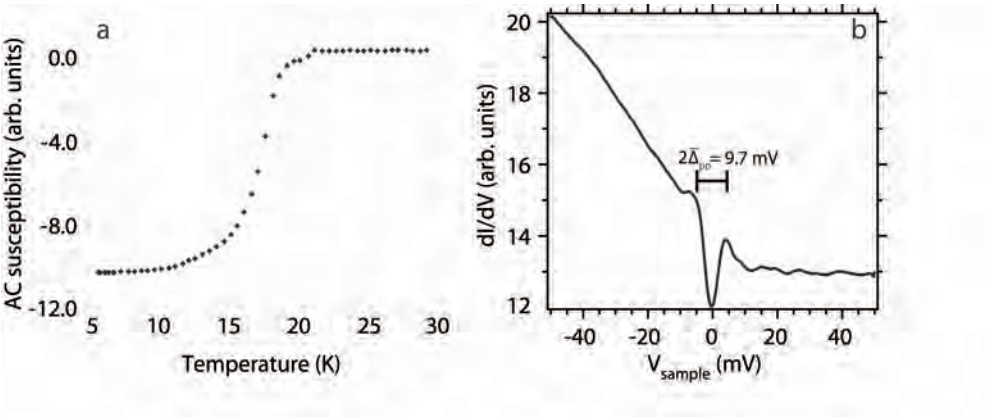

Figure 7.4: (a) AC susceptibility trace of the rather broad transition into the superconducting state. (b) Average of thousands of spectra taken on a 100×100 Å^2 field of view on a (2×1) reconstructed surface of $BaRu_xFe_{2-x}As_2$ (x=0.75, T_c = 17 $\pm$ 3 K).

Spectroscopic surveys on different parts of the same sample with similar (2×1) surface structures showed average gaps from fields of view of hundreds of square Å varying from 7.5 to 9.7 mV. The average spectrum corresponding to the 9.7 mV gap is shown in Fig. 7.4b. The variation in average gap magnitude on the same sample is likely a result of the inhomogeneity of the samples that is also reflected by the broad transition into the superconducting state. Taking the uncertainty in the transition temperature into account it follows that the reduced gap is in the range 5-7, similar to the Co doped system. It should be noted that for similar transition

temperatures the Ru dopant concentration is considerably larger than the Co dopant concentration, suggesting that Co atoms act as stronger scattering centers than Ru.

7.4 Summary of the data

Fig. 7.5a summarises the doping dependence of the compositions studied here by plotting the values of $2\overline{\Delta}_{pp}$ versus doping on top of the critical temperatures determined from resistivity measurements. As can be seen, the superconducting gap deviates from the behaviour of the superconducting dome for the overdoped Co compounds, clearly differing from the cuprate scenario where the dome is tracked by $2\overline{\Delta}_{pp}$. As a comparison, $2\overline{\Delta}_{pp}$ and T_c of optimally doped BFPA are plotted in the shaded region, from which it is clear that in this compound the reduced gap is considerably smaller than for the Co doped compositions.

7.5 Discussion

Since Fig. 7.1 and 7.2 show a variation in $2\Delta_{pp}$ that is indeed a variation in apparent superconducting gap size (as shown in the previous chapter), the question arises as to what could cause such a variation. The normal state NMR signal of these materials has been characterised by inhomogeneities [136], and strong scattering from Co inhomogeneities could be a possible explanation of the T^2 behaviour in London penetration depth measurements [163]. It has already been suggested in chapter 5 that Co doping within the superconducting Fe layers could be the cause, as the spatial variation is on the same length scales as the Co dopant separation. This indeed holds for all measured compositions, i.e. the variations in $2\Delta_{pp}$ for all doping concentrations are on the nanometer scale, although the exact length scale of the variations does not seem to scale in a straightforward manner to the doping concentration and could be slightly different on different samples of the same doping concentration.

It has been shown using a four-probe scanning tunneling microscope, that there are local variations in the Co doping concentration on any given sample, leading to locally different T_c's [164]. However, these variations are not sufficient to explain the variation in $2\Delta_{pp}$ seen here, as some gaps are bigger than the average gap for optimally doping, requiring a T_c in excess of T_c^{max}, and the smaller gaps would need a local T_c of half the bulk T_c, which is clearly not the case as determined from temperature dependent STS measurements. Since $2\Delta_{pp}$ on optimally doped BFPA is very homogeneous over large fields of view, intrinsic sample inhomogeneities other than the dopants themselves, such as for instance defects, are ruled out as a cause of the gap magnitude variations. The fact that considerably more dopant atoms are present in the BFPA samples than in the overdoped BCFA samples (x = 0.64 versus x = 0.21 respectively) underlines this statement.

To shed more light on the cause of the gap variations, the spread in gap value normalised to the average gap magnitude, $\sigma/\overline{\Delta}_{pp}$, versus the reduced gap, $2\overline{\Delta}_{pp}/k_BT_c$, is shown in Fig. 7.5b. As can be seen, there seems to be an approximate relation

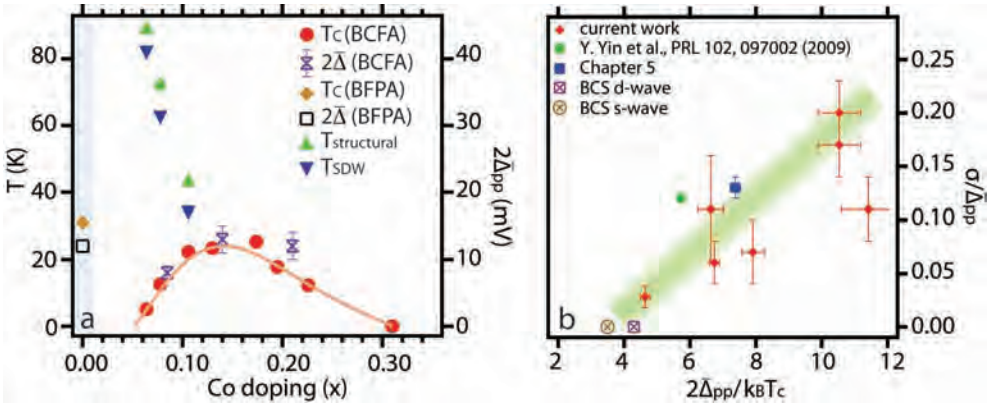

Figure 7.5: (a) Values of $2\overline{\Delta}_{pp}$ (right axis) for various Co-doping concentrations and for the P-doped system (since P substitution is not formally doping electrons, the values of BFPA are indicated at x=0), plotted on top of the phase diagram of the samples determined from resistivity measurements (left axis). (b) Plot of $\sigma/\overline{\Delta}_{pp}$ versus $2\overline{\Delta}_{pp}/k_BT_c$ for the compositions used in this study and taken from literature.

between these two parameters, highlighted by the shaded region in the figure. As a comparison, the values for pure single band s-wave and d-wave BCS superconductivity are shown as well, which are actually close to the point of intersection with the x-axis of the observed trend. Thus, as Fig. 7.5a shows, upon increasing the Co doping concentration, $2\Delta_{pp}$ slightly increases, and is more or less constant at optimal- and overdoping (x=0.14 and x=0.21). However, the decrease in T_c then leads to an increase in reduced gap (Fig. 7.5b). Secondly, as the Co doping concentration increases, the normalised spread increases. These factors combined suggest that Co dopants within the superconducting plane act as scattering centers, which reduce T_c faster than the gap, 2Δ. Locally, such a scattering center could reduce the gap size due to a reduction of the pairing interaction. At the same time, the presence or absence of Co atoms could perhaps locally enhance the pairing interaction, leading to the larger gaps seen with STS. Note that even though lifetime broadening due to impurities effectively pushes out the coherence peaks, variation in peak-to-peak separation cannot be explained by such broadening alone. For instance, small gaps have been seen to have a relatively high zero bias conductance and large gaps can have relatively large coherence peaks (see Fig. 7.1c), opposite to what is expected in case of lifetime broadening only.

Seeing as the surface layer of the 122 pnictides is distorted with respect to the bulk as was shown in chapter 4, one should not overlook the possibility that the surface might in fact not be superconducting, but that superconducting signatures are picked up in STS at the surface due to the proximity effect. Depending on the distance from the tip to the superconducting condensate below the surface layer, gaps will have different magnitudes. It has been reported in Ref. [153] that one of the

signatures of the proximity effect in tunneling spectra is the appearance of a dip just outside the coherence peaks, a feature that is readily observed in Fig. 7.2c. Such features, however, are not conclusive as they could be a result of the division of the low temperature spectrum by the high temperature (i.e. temperature broadened spectrum) and can also for instance mark the energy of a bosonic mode. More importantly, the absence of any correlation between the gap magnitude and topography, and the lack of variation in gap magnitude in the possibly even more distorted P doped Ba122 seem to argue strongly against such a proximity effect scenario.

Nanometer scale spatial variations in the superconducting gap magnitude have previously been reported in literature in dirty limit superconductors close to the superconductor-to-insulator (SI) transition [165]. Upon increasing the disorder in these materials, the variations in the superconducting gap were seen to increase and due to a disorder induced decrease in T_c, the ratio $\overline{\Delta}_{pp}/T_c$ was seen to increase upon increasing disorder. Although the pnictide superconductors studied here are not close to an SI transition, the observations are very similar to this scenario, which strongly suggests that scattering from Co dopants within the superconducting Fe plane are important in these systems and strongly affect the tunneling signatures and reduced gap values. This picture is corroborated by theoretical calculations [166], which argue that the extra d-electrons coming from the Co dopant atoms are actually not charge doping the system, but are localised on the Co atoms. The Co dopants are therefore suggested to act as scattering centers that scramble k-space such that the spin density wave order is suppressed, enabling superconductivity to emerge.

Another noteworthy point is that since an increase in the Co doping leads to an increase in reduced gap value, care should be taken with the interpretation of the reduced gap extracted from peak-to-peak separations in STM/S, but also those extracted from ARPES measurements. The data presented here show that a simple conclusion as regards the validity or otherwise of BCS theory based on the reduced gap value on Co-doped 122 systems cannot be made, prior to a careful examination of the scattering effects of the dopants in the Fe plane. Fig. 7.5b does indicate, however, that upon extrapolation to the point where no scattering is present (i.e. $\sigma/\overline{\Delta}_{pp} \downarrow 0$, the reduced gap value comes out within the BCS range.

7.6 Summary

Spatially resolved tunneling spectra have been taken on $BaCo_xFe_{2-x}As_2$ samples for doping concentrations spanning the superconducting dome. Unlike for the cuprates, the reduced gap, $2\Delta/k_BT_c$, is seen to increase for increasing doping concentrations, reaching values as high as 10 for overdoped compounds. At the same time, the variation in the gap normalised to the average gap, $\sigma/\overline{\Delta}_{pp}$ increases for increasing Co doping concentrations, reminiscent of inhomogeneity induced gap variations seen in superconductors close to a superconductor-to-insulator transition. The absence of variation in peak-to-peak separation in spectra taken on $BaFe_2P_xAs_{2-x}$ strongly suggest that the Co atoms in the Fe plane are responsible for the large spatial vari-

ation in the reduced gap and the large value thereof. The latter notion is supported by preliminary measurements on isovalently doped $BaRu_xFe_{2-x}As_2$, which suggest the inhomogeneity in the Fe plane is crucial in the interpretation of the data, but also that the details of the type of dopant are important as Co seems to act as a stronger scattering center than Ru. The suggestion put forwards in Ref. [166] that dopant atoms act as k-space scramblers instead of charge dopants seems to fit nicely within this picture. Aside from highlighting the effect of Co dopants in the Fe plane, the measurements on P doped Ba122 furthermore argue against a proximity effect induced spatial variation in the superconducting gap. Such a scenario was not unlikely in light of the deviation of the surface from the regular bulk structure as has been shown in chapter 4. Having thereby shown that the tunneling spectra are indeed a result of a spatially varying superconducting condensate, the inhomogeneity induced increase of the reduced gap puts restrictions on the applicability of $2\Delta/k_BT_c$ in the discussion of the pairing strength of the pnictides. A proper understanding of the STM/S data presented here requires a better theoretical understanding of the local pair-breaking or pair-enhancing effects of dopant atoms in a multiband superconductor.

Part II

Bilayered colossal magnetoresistant manganites

CHAPTER

8 Introduction to $La_{2-2x}Sr_{1+2x}Mn_2O_7$

Next to the high temperature superconductors, the colossal magnetoresistant manganites are one of the flagships of condensed matter research. In this chapter the manganite family of materials, and in particular the bilayered manganite $La_{2-2x}Sr_{1+2x}Mn_2O_7$, is introduced and the most relevant literature on the subject is reviewed. This section will be closely following Ref. [6], see also Refs. [167, 168] and references therein for more details on the bilayered manganites.

8.1 Magnetoresistance

Magnetoresistance is a change of the resistivity of a material upon application of an external magnetic field, which was first observed in 1856 by W. Thomson, a.k.a. Lord Kelvin. Whereas this effect is small in most materials, typically less than 5%, some materials exhibit a rather large magnetoresistive effect. These materials can be divided into two groups, the giant magnetoresistive (GMR) and colossal magnetoresistive (CMR) materials. Although the physics underlying these two groups is completely different, from an application point of view they have identical properties. GMR materials already form the basis of modern day hard drives and signalled the birth of spintronics. In a nutshell, GMR materials consist of ferromagnetic layers separated by a thin non-magnetic layer. For certain thicknesses of the separation layer, it becomes energetically favourable for the ferromagnetic layers to have their spins anti-parallel. Since hopping perpendicular to the layers requires a spin-flip, the resistivity is about 10% higher than when the layers have their spins parallel, which can be achieved by application of an external magnetic field. Independent switching of the spin orientation of a single layer is generally used in hard drives, where the two spin orientations (up and down) encode a 0 and 1, respectively. For an overview on the history of the GMR effect, see the 2007 Nobel Lectures [169, 170].

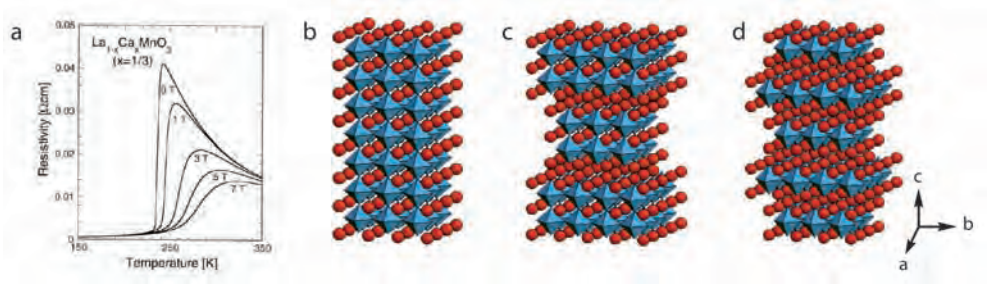

Figure 8.1: (a) The colossal magnetoresistant effect in $La_{1-x}Ca_xMnO_3$. The large drop in resistivity caused by a metal-to-insulator transition is shifted to higher temperatures with application of an external magnetic field. Image taken from [168]. The CMR effect is seen in several Mn compounds with a crystal structure of the Ruddlesden-Popper series, $(A,B)_{N+1}Mn_NO_{3N+1}$. Shown here are (b) N=∞, (c) N=2 and (d) N=1, where only the N=1 compound does not display the CMR effect. The MnO octahedra are shaded in blue and the red balls indicate the A and B ion positions. The crystallographic orientation is indicated at the bottom right of the figure.

The CMR effect on the other hand does not involve a sandwich of magnetic and non-magnetic materials, but is observed in mostly manganese based perovskite oxides [171]. The resistivity in such materials can change with several orders of magnitude upon application of an external magnetic field, see Fig. 8.1a, which is much larger than in any other material. However, the precise mechanism driving this colossal change in resistivity is still under debate. In the remainder of this section,

the bilayered manganite $La_{2-2x}Sr_{1+2x}Mn_2O_7$ (LSMO) will mainly be discussed, for two reasons. Firstly, the CMR effect in this material is largest of all manganite materials (see section 8.3), making it one of the most studied systems within the family of CMR manganites. Secondly, the presence of a natural, non-polar cleavage plane (see section 8.2) makes this material ideal for surface sensitive studies such as scanning tunneling microscopy and spectroscopy (STM/S) and angle resolved photoemission spectroscopy (ARPES).

8.2 Ruddlesden-Popper crystal structure

The general chemical formula for all manganite CMR materials is $(A,B)_{N+1}Mn_NO_{3N+1}$, where A and B are di- or trivalent alkaline earth or Lanthanide metal ions, and N stands for the number of stacked MnO planes. This commonly termed Ruddlesden-Popper series of structures forms the basis of many materials, ranging from insulators to high temperature superconductors (i.e. the cuprates), where the fine details of the different constituents of the material determine its properties.

The Mn ion is at the center of an octahedron spanned by six oxygen ions, where each oxygen ion is part of at least two octahedra, leading to a two dimensional (2D) plane of MnO_6 octahedra. The remaining interstitial sites are filled with A (and B) ions. In case the A ion is divalent, and assigning the formal charge of 2- to the oxygen ions, the charge on the Mn ion will be 4+ in order to have a charge neutral material. By partial substitution of the divalent A ions for trivalent (B) ions, the charge on the manganese ion will be between 4+ and 3+, and the system will be in a mixed-valence state. The exact properties of the material will then depend on the properties of the A and B ions and their ratio.

In the simplest case, where $N=\infty$, an infinite number of MnO_6 octahedra planes are stacked in the out-of-plane direction, giving a cubic, three dimensional (3D) compound. Due to the three dimensionality of the structure, there will not be a natural cleavage plane, leading to a 3D surface, i.e. one with many cracks and ridges. Moreover, to avoid a polar surface, there will not be a low energy (unreconstructed) surface, making this material less than ideal for STM/S or ARPES investigations.

By decreasing the stacking number, N, the dimensionality of the structure is lowered. In the extreme case, where N=1, single planes of MnO_6 octahedra are separated by more weakly bound AO layers, giving a nearly 2D structure. The material studied in this thesis is the intermediate, N=2, bilayered manganite. Since the manganese octahedra are more strongly bound than the interstitial AO layers, the $N \neq \infty$ crystals are more easily cleaved and will give a flat, two dimensional cleavage surface, which is ideal for surface sensitive techniques. Figure 8.1b-d show the crystal structure of the cubic, bilayered and single layered Ruddlesden-Popper compounds, respectively.

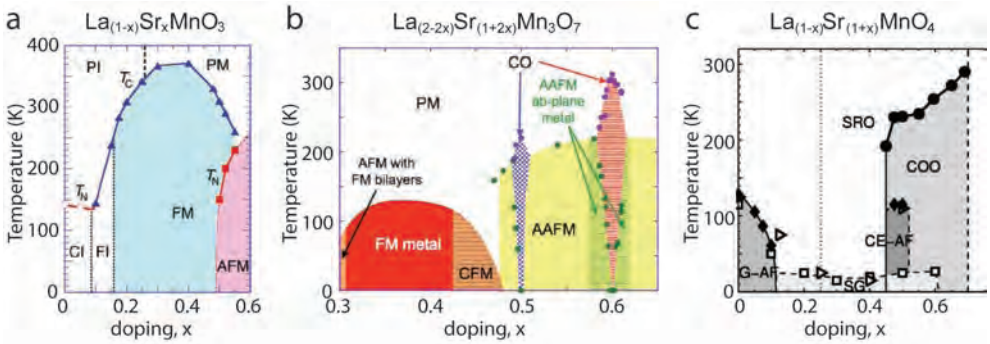

Figure 8.2: Phase diagrams $(La,Sr)_{N+1}Mn_NO_{3N+1}$, for (a) N=$\infty$ [168], (b) N=2 [173] and (c) N=1 [174].

8.3 Transport and magnetic properties

To illustrate the effect of a change in the dimensionality of the crystal structure on the electronic and magnetic properties of the material, the phase diagrams of the cubic, bilayered and single layered manganites in the series $(La,Sr)_{N+1}Mn_NO_{3N+1}$ are shown in Fig. 8.2a-c. As can be seen from the figure, there is a large variation in the properties of all three systems as a function of doping. The high temperature phase is paramagnetic insulating (PI) for almost all doping concentrations. Upon cooling, the materials can have a transition to a ferromagnetic metallic (FM), antiferromagnetic metallic (AFM), and several insulating phases, which are often charge and/or orbitally ordered (CO/OO). The CMR effect occurs at the transition from the high temperature insulating phase to the low temperature metallic phase. At some particular doping concentrations, and for many systems where A ions other than La and Sr are used, canted ferromagnetic metallic phases (CFM) appear. This means that the MnO_6 octahedra, which carry the spin that cause the magnetic order, are canted slightly out of plane such that the Mn-O-Mn bonds angles deviate from 180 degrees. The canting of the octahedra can be directly related to the radii of the A ions, r_A, with respect to the radii of the Mn (r_{Mn}) and O (r_O) ions, and is commonly expressed in terms of the tolerance factor [172], $f = (r_{Mn} + r_O)/\sqrt{2}(\langle r_A \rangle + r_O)$. The more this factor deviates from unity, the more the octahedra are distorted.

To be able to explain the wealth of phases, even over small doping regions where the tolerance factor is barely altered, electron-lattice coupling has to be taken into account [175]. The electrons on the manganese sites have orbital, spin and charge degrees of freedom. Starting from the simplest scenario, where the MnO_6 octahedron is undistorted and has a $3d^4$ electronic configuration, the five degenerate d-levels split into an e_g and t_{2g} orbital set due to the ligand field, see Fig. 8.3a. The system can lower its energy even more by a distortion of the octahedron, a so called Jahn-Teller distortion, which will lift the degeneracy of the e_g and t_{2g} orbital sets, see Fig. 8.3b and c. To compensate for the strain in the lattice due to Jahn-Teller distortions,

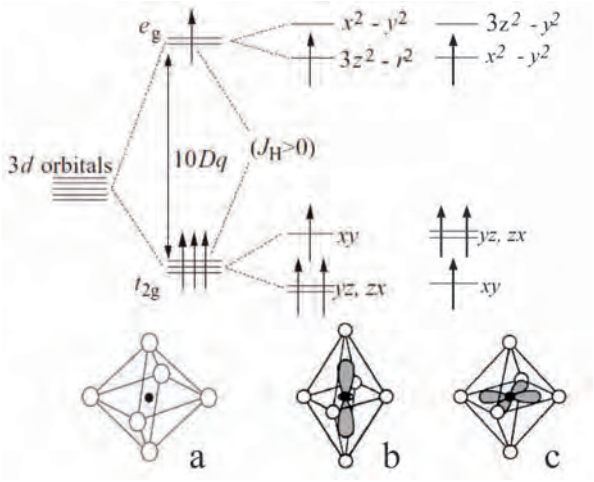

Figure 8.3: Energy level scheme of the Mn 3d-states for various scenarios. (a) The five-fold degenerate d-levels will split due to the ligand field in an e_g and t_{2g} level. Jahn-Teller distortion of the octahedron will split the levels further, where depending on the distortion either (b) a z^2-r^2 orbital or (c) an x^2-y^2 orbital will be the highest occupied level. Adapted from [167] and [168].

the crystal will have to distort cooperatively, where elongation and compression of the apical Mn-O bonds are intermingled, which for the non-doped, Mn^{4+}, parent compound will result in a regular lattice of alternating elongated ($d_{z^2-r^2}$) and compressed ($d_{x^2-y^2}$) octahedra. This orbital ordering will give an in plane ferromagnetic order, but will lead via the superexchange mechanism [176] to an anti-ferromagnetic out-of-plane ordering of the spins, also called A-type anti-ferromagnetism. Upon doping the system, electrons will be effectively removed from the system and at half doping, equal amounts of 3+ and 4+ Mn ions are present. In this case, the orbitals can order cooperatively again into alternating Jahn-Teller distorted and undistorted octahedra, which implies a charge ordering as well.

At intermediate doping concentrations, $0<x<0.5$, competition between the energy lowering by Jahn-Teller distortions and the energy gain due to induced strain will lead to short-ranged orbital order which eventually will break down. In the absence of (static) long-range orbital and anti-ferromagnetic order, and in the presence of empty orbitals on some of the Mn ions, Hund's rule coupling, which aligns all spins on a single Mn ion, will become an important parameter. In order to increase the hopping of electrons from neighbouring sites with different valence, and thereby reduce the energy of the system, spins on neighbouring Mn atoms will start to align parallel via the double exchange mechanism. In a fully ferromagnetic double exchange metal, all bond lengths will therefore be equal and all spins aligned, which is exactly opposite to the superexchange driven anti-ferromagnet.

If the spins in the double exchange metal are not perfectly aligned, but tilted by

an angle θ, hopping from site i to site j is given by $t_{ij} = \cos\theta$ [177, 178]. Therefore, if the temperature is increased and the spins will start to fluctuate due to an increase in thermal energy, the double exchange hopping is gradually reduced. If the temperature is raised high enough, the balance between double exchange and lattice distortions due to electron-phonon coupling is tipped towards the latter, leading to a paramagnetic insulating state at high temperatures. This relation also implies that materials with tolerance factors close to unity, in which the MnO_6 octahedra are barely canted, have the highest hopping and lowest resistivity at low temperature [179]. The system studied in this thesis, where La and Sr are the A and B ions, turns out to have the highest tolerance factor of all manganites [180], also giving it the largest CMR effect.

The super-exchange vs. double exchange picture seems to explain the exotic phase diagram of the CMR manganites qualitatively rather well. The temperature induced metal-to-insulator transition, where the system goes from a low temperature double exchange metal to a high temperature paramagnetic insulator, can be tuned with an external magnetic field, leading to the CMR effect. However, quantitative theoretical studies and numerous experimental observations seem to indicate that this is not the complete story. It has for instance been shown that double exchange in the cubic compound can only account for ~ 30% of the the colossal change in resistivity [181, 182].

8.4 Colossal magnetoresistance in $La_{2-2x}Sr_{1+2x}Mn_2O_7$

Returning to the phase diagrams shown in Fig. 8.2, the 3D, cubic compound has a broad doping range where the material is truly metallic, with a low temperature resistivity on the order of 0.1 $m\Omega cm^{-1}$ [183]. In optical conductivity measurements, a clear Drude peak can be seen [184], indicating that this material is a real metal with coherent spectral weight at the Fermi level. Moreover, as all bond lengths are equal [185,186], this compound is truly a double exchange metal at low temperature. The transition of the paramagnetic insulating to ferromagnetic metallic phase, i.e. at $\sim 0.15<x<0.5$, is where the CMR effect occurs [183].

The single layered compound on the other side of the scale, remains insulating for all doping concentrations down to the lowest temperatures, displaying no CMR effect [187]. The extra freedom given to the MnO_6 octahedra by the interstitial AO layers allows them to Jahn-Teller distort more easily without inducing energetically unfavourable strain, leading to a situation where a charge carrier can only hop if it drags along the lattice distortion present on its original site. Such a charge carrier, one that is heavily dressed with the lattice, is called a polaron.

The bilayered system is somewhere in between these two extremes, as it is not as two dimensional as the single layered compound, but also not three dimensional like the cubic compound. The material will adopt a Jahn-Teller distortion more easily than the cubic compound, but the strain energy penalty is increased with respect to the single layered material. A metallic-like region can be found in a narrow part

of the phase diagram, and it is this region where the CMR effect is largest of all manganites [188, 189]. However, the resistivity in this low temperature phase is on the order of 5 $m\Omega cm^{-1}$, which is actually in excess of the Mott maximum of 1 $m\Omega cm^{-1}$ [190, 191], making this material a poor metal at most. Optical conductivity measurements on the bilayered material show the material lacks a coherent Drude peak even down to the lowest temperatures [192–194], indicating an absence of coherent spectral weight at the Fermi level, much unlike its cubic cousin. Lastly, a low temperature neutron diffraction study shows that the Mn-O bond lengths are in fact more distorted in the low temperature metallic phase than in the insulating phase [195], opposite to what is expected for a double exchange metal.

Having shown that the low temperature phase of bilayered LSMO is not a simple double exchange metal, but rather a poor metal at most with little or no coherent spectral weight at the Fermi level, it is interesting to have a look at the properties of the high temperature insulating phase. From neutron and x-ray scattering studies it is clear that the static charge and orbital order seen at undoped and half-doped LSMO become short-ranged and dynamic at intermediate doping concentrations [196,197]. The main Bragg peaks in scattering experiments have diffuse scattering intensity around them above the Curie temperature (T_c), which is typically associated with polaronic lattice deformations [198]. The scattering measurements also reveal in-plane, incommensurate supermodulation peaks above T_c, characterised by a wave vector (± 0.3, 0, ± 1) in terms of reciprocal lattice units ($2\pi/a$, 0, $2\pi/c$), which is associated with polaron correlations. Rather than singular polarons, the CMR manganites are believed to 'possess a dense population of polarons that interact via overlapping strain fields and electronic wave functions, and might be described as

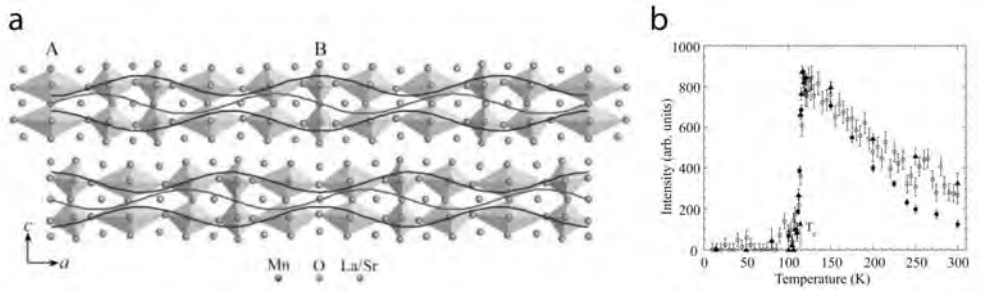

Figure 8.4: (a) Schematic of the distortion of the MnO_6 octahedra in bilayered LSMO at an intermediate doping concentration (x=0.4) in the high temperature paramagnetic insulating phase. The polarons form a strain field with a period of ~3 unit cells and have a correlation length of 6 unit cells, as determined from x-ray scattering measurements. Image from [196]. (b) The strength of both the diffuse scattering around the main Bragg peaks (open symbols) and of the supermodulation peaks (closed symbols) seen in scattering experiments, plotted as a function of temperature, taken from [197]. Reducing the temperature from room temperature, both signals increase, but abruptly drop at T_C.

polaronic liquids' [196]. From the incommensurate wave vector, these strain fields are estimated to have a correlation length in the MnO_2, or ab-plane of 26 Å, which corresponds to approximately 6 unit cells, see Fig. 8.4a.

Both the polaronic lattice deformations seen in the form of diffuse (or Huang) scattering, and the incommensurate supermodulation peaks, increase in intensity as the temperature is lowered towards the insulator-to-metal transition, but abruptly vanish at the transition, see Fig. 8.4b. This behaviour is commonly explained along the lines of the following reasoning. Initially, the polaronic liquid observed at high temperatures starts to freeze in upon lowering the temperature. However, before the system reaches a static polaronic crystal, double exchange kicks in and the Jahn-Teller lattice distortions vanish. It has already been mentioned that the low temperature phase is not a true double exchange metal, but a system where lattice correlations still play a role. Indeed, recent scattering experiments have found that well in the ferromagnetic phase, at 10 K, polarons remain as fluctuations that strongly broaden and soften certain lattice vibrations near the wave vectors where the charge-order peaks appeared in the insulating phase [199], shedding doubt on this commonly adopted description of the physics driving the colossal magnetoresistant effect in the bilayered manganites. In chapter 9, STM/S data will be presented which, taken together with ARPES data gathered on identical samples, show that the bilayered manganites are indeed better described by a polaronic 'bad metal' picture on the verge of breaking down into a truly double exchange metal in the low temperature phase across the 'metallic' region in the phase diagram.

CHAPTER

9 Bilayered $La_{2-2x}Sr_{1+2x}Mn_2O_7$: polarons on the verge of a metallic breakdown

STM/S studies have been performed on the bilayered manganite $La_{2-2x}Sr_{1+2x}Mn_2O_7$ for $0.3 \leq x \leq 0.425$. Over this entire doping range, two distinct types of topography are typically observed, one showing little contrast and a more or less disordered patchiness, while the other displays a square-like pattern with typical length scales of 2.3 nm. The latter structures are suggested to be remnants of polaron correlations that survive at the surface below the bulk T_c. Tunneling spectra taken on these two types of topography are very similar, vary only slightly as a function of doping concentration and show a (pseudo)gap for all doping concentrations studied. Interestingly, on one particular cleave, unprecedented atomic resolution over a large field of view was observed, which we argue to be a single layered intergrowth at the surface of an otherwise bilayered material. Temperature dependent measurements on the x=0.36 doped compound show a difference between the high- and low temperature data, and as they are both gapped at the Fermi level, these data highlight the importance of polarons for this doping concentration. The picture emerging from these data and ARPES data taken on identical crystals reported in Ref. [6] is that of a polaronic, bad metal at low temperature which does not support coherent electronic excitations at the Fermi level. This system is very close to tipping over into a good, coherent metallic state, something that does occur in N>2 intergrowths inside the N=2 single crystals. Upon increasing the temperature, the N=2 material undergoes a transition into a truly insulating state. The precarious balance of the bad metal state between the extremes of coherent metallic and strongly insulating behaviour provides the enormous sensitivity to external stimuli, such as the application of an external magnetic field, thereby giving rise to the CMR effect.

9.1 Introduction

The exact nature of the low temperature electronic phase of the manganite materials family, and hence the origin of their colossal magnetoresistive (CMR) transition is the subject of lively scientific debate. As has been shown in chapter 8, there is a strong dependence of the electronic structure and its temperature dependence on the dimensionality of the material. While the cubic compound of $(La,Sr)_{N+1}Mn_NO_{3N+1}$ (i.e. $N = \infty$) has a metallic phase over a wide Sr doping range [183], the almost two-dimensional single layered compound is not metallic for any doping concentration and has charge and/or orbital ordered (CO/OO) insulating phases that do not display the CMR effect [187]. The bilayered compound, $La_{2-2x}Sr_{1+2x}Mn_2O_7$, henceforth called LSMO, which has a natural cleavage plane between the (La,Sr)O rocksalt layers and displays the largest CMR effect of all manganites, is somewhere in between these two extremes and has a narrow region in the phase diagram where a low temperature metallic-like phase exists [188].

However, the metallic phase in the bilayered material has a resistivity in excess of the Mott limit [190, 191], placing it in the realm of a poor metal at most. This observation is compounded by the lack of a coherent Drude peak in optical conductivity measurements [192,194], in sharp contrast to the cubic compound where sharp Drude peaks are seen [184]. On the other hand, angle resolved photoemission seems to paint a different picture. Although early reports confirmed the poor metallicity by detecting vanishing spectral weight at the Fermi level [200, 201], later reports found sharp quasi-particle peaks at E_F, in some cases at specific k-locations [202, 203], in other reports for all momenta [204–206].

Investigating dozens of samples using ARPES, we found that for our samples such sharply peaked spectra can only be obtained on very specific locations on the sample, usually amounting in total to no more than a few percent of the sample surface. In a combined effort to elucidate the origin of these regions, detailed ARPES and STM/S investigations were started on crystals grown in two separate labs with doping concentrations spanning the entire 'metallic' region of the phase diagram of bilayered LSMO. In the following, the STM/S results will be presented. The reader is referred to Ref. [6] for details on the ARPES investigation.

9.2 Experimental

High quality bilayered single crystals of $La_{2-2x}Sr_{1+2x}Mn_2O_7$ have been grown using the traveling solvent, floating zone technique in Amsterdam by Y. K. Huang (x=0.3, 0.36 and 0.40) and Oxford by A. T. Boothroyd and D. Prabhakaran (x=0.3, 0.325, 0.40 and 0.425). After growth the crystal quality was confirmed by Laue and SQUID magnetometry. Figure 9.1a shows a typical example of a magnetisation curve recorded through the paramagnetic insulating to ferromagnetic metallic phase transition. The transition temperatures determined from such magnetisation curves for

various doping concentrations are plotted in Fig. 9.1b on top of a phase diagram taken from Ref. [207].

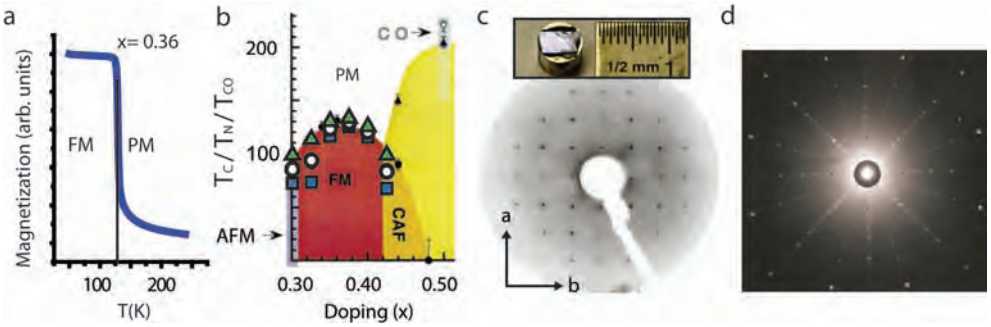

Figure 9.1: (a) Magnetisation versus temperature for an x = 0.36 sample measured using SQUID magnetometry. Data taken after zero field cooling, with an external field B = 100 G || c. The sample shows a sharp transition from a paramagnetic (PM) to a ferromagnetic (FM) state at T_C = 130 K with a total width smaller than 5 K. (b) Magnetic transitions as measured using SQUID magnetometry of LSMO with x = 0.30 (T_N) and $0.325 \geq x \geq 0.425$ (T_C), plotted on top of the magnetic phase diagram, taken from Ref. [207]. Depicted are the onset, midpoint and endpoint temperatures of the transition (triangles, circles and squares). (c) LEED image of a typical LSMO sample, E = 400 eV showing a very clear tetragonal pattern, without any signs of a structural reconstruction. The inset shows a cleaved crystal on top of a cleavage post, with a millimeter sized smooth and mirror-like surface. (d) Typical Laue image of the bilayered manganites, which displays the high quality and single crystallinity of the samples.

Samples were fractured *in situ* at a pressure better than $2.5\text{x}10^{-10}$ mbar at room temperature resulting in flat and shiny surfaces (see inset to Fig. 9.1c) and directly inserted into the STM which has a base pressure of $2.5\text{x}10^{-11}$ mbar. In the STM, the samples were cooled to 4.6 K. Electrochemically etched W tips and mechanically cut Pt/Ir tips were characterised on an Au(788) surface before a sample was measured. The orientation of the samples was furthermore obtained from *in situ* low energy electron diffraction (LEED), a typical example of which is shown in Fig. 9.1c. The single crystallinity of the samples was confirmed by Laue diffraction, see Fig. 9.1d.

9.3 The surface as seen with STM

A combined STM and angle dependent x-ray photoemission study showed that the bilayered manganites indeed cleave between the (La,Sr)O rocksalt layers as expected from the crystal structure [208]. Interestingly, it has been proven very hard to obtain atomic resolution on these (La,Sr)O surfaces with STM, and in the literature only one report exists where atomic resolution was obtained on nm-sized patches on an otherwise rather featureless surface [209]. The authors attributed this inability to resolve the atomic lattice to strong screening effects, and estimated that the atomic

corrugation would be as little as 0.02 Å, requiring either a very flat surface or a lifting of the screening due to strain or defects, to be able to detect the atoms.

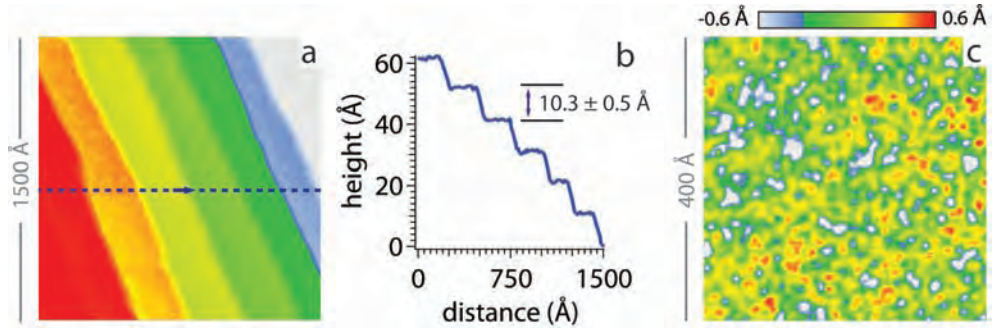

Figure 9.2: (a) Large field of view of a region with (an above average number of) half unit cell steps at the surface and (b) corresponding line scan along the dotted line (x=0.3, V = -500 mV, I = 100 pA). (c) Topographic image of an x=0.425 sample. The textures have little corrugation and are in this case disordered.

Imaging the cleavage surface of a typical bilayer LSMO single crystal in the CMR doping region using low temperature STM/S yields large, flat terraces, see Figs. 9.2a and b. The terraced, flat and debris-free surfaces we image indeed lack atomic corrugation, however they do posses a spatial texture in the tunneling signal. These structures are usually disordered as shown in Fig. 9.2c, but are - in some cases - ordered into a semi-regular, square-like lattice, displaying characteristic length scales of order of 2-3 nm. Figs. 9.3a-d shows a few examples of topographic images containing such semi-ordered structures for various doping concentrations. The quasi-ordered nature of these regions at the surface is evident from the autocorrelation traces from the STM topographs, as shown in Fig. 9.3e, which display clear structures at distances between 5-15 units cells. Comparison with low energy electron diffraction (LEED) data recorded in the STM chamber shows that the orientation of the quasi-periodic structures is not pinned to the underlying atomic lattice, and has even been seen in STM experiments to change as a function of macroscopic position on the sample. Furthermore, there seems to be no trend in the appearance or length scale of the quasi-ordered patterns as a function of doping concentration.

9.4 Tunneling spectroscopy on $La_{2-2x}Sr_{1+2x}Mn_2O_7$

To investigate whether the quasi-periodic structures seen in STM are of electronic nature or a structural feature, and to establish the typical tunneling signal as a function of doping of our bilayered LSMO samples, spatially resolved tunneling spectroscopy measurements have been performed. STM/S investigations to date on single crystalline LSMO showed a gapped density of states at the Fermi level at low temperatures [209,210], in line with the picture arising from various bulk probes of the mate-

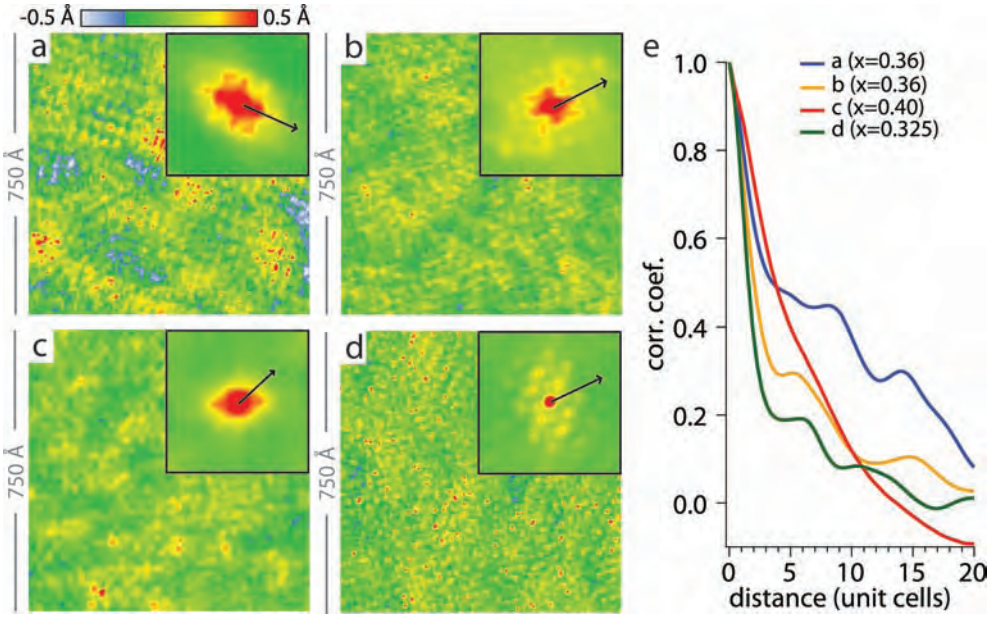

Figure 9.3: (a)-(d) Pseudo-periodic textures observed in the topographic STM images from different Sr doping concentrations of bilayer LSMO. Setup conditions are similar to those of Fig. 9.2a. The colour scale for all four images is as indicated above (a). The vertical corrugation at less than 1 Å is too small to be due to differing atomic layers of the crystal. Doping levels are given in panel (e), which shows line traces through the autocorrelation plots derived from the topographs shown as inset to (a)-(d) along the lines indicated. The traces show that the data support differing correlations ranging between 5-10 unit cells.

rial as being a bad metal. Point contact measurements on samples with a doping of x = 0.36, however, were found to be best described by an insulating surface bilayer through which a metallic signal of the bulk tunnels [211]. Support for the notion that the outermost surface layer might be different from the bulk and insulating instead of metallic was inferred by the same authors from resonant x-ray scattering experiments, where the outer bilayer was seen to have no ferromagnetic order [212–214]. Spin-polarised, scanning electron microscope data on x = 0.3 samples on the other hand demonstrate that even the topmost layer is ferromagnetic [215]. If this disagreement is related to the difference in doping concentration, it should be reflected in the doping dependent tunneling spectroscopy measurements. Furthermore, the suggestion that the surface layer is insulating, through which the metallic bulk density of states tunnels, seems at odds at best poor metal behaviour of the bulk states from transport and optical experiments.

Still, due to the increased freedom at the surface, caused by the removal of the constraining top-bilayer, the surface might indeed be more prone to insulating behaviour than the bulk as it is more two dimensional. A recent (hard) x-ray pho-

toemission study of the same crystals as studied here found no major difference between the surface and bulk in terms of charge transfer or composition [216], indicating that the differences between the outermost bilayer and the rest are subtle in nature. While recent LEED studies [214] have given no evidence for a lowering of the 2D surface symmetry, for example via a surface reconstruction, a finding LEED data taken on the samples measured with STM described in this thesis support, a contraction of the apical bond length for the outermost MnO_2-plane was observed [214], which could impact the mobility of the charge carriers at the surface.

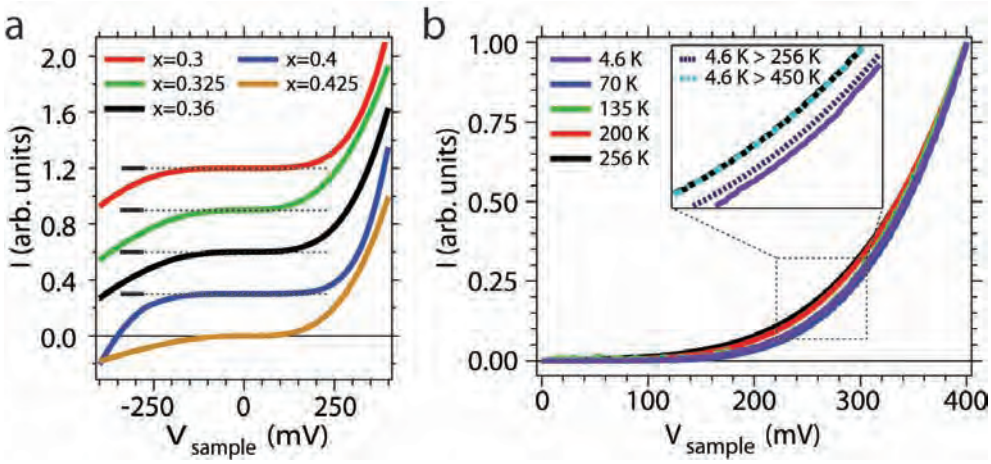

Figure 9.4: Doping and temperature dependence of the tunneling spectra. (a) I(V) curves taken at different temperatures on samples with different doping levels with comparable setup voltages and currents (~ 500 mV and 100 pA). All spectra taken across the 'metallic' phase are gapped with gaps on the order of 100 mV. (b) Temperature dependence of the tunneling spectra for x=0.36 taken well within the low temperature phase and well above T_C. To illustrate that thermal broadening alone cannot account for the difference between low and high temperature spectra, the 4.6 K spectrum is thermally broadened to 256 K and 450 K respectively, the latter showing a near perfect match with the high temperature STS spectrum. All spectra are normalised at 400 mV.

As it turns out, the tunneling spectra of bilayer LSMO from all cleavage surfaces measured are gapped (symmetrically) around E_F over an energy range of ~100 mV at low temperature for all doping concentrations studied, as shown in Fig. 9.4a. The tunneling spectra themselves show no major variations from point to point. This suggests that the observed spatial textures seen in the STM data are a subtle, 'higher order' structural ordering phenomenon, leading to modest, periodic signatures, somewhat reminiscent of the 2.5 nm correlated regions seen in the high-T, polaronic liquid phase described in Ref. [196]. The authors of Ref. [217] suggest that aggregates of polarons resembling a charge ordered state should be observable in STM experiments above T_C. The STM data presented here shows that these kind of enti-

ties could exist at the surface even at low temperatures, possibly being a log-jammed form of the fluctuating polarons observed in recent neutron experiments [199].

9.5 Temperature dependence of x = 0.36

To investigate further, the temperature dependence of the tunneling spectra of x = 0.36 has been measured. From the magnetisation curve obtained for x = 0.36 samples shown in Fig. 9.1a the CMR transition is found to be around 135 K. The CMR is accompanied by a transition from a ferromagnetic 'metallic' to a paramagnetic insulating state, hence the tunneling spectra are expected to change across this transition. Figure 9.4b shows normalised tunneling spectra upon increasing temperature. At the time of measurement, the exact same position could not be regained after heating the sample to temperatures above ~50 K, hence the spectra could not be taken on the exact same location. However, since the variation of the spectra as a function of position on the sample is within the noise of the measurement, comparison of different temperatures (i.e. at different locations) is valid.

Immediately one sees that the spectra taken at different temperatures do not match one another. To investigate whether this difference is caused by thermal broadening, the average of spectra taken at 4.6 K has been broadened to 256 K by convolution with a Fermi-Dirac function. Since the broadened curve is far from matching the measured curve (see inset to Fig. 9.4b), thermal broadening alone cannot account for the difference between the curves measured at different temperatures. However, if the 4.6 K spectrum is thermally broadened to 450 K, a nearly perfect match with the 256 K spectrum is obtained. Similar results have been reported for x=0.3 and x=0.32 doped compounds [209,210], where in fact the spectra where found to be consistent with a thermally activated conductance across a single gap. Moreover, as the spectra at low temperature are already gapped in the low temperature phase, this is unlikely to be a metallic double exchange state, but still essentially a polaronic state.

9.6 Single layered intergrowth

During the STM investigation of numerous cleavage surfaces of bilayer LSMO, very clear atomic resolution was found over a large terrace of one particular cleave, (shown in Fig. 9.5a-b). Analysis of the Fourier transform shows reduced in-plane symmetry, with clear ($\sqrt{2} \times \sqrt{2}$) spots shown in the inset to Fig. 9.5a. This is atypical for bilayer LSMO, which has a (1×1) tetragonal lattice symmetry in the ferromagnetic 'metallic' phase that is observed in all LEED data (see inset to Fig. 9.5b and Ref. [214]). An important observation linked to this large scale STM imaging with atomic contrast is that the step bordering this terrace is only one quarter of the N=2 c-axis unit cell in height (5 Å, see Fig. 9.5c). Additionally, the STS spectra from this region were more strongly gapped compared to those from non-atomically resolved regions displaying 10 Å step heights, as shown in Fig. 9.5d. Taken together, these facts form a

compelling argument that in Fig. 9.5 - in fact - a stacking fault in the Ruddlesden-Popper manganite is imaged, in which an extra La_2O_2 block (or blocks) creates a region of the bilayer crystal which is effectively single layer $(La,Sr)_2MnO_4$. The fact that atomic contrast is readily observed in STM of cleaved single crystals of N=1 LSMO [218] also offers further support for this interpretation.

The observation with STM/S of such a surface inclusion with a different stacking number N is rare, but is not, in itself, wholly surprising. Numerous μSR studies [219], magnetisation measurements [220, 221] and transmission electron microscopy studies [222, 223] have established that stacking faults occur even in the very best crystals at the $\approx 1\%$ level [220, 221]. These intergrowths vary - locally - the stacking number N and are the cause of anomalous steps in the magnetisation above the bulk T_C common in bilayer LSMO between 200 and 350 K: small patches with N values above two deliver a higher T_C. Due to the strong connection between magnetism and metallic behavior in the manganites, it is a simple step to reason that $N > 2$ intergrowths would also be metallic above and beyond the bilayer T_C. In contrast, an $N = 1$ intergrowth will be more insulating than bilayer LSMO, in keeping with the STM/S data shown in Fig. 9.5d.

Additionally, small area electron diffraction experiments in transmission electron microscopy studies on bilayered LSMO with x = 0.40 have shown that inclusions have a $(\sqrt{2} \times \sqrt{2})$ reconstructed unit cell, with respect to the tetragonal structure of the bilayered matrix [222]. This would be exactly the type of reconstruction that is needed to explain the observed non-tetragonal spots in the Fourier transform in the inset to Fig. 9.5a.

In Fig. 9.5d, STS spectra are also compared to k-integrated angle resolved photoemission spectra. As mentioned previously, gapped and quasi-particle peaked photoemission spectra have been reported in literature. From the figure, it is immediately clear that the quasi-particle peaked spectra are very different from the STS spectra, having a peak at zero bias instead of a gap. This, and a number of other anomalies, including the non-tetragonal crystal symmetry also seen in ARPES experiments, can all be explained when stacking fault intergrowths are seen as the source of the quasi-particle peaked spectra, as has been discussed in Ref. [6]. As the photoemission current unlike the STS signal originates from deeper than only the first bilayer, the effect of the surface on the STS spectra can be appreciated. Assuming the matrix tunneling elements are similar for both techniques, the STS spectra are slightly more gapped than the ARPES spectra, indicating that indeed the surface is slightly more insulating. However, this is a difference between two poorly metallic spectra, not between a metal and an insulator.

9.7 Discussion

From the data shown and the ARPES data recorded within the group on the same single crystals, the physical nature of the charge carriers responsible for the electronic transport of the bilayered manganites can be addressed. The most suitable picture -

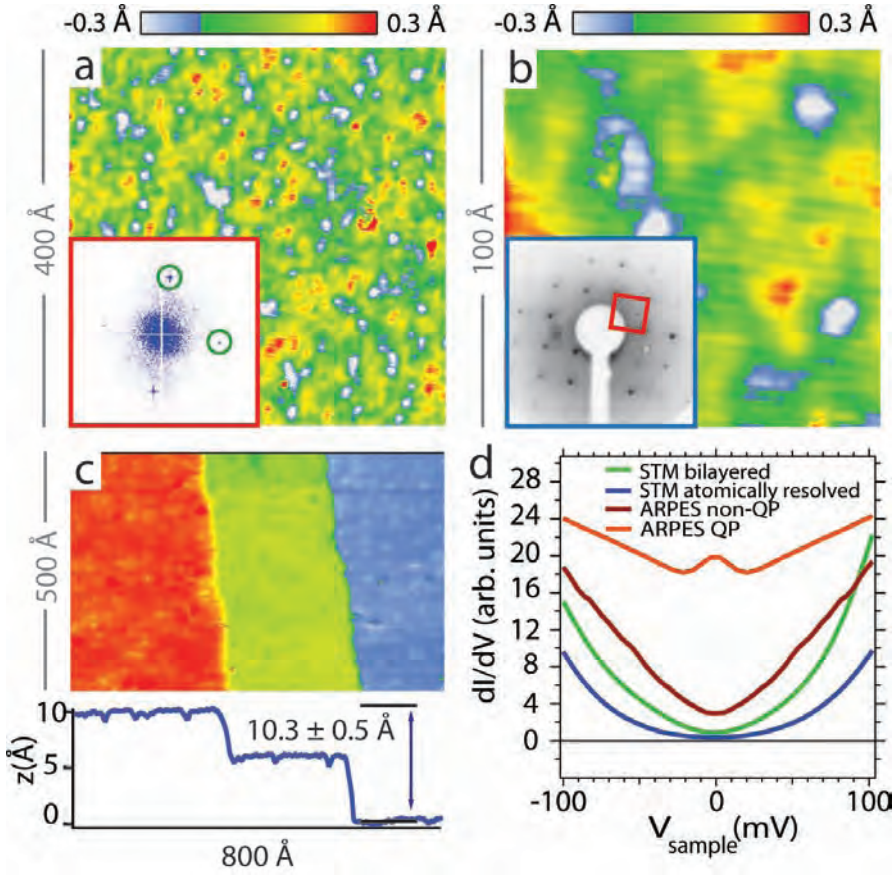

Figure 9.5: (a) 400 Å field of view with atomic resolution. The inset shows the Fourier transform of the image with clear spots corresponding to the unit cell distances (green circles). Interestingly, non-tetragonal spots appear in between the lattice spots, indicating an orthorhombic crystal symmetry. (b) 100 Å zoom of part of (b) showing the clear atomic resolution. The inset is the LEED pattern taken on the same sample confirming the lattice seen in STM has indeed the same orientation as the crystal structure. (c) Topography of stepped surface taken on the same region as (a) and (b), where the step height corresponds to that expected for single layer LSMO as can be seen from the line trace below the image. (d) Comparison between symmetrised, k-integrated ARPES spectra and STM dI/dV traces. The spectra taken on the region with atomic resolution is more strongly gapped than on non-atomically resolved areas. The non-peaked ARPES spectra are only slightly less gapped indicating that the surface is only marginally affecting the tunneling signal.

considering the results on both the dynamics of the charge carriers and the subtle yet clear structural anomalies they bring with them - is that of polaronic charge carriers above T_C, but also in the ferromagnetic (bad) metallic state. The fact that the STM signatures of the weakly self-organised polaronic carriers when 'log-jammed' at the

surface resemble the polaronic correlations seen above T_C in diffraction experiments suggest that in the bulk of the bilayer LSMO systems - which is more metallic than the surface - the system teeters on the edge of a breakdown of the fragile polaronic metal state into an insulting, charge and orbitally ordered state. This borderline situation, coupled to the disorder and enhanced fluctuations present in these quasi-2D systems, delivers all the ingredients for the colossal magnetoresistance transition [217].

As has been shown in chapter 2, the physics describing the manganites depends crucially on the propensity of the system to form ordered textures in spin, charge and orbital occupation. For the polaronic metal state to remain stable, it is vital that the degeneracy in the e_g orbital manifold is preserved, as this is the ticket to the double-exchange energy reduction that encourages hopping of the carriers. This condition - in turn - stipulates equality in the equatorial and axial bond lengths of the MnO_6 octahedra. The deviating axial bond lengths at the surface of bilayered LSMO compared to the bulk, as observed in Ref. [214] lift this degeneracy and thus push the surface of this material further into the insulating regime than the bulk already is: the correlated polarons can become prone to trapping in pseudo-periodic patterns the details of which will be influenced strongly by long-range strain fields between the polaronic entities. Our STM experiments have proven able to pick up these subtle surface modulations for doping ranges spanning the metallic low temperature phase in the bilayer phase diagram. On the other hand, the N>2 inclusions observed in ARPES experiments, structurally bear greater resemblance to the cubic compound, and thus show a higher propensity towards metallic behavior, including the existence of coherent spectral weight at E_F. Paradoxically, it is this fragility of the polaronic metal state in the bilayer systems that is the key to their colossal magnetoresistance, as it delivers the precarious balance between weakly metallic and insulating behavior required for such an enormous sensitivity to the extra impulse provided by an external magnetic field.

9.8 Summary

Imaging the bilayered colossal magnetoresistant manganites using STM yields large, flat terraces, where atomic resolution is generally absent. However, the images do possess a spatial texture that is usually disordered, but occasionally forms square-like patterns. These patterns are not pinned to the lattice as they are seen to change orientation as a function of position on the sample and is not aligned to the LEED patterns obtained from the same crystal surfaces after the STM investigation. As the typical length scales of these structures are similar to those of quasi-static polarons seen above T_C with neutron and resonant x-ray diffraction, what we are imaging in these cases in STM may be frozen-in polarons that survive in the low temperature phase due to an increased freedom of the MnO_6 octahedra at the surface.

Tunneling spectroscopy over a wide range of doping concentrations across the 'metallic' phase results in (symmetrically) gapped spectra where little to no variation

exists in the spectra as a function of position on the surface and no clear trend can be detected as a function of doping. Comparison with angle integrated photoemission spectra from the same crystals seems to indicate that the surface is slightly more insulating than the bulk (which is also pseudogapped). Temperature dependent STS sees a clear difference between the low temperature and high temperature phases, where the high temperature phase cannot be explained by thermal broadening alone. All these observations point to a situation where the low temperature phase is more conducting than the high temperature phase, but, instead of being a 'classic' double exchange metal, is a poorly conducting polaronic system, which teeters on the edge of a breakdown of the fragile polaronic metal state into an insulting, charge and orbitally ordered state. It is at this fine balance between metallic-like and insulating where the colossal magnetoresistant effect occurs.

A fine example of the role dimensionality plays in this balance is the observation of a single layered intergrowth on an otherwise bilayered material, as inferred from the clear atomic resolution, more strongly gapped spectrum and ~5 Å step edge. The lowering of the dimensionality increases the freedom of the MnO_6 octahedra, decreasing the metallicity due to increasing lattice distortions.

The results presented here formulate a clear challenge to develop a general theory for the transport in N = 2 systems involving practically incoherent charge carriers - fluctuating polarons - while also capturing the sensitivity to the stacking number, N. Aside from the lattice polaron generally considered, different types of polaron, such as spin and orbital polarons and combinations thereof, should be taken into consideration [224–226]. In these cases, the hopping of a hole through a spin- and/or orbitally ordered lattice[1] is hindered by the frustration of the spin- and/or orbital ordering of the system. An interesting proposal for the charge carrier dynamics in the manganites is the existence of so called Zener polarons [228, 229]. In such a polaron, the charge carrier is not localised on a single manganese atom, but on two neighbouring manganese atoms which are ferromagnetically coupled by the Zener double-exchange mechanism. These manganese dimers can then for instance spatially order to form a Zener polaron phase [230]. It has been shown that all these types of polaron lead to a large incoherent spectral weight such as is seen in our ARPES investigations [224–226, 231].

The new insight gained points towards the great potential of e.g. layer-by-layer thin-film engineering to generate tailor-made heterostructures, not only to lead to enhanced transition temperatures [232], but in combination with modern lithographic and patterning methods to tune and improve magnetoresistive properties on the sub-micron scale in a new generation of complex oxide devices.

[1] as we are far from half-doping, one would not expect long range CO/OO in the bulk of the sample. The topographs, however, with their signs of log-jammed, subtle distortions could be correlated groups of lattice/spin/orbital polarons. In any case, in the manganites, lattice polarons and orbitons are inextricably linked. [227]

Summary

One of the million dollar questions in condensed matter physics is what the origin is of high temperature superconductivity, as this knowledge could pave the way to the engineering of room temperature superconductors which would make a huge contribution to the solution of the ever increasing energy problem. After two decades of research on the family of materials with the highest known transition temperature, the copper oxide superconductors, there is still a lively debate on the physics responsible for the unusual behaviour of the materials. The discovery at the beginning of 2008 of a completely new family of high temperature superconductors containing iron therefore signalled a worldwide surge to investigate this new superconductor hoping that the similarities and differences with the cuprates could shed more light on high temperature superconductivity in general.

During the course of this Ph.D. research, the Amsterdam group hopped on the pnictide train to add angle resolved photoemission (ARPES), scanning tunneling microscopy and spectroscopy (STM/S) and low energy electron diffraction (LEED) data to the ever growing experimental database on these new superconductors. In this thesis, the STM/S and LEED data are presented in chapters 4 to 7 and are mainly focussed on one subfamily within the whole family of iron based superconductors, namely the $M\mathrm{Fe_2As_2}$ or '122' pnictides (here M = Ba, Ca, etc.). First, the cleavage surface of this family is investigated, which is an essential part of every surface sensitive technique. Using temperature dependent STM and LEED, the surface is shown to have a barium (Ba) (or calcium (Ca), etc.) termination layer, where half of a full Ba layer is left on each side of the cleave. This top layer mainly orders into two regular structures, $(\sqrt{2} \times \sqrt{2})$ and (2×1) respectively, or shows various degrees of disorder. Using a simple model, all different surface structures observed in STM are explained.

With a secure knowledge of the surface structure, a spectroscopic survey of the compound with an optimal cobalt (Co) doping concentration is subsequently performed of which the results are discussed in chapter 5. The peak-to-peak separation in tunneling spectroscopy, which is interpreted as the size of the superconducting gap, is seen to vary significantly as a function of real space position and can change from the maximum observed magnitude to the minimum over mere nanometers. Knowing the surface structure deviates from the regular bulk symmetry, a possible influence of this surface structure on the spectroscopic signals is checked to be absent by taking cross correlations between maps of the superconducting gap magnitude and the corresponding constant current images. As the typical length scale of the gap inhomogeneities corresponds rather well to the Co-Co separation, scattering ef-

fects of the Co dopant atoms are suggested to play a role in the gap inhomogeneities.

In the cuprates, spatial variations in the peak-to-peak separation on the order of nanometers have in the past been reported in literature, but these were eventually shown to be linked to the so called pseudogap, a gap that does not close at the superconducting transition temperature, T_c, but extends to well beyond it. The superconducting gap, on the other hand, which was extracted after division of spectra taken above and below T_c, showed much less spatial variation in magnitude. To investigate whether the variation of the peak-to-peak separation in the pnictides is also due to a pseudogap or truly a variation in the size of the superconducting gap, temperature dependent spectroscopy was performed. From these measurements, presented in chapter 6, where tunneling spectra are recorded at the exact same locations at various temperatures both below and above the bulk T_c, a pseudogap scenario as seen in the cuprates is excluded.

From a doping dependent study, and by comparing the variation in superconducting gap magnitude of '122' systems with a different dopant element, the origin of the spatial variations in gap magnitude is further investigated in chapter 7. It is suggested that scattering effects from Co dopants in the superconducting Fe-plane are responsible for numerous anomalous behaviours and that care should therefore be taken in the interpretation of the reduced gap values in these systems as determined from STS and ARPES measurements. Further experimental and theoretical study of scattering of different dopant atoms on the atomic scale is expected to lead to a better understanding of the microscopic mechanism behind superconductivity in the pnictides.

Before the pnictides entered the scene of condensed matter physics, the main focus of this Ph.D. research was the investigation of the colossal magnetoresistant manganite $La_{2-2x}Sr_{1+2x}Mn_2O_7$. The colossal magnetoresistant manganites as a family display a wide variety of exotic phases ranging from charge and orbitally ordered insulators to double exchange metals, phases which can change into one another by varying the electron or hole doping concentration only slightly. What makes the materials especially remarkable is the incredible sensitivity to a magnetic field of the transition from a low temperature metallic phase to a high temperature insulator at a wide range of doping concentrations. Near the transition temperature, an external magnetic field can lead to a change in resistivity of several orders of magnitude: the colossal magnetoresistant effect.

The exotic phase diagram of the manganites is commonly explained by the strong competition between charge, orbital and spin degrees of freedom. Due to a strong Hund's rule coupling, the spins on neighbouring Mn atoms tend to align parallel to enhance hopping of electrons via double exchange. However, energy gain via lattice distortions forces the spins to align anti-parallel via the super-exchange mechanism leading to an insulator. A slight change in doping concentration (i.e. occupation of the Mn3d orbitals) and temperature can alter this fine balance between these two main players, leading to a completely different behaviour.

Even though this physical picture to describe the phase diagram is appealing,

the detailed mechanism driving the colossal magnetoresistant (CMR) effect is still under debate. As the bilayered manganite $La_{2-2x}Sr_{1+2x}Mn_2O_7$ displays the largest CMR effect and has a natural cleavage plane, this material is best suited to investigate using surface sensitive probes such as STM/S and ARPES. Various bulk probes have shown that this material is in fact not a double exchange metal, but a poor metal at most with unequal bond lengths and polaronic correlations well into the 'metallic' phase. In contrast, sharp quasi-particle peaks have been observed in ARPES investigations signalling a truly metallic state, an observation that seems to link the manganites to the cuprates as a nodal metal. In a combined ARPES and STM/S investigation, of which the latter part is related in chapter 9, it is shown that even though nodal metallicity is an interesting proposition, it is not a requirement for the CMR effect. In fact, across the 'metallic' region of the phase diagram (with the exception of a singular doping concentration at x=0.4) the low temperature phase is shown to be an essentially polaronic system with poor hopping, where - at the surface - polarons[2] can freeze into a semi regular structure. On the other hand, small regions where not the bulk bilayered structure, but a structure with a different stacking number resides, are argued to be the reason for either more insulating (N=1) or truly metallic (N>2) behaviour seen with STM and ARPES. During the STM/S investigation presented here, one such single layered intergrowth was seen as deduced from the more strongly gapped tunneling spectra, the clear atomic resolution and the height of a nearby step edge. These new insights, where the bilayered manganite is seen as a fragile, polaronic, bad metal state at low temperature teetering at the edge of a transition into an insulting, charge and orbitally ordered state, and where stacking faults are seen as the cause of numerous anomalies, unite all seemingly contradictory reports in the literature and supply all the ingredients for the CMR transition.

Aside from the main research presented in chapters 4 to 9, several calibration measurements, software procedures and technical details on for instance the art of making sharp tips for STM are discussed in the appendices.

[2]these polarons are not strictly lattice polatons, but could for instance very well be spin- and/or orbital polarons or Zener polarons

Part III

Appendices

APPENDIX

A Benchmarking the STM: Bi2212 and (Pb,Bi)2212

In this first appendix, an overview is given of measurements performed on $Bi_2Sr_2CaCu_2O_{8+\delta}$ and $Pb_xBi_{2-x}Sr_2CaCu_2O_{8+\delta}$. These high temperature superconducting materials have been the focus of intense research since their discovery in the late 80's. STM/S has had an enormous impact on this field, as it is the ideal tool to study the local electronic structure on nanometer length scales. In particular the work of J. C. Davis and collaborators has caused a paradigm shift in the approach to these materials as it pointed out that the chemical doping required to obtain superconductivity introduces intrinsic disorder on (sub)nanometer length scales. A huge amount of work has been published around the time that we set out on this line of research, and these materials are therefore perfectly suited to serve as benchmark systems for our new STM instrument that was used throughout this thesis. After a very brief introduction of the crystal structure, band structure and momentum dependence of the superconducting gap, the concept of quasi-particle interference scattering is introduced. In the next two sections the main results reported in the literature obtained with STM over the past decades are discussed using our own data as a basis, both from $Bi_2Sr_2CaCu_2O_{8+\delta}$ and $Pb_xBi_{2-x}Sr_2CaCu_2O_{8+\delta}$. This appendix will close with a demonstration of the powerful technique of Fourier transform scanning tunneling spectroscopy (FT-STS). Using this technique, quasi-particle interference scattering in both pristine and Pb doped Bi2212 will be shown. Even though this appendix does not aim at the provision of 'new' insights into the physics of the cuprate superconductors in the sense that the measurements performed have been reported in literature already by others, it shows the possibilities of a commercially available STM such as the one used throughout this Ph.D. research.

A.1 Introduction

Scanning tunneling microscopy and spectroscopy have shown their full power in the field of high temperature superconductivity, and in particular on the $Bi_2Sr_2CaCu_2O_{8+\delta}$ system. No other strongly correlated material has been investigated as intensely as this superconductor which has a T_c^{max} of 95 K. The natural cleavage plane between the weakly bonded BiO sheets (see Fig. A.1a) ensures an extremely flat and clean surface essential for high quality imaging and spectroscopic mapping of the material. For a recent and very detailed overview of STM/S literature on this system, Ref. [125] is strongly recommended.

A.2 Quasi-particle interference scattering

The high T_c cuprate superconductor $Bi_2Sr_2CaCu_2O_{8+\delta}$, henceforth called Bi2212, has d-wave symmetry of the superconducting order parameter, see section 3.3. This means that the gap magnitude changes as a function of momentum, which is illustrated in Fig. A.1b where the gap magnitude is plotted on top of the Fermi surface of Bi2212. The symmetry of this $d_{x^2-y^2}$ gap with respect to the crystal structure is plotted in Fig. A.1c. At four lines in k_z in the first Brillouin zone, called the nodes, the superconducting gap vanishes, resulting in quasi-particle states up to the Fermi level. In a real-life material, there will always be scattering due to impurities and defects, see also section 3.7, meaning that the quasi-particles with a certain energy (E_1) and momentum ($\mathbf{k}_1$) can be scattered into a state with different energy and momentum, E_2 and $\mathbf{k}_2$ respectively. If only elastic scattering is considered, the energy of the particle is conserved, $E_1 = E_2$, and only the momentum is changed. As there are only four momenta at the Fermi level where a finite density of states resides in the superconducting state, there are only four inequivalent scattering vectors ($\mathbf{q}$) possible for $E = E_F$, i.e. the vectors connecting the four nodes (two sets of two vectors with equal length, but different orientation). In real-space, such a scattering vector corresponds to a modulation of the local density of states (LDOS, or g(r,E)) in the form of a standing wave centered on the impurities. In principle, these standing waves can be picked up by extracting the LDOS at a certain energy over a particular field of view. In practice, the modulations are not very strong, and are imposed on a background of an inhomogeneous LDOS, requiring g(r,E) maps to be taken over large fields of view (>450 Å) [126] in order to have sufficient contrast. In the Fourier transform of such an image, intensity spots will appear that correspond to the scattering vectors.

So far only the g(r,E) at the Fermi level is considered. For a finite excitation energy, E, not only the nodes will contribute to the total, $\mathbf{k}$-integrated, g(r,E), but also those $\mathbf{k}$ locations around the nodal points where E is large enough to bridge the superconducting gap, $|E| > \Delta(\mathbf{k})$. The banana-shaped regions around the nodes thus formed will increase in size as E increases towards the maximum gap at the antinode. Therefore, if the g(r,E) would be equal for all contributing $\mathbf{k}$ points, the original four scattering vectors seen at $E = E_F$ will become smeared out. However, for a given

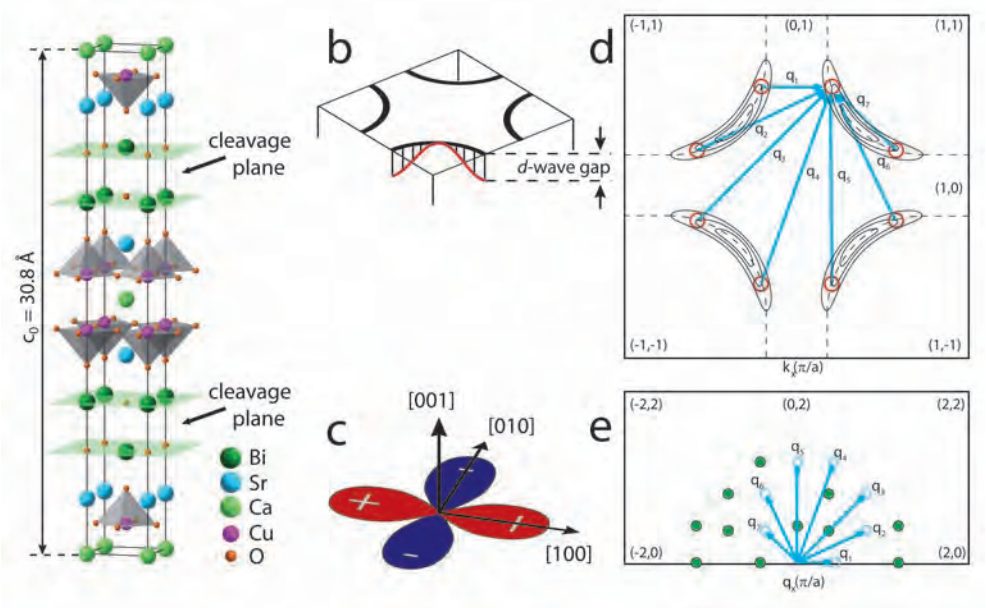

Figure A.1: (a) Tetragonal unit cell of the layered crystal structure of Bi2212. The superconducting CuO-planes are separated by several interstitial layers. The crystal cleaves between the weakly bonded BiO layers resulting in a flat cleavage plane. (b) Fermi surface and d-wave gap (bilayer splitting is omitted for simplicity). The gap is zero in the (0,0)-(π,π)-direction and increases in magnitude upon moving towards the zone face. (c) The symmetry of the $d_{x^2-y^2}$ superconducting gap with respect to the crystal structure. The lobes point along the Cu-O-Cu bonds. (d) Two dimensional representation of the Fermi surface with several constant absolute excitation energy contours plotted on top. The endpoints of these contours are the main contributor to the g(r,E), hence scattering will be dominated by these locations for a given energy. Scattering vectors between these locations are indicated and lead to a total of 16 inequivalent vectors. In Fourier space, these vectors correspond to sixteen inequivalent intensity spots as shown in (e). (a) and (c) after [125], (b) after [50], (d) and (e) after [126].

energy, the largest contribution to the total g(r,E) comes from the endpoints of the 'bananas'. This can easily be seen by looking at the density of states of a superconductor given by Equation (3.3). At the superconducting gap energy, Δ, the density of states diverges, which for a finite temperature results in a large quasi-particle peak. Whereas the g(r,E) contributions of all **k**-points where $E > \Delta$ are beyond this large peak, the LDOS contribution of the endpoints of the 'bananas' comes right from this large quasi-particle peak. Therefore, the total g(r,E) at finite energy can be approximated by the g(r,E) of the endpoints of the 'bananas'. The original four inequivalent scattering vectors will at finite energy become sixteen inequivalent scattering vectors, as can be seen from Fig. A.1d, corresponding in reciprocal space to sixteen inequivalent intensity spots as shown in Fig. A.1e. Due to the aforementioned expansion towards the anti-node of the 'bananas' as a function of energy, the length

and orientation of the scattering vectors will have an energy dependence.

The model described above, also termed the octet model after the eight points on the Fermi surface where the predominant contribution to scattering comes from for a finite energy, captures the LDOS variation with energy as seen with STM extremely well [126, 127] as will be shown below (section A.4).

A.3 Topography and the superconducting gap

A.3.1 $Bi_2Sr_2CaCu_2O_{8+\delta}$

Before moving on to show quasi-particle interference scattering using Fourier transform STS (FT-STS), the general properties of the surface and superconducting state of both slightly overdoped pristine Bi2212 (T_c = 86 K) and Pb doped Bi2212 (T_c ~ 80 K) will be discussed. Figure A.2a shows a typical topographic image of the cleavage surface of Bi2212, with sharp atomic resolution and characteristic snake-like features on the ridges of the (bulk) ~5b incommensurate supermodulation. The atoms seen in constant current images are the Bi atoms in the BiO cleavage plane which reside directly above the Cu atoms and act as a transmitter of the Cu density of states. The origin of the dark-row snakes is still under debate, but these seem to stem from additional oxygen atoms necessary to register a rotation of the Bi-O trimer in the BiO plane [233]. The 5b supermodulation is clearly discernible in the Fourier transform of the constant current image in the form of copies of the unit cell spots as can be seen in Fig. A.2b. An identical pattern is obtained in low energy electron diffraction (LEED) on the same sample in the same vacuum system directly after the STM investigations, see Fig. A.2c [1].

If one takes differential conductance spectra on a square grid on the field of view shown in Fig. A.2a and extracts the superconducting gap size for each individual spectrum, the gap map shown in Fig. A.2d can be constructed. From this, it immediately becomes clear that there is a large variation in superconducting gap size as a function of position, which had been observed early on in literature [234]. The variation is typically seen as networks of nanometer-scale islands, which have a width on the order of the coherence length (3-5 nm), with different gap magnitudes [235, 236]. Although there remains some controversy on the origin of these variations, the most compelling evidence seems to indicate that these spatial variations in the superconducting gap magnitude are due to sample inhomogeneities, in specific oxygen defects. For instance, properly annealing the samples has been shown to reduce the gap inhomogeneity [237] and a direct correlation between the gap amplitude and oxygen impurity distributions in real space has been found [238]. As for instance Pb doping does not change the variation in gap magnitude ([239], see also Fig. A.3.2), defects other than oxygen are believed to play a minor role.

Even though the spatial resolution of the map shown in A.2d is a mere ~5 Å, the spectra and gap size can vary significantly from pixel to pixel. To determine the

[1] The LEED image has to be mirrored in the vertical direction to match the orientation of the STM

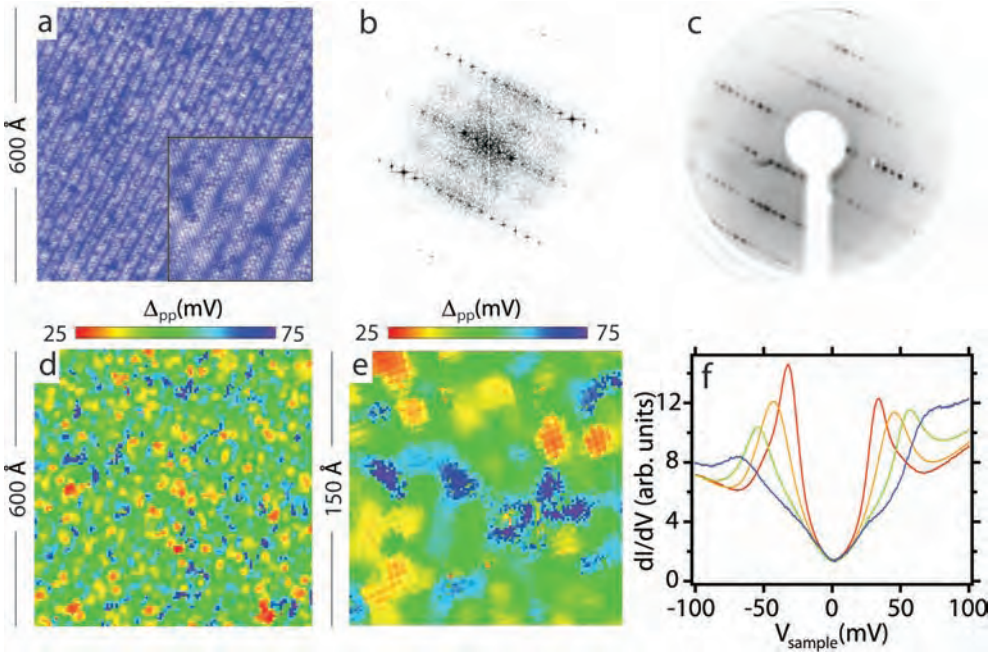

Figure A.2: (a) 600 Å constant current image of Bi2212 showing clear atomic resolution and the characteristic ~5b supermodulation. The inset is a zoom of 150 Å of the center top. (b) Fourier transform of (a). Due to the supermodulation, spots corresponding to the lattice constant distance are repeated in the b direction. (c) Low energy electron diffraction image taken at 94 eV on the same sample as shown in (a) directly taken after the STM/S investigation. (d) Spatial distribution of the superconducting gap (i.e. gap map) taken on (a), with typical nm-sized patches with similar gap magnitudes. (e) High resolution gap map on the 150 Å region shown in the inset of (a), where the evolution of the gap on the scale of the lattice can be seen. (f) Each gap has a distinct tunneling signature of which four of increasing magnitude are shown. The colours of the spectra correspond to the colour scale of the gap maps. For increasing gap size the coherence peaks become less pronounced. For the largest gaps, a kink can be seen indicating a possible second gap. All images and spectra throughout this appendix were taken at V_{sample} = 100 mV, I_{set} = 30 pA unless stated otherwise.

variation of the gap magnitude on the atomic scale, a high resolution, 118×188×512 pixel differential conductance map was taken on the center-top 150×150 Å^2 of the map shown in A.2d. This area is also shown as inset to Fig. A.2a. The resulting gap map, shown in Fig. A.2e, clearly shows gap variations on the scale of the atomic lattice and the aforementioned 3-5 nm islands of gaps with a similar magnitude.

Although the regions with small superconducting gaps appear smooth and continuous in the gap map, the regions with a large gap size (dark blue to purple) are somewhat noisy. To illustrate the cause for this discrepancy, Fig. A.2f plots four typical spectra with different gap sizes. Whereas the smallest gap has sharp and well defined quasi-particle coherence peaks, increasing gap magnitudes have decreasing

coherence peaks. The largest gaps barely have a coherence peak, but seem to develop a kink around 30 mV indicating the existence of a second, smaller gap. The large gap (Δ_{pp} >65 mV) has in fact been shown to be a pseudogap, which does not vanish at T_c, whereas the kink marks the superconducting gap [135, 240]. As this large gap is difficult to determine in an automated routine, which in some cases might also pick up the smaller gap, the large gap regions are slightly noisy in the gap map.

A.3.2 $Pb_xBi_{2-x}Sr_2CaCu_2O_{8+\delta}$

Having shown the properties of pristine Bi2212, the effect of introducing Pb into the system will now be discussed. As mentioned in the previous section, the spots corresponding to the atomic lattice spacing seen in LEED and the Fourier transform of

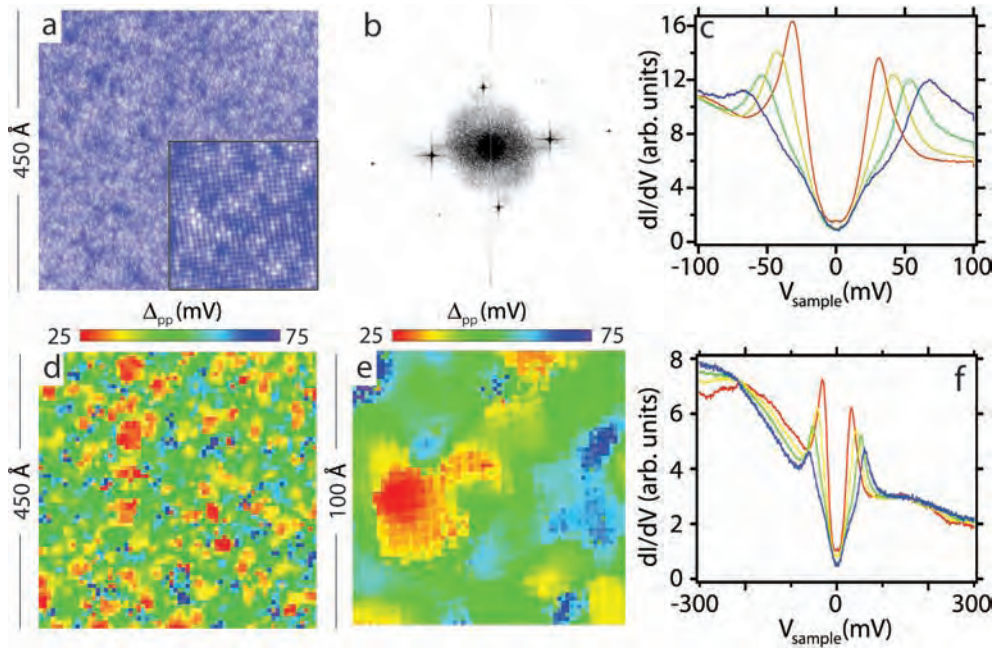

Figure A.3: (a) 450 Å constant current image of (Pb,Bi)2212 showing two distinct surface atoms (regular = Bi and bright = Pb) on an otherwise flat surface. The 100 Å inset shows a zoom of the top-center of (a). The suppression of the supermodulation seen in the pristine material is nicely illustrated by the Fourier transform of (a) shown in (b), where only the lattice parameter spots and higher orders thereof are present. (c) Spectra taken on this surface are identical to those taken on Bi2212, where larger gaps have a less pronounced coherence peak. The gap map extracted from the spectra taken on (a) shown in (d) has the same spatial variations of the superconducting gap and similar minor variations on the atomic scale as can be seen from the zoom taken on the 100 Å inset of (a) shown in (e). (f) Spectra taken up to energies well above the maximum superconducting gap energy show even more clearly the suppression of the coherence peak upon increasing gap size (V_{sample} = 300 mV, I_{set} = 15 pA).

constant current images are multiplied by the ~5b supermodulation leading to multiple copies of the original spots. As the supermodulation is a bulk property [241,242], all probes where diffraction plays a role will be affected. For instance, in angle resolved photoemission, not only the bands themselves are seen, but also their diffraction copies, making interpretation of the data cumbersome, see for instance Ref. [111] and references therein. In order to suppress the supermodulation, Pb doping has been introduced in the system as a partial replacement of the Bi atoms. In the thus formed material, $Pb_xBi_{2-x}Sr_2CaCu_2O_{8+\delta}$ or (Pb,Bi)2212, the period of the modulation is seen to increase [243,244] and for an effective Pb content of x = 0.36 it is completely suppressed [245].

Indeed, imaging the cleavage surface of (Pb,Bi)2212 gives a completely flat surface due to the absence of the supermodulation as shown in Fig. A.3a. The diffraction copies in both the Fourier transform and LEED images for the pristine system (Figs. A.2b and c) are completely absent in the Pb doped system as can be seen in Fig. A.3b where the Fourier transform of the constant current image is shown. Interestingly, two distinct surface atoms are visible on the surface of the Pb doped system, where the number of bright atoms seems to match the average Pb doping concentration rather well. As only Pb has been introduced with respect to the pristine system where no such distinct atoms are seen, these bright atoms must be the Pb atoms residing in the Bi layers. Following this reasoning, it is indeed the BiO layer, and not for instance the CuO layer, that is seen in STM topography measurements.

Aside from suppressing the superstructure, lead doping barely affects the superconducting properties seen with STM: the tunneling spectra observed on the Pb doped compound (Fig. A.3c), the gap map extracted from these spectra (Fig. A.3d) and the variation of gap magnitude both on large spatial scale and on the atomic level (see Fig. A.3e) can hardly be distinguished from what is observed on pristine Bi2212. The suppression of the height of the superconducting coherence peak upon increasing gap magnitude and the appearance of a kink in the spectra with a large gap indicating a second energy scale, the pseudogap, are especially clear in spectra taken over a larger energy range as shown in Fig. A.3f.

One peculiarity, however, is the presence of distinct (near-) zero bias conductance peaks in (Pb,Bi)2212, which are much less abundant in Bi2212. Fig. A.4a shows a g(r,E=-3$\pm$1 mV) image taken on the same field of view as Fig. A.3a. As can be seen, bright spots appear that are spread evenly over the surface. Zooming in on one of these spots in Fig. A.4b, a clear oscillation with a fourfold symmetry is observed, running along the unit cell directions. Taking a line trace from the center of the spot to the corner of the image, the oscillation is seen to dampen exponentially with a decay constant of ~6 Å and is completely gone after approximately 2 nm as shown in Fig. A.4c. To illustrate that this feature is independent of the surface structure and therefore not an artifact caused by a scattering center on the surface, the topograph on which Fig. A.4b is taken is shown in Fig. A.4d. From this comparison, one can also see that the zero bias conductance peak is centered on a surface atom (marked by the cross) and that the first oscillations are located on the next nearest neighbours. To

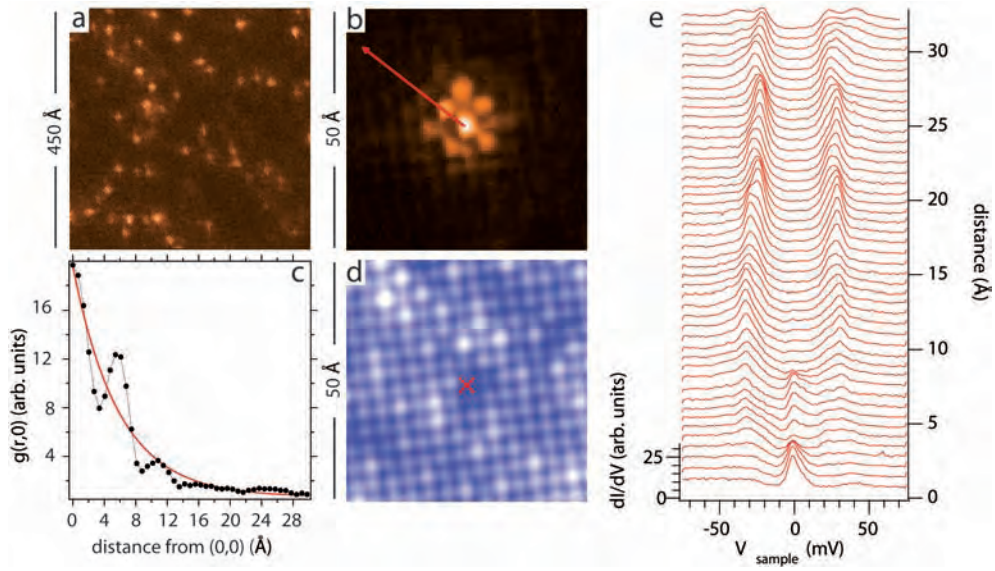

Figure A.4: (a) g(r,E) image for E = -3 ± 1 mV on the same field of view as Fig. A.3a. Spread evenly over the entire field of view are bright spots corresponding to zero bias conductance peaks in the tunneling spectra. (b) A fourfold symmetry around the main peak is observed upon enlargement of such an object. (c) Plotting g(r,-3 mV) along the line indicated in (b) shows the exponentially dampened oscillation away from the center, which drops off with a decay length of τ = 5.9 Å(red curve). (d) Comparison to the topograph on which the g(r,E) map is taken rules out scattering due to a surface defect (the location of the scattering center is indicated with a cross). (e) The evolution of the zero bias peak and its effect on the superconducting gap are illustrated by the spectra along the line in (b).

show the evolution of the spectra from the center of the zero bias conductance peak to far from it, Fig. A.4e plots the spectra taken along the line indicated in Fig. A.4b.

Zero bias conductance peaks are typically seen when the electrons in Cooper pairs are scattered by impurities. In literature, both non-magnetic Zn atoms [98] and magnetic Ni atoms [99] have been deliberately introduced in Bi2212 to investigate the properties of the superconductor. Due to the d-wave pairing symmetry of Bi2212, magnetic impurities were seen to create in-gap states, without suppressing superconductivity altogether. Non-magnetic impurities on the other hand effect a strong suppression of the superconducting state at the scattering site, which is recovered after approximately a coherence length from the center, very similar to what we describe here on (Pb,Bi)2212.

With the superconducting gap away from the scattering center known (Δ_0 = 32 mV) and the energy of the resonance, Ω = -3.7 mV, the strength of the scatterer can be estimated by [246, 247]:

$$|\frac{\Omega}{\Delta_0}| = \frac{\pi c/2}{\ln(8/\pi c)}, \tag{A.1}$$

where c is a dimensionless variable that is inversely proportional to the strength of the impurity potential U via $c = (\pi N_F U)^{-1}$. Here, N_F is the density of states per unit volume at the Fermi energy in the normal state. One can express c in terms of the scattering phase shift, δ_0, as $c = \cot(\delta_0)$, giving $\delta_0 \sim 0.47\pi$. This result is comparable to the phase shift determined for Zn scatterers [98] and unidentified native scatterers, likely missing Cu atoms, [248] in Bi2212 and indicates nearly unitary (i.e. $\pi/2$) potential scattering centers.

The nature of the scattering centers in the Pb doped Bi2212 material shown here could in principle be missing Cu atoms underneath the BiO layer. However, unlike in Ref. [248], the surface atoms where scattering centers are located do not appear to be suppressed due a missing atom underneath. Furthermore, the near absence in the pristine material of such scattering is surprising. As only (very pure) Pb has been introduced into the system, one could imagine that a few Pb atoms have substituted for Cu in the CuO plane, but this is rather unlikely due to the large difference in size and properties of Cu and Pb. It should be noted that the Pb doped system has been grown in air, contrary to the pristine samples that were grown in an oxygen atmosphere. Perhaps this difference in growth environment explains the relatively large number of scattering centers in the Pb doped sample. To determine the exact nature of the scattering centers, more study will have to be performed, for instance by making LDOS images up to large bias voltages (1-2 eV), which has been used by others to detect localised impurities in the blocking layers of Bi2212 [249] or by growing the Pb doped samples in oxygen.

Identical zero bias conductance features to those shown here have been reported on the single layered relative of Bi2212, Bi2201 [250]. As this material has a relative low T_c, it is possible to measure above the superconducting transition temperature without having too much thermal smearing of the tunneling signal. Therefore, the authors were able to track the ZBC pattern as a function of temperature and showed that it remains present in the normal state, signalling that not the superconducting gap, but the pseudogap is responsible, and suggesting an interesting interplay between superconductivity and the pseudogap.

It is worth noting that the energy of the scattering center, Ω, reported for the single layer Bi-based system is very similar to that observed on the bilayered compound shown here. As the gap size in the single layered compound is much smaller, the resulting phase shift δ_0 is smaller than in the bilayered system. Assuming that the impurity causing the scattering in both systems is identical, the effect of this impurity is thus much reduced in the single layer compound. It would be interesting to find such impurities in Pb doped trilayered Bi2223, to determine if this is indeed a trend or merely a coincidence.

A.4 QPI on $Bi_2Sr_2CaCu_2O_{8+\delta}$ and $Pb_xBi_{2-x}Sr_2CaCu_2O_{8+\delta}$

Having shown the surface structure of Bi2212 and (Pb,Bi)2212 and their superconducting gap as a function of position, we now turn our attention to quasi-particle interference scattering as seen with FT-STS measurements on both systems. The first authors to report QPI could resolve several distinct scattering vectors, though not all sixteen inequivalent vectors [127, 251, 252]. In later work, where larger fields of view were used, an increased signal to noise ratio was achieved and intricate data analysis techniques were used to enhance the contrast of the images, all vectors were identified [126]. Figs. A.5b-d show g(r,E), or LDOS, images on a $Bi_2Sr_2CaCu_2O_{8+\delta}$ sample for three different energies taken on the same field of view shown in Fig. A.5a. The constant current image in Fig. A.5a is identical to the one of Fig. A.2, but shown again to enable easy comparison. Clearly, there are periodic structures in the LDOS images, which change as a function of energy.

To quantify the structures in the g(r,E) images, Fig. A.6 shows a series of Fourier transforms of LDOS images at different energies. The Fourier transformed images have been rotated to ease comparison with Fig. A.1. To enhance the contrast of the images, the Fourier transforms have been folded and averaged with respect to the two symmetry lines. As a comparison, the right bottom image of Fig. A.6 shows a raw data Fourier transform of the image directly above it (taken at -20 mV), illustrating that all features are also present in the raw data. Identically dispersing FT-STS images were obtained on the Pb doped compound (not shown).

The exact locations of the scattering vectors in Fourier space are subsequently determined by fitting an exponential decay plus a Lorentzian to the line traces through the intensity spots from the center of the Fourier transform as shown in Fig. A.7a. The result of this analysis is plotted in Fig. A.7b. For energies close to E_F the intensity of the spots becomes very weak and an accurate position cannot be determined. Two scattering vectors, q_4 and q_5, could not be resolved in the Fourier transforms. In the case of q_5, a non-dispersive feature is obscuring the region where the scattering vector is expected to reside. Due to the non-dispersive nature of this feature, it could very well be an artifact of the measurement. An interesting point to note is that in the Fourier transform of the LDOS images recorded here, an up shifted copy of the expected pattern appears (not shown), which could be the source of the non-dispersive feature. One explanation for such a shifted copy could be the presence of two distinct step sizes in the y-scan direction of our instrument. At this point it is not clear where such a difference in step sizes should come from and if this is indeed the cause of the copy. As the LDOS maps described here are currently stretching the limits of the measurement software, which has difficulties in processing the near-maximum amount of pixels possible during the 65 hours of measurement, the artifacts could very well come from software limitations. At the time of writing the software is being adapted to lift these limitations.

Having determined the lengths of the scattering vectors, and assuming a fourfold symmetric Fermi surface as shown in Fig. A.1d, one can plot the loci of scattering in

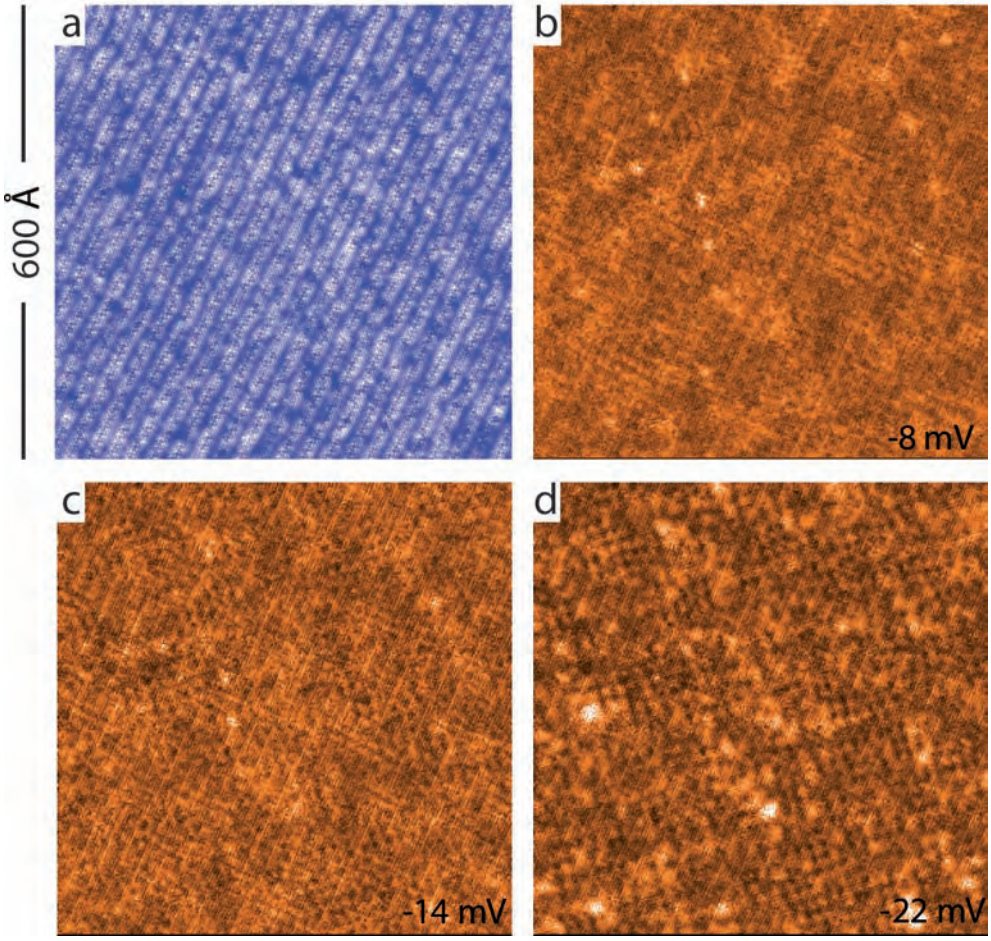

Figure A.5: (a) 600 Å constant current image of Bi2212, taken on the same field of view as Fig. A.2a. (b)-(d) LDOS images taken at -8 mV, -14 mV and -22 mV respectively. The regular patterns in the images are the standing waves corresponding to the scattering vectors shown in Fig. A.1d.

k-space, see Fig. A.7c. In principle only q_1 and q_7 are sufficient to extract k_x and k_y, the others are used to check for consistency. As a comparison, a Fermi surface calculated using a tight binding model[2] is plotted on top of the data points, illustrating the remarkable agreement of the octet model with experiment.

Lastly, using this data, the energy gap $\Delta(k)$ can be estimated. Following the convention in angle resolved photoemission, the gap is plotted as a function of Fermi surface angle, θ_k, which is the angle with $(\pi,0)$-(π,π). Figure A.7d shows the gap for both the occupied (-) and unoccupied (+) density of states. A d-wave fit of the form

[2] $E(k_x, k_y) = dE - 2t(\cos(k_x\pi) + \cos(k_y\pi)) + 4t_1\cos(k_x\pi)\cos(k_y\pi) - 2t_2(\cos(2k_x\pi) + \cos(2k_y\pi)) + \frac{t_p}{4}(\cos(k_x\pi) - \cos(k_y\pi))^2$, using t = 0.4, t_1 = 0.095, t_2 = 0.06, t_p = -0.2 and dE = 0.4

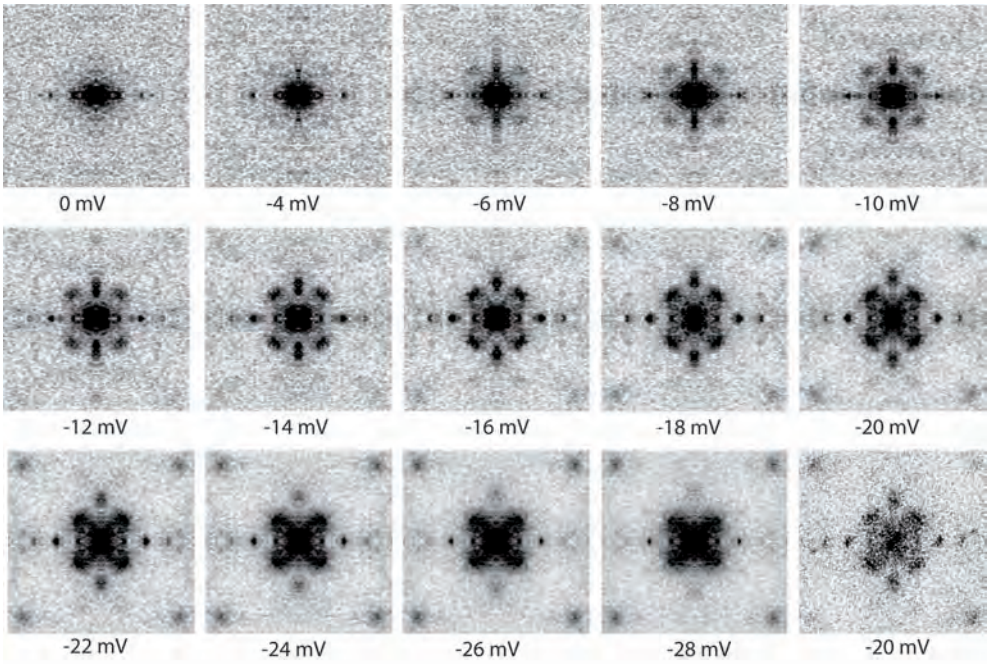

Figure A.6: Fourier transforms of LDOS images taken at the energies indicated underneath the images. All Fourier transforms have been rotated to ease comparison with Fig. A.1 and are folded and averaged with respect to the two high symmetry lines to increase the contrast. The right-bottom image is a raw Fourier transform of the same energy as the image directly above it, illustrating that all features are also present in the raw data.

$\Delta(\theta_k = \Delta_0(A\cos(2\theta_k) + B\cos(6\theta_k))$ is fitted to the data giving Δ_0 = 40 $\pm$ 5 mV, A = 0.82 and B = 0.10. As has been shown in literature [126], these results extracted from Fourier transform STS (FT-STS) are consistent with ARPES measurements on the same system, compounding the strength of STM/S: it is not only a high spatial and energy resolution real space probe, but also a k-space probe of both the occupied and unoccupied states.

From the analysis presented in Fig. A.1 it is also clear that the Pb doping introduced into the system to remove the ~5b superstructure does not affect the electronic structure of the material as seen with STM/S in any way. The Bi2212 and (Pb,Bi)2212 used in this investigation have a nearly identical doping concentration and indeed behave identical in every aspect except the surface appearance. This also supports the validity of the use of the Pb doped materials in ARPES studies where it has the advantage of yielding data that are free of diffraction replicas.

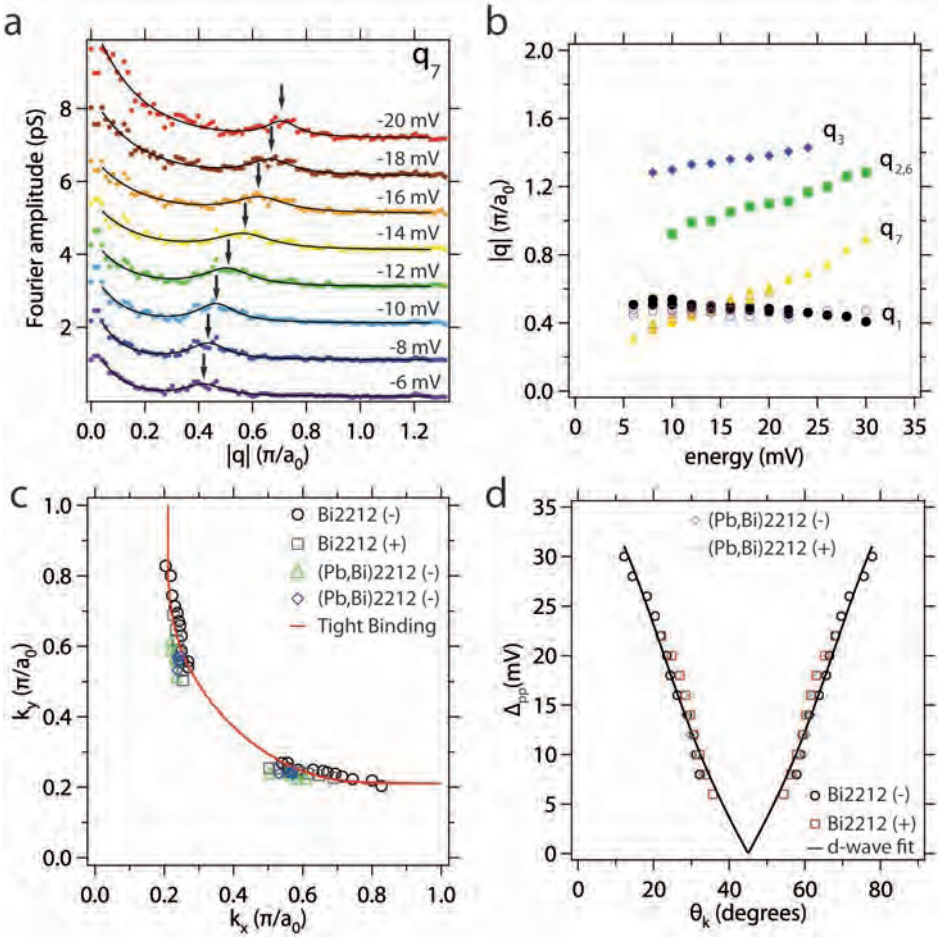

Figure A.7: (a) Energy dependence of the trace through the center of the Fourier transform and scattering vector q_7 taken on Bi2212. The trace is fitted with an exponential plus a Lorentzian to extract the position of the scattering vector. (b) Length of the various scattering vectors seen in the Fourier transforms of the LDOS images, from both positive and negative bias voltage. Closed symbols are from Bi2212, open symbols (Pb,Bi)2212. The Pb doped sample has approximately the same doping concentration as the pristine sample. From the scattering vectors in (b), the loci of scattering can be extracted using the mirror symmetries of the Brillouin zone. A tight binding model Fermi surface is plotted on the data points to show the excellent agreement. (c) Energy gap $\Delta(k)$ as a function of Fermi surface angle θ_k for both occupied and unoccupied density of states. The solid line is a d-wave gap fit, with $\Delta_0 = 40 \pm 5$ mV, A = 0.82 and B = 0.10. Panels (a)-(c) are in excellent agreement with Ref. [126].

A.5 Summary

The possibilities of the Createc scanning tunneling microscope have been investigated on the well studied cuprate superconductors Bi2212 and (Pb,Bi)2212, where

samples with a similar doping/transition temperature were chosen to ease comparison. Aside from high resolution topographic images of both systems, spatially resolved maps of the superconducting gap have been measured which are very similar and are in excellent agreement with the existing literature. On the Pb doped compound, a relatively large number of (near-) zero bias conductance peaks have been observed which are due to (as yet undetermined) near-unitary potential scattering centers. Lastly, LDOS, or g(r, E), maps on both pristine and Pb doped Bi2212 have been measured as were found earlier in other systems which clearly show modulations due to quasi-particle interference scattering. Fourier transforming the g(r, E) images and tracking the loci of the scattering intensities, the Fermi surface and d-wave gap of these two cuprate superconductors have been determined. From the comparison of the two compounds it becomes clear that Pb doping does not affect the properties of the superconductor as seen with STM/S in any way other than removing the ~5b supermodulation. This also strengthens the appropriateness of using Pb doped material for ARPES investigations, where it has the advantage of giving data free of diffraction replicas. Lastly, the measurements presented underline the competitive capabilities of a commercially available system compared to state of the art home build machines.

APPENDIX

B Tip preparation and characterisation

One of the key ingredients in STM/S is the tip. There exists a great wealth of literature on how to make good tips and each group doing STM/S measurements has its own recipe, ranging from buying commercially available tips to intricate schemes using etching techniques and *in situ* treatments. Since considerable time has been spent during this Ph.D. research to find an optimum procedure to produce tips, this appendix will review several techniques adopted. Basically two types of material are used to make tips, tungsten (W) and an alloy of platinum and iridium (Pt/Ir).

B.1 Tungsten tips

B.1.1 Etched W tips

Tungsten is a very tough material which, with 3695 K, has the highest melting point and the highest tensile strength of all pure metals [118]. Tips made from W are therefore very stable over a wide temperature range and might even survive a tip crash. Moreover, the material can be etched into very sharp tips using for instance a harmless NaOH solution. The main drawback is that the material oxidizes rapidly, which requires difficult ex- or *in situ* treatments to remove the oxide layer.

To etch a tungsten tip, a piece of tungsten wire is immersed into a NaOH solution and connected to a voltage supply. A counter electrode is placed in the same solution to enable a current to flow. Figure B.1 shows two ways to immerse the tip into the solution. In Fig. B.1a, the tip is immersed into a beaker so the bottom of the wire is fully in the solution. To prevent disturbance of the meniscus at the tip by bubbles forming at the counter electrode, a glass ring is placed around the wire. Part of the wire in the solution can furthermore be covered by a Teflon tube to prevent an etching reaction taking place there, but this is not essential (see below). Figure B.1b displays a slightly different technique: a platinum ring supports a sheet of NaOH

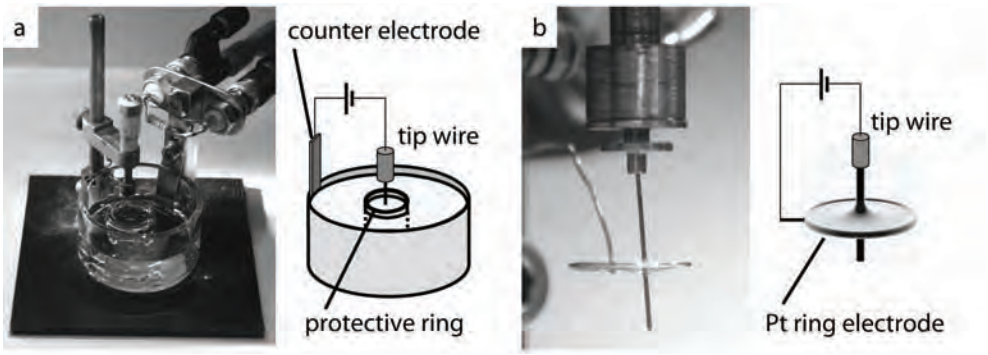

Figure B.1: Two types of etching methods: (a) the bottom part of the tip is completely immersed in the etching solution, or (b) is immersed through a thin film of etching solution suspended from a platinum ring.

solution into which the tungsten wire is stuck. This way, the etching process is very local and requires little NaOH. Since the entire solution can be replaced easily in this case, dust and other impurities in the solution are swiftly removed. A further advantage of this method is the formation of a double meniscus, making the etching process highly symmetric.

The voltage driven reaction used to etch tungsten in simplified form is [253]: $W(s) + 2OH^- + 2H_2O \rightarrow WO_4^{2-} + 3H_2(g)$, where (s) and (g) denote the solid and gas phase of the materials, respectively. Due to the formation of a meniscus when the tip wire is immersed in the etching solution, a concentration gradient of OH^- from the top of the meniscus to the bottom is created. Since the reaction product, WO_4^{2-}, drops downward after creation, a second gradient of OH^- is created. The strongest etching thus takes place at the bottom of the meniscus, where the tungsten wire is formed into an hourglass shape. When the wire gets too thin it will break and two sharp tips are produced. To prevent blunting of the formed tip, the etching reaction should be stopped the moment the wire breaks. This can be done by monitoring the etching current which has a dip when the wires break. An often adopted procedure is to use the tip that drops into the solution instead of the one that is connected to the voltage supply. This is especially useful when using the etching scheme depicted in Fig. B.1b since the tip falls completely out of the etching solution. However, the design of the tip holder used in this work prohibits this options, since the tip wire has to be mounted in the holder before it can be etched.

The time it takes to etch a tip and its shape depend mainly on the concentration of the NaOH solution and the applied voltage. In this study, tungsten wire with a diameter of 0.3 mm, a typical concentrations of 2 mol/l, or 4 g NaOH in 50 mL distilled water, and a DC voltage of 7-10 V has been used, resulting in sharp tips after 10-15 minutes of etching. In general, a lower voltage tends to lead to a slower etching and a tip with a longer taper length. Using an AC voltage instead of a DC

voltage has been tried, but due to the formation of H_2O bubbles at the tip this usually resulted in microscopically irregular tips, increasing the chances on a double tip. See Refs. [253–256] for more details on tip etching schemes.

B.1.2 Oxide removal techniques

The main drawback of using tungsten for STM tips is that a thick oxide layer (WO_3) forms on the surface of the material which prohibits a tunneling current to flow from it. There are several recipes to remove this oxide layer, either just before insertion into the vacuum chamber or *in situ*. One such ex situ treatment is to dip the tip in the highly acidic HF [257]. As can be seen in Fig. B.2a and b, HF dipping effectively removes all unwanted features from the tip apex. However, the acid is rather dangerous and special protection should be used in the process of dipping the tips. Moreover, there is a finite time between the HF dip and the actual insertion into the vacuum chamber, enabling oxide to form again on the tip. Therefore, a more user friendly *in situ* method seems more appropriate.

The simplest *in situ* treatment is to anneal the tip which is mostly done by electron bombardment [258–261]. At approximately 1000 K the WO_3 layer will react with pure tungsten to form WO_2 which will sublimate [262,263]. Due to the high melting point of tungsten, the tip itself will not be affected. Raising the temperature too high might make the tip blunt though.

A slightly different method to remove the oxide layer *in situ*, often in combination with an annealing treatment, is by ion bombardment or self-sputtering [255,259,260, 264,265]. The advantage of the latter is that this technique opens up the possibility of field emission to estimate the sharpness of the tip even before having to place it in the STM (see section B.2). For this reason, only self-sputtering, or electron beam heating, was attempted.

As the name suggests, during electron beam heating a beam of electrons is directed onto the tip. The easiest way to achieve this is by placing a filament through which a current is applied in proximity to the tip and applying a high voltage difference between the filament and the tip. Depending on the sign of this high voltage, either the tip is bombarded with electrons (positive voltage on the tip) or serves as a source of an electron beam (negative voltage on the tip). To this end, a vacuum manipulator was constructed which is pictured in Fig. B.3b. The installation of this fork also required an adaptation to the arm in the load lock itself which is depicted in Fig. B.3a. With the 'glowfork' a tip can be picked up from the load lock arm and slid underneath the filament (made from tungsten). High voltage between the filament and tip can be applied and the filament itself can simultaneously be heated via a direct current. Typically, the filament was made to glow white and a 1000 V difference was applied between the tip and the filament for approximately one minute yielding oxide free tips as can be seen from Fig. B.2d.

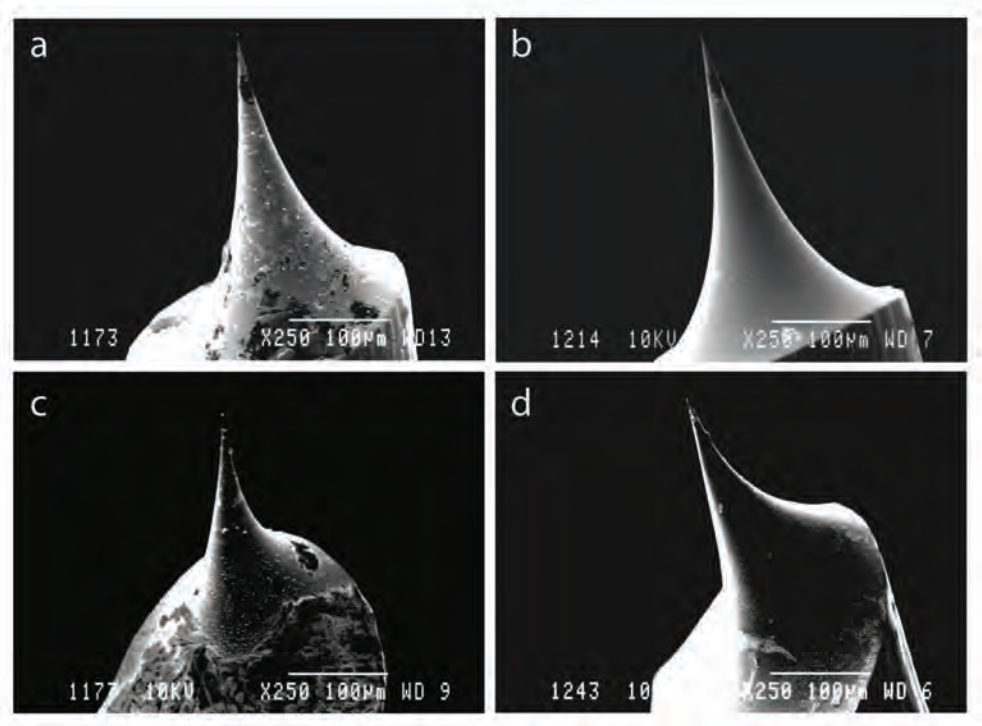

Figure B.2: Scanning Electron Microscope (SEM) images of tips before and after two different oxide removal techniques. Panel (a) and (c) show tungsten tips just after etching. The result of dipping the tip shown in panel (a) in HF is imaged in (b). Panel (d) shows the result of (electron beam) heating the tip shown in panel (c) in vacuum. All contaminations are gone for both techniques.

B.2 Field emission as a test of sharpness

Once the oxide layer of a tungsten tip has been removed using the technique described in the previous section, the same setup (Fig. B.3b) can be used to estimate the sharpness of the tip by field emission. Field emission from bulk metals was theoretically described by Fowler and Nordheim in 1928 [266] and refined the following year [267]. They showed that the current density J flowing from a metal can be described by the following equation:

$$J = \frac{e^3}{2\pi\hbar}\frac{\sqrt{\mu}}{(\Phi+\mu)\sqrt{\Phi}}\mathbf{E}^2 \exp[\frac{8\pi\sqrt{2m}}{3e\hbar}\frac{\Phi^{3/2}}{\mathbf{E}}]. \tag{B.1}$$

where e is the elementary charge, $\hbar$ Planck's constant, Φ the work function of the material, μ the chemical potential, m the mass of the electron and $\mathbf{E}$ the electric field. For actual comparison with experimental values for the current density, correction for Coulomb interaction between electrons should be taken into account [268], which

only introduces a field independent factor into the equation. From Equation (B.1), it

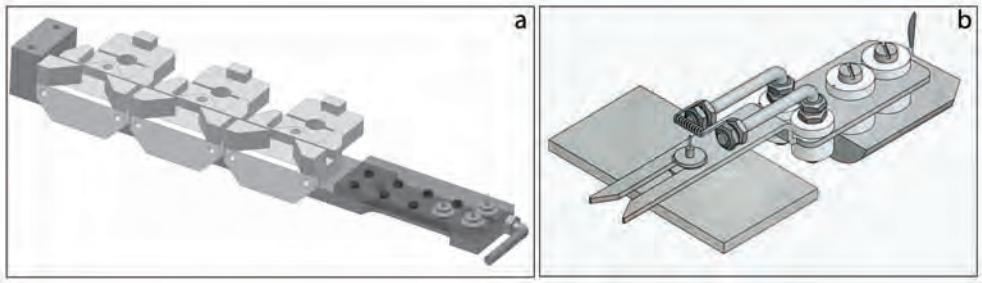

Figure B.3: Designs for load lock manipulators. (a) Main load lock manipulator, with place for three samples and up to ten tips. (b) 'Glowfork' where a tungsten tip can be heated by a filament, bombarded by electrons and used as an electron emitter, all in UHV. Drawings courtesy of R. Manuputy.

readily follows that the stronger the electric field, the higher the current density (and thus a higher tunneling current).

In order make the link to field emission from a tip, the electric field at the tip apex as a function of the applied voltage (V) has to be known. If the tip is assumed to be a simple sphere, the field at the edge of the sphere and thus at the tip apex is given by $\mathbf{E} = V/R$, where R is the radius of the tip apex. To correct for the fact that the tip is not a perfect sphere, but more like a sphere on a cone, a correction factor k is introduced, $\mathbf{E} = V/kR$. Immediately one sees that a smaller tip radius leads to a larger electric field, which from Equation (B.1) means a larger current density. Using the design of Fig. B.3b, upon applying a negative voltage to the tip, a current will flow to the earthed filament. The voltage required to establish a certain tunneling current is directly linked to the radius of the tip apex. In this work, tips which gave a tunneling current of 10 nA at less than 800 V were considered sharp enough to be used in the STM.

The implementation of the 'glowfork' manipulator therefore enables the removal of oxide from the freshly etched tungsten tips and can give an indication of the radius of the tip apex. The tips that passed the field emission test were characterised on an Au(788) sample (see section B.4) and resulted most of the time in sharp tips which gave proper tunneling spectroscopy. Due to an adaptation to the design of the tool that is used to place tips in the STM[1] the time to replace a tip in the STM is less than 15 minutes, making a more detailed knowledge of the tip apex less relevant. Therefore, even more sophisticated techniques to estimate the tip sharpness than the quick test described above have not been attempted. See Ref. [256] and references

[1]Originally the tip transfer tool was like that shown in Fig. B.3b, in which case the sample in the STM underneath the tip had to be removed in order to get the tip far enough from the magnet holding it to be taken out of the STM. A hook-like adaptation resolved this by no longer having to move the tip down, but simply pull it out of the magnetic field.

therein for more details on more intricate sharpness tests and other treatments of etched tungsten tip and their effect.

B.3 Platinum Iridium tips

B.3.1 Mechanically cut Pt/Ir tips

Although tungsten tips can be made very sharp using etching techniques, the formation of an oxide layer on the tip poses considerable problems, and the process becomes therefore rather time consuming. The toughness of a tungsten tip ensures that it will not change easily over a wide temperature range. However, this can also be considered a drawback, since a tip cannot be conditioned easily on an Au(788) sample to meet the requirements (see section B.4). Therefore Pt/Ir (in a ratio of 80%/20%) is often used to make STM/S tips. Pt/Ir does not easily form an oxide layer, so once the tip has been made, it can be used immediately without further treatments. Since Pt/Ir is much softer than tungsten, it is much more easily conditioned on an Au(788) sample. Au also tends to stick much better to Pt/Ir than to W, making Pt/Ir a much more user friendly material. Lastly, due to the softness of Pt/Ir, a simple wirecutter can be used to make a tip. If the cutting is combined by a pulling motion, the tip more or less flows out into a sharp protrusion. Although such a cut tip is rather blunt by eye compared to etched tungsten tips, a single microscopic protrusion is sufficient for tunneling experiments. The only drawback of tips produced this way is that there are likely to be several of such protrusions in close vicinity to each other, i.e. double or triple tips, obscuring proper tunneling experiments. As demonstrated in Ref. [269], a few seconds at 12 V AC in a solution of $CaCl_2 \cdot 2H_2O$ (35 g), de-ionised water (200 ml), and acetone (10 ml) is sufficient to remove most of these protrusions obtained by mechanically cutting Pt/Ir tips. However, the main tip might be somewhat blunted after etching as well. Often, but unfortunately not always, the multiple tips can also be reduced to a single tip on an Au(788) sample.

B.3.2 Etched Pt/Ir tips

A more foolproof method than cutting would be to etch the Pt/Ir like is done with W tips. There are several techniques to etch a Pt/Ir wire, either using highly toxic cyanides [270–272], or molten salt etchants [273], both of which are not attractive alternatives to etching and cleaning W tips. However, there are several reports of successful etching strategies using a rather harmless solution of $CaCl_2 \cdot 2H_2O$ [274–279] using an AC current and a graphite ring as counter electrode. Although little time has been spent etching Pt/Ir tips in this project, a few tips have been produced using a simple drop-off etching technique as has been described above for the etching of W tips. The thick black oxide layer which is a product of the etching can be easily removed before the final drop-off using tweezers, leaving a relatively sharp and clean tip which in principle can be used without further processing in the STM. However, often upon drop-off a spark occurs between the two parts of the etched

wire, melting the tip apex into a metal droplet. In such cases, and in general for blunt or already used tips, multiple step processes can still lead to a further sharpening [274,276,278,279]. Fig. B.4 shows a typical etched Pt/Ir tip for two magnifications. As can be seen, the tips are much more cone-shaped than the W etched tips, but have a much larger tip apex radius of curvature.

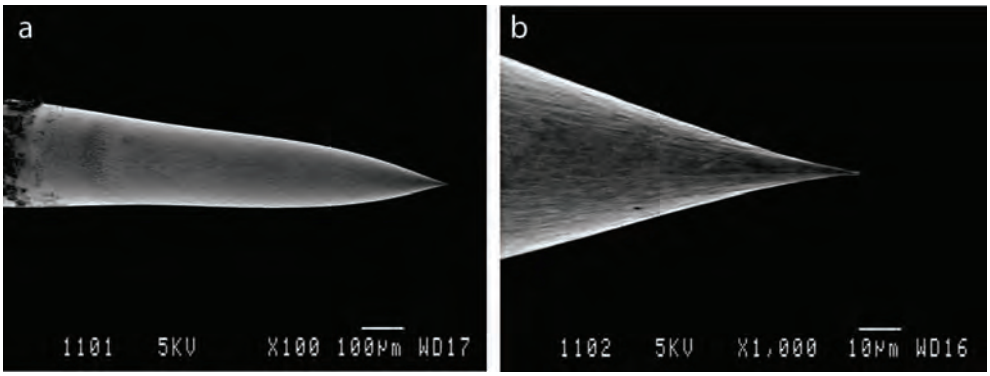

Figure B.4: Etched Pt/Ir tip at two different magnifications, indicated at the bottom of the images.

The main advantage of etching Pt/Ir tips with respect to mechanically cutting the tip is a reduced chance of having multiple protrusions, and the more symmetric shape of the tip could be advantageous in terms of stability and handling in the STM. However, etching is more time consuming, and if the AC current is not switched off directly upon drop-off, the tip will become blunt. Furthermore, as in the case of etched W tips, a thick oxide layer is formed as a result of the etching process and will have to be removed.

Whether Pt/Ir tips are cut or etched, they are a good alternative to time-consuming and oxidizing W tips. Which type of tip is used is mostly a user dependent choice: Pt/Ir tips are easy to make, but are less stable once properly characterised on for instance an Au(788) single crystal due to their softness; W tips are time consuming to produce and difficult to adjust to meet demands *in situ*, but very stable once properly characterised. Throughout this work, both types of tip have been used giving identical results.

B.4 Characterisation and conditioning of tips on an Au(788) surface

Once a tip has been either etched or cut, inserted into the UHV system and, if required, treated to remove oxides, it has to be characterised on a known surface before an actual measurement is performed on an unknown material. For this purpose, an Au(788) sample is used for two reasons. The first is that Au as a metal has a flat

density of states near the Fermi energy and is therefore ideally suited to test the density of states of the tip. As described in section 2.1.1, the actual tunneling current is a convolution of the density of states of the tip and the sample. In order to discard the contribution of the tip density of states, it should be constant in the energy range used during measurements. Since Au has a constant density of states, I(V) spectra between the tip and an Au(788) sample should be linear as a function of energy for a tip to be suitable for further measurements.

The second reason to use an Au(788) sample to characterise the tips is that is has steps at the surface of a regular height and with a fairly regular step width. Therefore, the piezos (especially the z-piezo) can be calibrated on a regular basis. Figure B.5 shows a schematic view of an Au(788) sample, two constant current images, a very corrugated and a typical image, and a typical I(V) and dI/dV curve. Since atomic resolution on Au(788) is not a regular occurrence due to delocalisation of the electrons, see section 2.1.1, it was not deemed essential for a proper tip. If the step edges are sharp, and the I(V) spectrum is linear as a function of applied voltage, the tip is considered suitable for further studies.

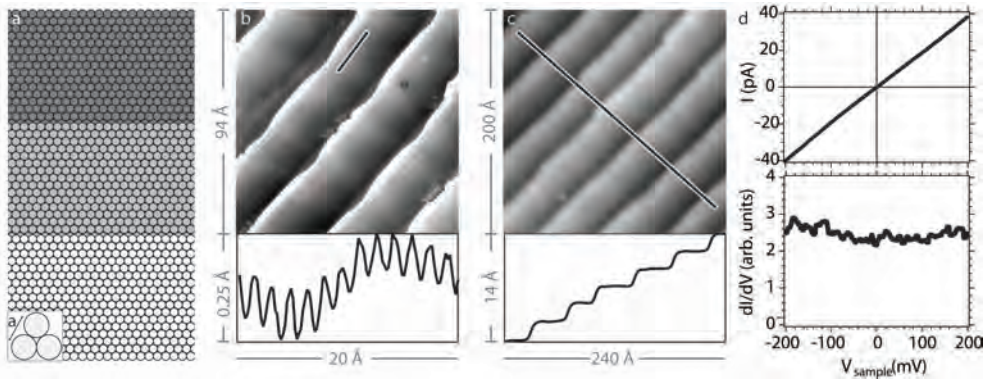

Figure B.5: (a) Schematic representation of the unreconstructed Au(788) surface, after [22]. The atoms are close packed hexagonally ordered with an inter atomic distance of 2.88 Å (see inset), leading to a step height of 2.35 Å. (b) STM topograph of exceptional atomic resolution on Au(788). The atomic corrugation can clearly be seen from the line scan shown below the image, which is taken along the line indicated in the image. (c) Typical constant current image on the same Au(788) crystal as was used for (b), without atomic corrugation, but with sharp step edges. (d) Tunneling I(V) spectrum (top) and its derivative (bottom) taken on (c) displaying a simple Ohmic behaviour as is required for the tip density of states.

Often, either the topography is very sharp or the spectroscopy gives a linear response, but not both. Several tricks can be used to get both to meet demands. One frequently used procedure reported in literature is to purposely crash the tip into the Au sample in order to coat the tip apex with Au atoms, see for instance Ref. [280] and references therein. This method was not opted for, since there is a big chance the tip gets damaged beyond 'repair'. Another reported technique is to apply a high volt-

age to the sample with a high current setpoint in order to create a large electric field between the tip and the sample, which will also result in the coating of the tip apex with Au atoms, see for example [133, 135, 153]. Since this field emission technique is a non-contact way to coat the tip, it has been applied throughout this research. The higher the voltage, the bigger the chance to coat the tip properly. The drawback is that too high voltages could blunt the tip, for instance because a large piece of the tip breaks off due to the electric force on it. In practice, voltages higher than 150 V were rarely used and usually $<$50 V was enough to modify the tip apex to meet demands. If the feedback loop is set rather high, it will start to resonate as a response to its own response, which leads to the tip oscillating near the sample at a high frequency, which often assisted the Au atoms in coating the tip in a relatively controlled way.

Of the tips inserted into the STM head after an initial selection with the optical microscope, and for tungsten tips a second selection using the field emission results, more than 70% of the tips were deemed suitable for further studies after characterisation on the Au(788) sample.

APPENDIX

C Temperature calibration measurements

Before conclusions can be drawn from temperature dependent measurements such as the ones presented in chapters 6 and 9, the temperature of the sample in the STM should be calibrated. In the first section of this appendix, the sample temperature will be discussed which was measured with a thermometer mounted on a sample holder and inserted into the STM. The response of the sample temperature to a heater mounted on the base of the STM is shown. In the second section, the settings of the PID temperature controller are briefly discussed. In the third section, the effective temperature during a measurement at various sample temperatures is discussed using temperature dependent measurements of the superconducting gap of the BCS superconductor niobium. The last section briefly discusses the temperature dependence of the piezo constants.

C.1 Sample temperature

As has been shown in chapter 2, Fig. 2.3, the STM head is equipped with a silicon diode thermometer and a diode heater to regulate the temperature. Even though the sample holder and sample are thermally connected to the main STM block where the two diodes are fixed to, they could in principle still have a differing temperature due to radiative heating through one of the viewports directed at the sample area. In order to determine if the sample temperature deviates from the temperature measured by the thermometer on the STM block, a thermometer has been mounted on a sample holder and placed in the STM. For a given set temperature (of the STM block), the temperature of the sample was monitored. At the base temperature of 4.6 K, both the STM block and sample gave identical readings.

Upon increasing the temperature by heating, or decreasing by pumping on the He cryostat, both the sample and STM block require a certain amount of time to come to a new equilibrium. An example of such an exponential reaction to the equi-

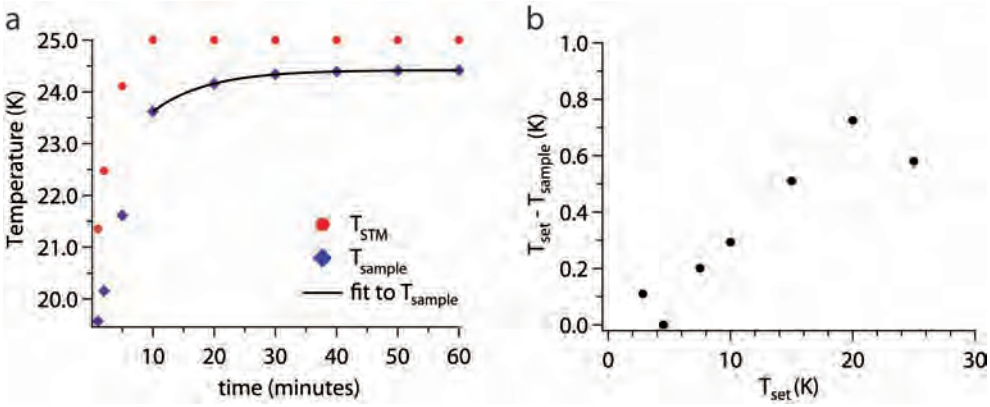

Figure C.1: (a) Relaxation of the sample- and STM block temperature as a function of time after a change in temperature from 20 K to 25 K. The sample temperature is fitted with an exponential of the form $y = y_0 + \exp(-x/\tau)$, where τ ~9 seconds. In the fit, only data points are considered from the moment the STM block has reached its equilibrium temperature. The higher the difference between initial and final temperature and the higher the absolute final temperature, the higher the relaxation time τ. (b) Difference between the sample- and STM block equilibrium temperature as a function of temperature. For temperatures up to 300 K the difference is always less than a few Kelvin.

librium temperature is shown in Fig. C.1a. In this instance, the sample was held at a constant temperature of 20 K before the heater was set to 25 K. As can be seen, the STM block temperature reaches the set temperature very rapidly, due to a proper setting of the PID controller (see section C.2). As there are several mechanical interfaces between the sample and the block that contains the heater and temperature sensor, the relaxation of the sample temperature is somewhat slower. A fit to the sample temperature from the moment where the STM block has reached its equilibrium temperature (solid line in Fig. C.1a) gives a decay constant of approximately 9 minutes. For any temperature step, the decay constant is on this order of magnitude, although it increases for increasing absolute temperature and temperature difference between original and final temperature. In any case, after approximately half an hour, the system is more or less in its new equilibrium and tunneling contact can be established again [1].

The difference in temperature between the set temperature (i.e. STM block temperature) and sample temperature for various set temperatures is shown in Fig. C.1b. In the temperature range used in chapter 6, the deviation is always less than 0.8 K, ensuring that the conclusions drawn from the temperature dependence are valid. For temperatures up to 300 K, the difference has been checked to be less than a few K.

[1] due to the temperature dependence of the piezos, it is not safe to remain in tunneling contact during heating as the tip-sample distance will change as a function of temperature

C.2 PID settings

The *Neocera LTC-21* temperature controller used to regulate the temperature of the STM uses a PID algorithm to stabilise the temperature. This algorithm adjusts the heater settings using three parameters: (i) the **P**roportionality term, which is proportional to the difference between the actual and set temperature (ΔT) times a constant P, (ii) the **I**ntegral term, which is proportional to the time integral over the temperature difference over a time I (i.e. $\int_0^I \Delta T dt$) and (iii) the **D**erivative term, which is proportional to the time derivative of the temperature difference ($\frac{dT}{dt}$) times a constant D. Using the Ziegler-Nichols tuning method [281], the optimal settings for this temperature controller and STM were found to be P = 100000, I = 9 sec. and D = 2.25 sec.

C.3 Temperature dependence of a Niobium superconductor

Having established that the sample temperature is nearly identical to the set temperature, the question remains what the effective temperature is of the STM, and how broadening due to experimental noise affects the spectra. The main motivation for this investigation, aside from a general characterisation of the system, is that the gaps seen on the '122' pnictides always have a rather shallow gap minimum. This apparent filling of the gap could be intrinsic to the '122' pnictides, for instance due to large scattering effects or a non-superconducting band at the Fermi level. However, it could also be an experimental issue, where the spectra are smeared by either an effective temperature that is different from the sample temperature or a large experimental broadening factor Γ which could furthermore be temperature dependent.

An ideal system to do characterisation measurements on is the BCS superconductor niobium (Nb), which has the largest transition temperature of all pure elements - T_c = 9.2 K for very pure Nb - well above the STM base temperature. The gap size Δ has been shown to be 1.52 mV [282], similar to the smallest gaps reported in literature on the pnictide superconductors [283]. Therefore, detection of the Nb gap would show that if gaps of such size would be present in the materials studied, they would have been picked up. Furthermore, by fitting the s-wave gap of Nb (if detected) with the BCS equation for the density of states, i.e. Equation (3.4), the effective temperature and broadening can be extracted as a function of sample temperature.

As there was no Nb single crystal available at the time, a Nb tip was used to measure the Au(788) characterisation sample, which should give identical results. Fig. C.2a shows the tunneling spectrum thus obtained at a measurement temperature of 5 K. From the BCS fit, the superconducting gap was found to be Δ = 1.47 mV, with an effective temperature of T = 7.1 K, and a broadening of Γ = 0.17 mV. Although the spectra are thus slightly more broadened due to an effective temperature that is larger than the sample temperature, the experimental broadening is rather small and the resolution overall is rather good. The slightly lower value for the superconducting gap is not unusual (see for instance Ref. [153]), but not well understood. The

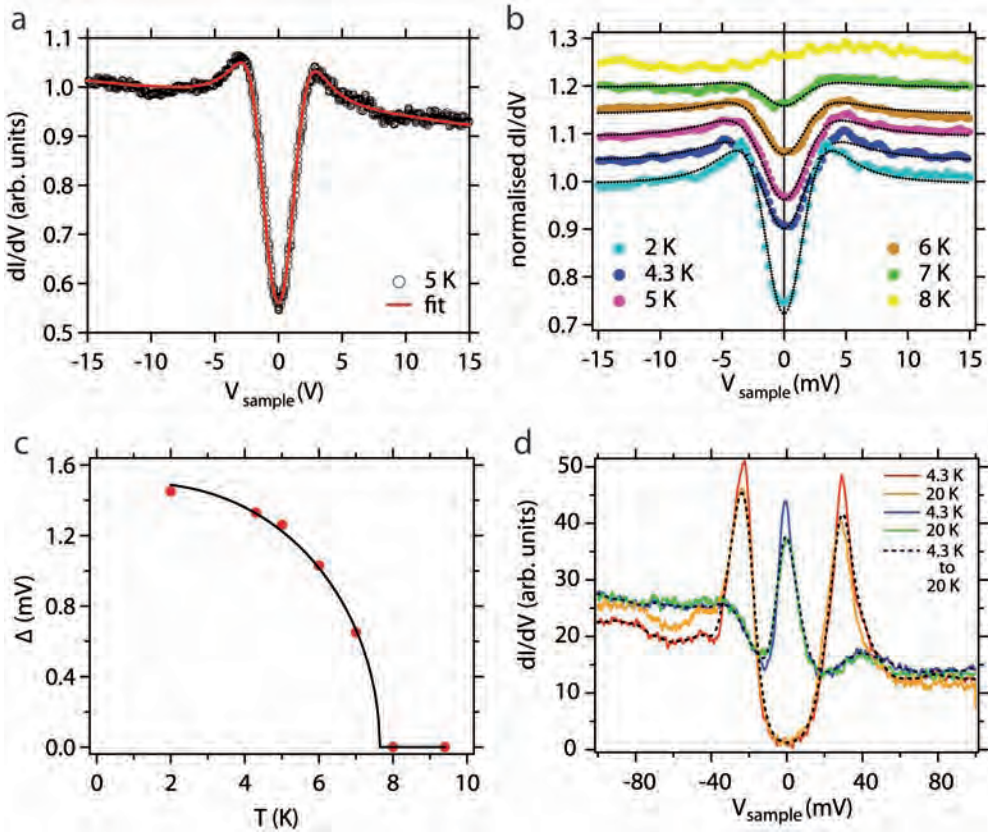

Figure C.2: (a) Tunneling spectrum of a Nb tip on an Au(788) sample taken at 5 K, with Δ = 1.47 mV, Γ = 0.17 mV and T = 7.1 K from the fit. (b) Temperature dependence of a tunneling spectrum taken with a Pt/Ir tip on a polycrystalline Nb sample. The spectra are normalised to a spectrum taken at 9 K, the lines are BCS fits to the experimental data, giving Γ = 0.02 mV for all spectra, T = 13 K for the 2 K spectrum and T = 17 K for all other spectra. The extracted gap sizes are plotted in (c) and are in excellent agreement with BCS theory (solid line), giving Δ_0 = 1.50 mV. (d) Spectra taken on (Pb,Bi)2212, both gapped (red = 4.3 K, orange = 20 K) and peaked around zero bias (blue = 4.3 K, green = 20 K). Thermally broadening the spectra taken at 4.3 K to 20 K (black dashed lines) matches the high temperature spectra perfectly. As the gap itself is nearly constant over this temperature range (T_c = 90 K), experimental thermal broadening alone can account for the difference between the temperatures.

measurement shown in Fig. C.2a has been performed using the 'old' z-piezo, where a single magnet is used to attach the tip to the piezo (see section 2.1.3 for details).

During the coarse of the research, the z-piezo that holds the tip has been replaced, and in the new design of the z-piezo, the electric contact to the tip has also been changed from a ring-electrode contacting the entire tip, to three point-like contacts. While indeed reducing the magnetic field at the sample position, the new holder

turned out to have much poorer thermal contact to the piezo. This fact went undetected for approximately a year and only at the end of this Ph.D. research it was decided to characterise the STM once again on a Nb superconductor.

This time, it proved impossible to see a gap using a Nb tip on the Au(788) sample. Therefore, a finely polished polycrystalline piece of Nb was repeatedly sputtered with Ne and annealed to ~800 K in vacuum before insertion into the STM underneath a regular Pt/Ir tip. In this configuration the tunneling spectra did show the typical signature of a superconducting gap, and its temperature dependence was investigated. Spectra taken at various temperatures on the same position, normalised to the spectrum taken at 9 K, are shown in Fig. C.2b. Note that the spectrum taken at the lowest temperature (i.e. 2 K) is achieved by pumping on the Helium cryostat from which the STM is suspended by springs. This not only cools the STM itself but also the inner radiation shield, and therefore reduces the radiative heating on the STM itself.

The superconducting gap extracted by fitting the spectra is plotted as a function of temperature in Fig. C.2c and shows excellent agreement with the behaviour predicted from BCS theory given in Eqn. (3.2) (shown in Fig. C.2c as a solid line), from which follows that Δ_0 = 1.50 and T_c = 7.6 K. From the fits it follows that the experimental broadening, Γ, for all temperatures is on the order of 0.02 mV, which is an improvement with respect to the 'old' z-piezo. The effective temperature on the other hand is for all temperatures, except the lowest, as high as 17 K. The spectrum taken at 2 K has an effective temperature of 13 K. The only possible explanation is that the tip is at a much higher temperature than the sample: it is well above the transition temperature of Nb explaining the inability to see a gap with a Nb tip, and causes significant broadening of the spectra. It must be noted that the pnictides have also been measured with the 'old' z-piezo, also resulting in rather broad spectra, indicating thermal broadening due to a warm tip is not the only factor playing a role. Notwithstanding, the large effective temperature of the current z-piezo is clearly affecting the spectra.

The main reason why the tip is warmer than in the old configuration is probably the poor thermal contact to the tip (by three point-like contacts instead of a ring). As the cooling power is therefore reduced, radiative heating through the view-ports directed at the tip effectively warms the tip up. To counter this effect so as to ensure the tip is at the same temperature as the sample, gold plated window shutters (as radiation shields) are currently in the process of being installed, which in the near future will hopefully lower the effective temperature of the system and increase the resolution.

In closing this discussion, it should be mentioned that the fact that gaps on the order of 1 mV were observed, shows with the current status of the machine, detection of very small gaps is possible. Also, from a temperature dependent measurement on (Pb,Bi)2212 shown in Fig. C.2d, a 86 K superconductor, it can be seen that there is no broadening of the spectra other than thermal broadening as a function of temperature, i.e. the experimental broadening Γ is not temperature dependent. All of these

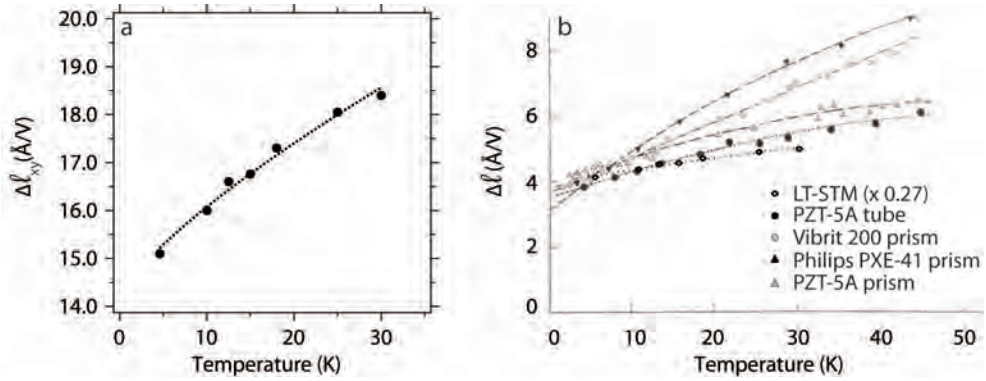

Figure C.3: (a) Piezo constants in the xy plane as determined from measurements of atomically resolved surfaces at different temperatures. The dashed line is a fit using Eqn. C.1, whereby n has been fixed to 0.75. (b) Temperature dependence of four different piezoelectric materials taken from Ref. [284]. The coefficient n of both PZT samples has been determined to be 0.75. The data points of panel (a) scaled by a factor 0.27 to compensate for a difference in piezo length are plotted on top of the figure for comparison.

findings strongly support that if there would be a pseudogap in the pnictides, the temperature dependent study described in chapter 5 would have detected it, even though the effective experimental temperature was higher due to the sub-optimal cooling of the tip.

C.4 Piezo constants

Exact determination of the piezo constants is essential for proper analysis of the topographic data. Before each measurement, the z-piezo constant is checked on the stepped Au(788) calibration sample. As atoms are difficult to detect on an Au surface, other samples have been used to calibrate the x- and y piezo constants, namely highly oriented pyrolytic graphite (HOPG) and well studied systems such as Bi2212 and (Pb,Bi)2212 (see appendix A). Approximately twice a year the piezo constants were checked using one of these samples and were not seen to vary throughout this research even though piezoelectric crystals are known to age. The x- and y piezo constants at base temperature (4.2 K) are 15.1 Å per Volt, while the z-piezo constant is 7.5 Å per Volt. Increasing the temperature of a piezo increases its piezoelectric response, meaning that the piezo constant increases as a function of temperature. By measuring the size of a particular field of view at base temperature, and comparing this to the same field of view at elevated temperatures, the x- and y piezo constants were determined for various temperatures. Fig. C.3a plots these values versus temperature.

According to Ref. [284], the temperature dependence of the deformation of a

piezoelectric material can be described by:

$$\frac{\Delta\ell}{\ell_0} = \alpha(0) + cT^n + \beta\ln(t), \tag{C.1}$$

where $\Delta\ell$ and ℓ are the length deformation and undeformed total length respectively, T is the temperature and t is the time. As the slow relaxation given by βln(t) is small at low temperatures this term can be omitted. The dashed line in Fig. C.3a is a fit of the data points with Eqn. C.1, whereby n has been fixed to 0.75, giving $\alpha(0)$ = 14.1 Å/V and c = 0.35 Å/V. These values are similar to those obtained in a temperature dependent study on various piezo electric materials that includes two piezos from the family of materials used in this study, lead zirconate titanate (PZT) [2] [284]. The summary plot from Ref. [284] is shown in Fig. C.3b for comparison.

Using the parameters from the fit, and assuming the piezo constants have not changed considerably since the last calibration, a good guess of the piezo constants at any given temperature below 40 K can be calculated.

[2] The piezos used in this study are PCC255 by PI Ceramics

APPENDIX

D Noise reduction

The limiting factor in an STM setup is the noise, which is caused by a combination of electromagnetic and vibrational noise present at the location of the setup. In the this appendix these different types of noise will be discussed, as well as how to reduce them and their impact on the data.

D.1 Electromagnetic noise

Tunneling currents in STM/S experiments are typically on the order of a few tens to hundreds of pico-Ampères. To detect such small currents with an acceptable signal to noise ratio, electromagnetic shielding is essential. Two main contributions to electromagnetic noise in the tunneling signal can be distinguished:

i. noise in the power supply of the system (most predominantly 50 Hz in Europe)

ii. noise induced in the cabling due to external electric and magnetic fields

To reduce (i), it is important to power the measurement equipment from a single point and to disconnect all non-essential elements. The main power supply can also be galvanically isolated from the grid by using an isolation transformer. The advantage of a galvanically isolated main power supply is to break any ground loops, which are very effective in picking up noise due to external fields. If a balanced isolation transformer is used, everything but the pure AC power sine wave will be canceled. Ground loops in the system setup can moreover be prevented by using a star topology for the ground circuit. Single or double shielded coaxial cables should be used to reduce noise due to (ii) and all contacts, either BNC connections or soldered, should be robust.

Even though applying these basic system design rules to the setup is a good start, there might still be considerable noise due to unforseen/unpredictable factors. The

various hardware consoles essential for the experiment, for instance temperature control unit, ion pump power supply etc., all produce their own fields which can be picked up by neighbouring consoles and thereby introduce noise. Since shielding each console from the others is difficult, changing the configuration of the consoles within a rack can make a considerable difference. Achieving the optimal configuration mostly boils down to trial and error.

Lastly, many consoles, for instance ion pump power supplies, use rectifiers to transform the AC signal from the main power supply to a DC signal. In such rectifier circuits, usually one of the two poles is internally connected to ground, leading to an asymmetry between the poles. Since European power plugs are completely symmetric, there is a 50% chance of introducing a ground loop by plugging the console the wrong way around, leading to noise (the same effect can also lead to hum in radios). Fortunately this type of noise is easily detected and removed by monitoring the noise as a function of plug orientation.

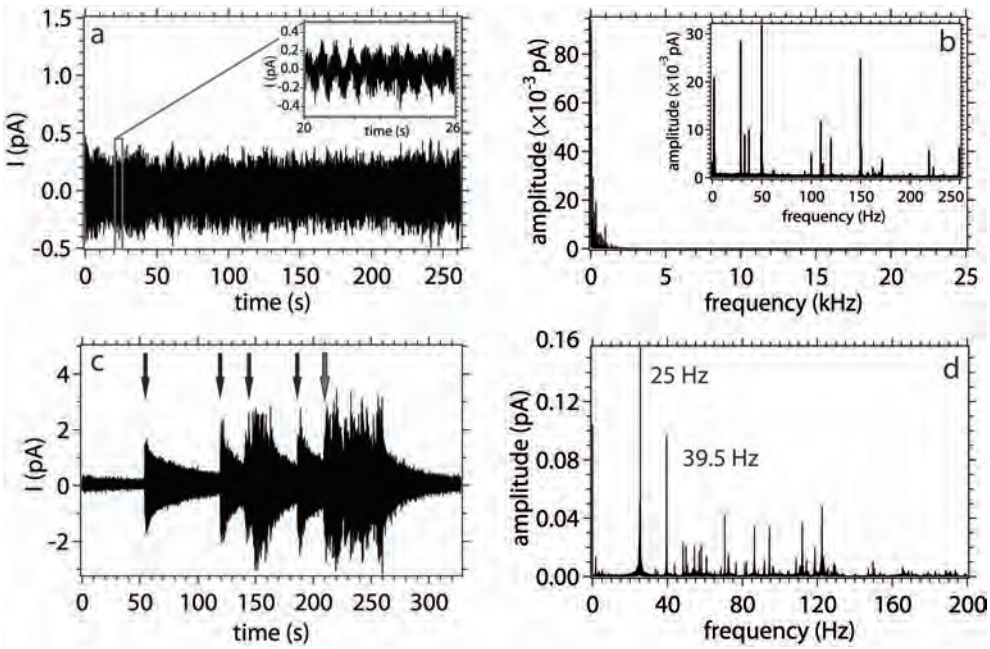

Figure D.1: Noise analysis while out of tunneling contact: (a) current spectrum over time, with in the inset a zoom of 6 seconds. The Fourier transform of (a) is shown in (b) from which the frequencies of the main noise contributions can be extracted. A combination of vibrations (mainly < 50 Hz) and electromagnetic noise is picked up. (c) and (d) are identical measurements to (a) and (b), but taken during construction work on a nearby building. The arrows indicate instances where a large drilling machine was slightly moved at the construction site, at least 100 meter from the STM lab. The rightmost arrow is the point where drilling into the ground commenced.

D.2 Vibrational noise

Since the STM setup is not suspended from air in a sound proof room, vibrational noise will always be present. For instance the floor, the air conditioning and ventilation system can all transmit vibrations to the STM setup. To reduce the incoming vibrational noise, the entire system used throughout this research has been placed on *Newport I-2000* nitrogen gas pressurised dampening legs. Although these legs are effectively dampening vibrations beyond 2 Hz, they unfortunately marginally amplify vibrations with a frequency less than 2 Hz. At the time of writing, active dampening solutions, which use piezos to detect and subsequently counter vibrations, are being investigated in order to remove these low frequency vibrations as well. In the Createc design, a further mechanical decoupling is effected by suspending the STM head itself from springs above an eddy current dampener in the vacuum chamber. Even more improvements could be made by for instance placing the entire setup in a sound proof room, which in turn can be placed on dampening legs etc..

Given a finite vibrational excitation of the system from the outside world, the system itself will absorb primarily excitations of a frequency which are an eigenfrequency of the system. Of these eigenfrequencies, the most important in the system used here are the following:

i. STM head suspended from three long springs

ii. entire system on vibrational dampeners

iii. pendulum motion of the inner cryostat

iv. liquid nitrogen cryostat.

The frequencies of these four different vibrations are estimated by *Createc GmbH.* to be 2.5 Hz, 2 Hz, 2-3 Hz and 44 Hz, respectively. Changing to an active vibration dampening is in this case therefore even more advisable since the main eigenfrequencies of the system are dampened less effectively by the passive pressurised dampening legs.

To analyse which kind of noise is contributing to the tunneling signal in what proportion, one has to read out the tunneling signal for a certain period of time. This can be done while in- or out of tunneling contact with a sample. As there is no closed current loop in the out-of-contact situation, mainly noise induced by vibrations of the cables in and to the setup will be picked up. This type of measurement therefore serves only as an indication of the noise level of the system, merely to determine whether it is advisable to try to get into tunneling contact with a sample or not. If the out-of-contact noise is already too high, the in-contact noise will likely not be better and the tip might be damaged. A typical example of a good out-of-contact I(t) measurement is shown in Fig. D.1a. From the height and positions of the peaks in the Fourier transform of this signal, shown in Fig. D.1b, one can immediately see

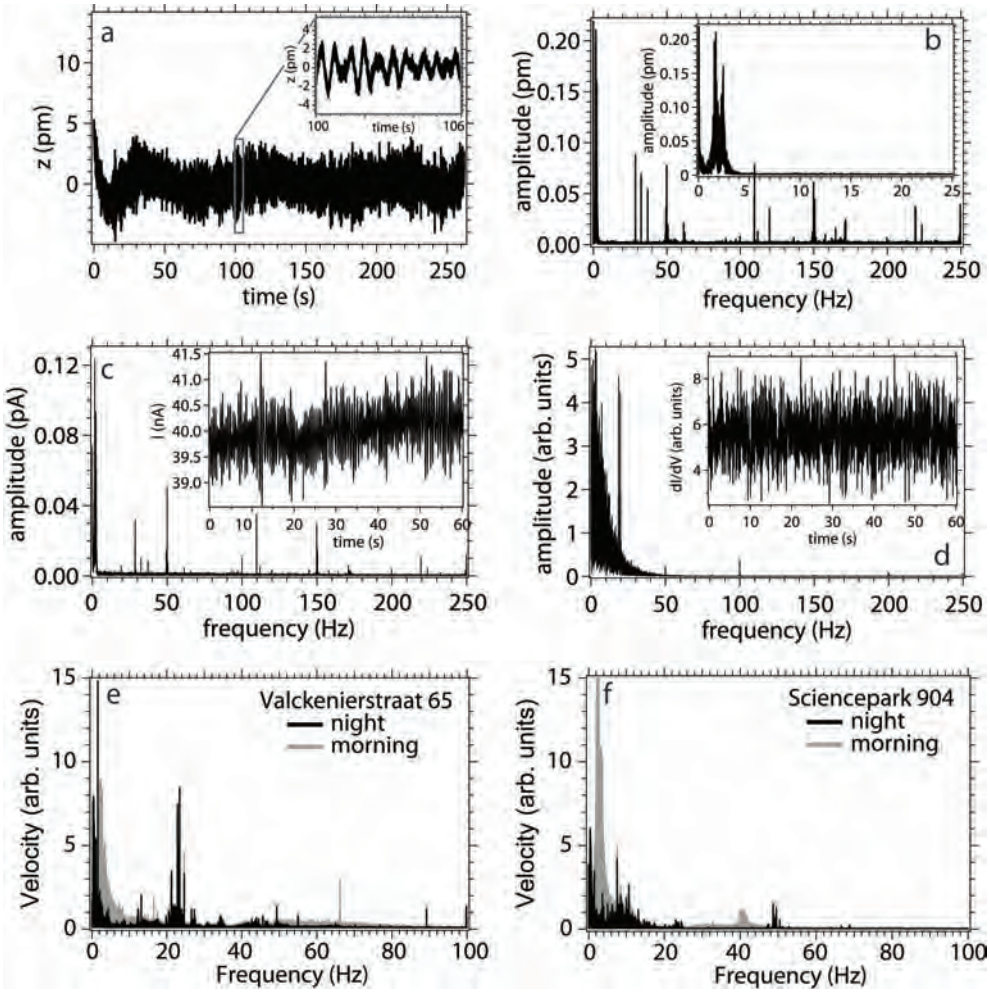

Figure D.2: Noise analysis while in tunneling contact: (a) height spectrum over time, with in the inset a zoom of 6 seconds. The Fourier transform of (a) is shown in (b) from which the frequencies of the main noise contributions can be extracted. As the feedback loop is turned on, the height variations are a response to both vibrational noise as well as electro-magnetic noise in the tunneling current. Current (c) and differential conductance (d) signal over time measured with the feedback loop off. In this mode tunneling spectra shown throughout this work are acquired. Mainly low frequency, vibrational noise is picked up. Panels (e) and (f) show the Fourier transform of vibration measurements performed at the location of the lab where the presented research has been performed and at the new location, respectively.

if the noise is electronic (mainly 50 Hz) or vibrational (usually large low frequency noise) in nature and decide to try to do something about it [1].

[1] the absolute value of all Fourier transforms shown is defined such that the peak of the Fourier trans-

A striking example of a bad out-of-contact signal and a demonstration of the sensitivity of the setup and the effectiveness of the dampening system can be seen in the time spectrum and corresponding Fourier transform of Fig. D.1c and d. During the last half year of the research described in this thesis, construction work began on a nearby building, approximately 100 meters from the STM lab. At a certain point holes were drilled and filled with concrete to support the building. The arrows in the Figure indicate the moment the drill was moved slightly to get into drilling position. The drilling eventually commenced at the last arrow. As this example clearly illustrates, the best time to do measurements is at night and during the weekend, also without construction work nearby as a passing truck can have similar effects. Most of the measurements presented throughout this thesis were done outside working hours for this reason.

The most important noise measurement is obviously in tunneling contact and consists of two parts, the height signal with the feedback loop on and the tunneling current with the feedback loop off as a function of time. The first gives the vertical resolution of the STM, while the latter is an indication of the energy resolution of the system. Fig. D.2a and b show the variation in height as a function of time and its Fourier transform, respectively. The main contribution is from a low frequency vibration, ~ 1.5 Hz, which is clearly visible in the blowup in the inset to Fig. D.2a and limits the vertical resolution to a few picometer. The variations in the tunneling current (Fig. D.2c) and its derivative (Fig. D.2d) taken with the feedback loop off are basically a direct response of the tunneling current to the changes in height, as given by Equation (2.1). Therefore these signals, which are the actual signals used in spectroscopic surveys, are also mainly dominated by the low frequency noise. Electromagnetic noise, usually in the form of 50 Hz, is nicely shielded as it is only a minor contribution to the total noise.

At the time of writing of this thesis, the whole physics department of the University of Amsterdam was in the process of moving to a new building. In order to ensure that the specifications of the new building are the same or better than the old building, measurements of the vibrations of both the new and old site of the STM have been performed using the same equipment with identical settings. The striking result was that the two most dominant noise frequencies in the STM measurements encountered throughout this work, ~1.5 Hz and ~21.5 Hz, which can clearly be distinguished in Fig. D.2d, are actually vibrations of the (old) building itself, see Fig. D.2e. At night, when most measurements were performed, the amplitude of these frequencies are reduced with respect to their daytime contribution, but are still the limiting factor in height and energy resolution of the system. Preliminary measurements of the vibrations in the new building, see Fig. D.2f, seem to indicate that the vibrations at the time of measurement (i.e. when the experimental hall was still nearly empty) in the new building are similar to those in the old building. Together with an active vibration dampening system, the STM will therefore hopefully perform even better at the new location.

form of sin(t) is equal to 1.

APPENDIX

E

Software and measurement procedures

During this Ph.D. work software to analyze the experimental data has been written in the program Igor [285]. The software consists of one main program in which both spectroscopic and topographic data can be opened and analyzed. Independent modules to for instance extract gaps from spectroscopic maps, to compare maps taken at the same field of view at different settings and to analyze I(z) measurements have been written as well. In this appendix, the loading of files saved by the Createc measurement software into Igor, and the algorithm to extract gaps from spectra will be discussed. Around halfway through the research, new electronics and software was installed, which required a slightly different code as for instance more variables are saved. In the following, only the software required to analyze data taken with the new software will be considered. The reader is referred to the Createc software manual for details on file formats and parameters. The last part of this appendix lists various typical parameters used for the measurements.

E.1 STM software: loading the data

Without going into all the details of the main program, the code used to load the data will be discussed, as this is the most tricky part of the program. Once the data is loaded, a simple block of numbers is obtained with which further analysis can easily be done. Several types of data can be taken with a *Createc GmbH* STM, each of which have their own particular method of storage into a file. Below the .dat (topography), .vert (I(V) and I(z) spectroscopy), .specgrid (conduction maps) and .tspec (time spectroscopy) will be discussed. The names of strings and variables used below do not necessarily match with the code of the actual software as multiple names had to be used in the software to prevent overwriting. It has to be noted that the Createc measurement program saves both the header and the data *after* the scan has finished. If for whatever reason the user changes a setting after the scan, but

before saving a file, the header file will contain the 'wrong' parameters which will affect the workings of the program described below. In the software written, the code given below is placed in functions that are all interwoven into a data structure with folders to be able to open, analyze and save multiple files. Build-in securities are also added, to prevent errors when for instance a user aborts the load of a file. A typical example of such a security is:

```
Variable refNum
Open/Z=2/R/T="????" refNum
if(V_flag!=0)
 return 0
endif
```

which prevents the code below such a statement to be run when the user does not select a file, but cancels the file-load. For details on particular flags and build-in Igor functions the reader is referred to the Igor user manual.

E.1.1 Topographic .dat files

A topographic .dat file consists of a header containing all parameters used by the Createc software, followed by the data. The header is 128×128 bytes and in ASCII format plus four unused bytes. A typical entry is of the form: Biasvolt[mV]=22.50. The data is written (in uncompressed form) in 4 byte floating point format in the order it is acquired, i.e. line per line from left to right and from top to bottom. If not only the topographic data is stored, but also for instance the current, or the topographic data taken while the tip moves from right to left to start a new row (i.e. the backwards scan), these data will be saved in a separate block after the topographic (forwards scan) data. The total file size is thus given by $128\times128+4+4\times n_x\times n_y\times n_{channels}$ bytes, where n_x and n_y are the number of pixels in the x and y direction respectively and $n_{channels}$ is the number of data types are stored (i.e. forwards topographic scan, backwards topographic scan etc.).

The code used to load such a file into Igor is as follows:

```
Variable refNum
String fullfilename
Open/D/R/T=".dat" refNum
fullfilename = S_fileName
LoadWave/Q/A=parameters/J/K=0/L={0,0,254,0,0}/N fullfilename
GBLoadWave/Q/B/T={2,4}/S=16388 fullfilename
```

Two files will be saved in the current data folder in Igor, namely `parameters0`, which is a text wave[1] containing the header of the .dat file, and `wave0`, a wave containing the data as they are stored in the .dat file (i.e. one long list of numbers). Assuming only the forwards topographic scan has been saved, the data is then put into a wave of dimension $n_x\times n_y$, or `xres`×`yres`, using:

[1] a wave is the Igor version of a matrix with data

```
Variable xres, yres, x, y
sscanf parameters0[5], "Num.X / Num.X=\%f", xres
sscanf parameters0[6], "Num.Y / Num.Y=\%f", yres
Make/O/N=(xres,yres) topo2Dforward
for(y=0;y<yres;y+=1)
 for(x=0;x<xres;x+=1)
  topo2Dforward[x][y]=wave0[y*xres+x]
 endfor
endfor
```

The data in the newly created 2D wave `topo2Dforward` is in DAC (Digital to Analogue Converter) units and should still be converted to Å for topographic data, or nA for current data etc.. The DAC is 20 bit, giving 2^{20} steps to divide the total voltage range of the computer of 20 Volts into. Before reaching the z-piezo, which has a piezo constant, `piezoz`, the signal is amplified by a factor `gainz`. Conversion to Å is therefore done using:

```
Variable stepsize, gainz, piezoz
stepsize = 2^20
sscanf parameters0[13], "GainZ / GainZ=\%f", gainz
sscanf parameters0[217], "ZPiezoconst= \%f", piezoz
topo2Dforward[][]*=gainz*piezoz*20/stepsize
```

In the final step, the 2D wave should be scaled such that the size in Å corresponds to the actual size of the image. The size in the x-direction of the image is given by the pixel stepsize, `xdeltax`, times the gain of the high voltage power supply, `gainx`, times the piezo constant, `piezox`, hence the following code is used:

```
Variable xdeltax, ydeltay, gainx, gainy, piezox, piezoy
sscanf parameters0[3], "Delta X / Delta X [Dac]=\%f", xdeltax
sscanf parameters0[4], "Delta Y / Delta Y [Dac]=\%f", ydeltay
sscanf parameters0[11], "GainX / GainX=\%f", gainx
sscanf parameters0[12], "GainY / GainY=\%f", gainy
sscanf parameters0[218], "Xpiezoconst= \%f", piezox
sscanf parameters0[219], "YPiezoconst= \%f", piezoy
SetScale/I x, 0, xres*xdeltax*gainx*piezox*20/stepsize, topo2Dforward
SetScale/I y, 0, yres*ydeltay*gainy*piezoy*20/stepsize, topo2Dforward
```

A 2D block of numbers corresponding to the height of the z-piezo is now obtained, which has the size of the field of view in Å. Further analysis, for instance Fourier transforming the image, can now be done using straightforward matrix operations. If not only the forward topographic image is stored, several loops should be implemented to load also backwards scans and data acquired with different channels.

E.1.2 Spectroscopic .vert files

Having dealt with the topographic images in the previous section, single pixel spectroscopic files will now be discussed. These .vert files have the same header as the to-

pographic files, hence an identical code can be used to load these parameters. However, instead of 4 unused bytes after the 128×128 byte header, three numbers appear, the number of pixel points of the spectrum, and the x and y position of the tip at the time the spectrum was taken. The data then follows in four (or more) columns, where the first three columns are the pixels number (starting from 0), the voltage and height, respectively. The fourth (and following) columns are reserved for the current or differential current (or any other input parameter). Depending on the input, the data is saved as a float either in mV (voltage or z height input) or DAC units (everything else).

To load the file, and assuming only I(V) or I(z), and dI/dV are acquired, the following code is used:

```
Variable refNum
String fullfilename
Open/D/R/T="????" refNum
fullfilename = S_fileName
LoadWave/Q/A=parameters/J/K=0/L={0,0,254,0,0}/N fullfilename
LoadWave/Q/A/G/L={0,0,0,1,4}/N fullfilename
```

This code is similar to that used for the topographic file, but in this case the data is in float format hence the /G option can be used in LoadWave instead of /T in GBLoadWave. Aside from the `parameters0` text wave, wave0, wave1, wave2 and wave3 are loaded containing voltage, height, I and dI/dV respectively[2]. Converting the DAC units to Å, nA and nS is then rather straightforward:

```
Variable stepsize, gfactor, current, sens, modamp
sensitivity = <user input>
modamp = <user input>
stepsize = 2^20
sscanf parameters0[16], "Gainpreamp / GainPre 10^=\%f", gfactor
sscanf parameters0[205], "Current[A]=\%f", current
wave1[] *= 10^(-3)*piezoz
wave2[] *= 20*10^(-gfactor+9)/stepsize
wave3[] *= 20*(sens)/(10*modamp)*10^(-gfactor+9)/stepsize/current
```

where the sensitivity (`sens`) and modulation amplitude (`modamp`) of the lock-in amplifier should be given by the user (in mV). `gfactor` is the gain of the preamplifier that converts the current to mV. With these four waves, I(z), I(V) and dI/dV plots can then be made.

E.1.3 Conduction map .specgrid files

In this section the file format of conduction map (.specgrid) data is discussed. As this is one of the most important features of the STM, the loading procedure of these files

[2] if wave0 already existed before loading, the first new wave will be wave1, etc.

will be shown in some detail. A .specgrid file is actually part of two files, one containing the spectroscopic data (the .specgrid file) and one containing the topographic data recorded simultaneously with the spectroscopic map (a .specgrid.dat file). The .specgrid.dat file can be loaded as a regular topographic file. To load the .specgrid file, the path to the file and its header are first loaded in the regular fashion:

```
Variable refNum
String fullfilename, topofilename
Open/D/R/T="????" refNum
fullfilename = S_fileName
topofilename = fullfilename + ".dat"
LoadWave/Q/A=parameters/J/K=0/L={0,0,254,0,0}/N topofilename
```

where the parameters are actually loaded from the topographic .specgrid.dat file going by the name `topogridname`. The data in the specgrid file itself consists of a header of 1024 bytes containing several parameters - such as the set current - in integer and single floating point format, depending on the parameter. The data itself follows in single floating point format. Both header (given the name `specgridparam0`) and data (`wave0`) are loaded using:

```
GBLoadWave/N=specgridparam/O/Q/B/T={16,2}/S=0/W=1/U=40 fullfilename
GBLoadWave/O/Q/B/T={2,2}/S=1024/W=1 fullfilename
```

Directly after the header and before the actual data, a list of the voltage and height of each pixel point is given in a single column, i.e. voltage[0], z[0], voltage[1], etc., hence the actual data starts at row number 2×`filepixels`, where `filepixels` is the number of pixels in a single spectrum. If more than one channel is used to obtain data from, the data is written in single column format, grouped per pixel. Assuming only I(V) and dI/dV are recorded in the spectroscopic map (this can be confirmed with the `Vertchannelselectval` parameter in the header of the .specgrid.dat file), the data is written in two waves and simultaneously transformed to the proper units (pA and nS respectively) from ADC units:

```
Variable xgrid, ygrid, xnum, ynum, nreal, pointsinfile
sscanf parameters0[92], "SpecXGrid=\%f", xgrid
sscanf parameters0[93], "SpecYGrid=\%f", ygrid
sscanf parameters0[5], "Num.X / Num.X=\%f", xnum
sscanf parameters0[6], "Num.Y / Num.Y=\%f", ynum
sscanf parameters0[100], "Vertchannelselectval=\%f", channels
nreal = 2*filepixels
pointsinfile = floor(xnum/xgrid)*floor(ynum/ygrid)*filepixels*channels

for(x=0;x<(pointsinfile);x+=1)
 wave0[x] = wave0[x+nreal]
endfor
Redimension/N=(pointsinfile) wave0
```

```
Make/O/N=(DimSize(wave0,0)/2) wave1, wave2

Variable gfactor, current, imagex, imagey, sens, modamp, stepsize
sscanf parameters0[16], "Gainpreamp / GainPre 10^=\%f", gfactor
sscanf parameters0[205], "Current[A]=\%f", current
sens = <user input>
modamp = <user input>
current *= 10^12
stepsize = 2^20
for(x=0;x<DimSize(wave1,0);x+=1)
 wave1[x] = wave0[2*x]*20*10^(-gfactor+9)/stepsize
 wave2[x] = wave0[2*x+1]*20*sens*10^(-gfactor+9)/(stepsize*current*
endfor                                                          10*modamp)
```

As it is not unlikely that there are multiple pixels in a single spectrum with identical voltages (for instance due to multiple sweeps per spectrum), all points taken at the same voltage should be averaged. To this end the voltages are put in a single wave (`volt`) and sorted. In order to keep track of where the original data points were located, a separate wave containing the entry positions (`row`) is sorted simultaneously. After sorting, both waves are combined into a single 2D wave, (`vrow`):

```
Variable filepixels = specgridparam0[14]
Make/O/N=(filepixels) voltagelist
for(x=0;x<filepixels;x+=1)
 volt[x] = wave0[2*x]
 row[x] = x
endfor

Make/O/N=(filepixels,2) vrow
vrow[][0] = volt[p]; vrow[][1] = row[p]
```

The total number of unique voltages is then given by `absVs`:

```
Variable absVs = 0
for(x=1;x<DimSize(vrow,0);x+=1)
 if(vrow[x][0] != vrow[x-1][0])
  absVs+=1
 endif
endfor
```

As a last step, all pixels in a single spectrum taken at the same energy will be averaged, and every individual spectrum will be placed in a 3D matrix with dimensions x, y, and energy. Since both I(V) and dI/dV data are saved, two 3D matrices (`ivmap` and `didvmap`) will be obtained. In the following, a single step size in energy will be considered for simplicity. Generalisation to multiple step sizes can easily be incorporated using the greatest common denominator (gcd(A,B) in Igor) as the step size

in the file and leaving non-existent entries blank. For a proper averaging, a separate wave (`shadowfile`) is constructed that keeps track of the number of times a voltage exists. As all spectra in the map are identical, this file needs to be made only once.

```
Make/O/N=(floor(xnum/xgrid), floor(ynum/ygrid), absVs+1) didvmap, ivmap
Make/O/N=(absVs+1) shadowfile
shadowfile = 0; didvmap = 0; ivmap = 0

Variable xrange, yrange, zrange, vcol, counter = 0
for(yrange=0;yrange<floor(ynum/ygrid);yrange+=1)
 for(xrange=0;xrange<floor(xnum/xgrid);xrange+=1)
  for(zrange=0;zrange<DimSize(vrow,0);zrange+=1)
   vcol = round((vrow[zrange][0]-DimOffset(didvmap,2))/DimDelta(didvmap,2))
   ivmap[xrange][yrange][vcol]+=wave1[counter*filepixels+vrow[zrange][1]]
   didvmap[xrange][yrange][vcol]+=wave2[counter*filepixels+vrow[zrange][1]]
   if(xrange==0&&yrange==0)
    shadowfile[vcol] += 1
   endif
  endfor
  counter+=1

  didvmap[xrange][yrange][]/=shadowfile[p]
  ivmap[xrange][yrange][]/=shadowfile[p]
 endfor
endfor
```

Scaling of the two 3D matrices to the actual spatial and energy size is then done using:

```
Variable imagex, imagey
sscanf parameters0[202], "Length x[A]=\%f", imagex
sscanf parameters0[203], "Length y[A]=\%f", imagey
SetScale/I z, vrow[0][0], vrow[DimSize(vrow,0)][0], didvmap, ivmap
SetScale/I x, 0, imagex, didvmap, ivmap
SetScale/I y, 0, imagey, didvmap, ivmap
```

Using the procedure described above, two 3D blocks of data are obtained, which can easily be used for further analysis. Taking slices at a specific energy and Fourier transforming these can for instance give Fourier space images of quasi-particle interference scattering (see appendix A). With a loop over all x- and y-coordinates, gaps in every spectrum can independently extracted as a function of position, etc..

E.1.4 Time spectroscopy .tspec files

Especially useful for noise detection and analysis is the option to record a certain signal over a period of time. Loading such .tspec files will be discussed below. The structure of .tspec files is identical to .vert files, where the data is stored as floats in

columns. Preceding the data, three floats appear containing the number of points, the number of channels used and the encoding of the channels. The first column then corresponds to the pixel number, the content of the subsequent columns depends on what channel has been measured. If for instance only the height and current have been measured as a function of time, the second and third columns will contain these data in Volts, followed by two columns containing their respective Fourier transforms. To load the file, like before, the path to the file and the header are imported using:

```
Variable refNum
String/G fullfilename
Open/D/R/T="????" refNum
fullfilename = S_fileName
LoadWave/Q/A=parameters/J/K=0/L={0,0,254,0,0}/N fullfilename
```

Subsequently, the number of channels (`nchannels`) is taken from the header file and the various columns are imported:

```
Variable npoints, nchannels
sscanf parameters0[253], "\%f \%f", npoints, nchannels
LoadWave/Q/A/G/L={0,0,0,1,nchannels}/N fullfilename
```

Lastly, the loaded waves need to be scaled properly and the entries should be converted to the proper units (i.e. Å, pA etc.). Assuming as an example that the height (`wave0`) and current (`wave1`) channels have been acquired, the following code is used:

```
Variable sfreq, gfactor, gainz, piezoz
sscanf parameters0[150], "SpecFreq=\%f", sfreq
sscanf parameters0[16], "Gainpreamp / GainPre 10^=\%f", gfactor
sscanf parameters0[13], "GainZ / GainZ=\%f", gainz
sscanf parameters0[217], "ZPiezoconst=\%f", piezoz

SetScale/I x, 0, npoints/sfreq, wave0, wave1
wave0[] *= gainz*piezoz
wave1[] *= 10^(-gfactor+12)
```

which results in two waves with a proper wave-scaling in seconds and entries in the right units (Å and pA respectively). These files can then for instance be Fourier transformed using the standard Igor function `FFT` to visualise dominant noise frequencies as has been done in chapter 2.

E.2 Superconducting gap algorithm

Typical conduction maps are on the order of 64×64 pixels or more, so extracting superconducting gaps by hand will take forever and lacks a certain reproducibility as

the user can steer the results in a certain way. Therefore, to determine the superconducting gap of single pixels spectra that are part of a conduction map, a routine has been written in Igor. In case of superconducting gap spectra taken on a high-T_c superconductor such as Bi2212, the coherence peaks are well defined entities (see appendix A) and a peak finding routine can already be enough to determine the gap. However, in the iron based superconductors, the coherence peaks are not as well defined and are usually found on a sloping background, making it slightly more difficult to determine the gap. Therefore, instead of finding the absolute maximum of a spectrum, the first point with respect to zero bias where the slope of the curve is zero was determined, which should correspond to the top of the coherence peak. To get a reliable value for the gap, this value was determined both at positive and negative bias.

To increase the visibility of the coherence peaks, two methods were used. The first was to divide the spectra taken at low temperature by those taken at the exact same location above T_c. As this was not always possible (not all maps were taken above and below T_c), a second technique was applied. The original spectrum was smoothed a number of times, where in each smoothing step a point is assigned to be the average of its neighbours. The effect is that features that vary strongly as a function of bias voltage, i.e. the coherence peaks, are rapidly suppressed, while the slowly varying background remains more or less unchanged. Dividing the original curve by such a smoothed curve thus enhances the coherence peaks and at the same time removes the static background. Using maps recorded both above and below T_c on the same field of view, this data analysis technique used to enhance the contrast of the superconducting gap signatures has been checked not to remove or add information to the spectra.

Not only the first point of zero slope was determined, but also the point of maximum slope closest to zero bias both at positive and negative bias. Even though this value is not the superconducting gap itself, one can assume the maximum slope is for all spectra the same fraction of the superconducting gap, allowing for comparison of the spatial variation of the gap.

Using these two methods, a total of four maps is obtained, a gap map and maximum slope map both at positive and negative bias voltage. The two gap maps were first of all confirmed to match both in spatial variation and absolute value, and averaged. Lastly, the gap map was compared to the maximum slope map and checked to be similar in spatial variation. As a last check, several random spectra were investigated by hand and confirmed to give the same gap value as the one given by the algorithm.

E.3 Measurement procedures and parameters

Throughout this work, the modulation frequency of the lock-in amplifier has initially been set to 427.3 Hz but for later studies was changed to 969 Hz. The advantage of a higher frequency is that a shorter integration time can be used. Care should be

taken to pick frequencies that are far away from noise frequencies. Typical single pixel tunneling spectra consisted of a forwards and backwards sweeps in voltage (to exclude lagging due to a too high integration time) of 1024 pixels each. Averaging of the two sweeps and of points taken at the same approximate energy in a single sweep was performed to reduce noise.

For the QPI measurements presented in appendix A, a voltage staircase was used with 31 steps and 5 points per step (leading to a total of 155 pixels per sweep). Each set of two sweeps was taken in 2.8 seconds. With an integration time of 3 ms, no lagging occurred. Using a software limited maximum of 280×280 spatial pixels, the total length of the measurement at 62 hours could just fit in a (noise free) weekend. As the material is very easily destroyed, V_{sample} and I_{set} were chosen at 100 mV and 30 pA respectively. Larger currents will reduce both the noise and the success rate.

In topographic imaging mode, the scan speed was set to 1500 Å/sec for nearly all measurements, which was the highest speed where no deformation effects occurred.

The parameters used in the automated approach module of the Createc software are: ~10 V pulse height, ~0.001 sec pulse duration, 0.3 seconds per burst and 1 burst at a time. The z-gain of the high voltage amplifier is set to 3. Tunneling contact was typically established within an hour. Larger steps by taking either a higher burst count or higher pulse height often resulted in tip crashes. On the pnictides V_{sample} and I_{set} during approach were typically set to 50 mV and 40 pA respectively, settings which were also used for subsequent imaging and spectroscopic mapping. The manganites were usually approached using V_{sample} = 250 mV and I_{set} = 100 pA.

As mentioned in appendix A, LEED images taken in the STM chamber should be mirrored in the vertical axis to match the STM orientation. The ~5b supermodulation in pristine Bi2212 has been used to exclude any other set of rotations and translations to get a match between LEED and STM.

Bibliography

[1] Y. Kamihara, T. Watanabe, M. Hirano, and H. Hosono, J. AM. CHEM. SOC. **130**, 3296 (2008), *Iron-based layered superconductor La[$O_{1-x}F_x$]FeAs (x = 0.05-0.12) with T_c = 26 K*.

[2] Z. A. Ren, W. Lu, J. Yang, W. Yi, X. L. Shen, C. Zheng, G. C. Che, X. L. Dong, L. L. Sun, F. Zhou, and Z. X. Zhao, CHINESE PHYSICS LETTERS **25**, 2215 (2008), *Superconductivity at 55 K in iron-based F-doped layered quaternary compound Sm[$O_{1-x}F_x$]FeAs*.

[3] M. L. Cohen and P. W. Anderson, SUPERCONDUCTIVITY IN D- AND F-BAND METALS, AIP, New York, 1972.

[4] D. A. Kirzhnits, SOV. PHYS. -USP. **19**, 530 (1976).

[5] O. V. Dolgov, D. A. Kirzhnits, and E. G. Maksimov, REV. MOD. PHYS. **53**, 81 (1981), *On an admissable sign of the static dielectric function of matter*.

[6] S. de Jong, EMERGENT ELECTRONIC MATTER: FERMI SURFACES, QUASIPARTICLES AND MAGNETISM IN MANGANITES AND PNICTIDES, PhD thesis, University of Amsterdam, 2010, `http://www.science.uva.nl/research/cmp/docs/Golden/thesis/Proefschrift_SdeJong_compressed.pdf`.

[7] `http://www.lt-stm.com/`.

[8] I. Giaever, PHYS. REV. LETT. **5**, 147 (1960), *Energy gap in superconductors measured by electron tunneling*.

[9] G. Binnig, H. Rohrer, C. Gerber, and E. Weibel, APPL. PHYS. LETT. **40**, 178 (1982), *Tunneling through a controllable vacuum gap*.

[10] G. Binnig, H. Rohrer, C. Gerber, and E. Weibel, REV. MOD. PHYS **59**, 3 (1987), *Scanning tunneling microscopy - from birth to adolescence*.

[11] G. Binnig, H. Rohrer, C. Gerber, and E. Weibel, PHYS. REV. LETT. **49**, 57 (1982), *Surface studies by scanning tunneling microscopy*.

[12] G. Binnig, H. Rohrer, C. Gerber, and E. Weibel, PHYS. REV. LETT. **50**, 120 (1983), *7x7 reconstruction on Si(111) resolved in real space*.

[13] A. L. de Lozanne, S. A. Elrod, and C. F. Quate, PHYS. REV. LETT. **54**, 2433 (1985), *Spatial variation in the superconductivity of Nb_3Sn measured by low-temperature tunneling microscopy*.

[14] H. Ibach and H. Lüth, SOLID-STATE PHYSICS - AN INTRODUCTION TO PRINCIPLES OF MATERIALS SCIENCE, Springer New York, 3rd edition, 2003.

[15] J. Chen, INTRODUCTION TO SCANNING TUNNELING MICROSCOPY, Oxford University Press, 1993.

[16] J. Nicol, S. Shapiro, and P. H. Smith, PHYS. REV. LETT. **5**, 461 (1960), *Direct measurement of the superconducting energy gap*.

[17] J. Bardeen, PHYS. REV. LETT. **6**, 2 (1961), *Tunnelling from a many-particle point of view*.

[18] J. Tersoff and D. R. Hamann, PHYS. REV. LETT. **50**, 25 (1983), *Theory and application of the scanning tunneling microscope*.

[19] J. Tersoff and D. R. Hamann, PHYS. REV. B **31**, 2 (1985), *Theory of the scanning tunneling microscope*.

[20] W. A. Hofer, A. S. Foster, and A. L. Shluger, REV. MOD. PHYS. **75**, 1287 (2003), *Theories of scanning probe microscopes at the atomic scale*.

[21] H. Lin, J. M. C. Rauba, K. S. Thygesen, K. W. Jacobsen, M. Y. Simmins, and W. A. Hofer, FRONTIERS OF PHYSICS IN CHINA **5**, 369 (2010), *First-principles modelling of scanning tunneling microscopy using non-equilibrium Green's functions*.

[22] S. Rousset, V. Repain, G. Baudot, Y. Garreau, and J. Lecoeur, J. PHYS. COND. MAT. **15**, S3363 (2003), *Self-ordering of Au(111) vicinal surfaces and application to nanostructure organized growth*.

[23] V. M. Hallmark, S. Chiang, J. F. Rabolt, J. D. Swalen, and R. J. Wilson, PHYS. REV. LETT. **59**, 2879 (1987), *Observation of atomic corrugation on Au(111) by scanning tunneling microscopy*.

[24] C. J. Chen, PHYS. REV. LETT. **65**, 448 (1990), *Origin of atomic resolution on metal surfaces in scanning tunneling microscopy*.

[25] J. Wintterlin, J. Wiechers, H. Brune, T. Gritsch, H. Höfer, and R. J. Behm, PHYS. REV. LETT. **62**, 59 (1989), *Atomic-resolution imaging of close-packed metal surfaces by scanning tunneling microscopy*.

[26] D. Tománek, S. G. Louie, H. J. Mamin, D. W. Abraham, R. E. Thomson, E. Ganz, and J. Clarke, PHYS. REV. B **35**, 7790 (1987), *Theory and observation of highly asymmetric atomic structure in scanning tunneling microscopy images of graphite*.

[27] G. Binnig, N. Garcia, H. Rohrer, J. M. Soler, and F. Flores, PHYS. REV. B **30**, 4816 (1984), *Electron-metal-surface interaction potential with vacuum tunneling: Observation of the image force*.

[28] J. M. Pitarke, P. M. Echenique, and F. Flores, SURF. SCI. **217**, 267 (1989), *Apparent barrier height for tunneling electrons in STM*.

[29] L. Olesen, M. Brandbyge, M. R. Sørensen, K. W. Jacobsen, E. Lægsgaard, I. Stensgaard, and F. Besenbacher, PHYS. REV. LETT. **76**, 1485 (1996), *Apparent barrier height in scanning tunneling microscopy revisited*.

[30] K. Besocke, SURF. SCI. **181**, 145 (1987), *An easily operable STM*.

[31] J. Frohn, J. F. Wolf, K. Besocke, and M. Teske, REV. SCI. INSTRUM. **60**, 1200 (1989), *Coarse tip distance adjustment and positioner for a scanning tunneling microscope*.

[32] R. Huisman, *Phase diagram of $BaFe_{2-x}Co_xAs_2$ pnictides using transport measurements*, Master's thesis, University of Amsterdam, 2010.

[33] H. K. Onnes, LEIDEN COMM. **120b, 122b, 124c** (1911), *On the sudden change in the rate at which the resistance of mercury disappears*.

[34] W. Meissner and R. Ochsenfeld, NATURWISSENSCHAFTEN **21**, 787 (1933), *Ein neuer effekt bei eintritt der supraleitfähigkeit*.

[35] J. Bardeen, L. N. Cooper, and J. R. Schrieffer, PHYS. REV. LETT. **106**, 162 (1957), *Microscopic theory of superconductivity*.

[36] J. Bardeen, L. N. Cooper, and J. R. Schrieffer, PHYS. REV. LETT. **108**, 1175 (1957), *Theory of superconductivity*.

[37] L. N. Cooper, PHYS. REV. **104**, 1189 (1956), *Bound electron pairs in a degenerate Fermi gas*.

[38] M. Tinkham, INTRODUCTION TO SUPERCONDUCTIVITY, McGraw-Hill, Inc., 2nd edition, 1996.

[39] F. Gross, B. S. Chandrasekhar, D. Einzel, K. Andres, P. J. Hirschfeld, H. R. Ott, J. Beuers, Z. Fisk, and J. L. Smith, Z. PHYS. B - COND. MAT. **64**, 175 (1986), *Anomalous temperature dependence of the magnetic field penetration depth in superconducting $UBe_{1\,3}$*.

[40] D. V. Evtushinsky, D. S. Inosov, V. B. Zabolotnyy, M. S. Viazovska, R. Khasanov, A. Amato, H.-H. Klauss, H. Luetkens, C. Niedermayer, G. L. Sun, V. Hinkov, C. T. Lin, A. Varykhalov, A. Koitzsch, M. Knupfer, B. Büchner, A. A. Kordyuk, and S. V. Borisenko, NEW J. PHYS. **11**, 055069 (2009), *Momentum-resolved superconducting gap in the bulk of $Ba_{1-x}K_xFe_2As_2$ from combined ARPES and μSR measurements*.

[41] R. Dynes, V. Narayanamurti, and J. P. Garno, PHYS. REV. LETT. **41**, 1509 (1978), *Direct measurement of quasiparticle-lifetime broadening in a strong-coupled superconductor*.

[42] G. M. Éliashberg, SOVIET PHYS. JETP **11**, 969 (1960), *Interactions between electrons and lattice vibrations in a superconductor*.

[43] J. P. Carbotte, REV. MOD. PHYS. **62**, 1027 (1990), *Properties of boson-exchange superconductors*.

[44] E. Maxwell, PHYS. REV. LETT. **78**, 477 (1950), *Isotope effect in the superconductivity of mercury*.

[45] J. G. Bednorz and K. A. Müller, Z. PHYS. B - CONDENSED MATTER **64**, 189 (1986), *Possible high T_c superconductivity in the Ba-La-Cu-O system*.

[46] M. K. Wu, J. R. Ashburn, C. J. Torng, P. H. Hor, R. L. Meng, L. Gao, Z. J. Huang, Y. Q. Wang, and C. W. Chu, PHYS. REV. LETT. **58**, 908 (1987), *Superconductivity at 93 K in a new mixed-phase Y-Ba-Cu-O compound system at ambient pressure*.

[47] H. Maeda, Y. Tanaka, M. Fukutomi, and T. Asano, JPN. J. APPL. PHYS. **27**, 209 (1988), *A new high-T_c oxide superconductor without a rare earth element*.

[48] W. J. Zhu, Y. Z. Huang, L. Q. Chen, C. Dong, B. Yin, and Z. Zhao, PHYSICA C **218**, 5 (1993), *Synthesis of the superconductors $HgBa_2CaCu_2O_{6+\delta}$ and $HgBa_2Ca_2Cu_3O_{8+\delta}$*.

[49] S. Hüfner, M. A. Hossain, A. Damascelli, and G. A. Sawatzky, REP. PROG. PHYS. **71**, 062501 (2008), *Two gaps make a high-temperature superconductor?*

[50] A. Damascelli, Z. Hussain, and Z. X. Shen, REV. MOD. PHYS. **75**, 473 (2003), *Angle-resolved photoemission studies of the cuprate superconductors*.

[51] E. Eremin, E. Tsoncheva, and A. V. Chubukov, PHYS. REV. B **77**, 024508 (2008), *Signature of the nonmonotonic d-wave gap in the electron-doped cuprates*.

[52] G.-M. Zhao and J. Wang, J. PHYS. COND. MAT. **22**, 352202 (2010), *Specific heat evidence for bulk s-wave gap symmetry of optimally electron-doped $Pr_{1.85}Ce_{0.15}CuO_{4-y}$ superconductors*.

[53] H. Won and K. Maki, PHYS. REV. B **49**, 1397 (1994), *d-wave superconductor as a model of high-T_c superconductors*.

[54] D. R. Harshman, J. D. Dow, and A. T. Fiory, PHYS. REV. B **77**, 024523 (2008), *Isotope effect in high-T_c superconductors*.

[55] A. S. Alexandrov and G. M. Zhao, PHYS. REV. B **80**, 136501 (2009), *Comment on "Isotope effect in high-T_c superconductors"*.

[56] D. R. Harshman, J. D. Dow, and A. T. Fiory, PHYS. REV. B **80**, 136502 (2009), *Reply to "Comment on 'Isotope effect in high-T_c superconductors'"*.

[57] X.-J. Chen, V. V. Struzhkin, Z. Wu, H.-Q. Lin, R. J. Hemley, and H. Mao, PNAS **104**, 3732 (2007), *Unified picture of the oxygen isotope effect in cuprate superconductors*.

[58] A. R. Bishop, A. Bussmann-Holder, O. Dolgov, A. Furrer, H. Kamimura, H. Keller, R. Khasanov, R. K. Kremer, D. Manske, K. Müller, and A. Simon, J. SUPERCOND. NOV. MAGN. **20**, 393 (2007), *Real and marginal isotope effects in cuprate superconductors*.

[59] D. J. Pringle, G. V. M. Williams, and J. L. Tallon, PHYS. REV. B **62**, 12527 (2000), *Effect of doping and impurities on the oxygen isotope effect in high-temperature superconducting cuprates*.

[60] M. Rotter, M. Tegel, and D. Johrendt, PHYS. REV. LETT. **101**, 107006 (2008), *Superconductivity at 38 K in the Iron Arsenide ($Ba_{1-x}K_x$)Fe_2As_2*.

[61] J. Paglione and R. L. Greene, NATURE PHYSICS **6**, 645 (2010), *High-temperature superconductivity in iron-based materials*.

[62] K. Terashima, Y. Sekiba, J. H. Bowen, K. Nakayama, T. Kawahara, T. Sato, P. Richard, Y.-M. Xu, L. J. Li, G. H. Cao, Z.-A. Xu, H. Ding, and T. Takahashi, PNAS **106**, 7330 (2009), *Fermi surface nesting induced strong pairing in iron-based superconductors*.

[63] V. Brouet, M. Marsi, B. Mansart, A. Nicolaou, A. Taleb-Ibrahimi, P. L. Fèvre, F. Bertran, F. Rullier-Albenque, A. Forget, and D. Colson, PHYS. REV. B **80**, 165115 (2009), *Nesting between hole and electron pockets in $Ba(Fe_{1-x}Co_x)_2As_2$ (x=0-0.3) observed with angle-resolved photoemission*.

[64] K. Sasmal, B. Lv, B. Lorenz, A. M. Guloy, F. Chen, Y. Y. Xue, and C. W. Chu, PHYS. REV. LETT. **101**, 107007 (2008), *Superconducting Fe-based compounds ($A_{1-x}Sr_x$)Fe_2As_2 with A = K and Cs with transition temperatures up to 37 K*.

[65] G. F. Chen, Z. Li, G. Li, W. Z. Hu, J. Dong, J. Zhou, X. D. Zhang, P. Zheng, N. L. Wang, and J. L. Luo, CHINESE PHYSICS LETTERS **25**, 3403 (2008), *Superconductivity in Hole-Doped ($Sr_{1-x}K_x$)Fe_2As_2*.

[66] H. S. Jeevan, Z. Hossain, D. Kasinathan, H. Rosner, C. Geibel, and P. Gegenwart, PHYS. REV. B **78**, 092406 (2008), *High-temperature superconductivity in $Eu_{0.5}K_{0.5}Fe_2As_2$*.

[67] A. S. Sefat, R. Jin, M. A. McGuire, B. C. Sales, D. J. Singh, and D. Mandrus, PHYS. REV. LETT. **101**, 117004 (2008), *Superconductivity at 22 K in Co-doped $BaFe_2As_2$ crystals*.

[68] A. Leithe-Jasper, W. Schnelle, C. Geibel, and H. Rosner, PHYS. REV. LETT. **101**, 207004 (2008), *Superconducting state in $SrFe_{2-x}Co_xAs_2$ by internal doping of the iron arsenide layers*.

[69] L. J. Li, Y. K. Luo, Q. B. Wang, H. Chen, Z. Ren, Q. Tao, Y. K. Li, X. Lin, M. He, Z. W. Zhu, G. H. Cao, and Z. A. Xu, NEW J. PHYS. **11**, 025008 (2009), *Superconductivity induced by Ni doping in $BaFe_2As_2$ single crystals*.

[70] J. H. Chu, J. G. Analytis, C. Kucharczyk, and I. R. Fisher, PHYS. REV. B **79**, 014506 (2009), *Determination of the phase diagram of the electron-doped superconductor $Ba(Fe_{1-x}Co_x)_2As_2$*.

[71] N. Kumar, S. Chi, Y. Chen, K. G. Rana, A. K. Nigam, A. Thamizhavel, W. R. II, S. K. Dhar, and J. W. Lynn, PHYS. REV. B **80**, 144524 (2009), *Evolution of the bulk properties, structure, magnetic order, and superconductivity with Ni doping in $CaFe_{2-x}Ni_xAs_2$*.

[72] Z. Ren, Q. Tao, S. Jiang, C. Feng, C. Wang, J. Dai, G. Cao, and Z. Xu, PHYS. REV. LETT. **102**, 137002 (2009), *Superconductivity induced by phosphorus doping and its coexistence with ferromagnetism in $EuFe_2(As_{0.7}P_{0.3})_2$*.

[73] S. Jiang, H. Xing, G. Xuan, C. Wang, Z. Ren, C. Feng, J. Dai, Z. Xu, and G. Cao, J. PHYS. COND. MAT. **21**, 382203 (2009), *Superconductivity up to 30 K in the vicinity of the quantum critical point in $BaFe_2(As_{1-x}P_x)_2$*.

[74] H. L. Shi, H. X. Yang, H. F. Tian, J. B. Lu, Z. W. Wang, Y. B. Qin, Y. J. Song, and J. Q. Li, J. PHYS. COND. MAT. **22**, 125702 (2010), *Structural properties and superconductivity of $SrFe_2As_{2-x}P_x$ ($0.0 \leq x \leq 1.0$) and $CaFe_2As_{2-y}P_y$ ($0.0 \leq y \leq 0.3$)*.

[75] W. Schnelle, A. Leithe-Jasper, R. Gumeniuk, U. Burkhardt, D. Kasinathan, and H. Rosner, PHYS. REV. B **79**, 214516 (2009), *Substitution-induced superconductivity in $SrFe_{2-x}Ru_xAs_2$ ($0 \leq x \leq 2$)*.

[76] S. Sharma, A. Bharathi, S. Chandra, V. R. Reddy, S. Paulraj, A. T. Satya, V. S. Sastry, A. Gupta, and C. S. Sundar, PHYS. REV. B **81**, 174512 (2010), *Superconductivity in Ru-substituted polycrystalline $BaFe_{2-x}Ru_xAs_2$*.

[77] F. Rullier-Albenque, D. Colson, A. Forget, P. Thuéry, and S. Poissonnet, PHYS. REV. B **81**, 224503 (2010), *Hole and electron contributions to the transport properties of $Ba(Fe_{1-x}Ru_x)_2As_2$ single crystals*.

[78] A. Maeda, T. Yabe, S. Takebayashi, M. Hase, and K. Uchinokura, PHYS. REV. B **41**, 4112 (1990), *Substitution of 3d metals for Cu in $Bi_2(Sr_{0.6}Ca_{0.4})_3Cu_2O_y$*.

[79] K. Ishida, Y. Kitaoka, T. Yoshitomi, N. Ogata, T. Kamino, and K. Asayama, PHYSICA C **179**, 29 (1991), *Gapless superconductivity in Zn-doped $YBa_2Cu_3O_7$ studied by Cu NMR and NQR*.

[80] H. Chen, Y. Ren, Y. Qiu, W. Bao, R. H. Liu, G. Wu, T. Wu, Y. L. Xie, X. F. Wang, Q. Huang, and X. H. Chen, EURO. PHYS. LETT. **85**, 17006 (2009), *Coexistence of the spin-density wave and superconductivity in $Ba_{1-x}K_xFe_2As_2$*.

[81] I. I. Mazin, D. J. Singh, M. D. Johannes, and M. H. Du, PHYS. REV. LETT. **101**, 057003 (2008), *Unconventional superconductivity with a sign reversal in the order parameter of $LaFeAsO_{1-x}F_x$*.

[82] I. Mazin and J. Schmalian, PHYSICA C **469**, 614 (2009), *Pairing symmetry and pairing state in ferropnictides, theoretical overview*.

[83] S. de Jong, Y. Huang, R. Huisman, F. Massee, S. Thirupathaiah, M. Gorgoi, F. Schaefers, R. Follath, J. B. Goedkoop, and M. S. Golden, PHYS. REV. B **79**, 115125 (2009), *High resolution, hard x-ray photoemission investigation of $BaFe_2As_2$: Moderate influence of the surface and evidence for a low degree of Fe 3d - As 4p hybridization of electronic states near the Fermi energy*.

[84] D. J. Singh, PHYSICA C **469**, 418 (2009), *Electronic structure of Fe-based superconductors*.

[85] M. E. Jones and R. E. Marsh, J. AM. CHEM. SOC. **76**, 1434 (1954), *The preparation and structure of Magnesium Boride, MgB_2*.

[86] J. Nagamatsu, N. Nakagawa, T. Muranaka, Y. Zenitani, and J. Akimitsu, NATURE **410**, 63 (2001), *Superconductivity at 39 K in magnesium diboride*.

[87] M. R. Eskildsen, M. Kugler, G. Levy, S. Tanaka, J. Jun, S. M. Kazakov, J. Karpinski, and O. Fischer, PHYSICA C **385**, 169 (2003), *Scanning tunneling spectroscopy on single crystal MgB_2*.

[88] E. A.Lynton, B. Serin, and M. Zucker, J. PHYS. CHEM. SOLIDS **3**, 165 (1957), *The superconducting critical temperature and the electronic specific heat of impure tin*.

[89] B. T. Matthias, H. Suhl, and E. Corenzwit, PHYS. REV. LETT. **1**, 92 (1958), *Spin exchange in superconductors*.

[90] P. W. Anderson, PHYS. REV. LETT. **3**, 325 (1959), *Knight shift in superconductors*.

[91] P. W. Anderson, J. PHYS. CHEM. SOLIDS **11**, 26 (1959), *Theory of dirty superconductors*.

[92] A. A. Abrikosov and L. P. Gor'kov, SOVIET PHYS. JETP **12**, 1243 (1961).

[93] D. Markowitz and L. P. Kadanoff, PHYS. REV. **131**, 563 (1963), *Effect of impurities upon critical temperature of anisotropic superconductors*.

[94] F. Reif and M. A. Woolf, PHYS. REV. LETT. **9**, 315 (1962), *Energy gap in superconductors containing paramagnetic impurities*.

[95] S. Skalski, O. Betbeder-Matibet, and P. R. Weiss, PHYS. REV. **136**, A1500 (1964), *Properties of superconducting alloys containing paramagnetic impurities.*

[96] A. Yazdani, B. A. Jones, C. P. Lutz, M. F. Crommie, and D. M. Eigler, SCIENCE **275**, 1767 (1997), *Probing the local effects of magnetic impurities on superconductivity*.

[97] A. Yazdani, C. Howald, C. P. Lutz, A. Kapitulnik, and D. M. Eigler, PHYS. REV. LETT. **83**, 176 (1999), *Impurity-induced bound excitations on the surface of* $Bi_2Sr_2CaCu_2O_8$.

[98] S. H. Pan, E. W. Hudson, K. M. Lang, H. Eisaki, S. Uchida, and J. C. Davis, NATURE **403**, 746 (2000), *Imaging the effects of individual zinc impurity atoms on superconductivity in* $Bi_2Sr_2CaCu_2O_{8+\delta}$.

[99] E. W. Hudson, K. M. Lang, V. Madhavan, S. H. Pan, H. Eisaki, S. Uchida, and J. C. Davis, NATURE **411**, 920 (2001), *Interplay of magnetism and high-*T_c *superconductivity at individual Ni impurity atoms in* $Bi_2Sr_2CaCu_2O_{8+\delta}$.

[100] H. Suhl, B. T. Matthias, and L. R. Walker, PHYS. REV. LETT. **3**, 552 (1959), *Bardeen-Cooper-Schrieffer theory of superconductivity in the case of overlapping bands*.

[101] I. I. Mazin and V. P. Antropov, PHYSICA C **385**, 49 (2003), *Electronic structure, electron-phonon coupling, and multiband effects in* MgB_2.

[102] J. Fink, S. Thirupathaiah, R. Ovsyannikov, H. A. Dürr, R. Follath, Y. Huang, S. de Jong, M. S. Golden, Y.-Z. Zhang, H. O. Jeschke, R. Valentí, C. Felser, S. D. Farahani, M. Rotter, and D. Johrendt, PHYS. REV. B **79**, 155118 (2009), *Electronic structure studies of* $BaFe_2As_2$ *by angle-resolved photoemission spectroscopy*.

[103] M. L. Kulić and O. V. Dolgov, PHYS. REV. B **60**, 13062 (1999), *Anisotropic impurities in anisotropic superconductors*.

[104] M. L. Kulić, S. L. Drechsler, and O. V. Dolgov, EPL **85**, 47008 (2009), *Conventional superconductivity in Fe-based pnictides: The relevance of intra-band electron-boson scattering*.

[105] J. Li and Y. Wang, EPL **88**, 17009 (2009), *Magnetic impurities in the two-band* $s_{\pm}$*-wave superconductors*.

[106] Y. Yin, M. Zech, T. Williams, and J. Hoffman, PHYSICA C **469**, 535 (2009), *Scanning tunneling microscopy and spectroscopy on iron-pnictides*.

[107] C. Liu, T. Kondo, A. D. Palczewski, G. D. Samolyuk, Y. Lee, M. E. Tillman, N. Ni, E. D. Muna, R. Gordon, A. F. Santander-Syro, S. L. BudŠko, J. L. McChesney, E. Rotenberg, A. V. Fedorov, T. Valla, O. Copie, M. A. Tanatar, C. Martin, B. N. Harmon, P. C. Canfield, R. Prozorov, J. Schmalian, and A. Kaminski, PHYSICA C **469**, 491 (2009), *Electronic properties of iron arsenic high temperature superconductors revealed by angle resolved photoemission spectroscopy (ARPES)*.

[108] F. Massee, Y. Huang, R. Huisman, S. de Jong, J. B. Goedkoop, and M. S. Golden, PHYS. REV. B **79**, 220517 (2009), *Nanoscale superconducting-gap variations and lack of phase separation in optimally doped $BaFe_{1.86}Co_{0.14}As_2$*.

[109] M. C. Boyer, K. Chatterjee, W. D. Wise, G. F. Chen, J. L. Luo, N. L. Wang, and E. W. Hudson, ARXIV: 0806.4400 (2008), *Scanning tunneling microscopy of the 32 K superconductor $(Sr_{1-x}K_x)Fe_2As_2$*.

[110] D. Hsieh, Y. Xia, L. Wray, D. Qian, K. Gomes, A. Yazdani, G. Chen, J. Luo, N. Wang, and M. Hasan, ARXIV: 0812.2289 (2008), *Experimental determination of the microscopic origin of magnetism in parent iron pnictides*.

[111] S. V. Borisenko, M. S. Golden, S. Legner, T. Pichler, C. Dürr, M. Knupfer, G. Yang, S. Abell, H. Berger, and J. Fink, PHYS. REV. LETT. **84**, 4453 (2000), *Joys and pitfalls of Fermi surface mapping in $Bi_2Sr_2CaCu_2O_{8+\delta}$ using angle resolved photoemission*.

[112] Y. Yin, M. Zech, T. L. Williams, X. F. Wang, G. Wu, X. H. Chen, and J. E. Hoffman, PHYS. REV. LETT. **102**, 097002 (2009), *Scanning tunneling spectroscopy and vortex imaging in the iron pnictide superconductor $BaFe_{1.8}Co_{0.2}As_2$*.

[113] V. B. Nascimento, A. Li, D. R. Jayasundara, Y. Xuan, J. O'Neal, S. Pan, T. Y. Chien, B. Hu, X. B. He, G. Li, A. S. Sefat, M. A. McGuire, B. C. Sales, D. Mandrus, M. H. Pan, J. Zhang, R. Jin, and E. W. Plummer, PHYS. REV. LETT. **103**, 076104 (2009), *Surface geometric and electronic structure of $BaFe_2As_2(001)$*.

[114] F. C. Niestemski, V. B. Nascimento, B. Hu, W. Plummer, J. Gillett, S. Sebastian, Z. Wang, and V. Madhavan, ARXIV: 0906.2761 (2009), *Unveiling the atomic and electronic structure at the surface of the parent pnictide $SrFe_2As_2$*.

[115] F. Massee, S. de Jong, Y. Huang, J. Kaas, E. van Heumen, J. B. Goedkoop, and M. S. Golden, PHYS. REV. B **80**, 140507(R) (2009), *Cleavage surfaces of the $BaFe_{2-x}Co_xAs_2$ and $Fe_ySe_{1-x}Te_x$ superconductors: A combined STM plus LEED study*.

[116] M. Gao, F. Ma, Z. Y. Lu, and T. Xiang, PHYS. REV. B **81**, 193409 (2010), *Surface structures of tenary iron arsenides AFe_2As_2 (A=Ba, Sr, or Ca)*.

[117] X. Duan, M. Peressi, and S. Baroni, PHYS. REV. B **75**, 035338 (2007), *Characterizing In and N impurities in GaAs from ab initio computer simulations of (110) cross-sectional STM images*.

[118] C. R. Hammond, THE ELEMENTS, IN HANDBOOK OF CHEMISTRY AND PHYSICS, CRC press, 81st edition, 2004.

[119] A. Lamouri and I. L. Krainsky, SURF. SCI. **278**, 286 (1992), *Angle-resolved inverse photoemission from one monolayer of Ba on W(001)*.

[120] J. B. Pendry, J. PHYS. C SOLID ST. PHYS. **13**, 937 (1980), *Reliable factors for LEED calculations*.

[121] E. van Heumen, J. Vuorinen, K. Koepernik, F. Massee, Y. K. Huang, M. Shi, J. Klei, J. B. Goedkoop, M. Lindroos, J. van den Brink, and M. S. Golden, PHYS. REV. LETT. **106**, 027002 (2010), *Existence, character and origin of surface-related bands in the high temperature iron pnictide superconductor* $BaFe_{2-x}Co_xAs_2$.

[122] Y. Laplace, J. Bobroff, F. Rullier-Albenque, D. Colson, and A. Forget, PHYS. REV. B **80**, 140501(R) (2009), *Atomic coexistence of superconductivity and incommensurate magnetic order in the pnictide* $Ba(Fe_{1-x}Co_x)_2As_2$.

[123] M. R. Norman, PHYSICS **1**, 21 (2008), *High-temperature superconductivity in the iron pnictides*.

[124] G. A. Sawatzky, I. S. Elfimov, J. van den Brink, and J. Zaanen, EPL **86**, 17006 (2009), *Heavy-anion solvation of polarity fluctuations in pnictides*.

[125] Ø. Fischer, M. Kugler, I. Maggio-Aprile, C. Berthod, and C. Renner, REV. MOD. PHYS. **79**, 353 (2007), *Scanning tunneling spectroscopy of high-temperature superconductors*.

[126] K. McElroy, R. W. Simmonds, J. E. Hoffman, D. H. Lee, J. Orenstein, H. Eisaki, S. Uchida, and J. C. Davis, NATURE **422**, 592 (2003), *Relating atomic-scale electronic phenomena to wave-like quasiparticle states in superconducting* $Bi_2Sr_2CaCu_2O_{8+\delta}$.

[127] J. E. Hoffman, K. McElroy, D. H. Lee, K. M. Lang, H. Eisaki, S. Uchida, and J. C. Davis, SCIENCE **297**, 1148 (2002), *Imaging quasiparticle interference in* $Bi_2Sr_2CaCu_2O_{8+\delta}$.

[128] K. K. Gomes, A. N. Pasupathy, A. Pushp, S. Ono, Y. Ando, and A. Yazdani, NATURE **447**, 569 (2007), *Visualizing pair formation on the atomic scale in the high-*T_c *superconductor* $Bi_2Sr_2CaCu_2O_{8+\delta}$.

[129] M. Rotter, M. Tegel, D. Johrendt, I. Schellenberg, W. Hermes, and R. Pöttgen, PHYS. REV. B **78**, 020503(R) (2008), *SDW anomaly at 140 K in the ternary iron arsenide* $BaFe_2As_2$.

[130] J. Dong, H. J. Zhang, G. Xu, Z. Li, G. Li, W. Z. Hu, D. Wu, G. F. Chen, X. Dai, J. L. Luo, Z. Fang, and N. L. Wang, EURO. PHYS. LETT. **83**, 27006 (2009), *Competing orders and spin-density-wave instability in* $La(O_{1-x}F_x)FeAs$.

[131] T. Nomura, S. W. Kim, Y. Kamihara, M. Hirano, P. V. Sushko, K. Kato, M. Takata, A. L. Shluger, and H. Hosono, SUPERCOND. SCI. TECHNOL. **21**, 1225028 (2008), *Crystallographic phase transition and high-T_c superconductivity in LaFeAsO:F*.

[132] C. F. Chen, Z. Li, D. Wu, G. Li, W. Z. Hu, J. Dong, J. L. Luo, and N. L. Wang, PHYS. REV. LETT. **100**, 247002 (2008), *Superconductivity at 41 K and its competition with spin-density-wave instability in layered $CeO_{1-x}F_xFeAs$*.

[133] C. Renner and Ø. Fischer, PHYS. REV. B **51**, 9208 (1995), *Vacuum tunneling spectroscopy and asymmetric density of states of $Bi_2Sr_2CaCu_2O_{8+\delta}$*.

[134] L. Wray, D. Qian, D. Hsieh, Y. Xia, L. Li, J. Checkelsky, A. Pasupathy, K. Gomes, A. Fedorov, G. Chen, J. Luo, A. Yazdani, N. Ong, N. Wang, and M. Hasan, ARXIV: 0808.2185 (2008), *Tightly-bound Cooper pair, quasiparticle kinks and clues on the pairing potential in a high T_c FeAs Superconductor*.

[135] M. C. Boyer, W. D. Wise, K. Chatterjee, M. Yi, T. Kondo, T. Takeuchi, H. Ikuta, and E. W. Hudson, NATURE PHYSICS **3**, 802 (2007), *Imaging the two gaps of the high-temperature superconductor $Bi_2Sr_2CuO_{6+x}$*.

[136] M.-H. Julien, H. Mayaffre, M. Horvatic, C. Berthier, X. D. Zhang, W. Wu, G. Chen, N. Wang, and J. Luo, EURO. PHYS. LETT. **87**, 37001 (2009), *Homogeneous vs. inhomogeneous coexistence of magnetic order and superconductivity probed by NMR in Co- and K-doped iron pnictides*.

[137] A. J. Drew, C. Niedermayer, P. J. Baker, F. L. Pratt, S. J. Blundell, T. Lancaster, R. H. Liu, G. Wu, X. H. Chen, I. Watanabe, V. K. Malik, A. Dubroka, M. Rössle, K. W. Kim, C. Bained, and C. Bernard, NATURE MATERIALS **8**, 2396 (2009), *Coexistence of static magnetism and superconductivity in $SmFeAsO_{1-x}F_x$ as revealed by muon spin rotation*.

[138] J. S. Kim, S. Khim, L. Yan, N. Manivannan, Y. Liu, I. Kim, G. R. Stewart, and K. H. Kim, J. PHYS. COND. MAT. **21**, 102203 (2009), *Evidence for coexistence of superconductivity and magnetism in single crystals of Co-doped $SrFe_2As_2$*.

[139] J. T. Park, D. S. Inosov, C. Niedermayer, G. L. Sun, D. Haug, N. B. Christensen, R. Dinnebier, A. Boris, A. J. Drew, L. Schulz, T. Shapoval, U. Wolff, V. Neu, X. Yang, C. T. Lin, B. Keimer, and V. Hinkov, PHYS. REV. LETT. **102**, 117006 (2009), *Electronic phase separation in the slightly underdoped $Ba_{1-x}K_xFe_2As_2$*.

[140] S. Takeshita and R. Kadono, NEW J. PHYS. **11**, 035006 (2009), *Competition/coexistence of magnetism and superconductivity in iron pnictides probed by muon spin rotation*.

[141] M. Buchanan, NATURE **409**, 8 (2001), *Mind the pseudogap*.

[142] T. Timusk and B. Statt, REP. PROG. PHYS. **62**, 61 (1999), *The pseudogap in high-temperature superconductors: an experimental survey*.

[143] C. Hess, A. Kondrat, A. Narduzzo, J. E. Hamann-Borrero, R. Klingeler, J. Werner, G. Behr, and B. Büchner, EPL **87**, 17005 (2009), *The intrinsic electronic phase diagram of iron-oxypnictide superconductors*.

[144] Y. Nakai, K. Ishida, Y. Kamihara, M. Hirano, and H. Hosono, J. PHYS. SOC. JPN. **77**, 073701 (2008), *Evolution from itinerant antiferromagnet to unconventional superconductor with fluorine doping in LaFeAs($O_{1-x}F_x$) revealed by ^{75}As and ^{139}La nuclear magnetic resonance*.

[145] H. J. Grafe, D. Paar, G. Lang, N. J. Curri, G. Behr, J. Werner, J. Hamann-Borrero, C. Hess, N. Leps, R. Klingeler, and B. Büchner, PHYS. REV. LETT. **101**, 047003 (2008), *^{75}As NMR studies of superconducting $LaFeAsO_{0.9}F_{0.1}$*.

[146] T. Sato, S. Souma, K. Nakayama, K. Terashima, K. Sugawara, T. Takahashi, Y. Kamihara, M. Hirano, and H. Hosono, J. PHYS. SOC. JPN. **77**, 063708 (2008), *Superconducting gap and pseudogap in iron-based layered superconductor La($O_{1-x}F_x$)FeAs*.

[147] T. Y. Chen, Z. Tesanovic, R. H. Liu, X. H. Chen, and C. L. Chien, NATURE **453**, 1224 (2008), *A BCS-like gap in the superconductor $SmFeAsO_{0.85}F_{0.15}$*.

[148] Y.-M. Xu, P. Richard, K. Nakayama, T. Kawahara, Y. Sekiba, T. Qian, M. Neupane, S. Souma, T. Sato, T. Takahashi, H. Luo, H.-H. Wen, G.-F. Chen, N.-L. Wang, Z. Wang, Z. Fang, X. Dai, and H. Ding, ARXIV: 0905.4467 (2009), *Fermi surface dichotomy of superconducting gap and pseudogap in underdoped pnictides*.

[149] Y. S. Kwon, J. B. Hong, Y. R. Jang, H. J. Oh, Y. Y. Song, B. H. Min, T. Iizuka, S. Kimura, A. V. Balatsky, and Y. Bang, ARXIV:1007.3617 (2010), *Pseudogap of superconducting correlation origin in iron-pnictide superconductor $Ba_{0.6+\delta}K_{0.4-\delta}Fe_2As_2$*.

[150] D. H. Torchinsky, G. F. Chen, J. L. Luo, N. L. Wang, and N. Gedik, PHYS. REV. LETT. **105**, 027005 (2010), *Band-dependent quasiparticle dynamics in single crystals of the $Ba_{0.6}K_{0.4}Fe_2As_2$ superconductor revealed by pump-probe spectroscopy*.

[151] L. Craco and M. S. Laad, ARXIV:1001.3273 (2010), *Theory of normal state pseudogap behavior in $FeSe_{1-x}Te_x$*.

[152] H. Zhang, J. Dai, Y. Zhang, D. Qu, H. Ji, G. Wu, X. F. Wang, X. H. Chen, B. Wang, C. Zeng, J. Yang, and J. G. Hou, PHYS. REV. B **104520**, 2010 (81), *$\sqrt{2} \times \sqrt{2}$ structure and charge inhomogeneity at the surface of superconducting $BaFe_{2-x}Co_xAs_2$ (x=0-0.32)*.

[153] S. H. Pan, E. W. Hudson, and J. C. Davis, APPL. PHYS. LETT. **73**, 2992 (1998), *Vacuum tunneling of superconducting quasiparticles from atomically sharp scanning tunneling microscopy tips*.

[154] F. Hardy, P. Burger, T. Wolf, R. A. Fisher, P. Schweiss, P. Adelmann, R. Heid, R. Fromknecht, R. Eder, D. Ernst, H. v. Löhneysen, and C. Meingast, EPL **91**, 47008 (2010), *Doping evolution of superconducting gaps and electronic densities of states in $Ba(Fe_{1-x}Co_x)_2As_2$ iron pnictides*.

[155] S. F. Sebastian, J. Gillet, N. Harrison, P. H. Lau, D. J. Singh, C. H. Mielke, and G. G. Lonzarich, J. PHYS. COND. MAT. **20**, 422203 (2008), *Quantum oscillations in the parent magnetic phase of an iron arsenide high temperature superconductor*.

[156] J. G. Analytis, R. D. McDonald, J. H. Chu, S. C. Riggs, A. F. Bangura, C. Kucharczyk, M. Johannes, and I. R. Fisher, PHYS. REV. B **80**, 064507 (2009), *Quantum oscillations in the parent pnictide $BaFe_2As_2$: Itinerant electrons in the reconstructed state*.

[157] S. de Jong, E. van Heumen, S. Thirupathaiah, R. Huisman, F. Massee, J. B. Goedkoop, R. Ovsyannikov, J. Fink, H. A. Dürr, A. Gloskovskii, H. S. Jeevan, P. Gegenwart, A. Erb, L. Patthey, M. Shi, R. Follath, A. Varykhalov, and M. S. Golden, EPL **89**, 27007 (2010), *Droplet-like Fermi surfaces in the anti-ferromagnetic phase of $EuFe_2As_2$, an Fe-pnictide superconductor parent compound*.

[158] N. P. Armitage, P. Fournier, and R. L. Greene, REV. MOD. PHYS. **82**, 2421 (2010), *Progress and perspectives on electron-doped cuprates*.

[159] M. L. Tacon, A. Sacuto, A. Georges, G. Kotliar, Y. Gallais, D. Colson, and A. Forget, NATURE PHYSICS **2**, 537 (2006), *Two energy scales and two distinct quasiparticle dynamics in the superconducting state of underdoped cuprates*.

[160] H. Eisaki, N. Kaneko, D. L. Feng, A. Damascelli, P. K. Mang, K. M. Shen, Z.-X. Shen, and M. Greven, PHYS. REV. B **69**, 064512 (2004), *Effect of chemical inhomogeneity in bismuth-based copper oxide superconductors*.

[161] A. Y. Liu, I. I. Mazin, and J. Kortus, PHYS. REV. LETT. **87**, 087005 (2001), *Beyond Eliashberg superconductivity in MgB_2: Anharmonicity, two-phonon scattering, and multiple gaps*.

[162] V. Brouet, F. Rullier-Albenque, M. Marsi, B. Mansart, M. Aichhorn, S. Biermann, J. Faure, L. Perfetti, A. Taleb-Ibrahimi, P. L. Feèvre, F. Bertran, A. Forget, and D. Colson, PHYS. REV. LETT. **105**, 087001 (2010), *Significant reduction of electronic correlations upon isovalent Ru substitution of $BaFe_2As_2$*.

[163] R. T. Gordon, C. Martin, H. Kim, N. Ni, M. A. Tanatar, J. Schmalian, I. I. Mazin, S. L. Bud'ko, P. C. Canfield, and R. Prozorov, PHYS. REV. B **79**, 100506(R) (2009), *London penetration depth in single crystals of $Ba(Fe_{1-x}Co_x)_2As_2$ spanning underdoped to overdoped compositions*.

[164] T.-H. Kim, R. Jin, L. R. Walker, J. Y. Howe, M. H. Pan, J. F. Wendelken, J. R. Thompson, A. S. Sefat, M. A. McGuire, B. C. Sales, D. Mandrus, and A. P. Li, PHYS. REV. B **80**, 214518 (2009), *Probing microscopic variations of superconductivity on the surface of* $Ba(Fe_{1-x}Co_x)_2As_2$.

[165] B. Sacépé, C. Chapelier, T. I. Baturina, V. M. Vinokur, M. R. Baklanov, and M. Sanquer, PHYS. REV. LETT. **101**, 157006 (2008), *Disorder-induced inhomogeneities of the superconducting state close to the superconductor-insulator transition*.

[166] H. Wadati, I. Elfimov, and G. A. Sawatzky, PHYS. REV. LETT. **105**, 157004 (2010), *Where are the extra d electrons in transition-metal substituted Fe pnictides?*

[167] T. Kimura and Y. Tokura, ANNU. REV. MATER. SCI. **30**, 451 (2000), *Layered magnetic materials*.

[168] Y. Tokura, REP. PROG. PHYS. **69**, 797 (2006), *Critical features of colossal magnetoresistive manganites*.

[169] A. Fert, REV. MOD. PHYS **80**, 1517 (2008), *Nobel lecture: Origin, development, and future of spintronics*.

[170] P. A. Grünberg, REV. MOD. PHYS. **80**, 1531 (2008), *Nobel lecture: From spin waves to giant magnetoresistance and beyond*.

[171] S. Jin, T. H. Tiefel, M. McCormack, R. A. Fastnacht, R. Ramesh, and L. H. Chen, SCIENCE **264**, 413 (1994), *Thousandfold Change in Resistivity in Magnetoresistive La-Ca-Mn-O Films*.

[172] J. B. Goodenough and J. M. Longo, MAGNETIC AND OTHER PROPERTIES OF OXIDES AND RELATED COMPOUNDS, Springer (Berlin), 1970.

[173] H. Zheng, Q. A. Li, K. E. Gray, and J. F. Mitchell, PHYS. REV. B **78**, 155103 (2008), *Charge and orbital ordered phases of* $La_{2-2x}Sr_{1+2x}Mn_2O_{7-\delta}$.

[174] S. Larochelle, A. Mehta, L. Lu, P. K. Mang, O. P. Vajk, N. Kaneko, J. W. Lynn, L. Zhou, and M. Greven, PHYS. REV. B **71**, 024435 (2005), *Structural and magnetic properties of the single-layer manganese oxide* $La_{1-x}Sr_{1+x}MnO_4$.

[175] J. B. Goodenough, PHYSICAL REVIEW **100**, 564 (1955), *Theory of the role of covalence in the perovskite-type manganites* $[La,M(II)]MnO_3$.

[176] P. W. Anderson, PHYSICAL REVIEW **79**, 350 (1950), *Antiferromagnetism. Theory of superexchange interaction*.

[177] P. W. Anderson and H. Hasegawa, PHYSICAL REVIEW **100**, 675 (1955), *Consideration on double exchange*.

[178] P. G. de Gennes, PHYSICAL REVIEW **118**, 141 (1960), *Effects of double exchange in magnetic crystals*.

[179] H. Y. Hwang, S. W. Cheong, P. G. Radaelli, M. Marezio, and B. Batlogg, PHYS. REV. LETT. **75**, 914 (1995), *Lattice effects on the magnetoresistance in doped $LaMnO_3$*.

[180] R. D. Shannon, ACTA CRYSTALLOGRAPHICA A **32**, 751 (1976), *Revised effective ionic radii and systematic studies of interatomic distances in halides and chalcogenides*.

[181] A. J. Millis, P. B. Littlewood, and B. I. Shraiman, PHYS. REV. LETT. **74**, 5144 (1995), *Double exchange alone does not explain the resistivity of $La_{1-x}Sr_xMnO_3$*.

[182] H. Röder, J. Zang, and A. R. Bishop, PHYS. REV. LETT. **76**, 1356 (1996), *Lattice effects in the colossal-magnetoresistance manganites*.

[183] A. Urishibara, Y. Moritomo, T. Arima, A. Asamitsu, G. Kido, and Y. Tokura, PHYS. REV. B **51**, 14103 (1995), *Insularot-metal transition and giant magnetoresistance in $La_{1-x}Sr_xMnO_3$*.

[184] Y. Okimoto, T. Katsufuji, T. Ishikawa, T. Arima, and Y. Tokura, PHYS. REV. B **55**, 4206 (1997), *Variation of electronic structure in $La_{1-x}Sr_xMnO_3$ ($0 \leq x \leq 0.3$) as investigated by optical conductivity spectra*.

[185] V. Caignaert, E. Suard, A. Maignan, C. Simon, and B. Raveau, JMMM **153**, L260 (1996), *Neutron diffraction evidence for an antiferromagnetic ordering in the CMR manganites $Pr_{0.7}Ca_{0.3-x}Sr_xMnO_3$*.

[186] P. G. Radaelli, G. Iannone, M. Marezio, H. Y. Hwang, S. W. Cheong, J. D. Jorgensen, and D. N. Argyriou, PHYS. REV. B **56**, 8265 (1997), *Structural effects on the magnetic and transport properties of perovskite $A_{1-x}A'_xMnO_3$ (x=0.25, 0.30)*.

[187] Y. Moritomo, PHYS. REV. B **51**, 3297 (1995), *Magnetic and electronic properties in hole-doped manganese oxides with layered structures: $La_{1-x}Sr_{1+x}MnO_4$*.

[188] Y. Moritomo, A. Asamitsu, H. Kuwahara, and Y. Tokura, NATURE **380**, 141 (1996), *Giant magnetoresistance of manganese oxides with a layered perovskite structure*.

[189] T. G. Perring, G. Aeppli, Y. Moritomo, and Y. Tokura, PHYS. REV. LETT. **78**, 3197 (1997), *Antiferromagnetic short range order in a two-dimensional manganite exhibiting giant magnetoresistance*.

[190] N. F. Mott, METAL-INSULATOR TRANSITIONS, Taylor and Francis (London), 1974.

[191] F. A. Chudnovskii, J. PHYS. C: SOLID STATE PHYS. **11**, L99 (1978), *The minimum conductivity and electron localisation in the metallic phase of transition metal compounds in the vicinity of a metal-insulator transition*.

[192] T. Ishikawa, K. Tobe, T. Kimura, T. Katsufuji, and T. Tokura, PHYS. REV. B **62**, 12354 (2000), *Optical study on the doping and temperature dependence of the anisotropic electronic structure in bilayered manganites, $La_{2-2x}Sr_{1+2x}Mn_2O_7$ (0.3≤x≤0.5)*.

[193] T. Takahashi, N. Kida, and M. Tonouchi, APPL. PHYS. LETT. **83**, 4303 (2003), *Observation of a pseudogap at terahertz frequencies in the ferromagnetic metallic phase of $La_{2-2x}Sr_{1+2x}Mn_2O_7$ (x=0.3)*.

[194] K. Takahashi, N. Kida, and M. Tonouchi, JMMM **272-276**, e669 (2004), *Optical evidence of a pseudogap in the ferromagnetic metallic phase of the bilayered manganite*.

[195] J. F. Mitchell, D. N. Argyriou, J. D. Jorgensen, D. G. Hinks, C. D. Potter, and S. D. Bader, PHYS. REV. B **55**, 63 (1997), *Charge delocalization and structural response in layered $La_{1.2}Sr_{1.8}Mn_2O_7$: Enhanced distortion in the metallic regime*.

[196] B. J. Campbell, R. Osborn, D. N. Argyriou, L. Vasiliu-Doloc, J. F. Mitchell, S. K. Sinha, U. Ruett, C. D. Ling, Z. Islam, and J. W. Lynn, PHYS. REV. B **65**, 014427 (2001), *Structure of nanoscale polaron correlations in $La_{1.2}Sr_{1.8}Mn_2O_7$*.

[197] L. Vasiliu-Doloc, S. Rosenkranz, R. Osborn, S. K. Sinha, J. W. Lynn, J. Mesot, O. H. Seeck, G. Preosti, A. J. Fedro, and J. F. Mitchell, PHYS. REV. LETT. **83**, 4393 (1999), *Charge Melting and Polaron Collapse in $La_{1.2}Sr_{1.8}Mn_2O_7$*.

[198] B. J. Campbell, S. K. Sinha, R. Osborn, S. Rosenkranz, J. F. Mitchell, D. N. Argyriou, L. Vasiliu-Doloc, O. H. Seeck, and J. W. Lynn, PHYS. REV. B **67**, 020409(R) (2003), *Polaronic orbital polarization in a layered colossal magnetoresistive manganite*.

[199] F. Weber, A. Aliouane, H. Zheng, J. F. Mitchell, D. N. Argyriou, and D. Reznik, NATURE MATERIALS **8**, 798 (2009), *Signature of checkerboard fluctuations in the phonon spectra of a possible polaronic metal $La_{1.2}Sr_{1.8}Mn_2O_7$*.

[200] Y. D. Chuang, A. D. Gromko, D. S. Dessau, T. Kimura, and Y. Tokura, SCIENCE **292**, 1509 (2001), *Fermi surface nesting and nanoscale fluctuating charge/orbital ordering in colossal magnetoresistive oxides*.

[201] M. Kubota, K. Ono, and T. Yoshida, J. ELECTRON SPEC. REL. PHENOM. **156-158**, 398 (2007), *Electronic structure of layered manganite $La_{1.1}Sr_{1.9}Mn_2O_7$ studied by angle-resolved photoemission spectroscopy at low temperatures*.

[202] N. Mannella, W. L. Yang, X. J. Zhou, H. Zheng, J. F. Mitchell, J. Zaanen, T. P. Devereaux, N. Nagaosa, Z. Hussain, and Z.-X. Shen, NATURE **438**, 474 (2005), *Nodal quasiparticles in pseudogapped mangetoresistive manganites*.

[203] N. Mannella, C. H. Booth, A. Rosenhahn, B. C. Sell, A. Nambu, S. Marchesini, B. S. Mun, S.-H. Yang, M. Watanabe, K. Ibrahim, E. Arenholz, A. Young, J. Guo,

Y. Tomioka, and C. S. Fadley, PHYS. REV. B **77**, 125134 (2008), *Temperature-dependent evolution of the electronic and local atomic structure in the cubic colossal magnetoresistive manganite $La_{1-x}Sr_xMnO_3$*.

[204] Z. Sun, Y. D. Chuang, A. V. Fedorov, J. F. Douglas, D. Reznik, F. Weber, N. Aliouane, D. N. Argyriou, H. Zheng, J. F. Mitchell, T. Kimura, Y. Tokura, A. Revcolevschi, and D. S. Dessau, PHYS. REV. LETT. **97**, 05601 (2006), *Quasiparticlelike peaks, kinks, and electron-phonon coupling at the (π, 0) regions in the CMR oxide $La_{2-2x}Sr_{1+2x}Mn_2O_7$*.

[205] Z. Sun, J. F. Douglas, A. V. Fedorov, Y. D. Chuang, H. Zheng, J. F. Mitchell, and D. S. Dessau, NATURE PHYSICS **3**, 248 (2007), *A local metallic state in globally insulating $La_{1.24}Sr_{1.76}Mn_2O_7$ well above the metal-insulator transition*.

[206] S. de Jong, Y. Huang, I. Santoso, F. Massee, R. Follath, O. Schwarzkopf, L. Patthey, M. Shi, and M. S. Golden, PHYS. REV. B **76**, 235117 (2007), *Quasiparticles and anomalous temperature dependence of the low-lying states in the colossal magnetoresistant oxide $La_{2-2x}Sr_{1+2x}Mn_2O_7$ (x=0.36) from angle-resolved photoemission*.

[207] C. D. Ling, J. E. Millburn, J. F. Mitchell, D. N. Argyriou, J. Linton, and H. N. Bordallo, PHYS. REV. B **62**, 15096 (2000), *Interplay of spin and orbital ordering in the layered colossal magnetoresistance manganite $La_{2-2x}Sr_{1+2x}Mn_2O_7$ ($0.5 \leq x \leq 1.0$)*.

[208] F. Loviat, H. Rønnow, C. Renner, G. Aeppli, T. Kimura, and Y. Tokura, NANOTECHNOLOGY **18**, 044020 (2007), *The surface layer of cleaved bilayer manganites*.

[209] H. M. Rønnow, C. Renner, G. Aeppli, T. Kimura, and Y. Tokura, NATURE **440**, 1025 (2006), *Polarons and confinement of electronic motion to two dimensions in a layered manganite*.

[210] S. D. Santis, B. Bryant, M. Warner, H. Wang, T. Kimura, Y, Tokura, C. Renner, A. Bianconi, and G. Aeppli, J. SUPERCOND. NOV. MAGN. **20**, 531 (2007), *Imaging of Polarons in Ferromagnetic Bilayered Manganites by Scanning Tunnelling Microscopy*.

[211] D. Mazur, K. E. Gray, J. F. Zasadzinski, L. Ozyuzer, I. S. Beloborodov, H. Zheng, and J. F. Mitchell, PHYS. REV. B **76**, 193102 (2007), *Redistribution of the density of states due to Coulomb interactions in $La_{2-2x}Sr_{1+2x}Mn_2O_7$*.

[212] J. W. Freeland, K. E. Gray, L. Ozyozer, P. Berghuis, E. Badica, J. KAvich, H. Zheng, and J. F. Mitchell, NATURE MATERIALS **4**, 62 (2004), *Full bulk spin polarization and intrinsic tunnel barriers at the surface of layered manganites*.

[213] J. W. Freeland, J. J. Kavich, K. E. Gray, L. Ozyuzer, H. Zheng, J. F.Mitchell, M. P. Warusawithana, P. Ryan, X. Zhai, R. H. Kodama, and J. N. Eckstein, J.

PHYS. COND. MAT. **19**, 315210 (2007), *Suppressed magnetization at the surfaces and interfaces of ferromagnetic metallic manganites*.

[214] V. B. Nascimento, J. W. Freeland, R. Saniz, R. G. Moore, D. Mazur, H. Liu, M. H. Pan, J. Rundgren, K. E. Gray, R. A. Rosenberg, H. Zheng, J. F. Mitchell, A. J. Freeman, K. Veltruska, and E. W. Plummer, PHYS. REV. LETT. **103**, 227201 (2009), *Surface-stabilized nonferromagnetic ordering of a layered ferromagnetic manganite*.

[215] M. Konoto, T. Kohashi, K. Koike, T. Arima, Y. Kaneko, T. Kimura, and Y. Tokura, PHYS. REV. LETT. **93**, 107201 (2004), *Direct imaging of temperature-dependent layered antiferromagnetism of a magnetic oxide*.

[216] S. de Jong, F. Massee, Y. Huang, M. Gorgoi, F. Schaefers, J. Fink, A. T. Boothroyd, D. Prabhakaran, J. B. Goedkoop, and M. S. Golden, PHYS. REV. B **80**, 205108 (2009), *High-resolution hard x-ray photoemission investigation of $La_{2-2x}Sr_{1+2x}Mn_2O_7$ (0.30<x<0.50): Microscopic phase separation and surface electronic structure of a bilayer colossal magnetoresistance manganite*.

[217] C. Şen, G. Alvarez, and E. Dagotto, PHYS. REV. LETT. **98**, 127202 (2007), *Competing ferromagnetic and charge-ordered states in models for manganites: The origin of the colossal magnetoresistance effect*.

[218] D. V. Evtushinsky, D. S. Isonov, G. Urbanik, V. B. Zabolotnyy, R. Schuster, P. Sass, T. Hänke, C. Hess, B. Büchner, R. Follath, P. Reutles, R. Revcolevschi, A. A. Kordyuk, and S. V. Borisenko, PHYS. REV. LETT. **105**, 147201 (2010), *Bridging charge-orbital ordering and Fermi surface instabilities in half-doped single-layered manganite $La_{0.5}Sr_{1.5}MnO_4$*.

[219] G. Allodli, M. Bimbi, R. D. Renzi, C. Baumann, and M. Apostu, PHYS. REV. B **78**, 064420 (2008), *Magnetic order in the double-layer manganites $(La_{1-x}Pr_z)_{1.2}Sr_{1.8}Mn_2O_7$: Intrinsic properties and role of intergrowth*.

[220] C. D. Potter, M. Swiatek, S. D. Bader, D. N. Argyriou, J. F. Mitchell, D. J. Miller, D. G. Hinks, and J. D. Jorgensen, PHYS. REV. B **57**, 72 (1998), *Two-dimensional intrinsic and extrinsic ferromagnetic behavior of layered $La_{1.2}Sr_{1.8}Mn_2O_7$ single crystals*.

[221] S. D. Bader, R. M. Osgood, D. J. Miller, J. F. Mitchell, and J. S. Jiang, J. APPL. PHYS. **83**, 6385 (1998), *Role of intergrowths in the properties of naturally layered manganite single crystals (invited)*.

[222] R. Seshadri, M. Hervieu, C. Martin, A. Maignan, B. Domenges, and B. Raveau, CHEM. MATTER. **9**, 1778 (1997), *Study of the layered magnetoresistive perovskite $La_{1.2}Sr_{1.8}Mn_2O_7$ by high-resolution electron microscopy and synchrotron x-ray powder diffraction*.

[223] J. Sloan, P. D. Battle, M. A. Green, M. J. Rosseinsky, and J. F. Vente, J. SOL. STATE. CHEM. **138**, 135 (1998), *A HRTEM study of the Ruddlesden-Popper compositions $Sr_2LnMn_2O_7$ (Ln = Y, La, Nd, Eu, Ho)*.

[224] J. van den Brink, P. Horsch, and A. M. Oleś, PHYS. REV. LETT. **85**, 5174 (2000), *Photoemission spectra of $LaMnO_3$ controlled by orbital excitations*.

[225] J. Bała, G. A. Sawatzky, A. M. Oleś, and A. Macridin, PHYS. REV. LETT. **87**, 067204 (2001), *Quantum decoherence in the spectral function of undoped $LaMnO_3$*.

[226] J. Bała, A. M. Oleś, and P. Horsch, PHYS. REV. B **65**, 134420 (2002), *Quasiparticles and the structure of orbital polarons in ferromagnetic $LaMnO_3$*.

[227] J. van den Brink, PHYS. REV. LETT. **87**, 217202 (2001), *Orbital excitations in $LaMnO_3$*.

[228] A. Daoud-Aladine, J. Rodríguez-Carvajal, L. Pinsard-Gaudart, M. T. Fernández-Díaz, and A. Revcolevschi, PHYS. REV. LETT. **89**, 097205 (2002), *Zener polaron ordering in half-doped manganites*.

[229] A. Daoud-Aladine, C. Perca, L. Pinsard-Gaudart, and J. Rodríguez-Carvajal, PHYS. REV. LETT. **101**, 166404 (2008), *Zener polaron ordering variants induced by A-site ordering in half-doped manganites*.

[230] C. Frontera, J. L. García-Muños, A. E. Carrillo, M. Hervieu, A. Calleja, X. G. Capdevila, M. T. Casias, and C. Ritter, PHYSICA B **350**, 48 (2004), *Charge and Zener polaron order in $Bi_{0.75}Sr_{0.25}MnO_3$: a comparison with $Bi_{0.75}Ca_{0.25}MnO_3$*.

[231] K. Wohlfeld, A. M. Oleś, and P. Horsch, PHYS. REV. B **79**, 224433 (2009), *Orbitally induced string formation in the spin-orbital polarons*.

[232] S. J. May, P. J. Ryan, J. L. Robertson, J. W. Kim, T. S. Santos, E. Karapetrova, J. L. Zarestky, X. Zhai, S. G. E. te Velthuis, J. N. Eckstein, S. D. Bader, and A. Bhattacharya, NATURE MATERIALS **8**, 892 (2009), *Enhanced ordering temperatures in antiferromagnetic manganite superlattices*.

[233] R. Gladyshevskii, N. Musolino, and R. Flükiger, PHYS. REV. B **70**, 184522 (2004), *Structural origin of the low superconducting anisotropy of $Bi_{1.7}Pb_{0.4}Sr_2Ca_{0.9}Cu_2O_8$ crystals*.

[234] C. Renner and Ø. Fischer, PROC. SPIE **2158**, 135 (1994), *Vacuum tunneling spectroscopy of superconducting $Bi_2Sr_2CaCu_2O_8$ using scanning tunneling microscopy*.

[235] C. Howald, P. Fournier, and A. Kapitulnik, PHYS. REV. B **64**, 100504(R) (2001), *Inherent inhomogeneities in tunneling spectra of $Bi_2Sr_2CaCu_2O_{8-x}$ crystals in the superconducting state*.

[236] K. Lang, V. Madhavan, J. E. Hoffman, E. W. Hiudson, H. Eisaki, S. Uchida, and J. C. Davis, NATURE **415**, 412 (2002), *Imaging the granular structure of high-T_c superconductivity in underdoped $Bi_2Sr_2CaCu_2O_{8+\delta}$*.

[237] B. W. Hoogenboom, K. Kadowaki, B. Revaz, and Ø. Fischer, PHYSICA C **391**, 376 (2003), *Homogeneous samples of $Bi_2Sr_2CaCu_2O_{8+\delta}$*.

[238] K. McElroy, J. Lee, J. A. Slezak, D. H. Lee, H. Eisaki, S. Uchida, and J. C. Davis, SCIENCE **309**, 1048 (2005), *Atomic-scale sources and mechanism of nanoscale electronic disorder in $Bi_2Sr_2CaCu_2O_{8+\delta}$*.

[239] G. Kinoda, T. Hasegawa, S. Nakao, T. Hanaguri, K. Kitazawa, K. Shimizu, J. Shimoyama, and K. Kishio, PHYS. REV. B **67**, 224509 (2003), *Observations of electronic inhomogeneity in heavily Pb-doped $Bi_2Sr_2CaCu_2O_y$ single crystals by scanning tunneling microscopy*.

[240] K. McElroy, D. H. Lee, J. E. Hoffman, K. M. Lang, J. Lee, E. W. Hudson, H. Eisaki, S. Uchida, and J. C. Davis, PHYS. REV. LETT. **94**, 197005 (2005), *Coincidence of checkerboard charge order and antinodal state decoherence in strongly underdoped superconducting $Bi_2Sr_2CaCu_2O_{8+\delta}$*.

[241] Y. Matsui, H. Maeda, Y. Tanaka, and S. Horiuchi, JAP. J. OF APPL. PHYS. **29**, L361 (1988), *High-resolution electron microscopy of modulated structure in the new high-T_c superconductors of the Bi-Sr-Ca-Cu-O system*.

[242] T. M. Shaw, S. A. Shivashankar, S. J. L. Placa, J. J. Cuomo, T. R. McGuire, R. A. Roy, K. H. Kelleher, and D. S. Yee, PHYS. REV. B **37**, 9856 (1988), *Incommensurate structure in the Bi-Sr-Ca-Cu-O 80-K superconductor*.

[243] N. Fukushima, H. Niu, S. Nakamura, S. Takeno, M. Hayashi, and K. Ando, PHYSICA C **159**, 777 (1989), *Structural modulation and superconducting properties in $Bi_{2-x}Pb_xSr_2CaCu_2O_{8+\delta}$ and $Bi_{2-y}Pb_ySr_2YCu_2O_{8+\delta}$*.

[244] O. Eibl, PHYSICA C **175**, 419 (1991), *Displacive modulation and chemical composition of (Bi,Pb)$_2Sr_2Ca_{n-1}Cu_nO_{2n+4}$ (n=2, 3) high T_c superconductors*.

[245] N. Musolino, S. Bals, G. van Tenderloo, N. Clayton, E. Walker, and R. Flükiger, PHYSICA C **399**, 1 (2003), *Modulation-free phase in heavily Pb-doped (Bi,Pb)2212 crystals*.

[246] A. V. Balatsky, M. I. Salkola, and A. Rosengren, PHYS. REV. B **51**, 15547 (1995), *Impurity-induced virtual bound state in d-wave superconductors*.

[247] M. I. Salkola, A. V. Balatsky, and D. J. Scalapino, PHYS. REV. LETT. **77**, 1841 (1996), *Theory of scanning tunneling microscopy probe of impurity states in a d-wave superconductor*.

[248] E. W. Hudson, V. Madhaven, K. McElroy, J. E. Hoffman, K. M. Lang, H. Eisaki, S. Uchida, and J. C. Davis, PHYSICA B **329-333**, 1365 (2003), *STM study of novel resonances in $Bi_2Sr_2CaCu_2O_{8+\delta}$*.

[249] G. Kinoda, H. Mashima, K. Shimizu, J. Shimoyama, K. Kishio, and T. Hasegawa, PHYS. REV. B **71**, 020502(R) (2005), *Direct determination of localized impurity levels located in the blocking layers of $Bi_2Sr_2CaCu_2O_y$ using scanning tunneling microscopy/spectroscopy*.

[250] K. Chatterjee, M. C. Boyer, W. D. Wise, T. Kondo, T. Takeuchi, H. Ikuta, and E. W. Hudson, NATURE PHYSICS **4**, 108 (2008), *Visualization of the interplay between high-temperature superconductivity, the pseudogap and impurity resonances*.

[251] C. Howald, H. Eisaki, N. Kaneko, and A. Kapitulnik, COND-MAT/0201546 (2002), *Coexistence of charged stripes and superconductivity in $Bi_2Sr_2CaCu_2O_{8+\delta}$*.

[252] C. Howald, H. Eisaki, N. Kaneko, M. Greven, and A. Kapitulnik, PHYS. REV. B **67**, 014533 (2003), *Periodic density-of-states modulations in superconducting $Bi_2Sr_2CaCu_2O_{8+\delta}$*.

[253] J. P. Ibe, P. P. B. Jr., S. L. Brandow, R. A. Brizzolara, N. A. Burnham, D. P. DiLella, K. P. Lee, C. R. K. Marrian, and R. J. Colton, J. VAC. SCI. TECHNOL. A **8**, 3570 (1990), *On the electrochemical etching of tips for scanning tunneling microscopy*.

[254] M. Klein and G. Schwitzgebel, REV. SCI. INSTRUM. **68**, 8 (1997), *An improved lamellae drop-off technique for sharp tip preparation in scanning tunneling microscopy*.

[255] R. Zhang and D. G. Ivey, J. VAC. SCI. TECHNOL. B **14**, 1 (1996), *Preparation of sharp polycrystalline tungsten tips for scanning tunneling microscopy imaging*.

[256] A.-S. Lucier, *Preparation and Characterization of Tungsten Tips Suitable for Molecular Electronics Studies*, Master's thesis, McGill University, Montréal, Canada, 2004.

[257] L. A. Hockett and S. E. Creager, REV. SCI. INSTRUM. **64**, 263 (1993), *A convenient method for removing surface oxides from W tips*.

[258] A. Cricenti, E. Paparazzo, M. A. Scarselli, L. Moretto, and S. Selci, REV. SCI. INSTRUM. **65**, 1558 (1994), *Preparation and characterization of tungsten tips for scanning tunneling microscopy*.

[259] O. Albrektsen, H. W. M. Salemink, K. A. Mørch, and A. R. ThöIen, J. VAC. SCI. TECHNOL. B **12**, 3187 (1994), *Reliable tip preparation for high resolution scanning tunneling microscopy*.

[260] I. Ekvall, E. Wahlström, D. Claesson, H. Olin, and E. Olsson, MEAS. SCI. TECHNOL. **10**, 11 (1999), *Preparation and characterization of electrochemically etched W tips for STM*.

[261] H. F. Ding, J. E. Pearson, D. Li, R. Cheng, F. Y. Fradin, and S. D. Bader, REV. SCI. INSTRUM **76**, 123703 (2005), *Electron-beam tip/sample heating device for a scanning tunneling microscopy*.

[262] K. C. Li and C. Y. Wang, TUNGSTEN: ITS HISTORY, GEOLOGY, ORE-DRESSING, METALLURGY, CHEMISTRY, ANALYSIS, APPLICATIONS, AND ECONOMICS, Reinhold Publishing Corporation, 3rd edition, 1955.

[263] S. W. H. Yih and C. T. Wang, TUNGSTEN: SOURCES, METALLURGY, PROPERTIES, AND APPLICATIONS, Springer, 1979.

[264] J. Kubby and B. M. Siegel, J. VAC. SCI. TECHNOL. B **4**, 120 (1986), *High resolution structuring of emitter tips for the gaseous field ionization source*.

[265] D. Biegelsen, F. A. Ponce, J. C. Tramontana, and S. M. Koch, APPL. PHYS. LETT. **50**, 696 (1987), *Ion milled tips for scanning tunneling microscopy*.

[266] R. H. Fowler and L. Nordheim, PROCEEDINGS OF THE ROYAL SOCIETY OF LONDON **119**, 173 (1928), *Electron emission in intense electric fields*.

[267] T. E. Stern, B. S. Gossling, and R. H. Fowler, PROCEEDINGS OF THE ROYAL SOCIETY OF LONDON **124**, 699 (1929), *Further studies in the emission of electrons from cold metals*.

[268] R. Gomer, FIELD EMISSION AND FIELD IONIZATION, volume 9 of *Harvard Monographs in Applied Science*, Harvard University Press, Cambridge, 1961.

[269] B. L. Rogers, J. G. Shaptera, W. M. Skinner, and K. Gascoigne, REV. SCI. INSTRUM. **71**, 1702 (2000), *A method for production of cheap, reliable Pt-Ir tips*.

[270] R. M. Penner, M. J. Heben, and N. S. Lewis, ANAL. CHEM. **61**, 1630 (1989), *Preparation and electrochemical characterization of conical and hemispherical ultramicroelectrodes*.

[271] L. A. Nagahara, T. Thundat, and S. M. Lindsay, REV. SCI. INSTRUM. **60**, 10 (1989), *Preparation and characterization of STM tips for electrochemical studies*.

[272] V. Weinstein, M. Slutzky, A. Arenshtam, and E. Ben-Jacob, REV. SCI. INSTRUM. **66**, 4 (1995), *A method for preparation of Pt-Ir tips for the STM*.

[273] S. P. Kounaves, PLATINUM METALS REV. **34**, 131 (1990), *Iridium Based Ultramicroelectrodes, development and use in electrochemical analysis*.

[274] A. Melmed, J. VAC. SCI. TECHNOL. B **9**, 601 (1991), *The art and science and other aspects of making sharp tips*.

[275] B. W. Mao, J. H. Ye, X. D. Zhuo, J. Q. Mu, Z. D. Fen, and Z. W. Tian, ULTRAMICROSCOPY **42-44**, 464 (1992), *A new method of STM tip fabrication for in-situ electrochemical studies*.

[276] L. Libioulle, Y. Houbion, and J. M. Gilles, REV. SCI. INSTRUM. **66**, 97 (1995), *Very sharp platinum tips for scanning tunneling microscopy*.

[277] A. J. Nam, A. Teren, T. A. Lusby, and A. J. Melmed, J. VAC. SCI. TECHNOL. B **13**, 1556 (1995), *Benign making of sharp tips for STM and FIM: Pt, Ir, Au, Pd, and Rh*.

[278] J. Lindahl, T. Takanen, and L. Montelius, J. VAC. SCI. TECHNOL. B **16**, 3077 (1998), *Easy and reproducible method for making sharp tips of Pt/Ir*.

[279] A. H. Sørensen, U. Hvid, M. W. Mortensen, and K. A. Mørch, REV. SCI. INSTRUM. **70**, 3059 (1999), *Preparation of platinum/iridium scanning probe microscopy tips*.

[280] G. M. Shedd and P. E. Russell, NANOTECHNOLOGY **1**, 67 (1990), *The scanning tunneling microscopy as a tool for nanofabrication*.

[281] J. G. Ziegler and N. B. Nichols, TRANSACTIONS OF THE ASME **64**, 759 (1942), *Optimum settings for automatic controllers*.

[282] P. Townsend and J. Sutton, PHYS. REV. **128**, 591 (1962), *Investigation by electron tunneling of the superconducting energy gaps in Nb, Ta, Sn and Pb*.

[283] T. Hanaguri, S. Niitaka, K. Kuroki, and H. Takagi, SCIENCE **328**, 474 (2010), *Unconventional s-wave superconductivity in Fe(Se,Te)*.

[284] S. Vieira, IBM J. RES. DEVELOP. **30**, 553 (1986), *The behavior and calibration of some piezoelectric ceramics used in the STM*.

[285] `http://www.wavemetrics.com/`.

Samenvatting

De hamvraag in de hedendaagse vastestoffysica is hoe hoge temperatuur supergeleiding tot stand komt. Kennis hiervan zou wellicht ertoe kunnen leiden dat een kamertemperatuur supergeleider gemaakt kan worden wat een enorme bijdrage zou leveren aan de oplossing van het steeds groter wordende energieprobleem. Na ongeveer twintig jaar onderzoek aan de groep materialen met de voor zover bekend hoogste overgangstemperatuur, de cupraten, is er nog steeds een hevige discussie gaande over de fysica die schuilt achter de bijzondere eigenschappen van deze materialen. De ontdekking van een compleet nieuwe groep materialen met bijzonder hoge overgangstemperaturen die ook nog eens ijzer bevatten, bracht een nieuwe golf van onderzoek teweeg in de hoop dat de overeenkomsten en verschillen met de cupraten tot een beter begrip zal leiden in hoge temperatuur supergeleiding in het algemeen.

In de onderzoeksgroep was besloten mee te surfen op deze 'pnictide golf' en met hoekopgeloste fotoemissie (ARPES), scanning tunneling microscopie en spectroscopie (STM/S) en lage energie elektronen diffractie (LEED) metingen een steentje bij te dragen aan de gestaag aanzwellende experimentele databank van deze nieuwe groep van supergeleiders. In dit proefschrift worden de STM/S en LEED data gepresenteerd in de hoofdstukken 4 tot 7. Deze metingen zijn voornamelijk toegespits op een subgroep van materialen binnen de familie van ijzer houdende supergeleiders, de $M\mathrm{Fe_2As_2}$ or '122' pnictiden (hier M = Ba, Ca, etc.). Eerst wordt het breukvlak van deze materialen onderzocht, een cruciaal onderdeel van elke oppervlaktegevoelige techniek. Gebruikmakend van temperatuurafhankelijke STM en LEED wordt aangetoond dat het oppervlak van de '122' pnictiden een halve barium (Ba) (of calcium (Ca), ...) laag is, zodanig dat de helft van deze volledige laag op beide kanten van het breukvlak achterblijft. Deze toplaag organiseert zich voornamelijk in twee regelmatige structuren, $(\sqrt{2}\times\sqrt{2})$ en (2×1) respectievelijk, of toont verschillende vormen van wanorde. Met een eenvoudig model worden alle met de STM geobserveerde oppervlaktestrukturen verklaard.

Met een gegronde kennis van het oppervlak wordt in hoofdstuk 5 een spectroscopisch onderzoek aan het materiaal met optimale kobalt (Co) dotering gepresenteerd. De piek-piek afstand in de spectra, die als de supergeleidende energiekloof wordt geïnterpreteerd, blijkt significant te variëren als functie van ruimtelijke lokatie. Een afstand van slechts een nanometer kan het verschil betekenen tussen de maximale en minimale kloof. Door middel van crosscorrelaties tussen hoogteplaatjes en de bijhorende ruimtelijke verdeling van de energiekloof is uitgesloten dat de in hoofdstuk 4 aangetoonde afwijking van de bulksymmetrie van het oppervlak de

oorzaak is van de ruimtelijke variatie in de energiekloof. Doordat de karakteristieke afstand in de kloofinhomogeniteiten vrij goed overeenkomt met de Co-Co separatie worden verstrooïngseffecten van de Co atomen aangedragen als mogelijke oorzaak van de grote variatie in energiekloof.

Vergelijkbare variaties in de piek-piek afstand zijn in het verleden in de cupraten gerapporteerd in de literatuur, maar deze bleken uiteindelijk niet gerelateerd te zijn aan de supergeleidende energiekloof, maar aan een pseudokloof, een energiekloof die niet sluit bij de supergeleidende overgangstemperatuur (T_c) maar tot ver hierboven open blijft. De supergeleidende energiekloof daarentegen, die na deling van een spectrum onder T_c door een spectrum boven T_c wordt verkregen, toonde een stuk minder variatie in grootte. Om te onderzoeken of de variatie in de piek-piek afstand in de pnictiden net als in de cupraten gerelateerd is aan een pseudogap of daadwerkelijk een variatie is in de supergeleidende energiekloof, is de temperatuurafhankelijkheid van de tunnelspectra gemeten met atomaire ruimtelijke precisie. Deze metingen, die in hoofdstuk 6 worden getoond, sluiten een pseudogapscenario in de pnictiden uit.

Door de doteringafhankelijkheid te onderzoeken en de variatie in supergeleidende energiekloof van '122' pnictides die gedoteerd zijn met verschillende elementen met elkaar te vergelijken wordt de oorzaak van de ruimtelijke variaties in de grootte van de energiekloof verder onderzocht in hoofdstuk 7. Geopperd wordt dat verstrooiingseffecten van de Co atomen in de supergeleidende Fe-laag verantwoordelijk zijn voor verscheidene ongewone eigenschappen, waaronder de grote variatie in de supergeleidende energiekloof. Hierdoor is voorzichtigheid geboden bij de interpretatie van de genormaliseerde supergeleidende energiekloof, $2\Delta/k_BT_c$, die uit STS- en fotoemissiemetingen bepaald wordt. Verdere experimentele en theoretische studie van verstrooiing van verschillende dotering atomen op atomaire schaal wordt verwacht een beter inzicht te geven in het mechanisme van supergeleiding in de pnictides.

Voordat de pnictiden de vastestoffysica op zijn kop zetten was het hoofdonderzoek van deze promotie de kolosale magnetoweerstand manganiet $La_{2-2x}Sr_{1+2x}Mn_2O_7$. De kolossale magnetoweerstand manganieten laten als familie een grote verscheidenheid aan exotisch gedrag zien van ladings- en orbitaal geordende isolatoren tot double exchange metalen. Deze verschillende fasen kunnen daarbij in elkaar overgaan door slechts een kleine verandering van elektron- of gatdotering. Wat de materialen zo uniek maakt, is de onwaarschijnlijke gevoeligheid voor een magnetisch veld bij de overgang van een lage temperatuur geleider naar een hoge temperatuur isolator die voor een groot bereik aan doteringconcentraties plaatsvindt. Rond de overgangstemperatuur kan een klein magnetisch veld hierdoor tot een verandering in de weerstand van enkele orden van grootte leiden: het kolossale magnetoweerstand effect.

Het exotische fasediagram van de manganieten is over het algemeen verklaard door de sterke competitie tussen ladings-, orbitaal- en spinvrijheidsgraden. Door

een sterke Hund's regel koppeling zullen de spins op naburige Mn atomen zich parallel uitrichten om hoppen te bevorderen via het het double exchange mechanisme. Aan de andere kant zal energiewinst door roostervervormingen de spins dwingen anti-parallel te ordenen via super-exchange, wat tot een isolator leidt. Een kleine verandering van dotering (m.a.w. Mn bezetting) en temperatuur kan het fragiele evenwicht tussen deze twee hoofdrolspelers veranderen wat tot een compleet ander gedrag kan leiden.

Ondanks dat dit fysisch beeld van het fasediagram aanspreekt, is er nog een hevige discussie gaande over wat precies het kolossale magnetoweerstand (CMR) effect veroorzaakt. Aangezien de tweelaagsmanganiet $La_{2-2x}Sr_{1+2x}Mn_2O_7$ het grootste CMR effect vertoont en het een natuurlijk breukvlak heeft, is dit materiaal bij uitstek geschikt om te onderzoeken met oppervlaktegevoelige technieken zoals STM/S en ARPES. Verscheidene bulktechnieken hebben het materiaal niet als double exchange metaal, maar als een slecht metaal gekarakteriseerd met ongelijke bindings
lengtes and polaronische korrelaties diep in de metaal-achtige toestand. ARPES daarentegen laat op sommige delen van het oppervlak sterke quasideeltjes aan het Fermi oppervlak zien, die de manganieten aan de cupraten lijken te linken als nodal metaal. Door ARPES en STM/S te combineren, waarvan het STM/S gedeelte in hoofdstuk 9 wordt getoond, laten we zien dat ondanks dat het idee van een nodal metaal aanspreekt, dit niet noodzakelijk is voor het CMR effect. Sterker nog, over het gehele gebied in faseruimte waar het CMR effect optreedt (met uitzondering van een singuliere dotering bij x=0.4) is het materiaal bij lage temperatuur in een hoofdzakelijk polaronische toestand wat gekarakteriseerd wordt door slecht ladingtransport en waar polaronen aan het oppervlak in een semi-geordende structuur kunnen vastvriezen. Aan de andere kant kunnen er kleine stukken in het monster voorkomen waar een afwijkende laagdikte voorkomt. Het zijn deze groeifouten waar ofwel meer isolerend (N=1) of echt metallisch (N>2) gedrag wordt gezien. Tijdens de STM/S studie die in dit proefschrift staat beschreven is een dergelijke groeifout met N=1 geobserveerd, wat afgeleid is uit het sterker isolerende gedrag, niet eerder vertoonde scherpe atomaire resolutie en de hoogte van een nabij gelegen stap. Deze nieuwe inzichten die de tweelaagsmanganieten als een fragiel polaronisch metaal op de rand van een overgang naar een isolerende, ladings- en orbitaalgeordende toestand beschrijven, en die stapelfouten als oorzaak van afwijkend gedrag aanwijzen, verenigen alle ogenschijnlijk tegenstrijdige resultaten in de literatuur en geven alle ingrediënten voor het CMR effect.

Naast het hoofdonderzoek in de hoofdstukken 4 tot en met 9, wordt in de appendices een aantal kalibratiemetingen, softwareprocedures en enkele technische details, bijvoorbeeld over het maken van scherpe STM-naalden, beschreven.

Eenvoudige samenvatting

Elk materiaal kan worden geklassificeerd aan de hand van de mate van geleiding. In alledaagse gebruiksvoorwerpen kunnen twee uitersten in geleiding worden gevonden, namelijk isolatoren en geleiders. Isolatoren hebben een bijzonder hoge elektrische weerstand en zullen geen enkele vorm van geleiding vertonen, wat ideaal is voor bijvoorbeeld omhulsels van stroomkabels en de behuizing van elektrische apparaten. Geleiders hebben daarentegen een relatief lage weerstand en geleiden makkelijk een stroom, wat van pas komt in de stroomkabels zelf of het binnenwerk van de elektrische apparaten. De weerstand van een geleider is echter niet volledig weg, maar is erg klein ten opzichte van die van isolatoren. Door deze weerstand zal een geleider nog steeds warm worden als er een hoge stroom doorheen wordt gestuurd (het idee achter een gloeilamp) en zal er energieverlies optreden bij transport van lading (in bijvoorbeeld hoogspanningskabels).

Een zeer bijzondere groep materialen, zogeheten supergeleiders, verliest beneden een bepaalde temperatuur zijn weerstand volledig: er is geen enkel verlies meer, alle stroom die in een supergeleidende draad wordt gestuurd komt er weer uit aan de andere kant. Deze materialen lijken de ideale uitkomst te bieden voor het oplopende energieprobleem aangezien er geen verlies meer is bij het transport van elektriciteit, maar er zit een addertje onder het gras. De hoogste temperatuur waarbij de meeste supergeleiders gaan supergeleiden, de overgangstemperatuur, is rond -240 °C... Er is echter een bepaalde groep koperoxideverbindingen, genaamd de cupraten, die een overgangstemperatuur hebben die kan oplopen tot -130 °C, wat voor fysische begrippen al aardig in de buurt van kamertemperatuur komt. Mogelijkerwijs zou een begrip van deze cupraten kunnen leiden tot de daadwerkelijke ontwikkeling van een kamertemperatuur supergeleider. Na twintig jaar onderzoek is veel opgehelderd over de oorzaak van hun bijzondere eigenschappen, maar is het exacte mechanisme van de hoge temperatuur supergeleiding nog steeds een mysterie. Gedurende dit promotieonderzoek is er door een Japanse onderzoeksgroep een nieuwe familie supergeleiders ontdekt met een onverwacht hoge overgangstemperatuur. Deze supergeleiders bevatten daarnaast ook nog ijzer, een element dat normaal gesproken bijzonder slecht samengaat met supergeleiding. In de hoop dat deze nieuwe familie van materialen een doorbraak zou kunnen forceren in het vraagstuk van de hoge temperatuur supergeleiding, werd het in korte tijd het meest bestudeerde materiaal in de vastestoffysica, zo ook binnen de eigen onderzoeksgroep.

In de hoofdstukken 4 tot en met 7 worden metingen met een scanning tunnel mi-

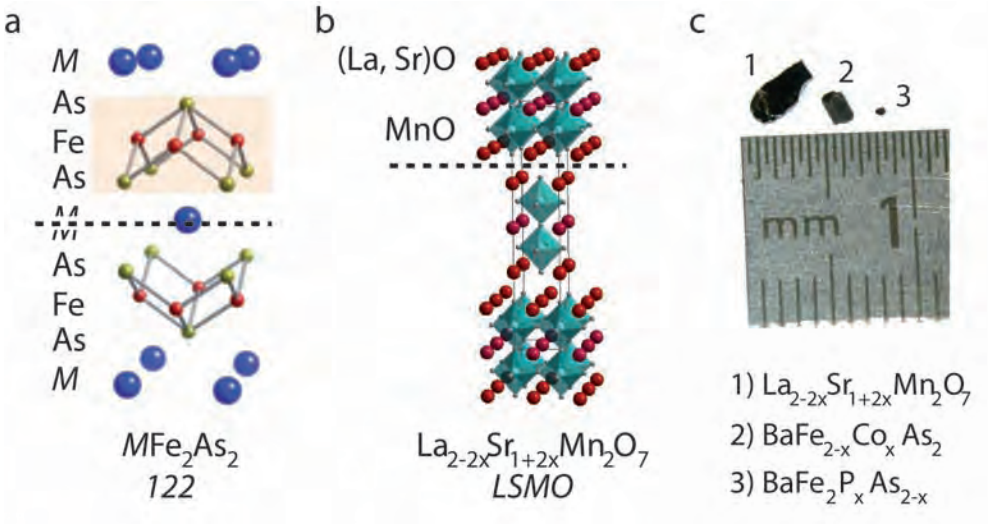

S 1: (a) Kristalstruktuur van MFe$_2$As$_2$, met M = Ba, Ca, Sr, ... Het materiaal wordt pas supergeleidend als een deel van een van de bouwstoffen wordt vervangen door een ander element, bijvoorbeeld kobalt voor ijzer of fosfor voor arseen. De stippelijn geeft het vlak aan waar het kristal breekt, wat in dit geval door de M-laag is. (b) De kristalstruktuur van $La_{2-2x}Sr_{1+2x}Mn_2O_7$. De blauwe octahedra zijn opgespannen door zuurstofatomen met een mangaanatoom in het centrum, de rode bollen zijn lantaan en strontium posities. Het breukvlak is in dit geval tussen de (La,Sr)O lagen in. (c) Ter illustratie zijn typische kristallen van de onderzochte materialen weergegeven.

croscoop aan een van deze nieuwe supergeleiders gepresenteerd. Het bestudeerde materiaal bestaat uit 'broodjes' van ijzer (Fe) en arseen (As) met daartussen als beleg een laag barium (Ba), calcium (Ca), strontium (Sr) of europium (Eu), zoals is weergegeven in figuur S1a. De structuurformule van deze materialen is MFe$_2$As$_2$, waar de M staat voor Ba, Ca, Sr of Eu. Vanwege de verhouding van de verschillende elementen wordt deze groep materialen ook wel de '122' groep genoemd. Om deze materialen supergeleidend te krijgen dient echter een van de elementen waaruit ze bestaan deels vervangen te worden door een ander element, bijvoorbeeld een deel van de ijzeratomen door kobaltatomen.

Zoals gezegd is het stofje te vergelijken met een gigantische stapel identieke ijzer-arseen broodjes met een laag barium (of calcium, ..) als beleg. Omdat het oppervlak van het monster (het bovenste sneetje brood) smerig kan zijn, zal voordat een meting gedaan kan worden het materiaal open moeten worden gebroken om een vers oppervlak te krijgen. Aangezien de bestudeerde stoffen nooit eerder gemaakt en gemeten waren, is eerst onderzocht welke laag na breken aan het oppervlak ligt: de ijzer-arseen laag, de barium laag of een tussenvariant. Het is belangrijk om exact te weten welke laag van het materiaal aan het oppervlak ligt omdat metingen die voornamelijk gevoelig zijn voor deze toplaag erdoor beïnvloed zouden kunnen

worden: het zou zomaar kunnen dat de metingen niet iets zeggen over de stof in het algemeen, maar alleen over het oppervlak. Aan de hand van de gepresenteerde metingen wordt geconcludeerd dat de bovenlaag na het breken de helft van een Ba laag (of Ca, ...) is die op verschillende manieren zich kan ordenen of wanordelijk is. Met deze kennis van het oppervlak in het achterhoofd zijn vervolgens metingen gedaan die meer inzicht in de elektronische eigenschappen van het materiaal kunnen geven.

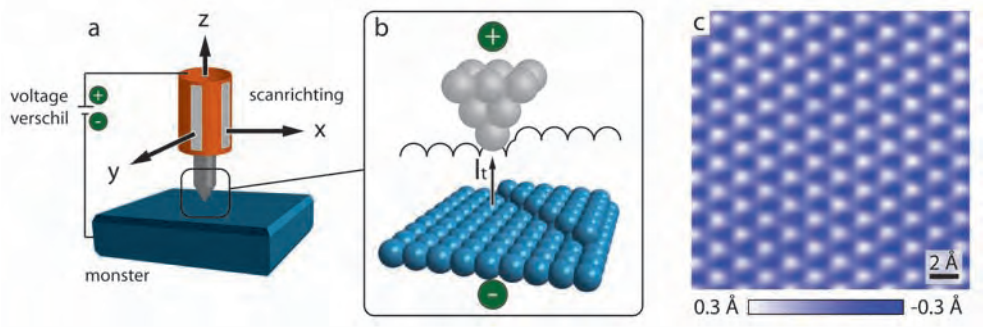

S 2: (a) Schematische weergave van de STM: een scherpe naald is op een xyz-scanner gemonteerd en dichtbij een oppervlak gebracht. Door een voltageverschil (V) tussen monster en naald zal er een stroom (I_t) lopen. (b) Als de stroom constant wordt gehouden door de hoogte aan te passen met een feedbackloop wordt de contour van het oppervlak gekregen. Een typisch voorbeeld van een dergelijk hoogteplaatje van grafiet is getoond in (c), de lichte bolletjes zijn de koolstof atomen.

Om deze metingen beter te begrijpen zal eerst de scanning tunnel microscoop (STM) kort worden uitgelegd. In feite is de microscoop niets anders dan een scherpe naald die dicht bij een oppervlak wordt gebracht, maar zonder het oppervlak daadwerkelijk aan te raken. Een elektron, een geladen deeltje, kan klassiek gezien niet van het oppervlak naar de naald bewegen omdat er vacuüm tussen beide zit. Het vacuüm fungeert in feite als het glas rond een leeuwenkooi: de leeuw (het elektron) kan vrij rondlopen in de kooi (de naald) of erbuiten (het monster), maar het glas (vacuüm) voorkomt dat hij ontsnapt uit de kooi. Een elektron is echter niet strikt genomen een deeltje, maar kan ook als golf beschreven worden. Deze golf kan wel het stukje vacuüm overbruggen zolang de door het vacuüm af te leggen afstand maar niet te groot is. Evenzo kan de schreeuw van de leeuw door het glas komen zolang het glas maar niet te dik is. Omdat het elektron zowel een deeltje als een golf is, kan het dus toch van het oppervlak naar de naald 'springen', terwijl de leeuw die alleen een 'deeltje' is gelukkig in zijn kooi blijft. Door een voltageverschil aan te leggen tussen de naald en het oppervlak worden de elektronen gedwongen 'slootje te springen' door het vacuüm. Het stroompje dat op deze manier gaat lopen tussen het oppervlak en de naald bevat een zee aan informatie over het materiaal. De grootte van het stroompje geeft een indicatie voor het aantal ladingsdragers dat beschikbaar

is en door het spanningsverschil tussen het oppervlak en de naald te variëren kan worden gekeken hoeveel ladingsdragers er aanwezig zijn als functie van de spanning. Deze gegevens kunnen vervolgens vergeleken worden met berekeningen om ze te interpreteren. Uit de analogie met de glazen kooi is ook te begrijpen dat de stroom groter wordt naarmate de naald dichter bij het oppervlak komt: een dunner stuk glas demp het geluid minder.

Stel nu dat de leeuw brult met een constant volume, maar dat het glas op sommige plekken dikker is dan op andere. Door naar voren en naar achteren te bewegen terwijl je langs de kooi loopt kan het ontvangen geluid gelijk worden gehouden. Op deze manier kunnen de verschillen in dikte van het glas exact bepaald worden zonder het glas aan te raken. Op dezelfde manier kan met de STM een plaatje van de hoogteverschillen gemaakt worden door de naald over het oppervlak te bewegen en de hoogte aan te passen opdat de stroom hetzelfde blijft. Een illustratie van de meettechniek wordt in figuur S2 getoond. Het bijzondere aan de STM is dat deze hoogteverschillen enkele picometers zijn en de stapgrootte in de horizontale richting klein genoeg is om atomen zichtbaar te maken zoals in figuur S2c te zien is. Ter vergelijking, een atoom verhoudt zich tot een pingpongbal als een pingpongbal zich tot de aarde verhoudt. Anders gezegd, atomen met de STM zien is vergelijkbaar met het detecteren van een haar met de punt van de Eiffeltoren. De elektronische eigenschappen van een materiaal kunnen met de STM dus op atomaire schaal bekeken worden!

Op de ijzerhoudende supergeleiders is onderzocht wat de elektronische eigenschappen zijn als functie van positie op het oppervlak. Bijvoorbeeld de supergeleidende bindingsenergie is bepaald uit energieafhankelijkheidsmetingen. Deze bindingsenergie geeft meer inzicht in het mechaniek van supergeleiding en blijkt in dit geval een bijzonder hoge waarde te hebben. Merkwaardig is dat de grootte van deze bindingsenergie een forse variatie vertoont als functie van de positie op het oppervlak. De typische afstanden van deze variatie en metingen aan monsters met een verschillende concentratie kobalt (Co) (die de ijzeratomen vervangen) suggereren dat de kobaltatomen voor een relatief grote wanorde in het supergeleidende ijzervlak zorgen. Dat ondanks deze wanorde het materiaal toch supergeleidend wordt en blijft is verbazingwekkend en kan ons meer te weten brengen over het mechaniek van de supergeleiding zelf.

Het laatste deel van het proefschrift, de hoofdstukken 8 en 9, beschrijft het onderzoek dat uitgevoerd is in het begin van de promotieperiode, voordat de ijzerhoudende supergeleiders ontdekt waren. Dit onderzoek richt zich op een ander bijzonder fenomeen dat zich afspeelt in een materiaal dat van een geleidende toestand bij lage temperatuur naar een isolerende bij hoge temperatuur overgaat. In de buurt van deze overgang, die zich rond -140 °C bevindt, kan door middel van een magneetveld de overgangstemperatuur verschoven worden. Hierdoor is het mogelijk bij dezelfde temperatuur een verschil in weerstand van een factor 100 tot 10000 tot stand te brengen door slechts een magneetveld aan te leggen. Dit effect wordt het kolossale magneetweerstandseffect genoemd en is al jaren bron voor veel discussie.

Binnen de onderzoeksgroep zijn metingen met verschillende technieken uitgevoerd, waarvan de STM metingen in dit proefschrift besproken worden. Al deze metingen samen tonen aan dat de geleidende lage temperatuur toestand in het stofje met het grootst mogelijke kolossale magneetweerstandseffect, de tweelaagsmanganiet $La_{2-2x}Sr_{1+2x}Mn_2O_7$ die in figuren S1b en c is weergegeven, eigenlijk een zeer matig geleidende toestand is. Dit resultaat staat haaks op het gangbare denkbeeld dat het materiaal bij lage temperatuur een goed metaal is. Het blijkt dat de elektronen die de lading dragen met hun aanwezigheid het kristalrooster vervormen. Hierdoor moeten ze als het ware het rooster met zich meeslepen als ze door het materiaal willen bewegen, wat de weerstand verhoogt. Uit de STM metingen lijkt zelfs te volgen dat deze zogenaamde polaronen (elektronen die het rooster vervormen) in een semi-geordend rooster aan het oppervlak vast kunnen komen te zitten bij lage temperatuur.

Ook wordt de bijzondere gevoeligheid van de elektronische eigenschappen voor de dimensionaliteit (de mate van gelaagdheid) in deze materialen aangetoond. Het is onvermijdelijk dat een paar procent van het materiaal niet de struktuur heeft zoals afgebeeld in figuur S1b, geen enkel kristal is perfect. Daardoor zal op sommige stukjes de stof niet telkens twee aaneengesloten mangaan-oxide vlakken (N=2) hebben, maar meer (N>2) of minder (N=1) (zie ook figuur 8.1). Een roostervervorming rond een elektron zal steeds kostbaarder worden naarmate het aantal aaneengesloten lagen toeneemt: er zijn steeds meer buren die tegenwerken. De vervorming zal dus afnemen, waardoor de elektronen makkelijker kunnen bewegen en de geleiding zal toenemen. In een enkellaags systeem is precies het omgekeerde aan de hand en zal een nog slechtere of zelfs isolerende toestand ontstaan. Een dergelijk stukje eenlaagsmanganiet is met de STM in beeld gebracht in hoofdstuk 9. In tegenstelling tot vrijwel alle metingen op de tweelaagsmanganiet, zijn op dit kleine stukje eenlaagsmanganiet de niet eerder op grote schaal zichtbaar gemaakte atomen duidelijk te zien. De resultaten van dit gecombineerde onderzoek verenigen alle op het eerste gezicht tegenstrijdige resultaten uit de literatuur en leggen de basis voor een beter begrip van het kolossale magneetweerstandseffect.

Publications

F. Massee, S. de Jong, Y. K. Huang, J. Kaas, E. van Heumen, J. B. Goedkoop and M. S. Golden
Cleavage surfaces of the $BaFe_{2-x}Co_xAs_2$ and $Fe_ySe_{1-x}Te_x$ superconductors: A combined STM plus LEED study
Phys. Rev. B **80**, 140507(R) (2009) (chapter 4)

E. van Heumen, J. Vuorinen, K. Koepernik, F. Massee, Y. K. Huang, M. Shi, J. Klei, J. B. Goedkoop, M. Lindroos, J. van den Brink, M. S. Golden
Existence, character and origin of surface-related bands in the high temperature iron pnictide superconductor $BaFe_{2-x}Co_xAs_2$
Phys. Rev. Lett. **106**, 027002 (2011) (chapter 4)

F. Massee, Y. K. Huang, R. Huisman, S. de Jong, J. B. Goedkoop and M. S. Golden
Nanoscale superconducting-gap variations and lack of phase separation in optimally doped $BaFe_{1.86}Co_{0.14}As_2$
Phys. Rev. B **79**, 220517(R) (2009) (chapter 5)

F. Massee, Y. K. Huang, J. Kaas, E. van Heumen, S. de Jong, R. Huisman, H. Luigjes, J. B. Goedkoop and M. S. Golden
Pseudogap-less high T_c superconductivity in $BaCo_xFe_{2-x}As_2$
EPL **92**, 57012 (2010) (chapter 6)

F. Massee, E. van Heumen, Y. K. Huang, J. Kaas, R. Huisman, H. Luigjes, J. B. Goedkoop and M. S. Golden
Disorder induced gap variations in the $BaCo_xFe_{2-x}As_2$ superconductor
in preparation (chapter 7)

F. Massee*, S. de Jong*, Y. Huang, W. K. Siu, I. Santoso, A. Mans, A. T. Boothroyd, D. Prabhakaran, R. Follath, A. Varykhalov, L. Patthey, M. Shi, J.B. Goedkoop and M. S. Golden
Bilayered manganites: polarons in the midst of a metallic breakdown
submitted (chapter 9)

S. de Jong, E. van Heumen, S. Thirupathaiah, R. Huisman, F. Massee, J. B. Goedkoop, R. Ovsyannikov, J. Fink, H. A. Dürr, A. Gloskovskii, H. S. Jeevan, P. Gegenwart, A.

Erb, L. Patthey, M. Shi, R. Follath, A. Varykhalov and M. S. Golden
Droplet-like Fermi surfaces in the anti-ferromagnetic phase of $EuFe_2As_2$, an Fe-pnictide superconductor parent compound
EPL **89**, 27007 (2010)

S. de Jong, F. Massee, Y. K. Huang, M. Gorgoi, F. Schaefers, J. Fink, A. T. Boothroyd, D. Prabhakaran, J. B. Goedkoop and M. S. Golden
High-resolution hard x-ray photoemission investigation of $La_{2-2x}Sr_{1+2x}Mn_2O_7$ (0.30<=x<0.50): Microscopic phase separation and surface electronic structure of a bilayer colossal magnetoresistance manganite
Phys. Rev. B **80**, 205108 (2009)

S. de Jong, Y. K. Huang, R. Huisman, F. Massee, S. Thirupathaiah, M. Gorgoi, F. Schaefers, R. Follath, J. B. Goedkoop and M. S. Golden
High-resolution, hard x-ray photoemission investigation of $BaFe_2As_2$: Moderate influence of the surface and evidence for a low degree of Fe 3d-As 4p hybridization of electronic states near the Fermi energy
Phys. Rev. B **79**, 115125 (2009)

S. de Jong, Y. K. Huang, I. Santoso, F. Massee, R. Follath, O. Schwarzkopf, L. Patthey, M. Shi and M. S. Golden
Quasiparticles and anomalous temperature dependence of the low-lying states in the colossal magnetoresistant oxide $La_{2-2x}Sr_{1+2x}Mn_2O_7$ (x=0.36) from angle-resolved photoemission
Phys. Rev. B **76**, 235117 (2007)

Nawoord

Als de dag van gisteren herinner ik me dat ik op gesprek mocht komen bij Jeroen om het over mijn intenties en gedrevenheid voor een promotie met de STM te hebben. De legendarische woorden, 'je zult in het eerste jaar moeten publiceren' en 'met een techniek als STM zul je moeten toeslaan wanneer het kan, wat soms langer doorwerken tot gevolg heeft...' bleven (zeker na het eerste jaar zonder publicatie) door mijn hoofd spoken. Uiteindelijk zijn de publicaties toch nog gekomen en mijn excuses aan Jeanette voor de vreemde werktijden (bijvoorbeeld het om 8.00 thuiskomen na de meting in figuur 6.1).

Ik ben erg blij dat ik dit promotieonderzoek heb mogen doen en wil in de eerste plaats Mark en Jeroen bedanken dat ik hierin de vrijheid heb gekregen mijn eigen weg uit te stippelen. Als ik dan na veel stoeien, prutsen en wat geluk een nieuw resultaat had, was altijd wel een van de twee beschikbaar om mee te denken over verklaringen, analyses en vervolgmetingen. De combinatie van jullie totaal verschillende (en soms ietwat botsende) ideeën en expertise waren voor mij ideaal om als koppige Noord-Hollander te proberen het beste uit te halen. Jeroen, ondanks dat ik niet je droom op tijds- en ruimtelijk opgeloste fluctuatie spectroscopie heb gerealiseerd, hoop ik dat je toch tevreden bent met het wegnemen van het voodoo element in STM (inmiddels gaan de metingen niet meer mis als je onverhoopt langskomt). Mark, van de zomerschool in Zuoz, tot conferenties in Vancouver en Tokio en tijdens de vele beamtimes, je gedrevenheid, enthousiasme en kennis van zaken hebben altijd aanstekelijk gewerkt.

Naast Mark en Jeroen zijn er nog een groot aantal mensen die hebben bijgedragen aan het hier beschreven onderzoek. Sanne, met geen ander heb ik zoveel meegemaakt: talloze beamtimes (non-stop Dire Straits), conferenties, MahJong/Street Fighter avonden en bezoekjes over en weer in het lab. Wat ik nooit zal vergeten is je ontembare passie (in nuchtere toestand) in de karaokekeet in Tokio (videomateriaal beschikbaar op aanvraag). Vooral de 5 minuten kelderbezoekjes zijn van grote waarde geweest in de voortdurende strijd beter te meten en analyseren. Erik van Heumen, bedankt voor je hulp en inzet bij het proberen te begrijpen van de metingen en je frisse, kritische blik op de gebruikte routines en meettechnieken. Speciale dank gaat uit naar de maestro van de samples, Ying Kai. Het was net Sinterklaas als ik weer een paar samples uit mocht zoeken! Huib, of het nu tips maken is, iets bestellen of gewoon voor een praatje, ik kan altijd bij jouw terecht. Ook dank aan de leden van de 'hard condensed matter' groep die tijdens groepsbesprekingen en daarbuiten bijdroegen aan het werk: Anne de Visser, Steve, Rein, Erik 'broodje Unox' Slooten,

'boom boom' Stan, Marco, Jochem, Alessia, Gianni (nogmaals excuses dat ik je bijna in het water liet vallen bij de Poldersurvival), Ton, Wim en Nick. Ook dank aan de wandelende encyclopedie van het instituut, Hugo: bij twijfel (of als je werkelijk geen enkel idee hebt), vraag Hugo. René Rik, bedankt voor de altijd aanwezige He of N_2 gasflessen/dewars (zelfs als ik vergeten was te bestellen).

In de doorlopende zoektocht naar verbeteringen van de opstelling gaat veel dank uit naar de elektronische en mechanische werkplaats van het Van der Waals Zeeman Instituut. Voor alle vragen over elektronica, ruis of iets willekeurig anders is Hans Agema de aangewezen persoon. Hans, ontzettend bedankt voor al die keren dat ik even aan kwam waaien en je me buiten de voorgeschreven gang van zaken (m.a.w. direct i.p.v. via via) hebt geholpen! Ook dank aan Piet en Johan voor de vele klusjes die altijd snel voor elkaar waren. Van de mechanische werkplaats en tekenafdeling, dank aan Ron, Hans Ellermeijer, Erik Hennes, Wietze, Harry, Diederik, Henk, Udo, Gerrit, Wim (SteadyShot werkt echt goed) voor alle tekeningen, aanpassingen en hand- en spandiensten waarvoor ik altijd wel terecht kon. En uiteraard niet te vergeten, Joost, ook voor de altijd riant aanwezige sinaasappelsap op borrels en de dag erna!

For all technical and software related troubleshooting I would like to thank Sven Zöphel of Createc GmbH, who kindly responded to all questions I could think of and helped get the machine to where it is now. Ad Ettema van Specs Nanotechnology, bedankt voor de snelle en flexibele afhandeling van bestellingen/vragen/etc..

I would like to thank Richard, for letting me borrow stuff without having to return it (or at least that's what I did...) and for the never ending running joke on our names.

Luuk, Rita en Ineke, en al diegene die tijdens pauzes, in de gangen of elders op het instituut het leven als promovendus hebben veraangenaamd, bedankt.

Ten slotte: Rob, Riet en Sandra, ziehier waar ik mij de afgelopen vier jaar mee heb beziggehouden en waardoor ik steeds minder kwam buurten. Het is altijd heerlijk om even de oase van rust op te zoeken in het mooie Zwaag (of Blokker) en weer even bij te praten (of spitten, deuren maken, motoren winterklaar maken etc.). Ik mag me gelukkig prijzen met een familie als jullie!

Over de auteur

Op 4 mei 1983 zag ik het licht in Hoorn waarna ik ben opgegroeid in het naburige Zwaag. Na mijn middelbare schoolperiode van 1995 tot 2001 op het O.S.G. Westfriesland te Hoorn te hebben doorgebracht ben ik voor een jaar naar Groningen vertrokken om een propedeuse Natuur- en Sterrenkunde aan de Rijksuniversiteit Groningen te behalen. Vervolgens heb ik in de jaren 2002 tot 2006 zowel het kandidaats- als master diploma aan de Universiteit van Amsterdam behaald (beide *cum laude*). Tijdens de master heb ik een korte stage aan het Natuurkundig Instituut van de Poolse Academie voor Wetenschappen te Warschau gedaan, alwaar metingen zijn verricht aan de magnetisatie van Fe-Pd nanodeeltjes met verschillende concentratieverhoudingen. Mijn masterscriptie was getiteld *The quest for underdoping - resistivity and ARPES measurements on* $(Pb,Bi)_2Sr_2CaCu_2O_{8+\delta}$. Tijdens dit onderzoek in de groep van Prof. Dr. M.S. Golden is geprobeerd door middel van warmtebehandelingen in verschillende atmosferen een veel bestudeerde koper-oxide hoge temperatuur supergeleider van zuurstof te ontdoen waardoor de interessante 'pseudogap' toestand bereikt kan worden. Weerstands- en hoekopgeloste fotoemissie metingen werden gebruikt om te onderzoeken of deze toestand daadwerkelijk bereikt was. Na het behalen van het masterdiploma ben ik voor vier maanden naar Australië en Nieuw-Zeeland vertrokken om vanaf april 2007 fris aan het hier beschreven promotieonderzoek te starten.